Contribution à la Modélisation et à l'Optimisation de la Machine Asynchrone Double Alimentation pour des Applications Hydrauliques de Pompage Turbinage

Thomas Lugand

UNIVERSITÉ DE GRENOBLE

THÈSE

Pour obtenir le grade de

DOCTEUR DE L'UNIVERSITÉ DE GRENOBLE

Spécialité : **Génie Électrique**

Arrêté ministériel : 7 aout 2006

Présentée par

Thomas LUGAND

Thèse dirigée par **Gérard Meunier**
et codirigée par **Albert Foggia**

préparée au sein du **Laboratoire de Génie Électrique de Grenoble (G2Elab)**
et de l'**École Doctorale Électronique, Électrotechnique, Automatique et Traitement du Signal (EEATS)**

Contribution to the Modeling and Optimization of the Double-Fed Induction Machine for Pumped-Storage Hydro Power Plant Applications

Thèse soutenue publiquement le **2 décembre 2013**,
devant le jury composé de :

Christophe ESPANET
Professeur à l'université de Franche-Comté, Président
Mohamed BENBOUZID
Professeur à l'université de Brest, Rapporteur
Yvan LEFEVRE
Chargé de Recherche au CNRS de Toulouse, Rapporteur
Alexander SCHWERY
Directeur R&D Électrique chez ALSTOM Renewable Power Switzerland, Examinateur
Albert FOGGIA
Professeur Émérite à Grenoble-INP, Co-Directeur de thèse
Gérard MEUNIER
Directeur de Recherche au CNRS de Grenoble, Directeur de thèse

Acknowledgements

I would like to thank Alexander Schwery, R&D Electrical Director at Alstom Renewable who proposed me this thesis subject and who gave me the chance to work in his department.

I would like to express my sincere gratitude to Albert Foggia, Professor at Grenoble-INP and Gérard Meunier, Senior Researcher at Grenoble CNRS, for their support and for having supervised my work.

I would like to thank all the members of the jury, Christophe Espanet, Professor at Franche-Comté University, Mohamed Benbouzid Professor at Brest University and Yvan Lefevre, Researcher at Toulouse CNRS for taking time to study and to review my work.

I am very grateful to my former colleague Georg Traxler-Samek as well as my colleagues from Alstom Birr, Carlos Ramirez and Glenn Ardley for their help and for sharing their experience about electrical machines.

I would like to thank Hans Werner Lorenzen, Professor at TU Munich, for his help and for sharing his experience about the double-fed induction machine.

I would like to thank Afef Lebouc, Senior Researcher at Grenoble CNRS, for sharing her experience about magnetic material modeling.

I am very grateful to Daho Taghezout from the company applied magnetics for his support and advices relative to electrical machines and finite element computations.

I would like to express my sincere gratitude to my colleagues from Global Technology Centre in Alstom Birr, in particular Peter Tönnies for his help with LaTeX, as well as all the personnel from Grenoble Electrical Engineering Laboratory for their support and for their kindness.

I would like to thank my friends for their support and in particular Bénédicte, Bernard, Jonathan, Nathanael and Michael for the good moments in Grenoble.

Finally I would like to thank my parents and Christina for their support as well as my little Lara for the perfect timing.

Contents

List of Figures

List of Tables

Acronyms

2D	Two-Dimensional
2DFE	Two-Dimensional Finite Element
3D	Three-Dimensional
3DFE	Three-Dimensional Finite Element
BDFIM	Brushless Double-Fed Induction Machine
BE	Boundary Element
BEM	Boundary Element Method
dc	direct-current
DFIM	Double-Fed Induction Machine
FE	Finite Element
FEM	Finite Element method
mmf	magneto-motive force
p.u.	Per Unit
PSP	Pumped-Storage Plants
PWM	Pulse Width Modulation
RMS	Root Mean Squared
rpm	Revolutions per minute
THD	Telephone Harmonic Distortion
THF	Telephone Harmonic Factor
VSI	Voltage Switched Inverter

1 Introduction

1.1 Regulating Power by using Pumped-Storage Hydro Power Plants

In order to respond to the increasing demand for electricity, more efficient solutions of energy production and storage have to be proposed.

Firstly, conventional sources of energy such as nuclear and gas power plants considered as the main *Base-Load* producers are able today to meet the principal demands of electricity. However such technologies are not able to respond quickly to sudden increases of energy demand. Solutions such as petrol or coal power plants are neither economical nor environmental-friendly.

Secondly, the tendency motivated by environmental concerns is to offer alternative or complementary solutions to these main sources of energy. In this context wind power installation, for example, is continuously increasing as shown in Figure 1.1. Although renewable energies are viable technologies, the issue of sporadic availability, wind and solar not being constant, leads to problems for planning and regulation of power available on the network. In some cases the total supplied power might exceed the demand. This leads to a perturbation of the network frequency and can affect other elements connected to the network.

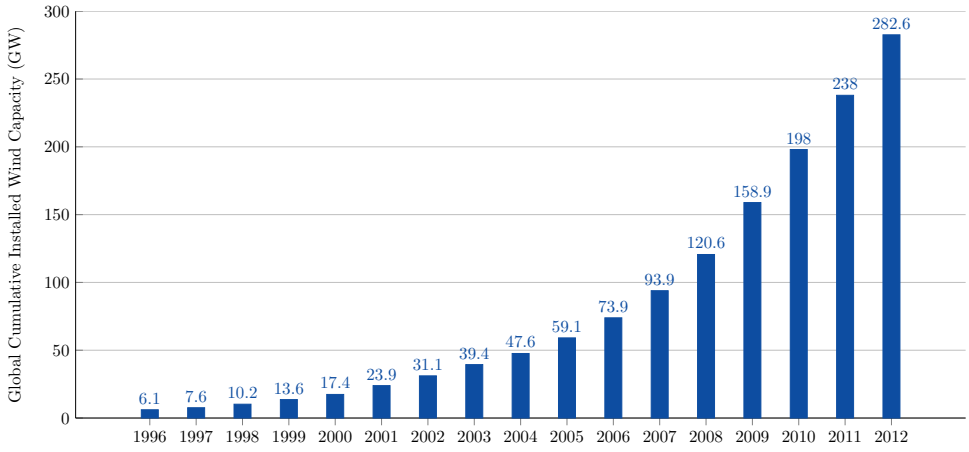

Figure 1.1: Global Cumulative Installed Wind Capacity 1996-2012 [GWE12]

Thirdly, electricity exchanges are today strongly governed by price and demand. This trading of energy leads to fluctuations of power and consequently instabilities of the network.

Hydro Pumped-Storage Plants (PSP) are used as network stabilizers and to achieve a balance between demand and supply. PSP are like any standard hydro power plant with motor/generator units coupled to hydro turbines. Such installations make it possible not only to deliver electricity

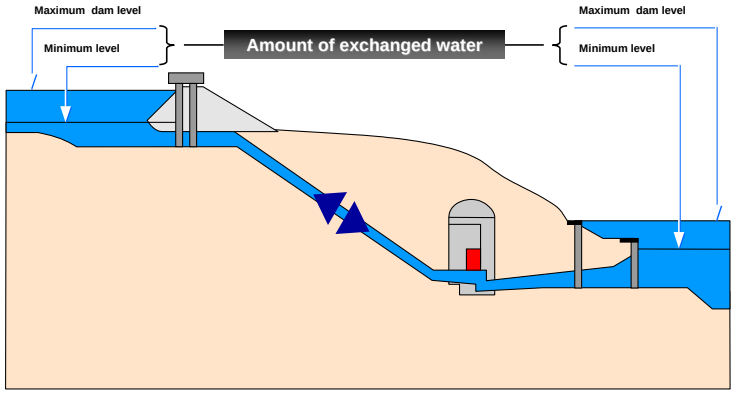

Figure 1.2: PSP structure [Sch06]

to the network but also to absorb power from the network. Electricity production is realized by providing water from an upper reservoir to a lower reservoir, mechanical power from the turbine is transformed into electricity via the motor/generator unit working as a generator. Electricity absorption is realized by pumping water from the lower reservoir to the upper reservoir. Electricity in this case is transformed into stored potential energy via the motor/generator unit operating as a motor. Figure 1.2 provides an overview of a PSP structure.

In turbine operation, PSP makes it possible to fill the power gap when the demand is higher than the supply from the available energy sources. Alternately when the supply is higher than the demand, PSP in pumping operation stores the surplus energy.

Consequently PSP appears as an efficient means of energy storage and network power regulation. PSP activity is continuously increasing which is directly linked to the expansion of renewable and nuclear energies, as shown in Figures 1.1 and 1.3. In order to improve the efficiency of PSP, variable-speed operation has been proposed. This is described in more detail in the next section.

1.2 Benefits of using Variable Speed for PSP applications

To dates conventional PSP installations have been mainly working at fixed speed. This means the turbine rotates at a fixed speed proportional to the network frequency. Such installations are equipped with a salient-pole synchronous motor/generator unit directly connected to the network via a transformer. Like standard synchronous machines, the stator consists of a three-phase winding carrying alternating current while the rotor is equipped with a simple winding, also called field winding, carrying a direct current. Figure 1.4 shows an example of such installation. Usually it is equipped with a reversible *Francis*-type runner, being able to work as a turbine in one direction and as a pump in the other direction. Note that, depending on the installation, generator and motor operations may also be done with a separate turbine and pump. This makes it possible to switch faster from the turbine to the pumping mode, but requires also more space than the reversible arrangement.

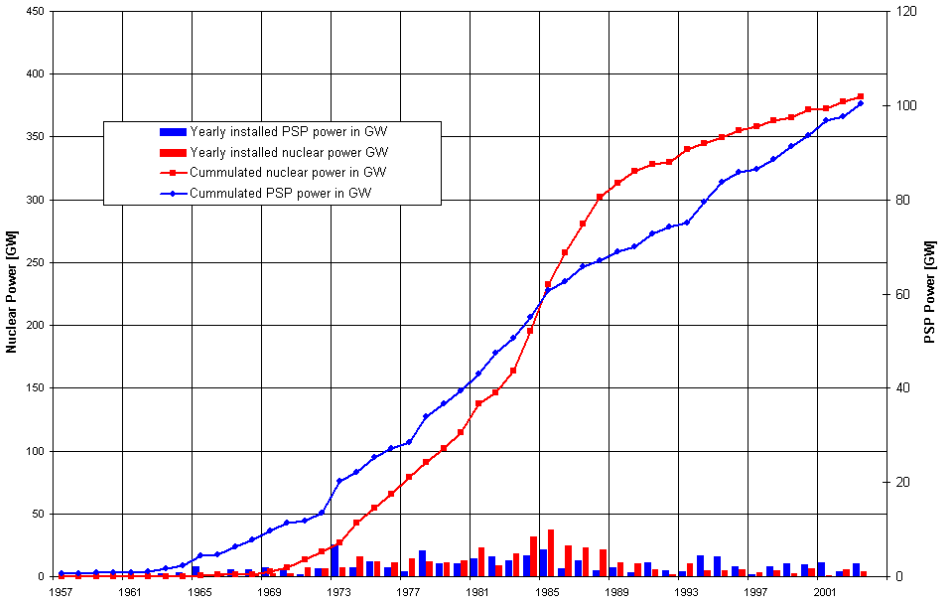

Figure 1.3: World wide expansion of PSP and nuclear activity [Sch+05]

In turbine operation, the active power is regulated by the opening and closing of the guide vanes. Regulation of the reactive power is done by controlling the field winding current. In motor operation the range of power variation is very limited. The only way to efficiently change the amount of power taken from the network is to change the speed of operation. For the past few years, variable-speed technology has been seriously studied as a relevant technology. With this technology it is possible to produce or absorb network power at constant frequency within a certain range of rotational speeds. In the following we describe the advantages of changing the speed of operation [SS97; Sch+05].

1.2.1 Better Control of the power in pumping mode

Pump characteristics are given as a function of Head (pressure) and Flow as shown in Figure 1.5. The operation point is obtained at the intersection between the actual head (on the graph H example) and the working speed. When considering a fixed speed, only one point exists (red circle). When the speed can be changed from N_1 to N_3, any operation points on the doted line can be reached. The blue circles are two accessible points and correspond to the minimum and maximum power. Depending on the head, the power can be varied over a range of thirty percent [Sch+05]. Changing the speed also makes it possible to work at the best efficiency given by the intersection (green circle) between the available head and the maximum efficiency line.

1.2.2 Work at the best operation point in turbine mode

Considering maximum and minimum operating head ($H_{\max}$ and $H_{\min}$) *Francis*-turbine design is normally optimized for pumping operation. As shown in Figure 1.6, the peak of the hill

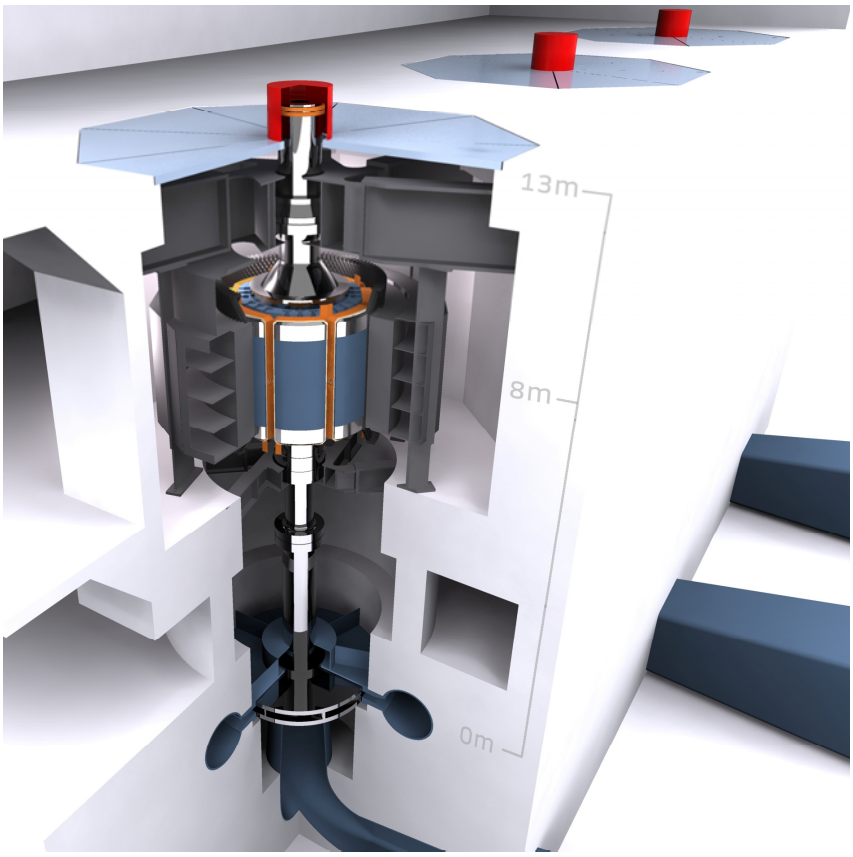

Figure 1.4: Salient-pole synchronous motor/generator and turbine (Alstom image)

chart (in green), which is linked to the optimum operation, cannot be reached. Consequently the efficiency is limited during turbine operation. Changing the speed makes it possible to find other optimum working points for the turbine. Furthermore, the head, which is linked to the water level, is not a constant parameter over the time. The operation point of the turbine is changing and consequently the efficiency may decrease. Adjusting the speed makes it possible to work again at the best efficiency, over a range of available head.

Figure 1.7 compares, for a given installation, turbine relative efficiencies when considering fixed and variable-speed operation. In this case the relative increase of efficiency is about one percent with variable-speed operation.

1.2.3 Better tracking of the power

In turbine operation, PSP fixed-speed units only work when the demand of power is maximum, i.e. 100% of the unit-s rated power. Out of this zone, the machine is stopped. On the contrary variable-speed units make it possible to better follow the variation of the power. Consequently the power regulation is better and the number of starts/stops is reduced. Figure 1.8 highlights the possible zones of operation of both technologies and demonstrates the better tracking of the

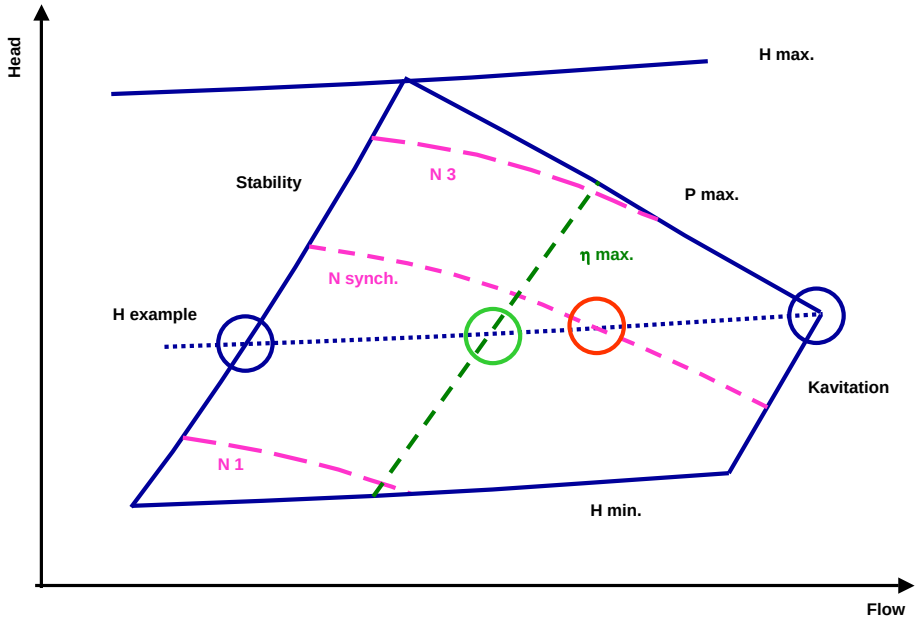

Figure 1.5: Pump characteristics example [Sch+05]

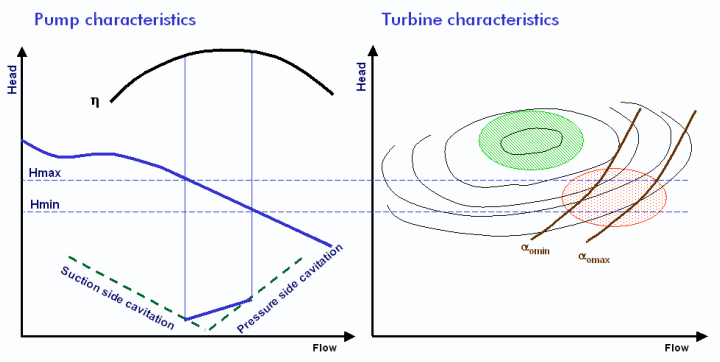

Figure 1.6: Pump and Turbine characteristics [Sch+05]

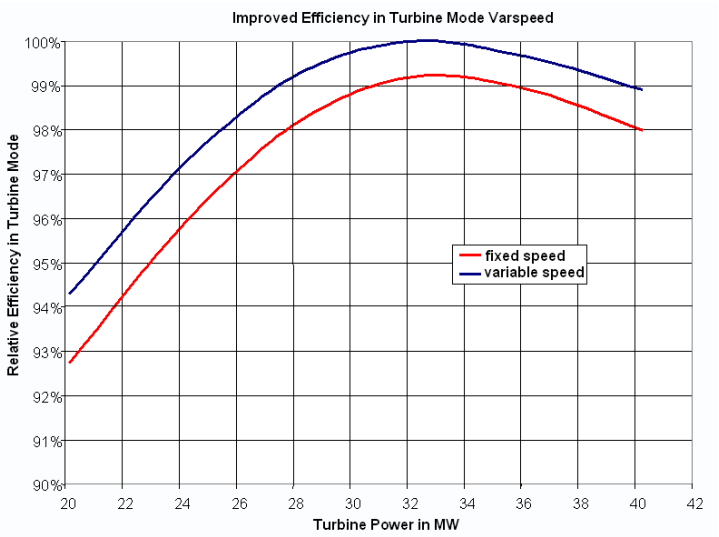

Figure 1.7: Relative turbine efficiency for fixed and variable speed [Sch+05]

power when using two variable-speed units compared to two fixed-speed units.

1.2.4 Better stabilization after a perturbation

In the case of DFIM machines (a specific type of variable-speed motor/generator unit which is described in Section 1.3.4) frequency, amplitude and phase shift of the rotor field can be regulated via an efficient control. Such machines re-stabilize the network faster after a perturbation than conventional generators. Figure 1.9 compares the behavior of fixed-speed and variable-speed units after a network voltage-drop perturbation.

1.3 Variable speed technologies

Given the theory of rotating magnetic fields [Cha80], stator and rotor magnetic fields must always rotate synchronously. This is expressed by:

$$f_s = f_r + f_m \tag{1.1}$$

where, f_s is the stator frequency, f_r is the rotor frequency and f_m is the mechanical frequency. The mechanical frequency is related to the rotational speed n expressed in Revolutions per minute (rpm),

$$f_m = \frac{n \cdot p}{60} \tag{1.2}$$

where p is the number of pole pairs . When changing the speed i.e f_m, f_s or f_r has to be adapted. However, f_s is set by the network and is constant and f_r is equal to zero for fixed-speed units, as the current is direct-current[1]. Changing the rotational speed is consequently not possible

[1]In this case n is called the synchronous speed n_s

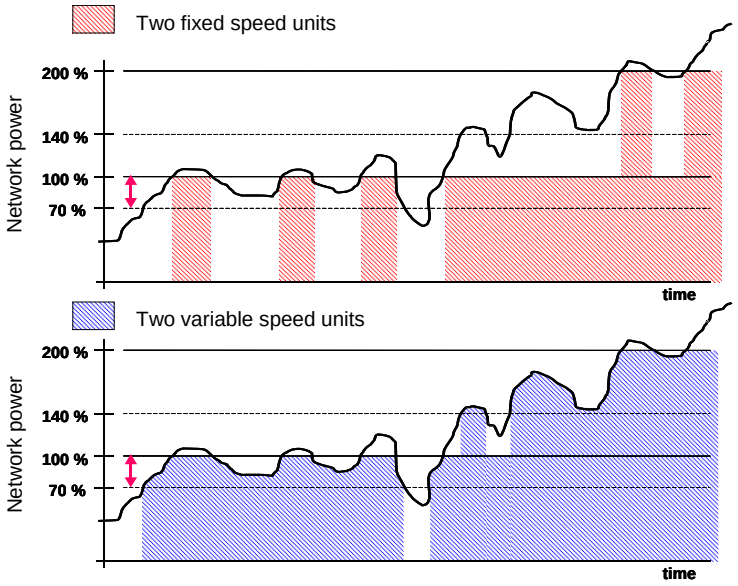

Figure 1.8: Power tracking in turbine mode [Sch06]

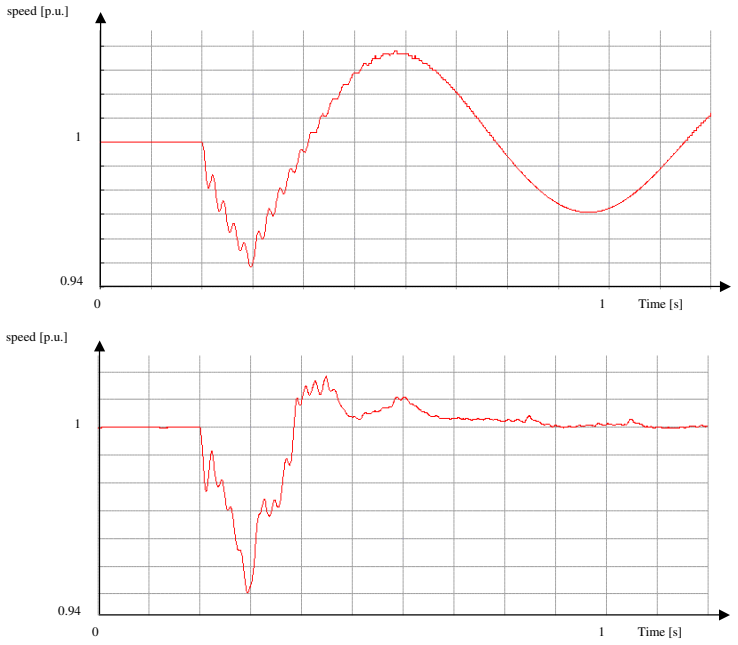

Figure 1.9: Fixed (above) and variable (below) speed dynamic behavior [Sch06]

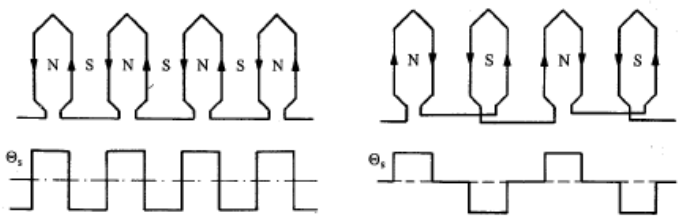

Figure 1.10: Dahlander couplings (left: $2 \cdot p$ pole-pairs), (right: p pole-pairs), [Cha80]

with a conventional installation and other technologies have to be proposed. There are several variable-speed technologies. Following is a review of the most common existing technologies.

1.3.1 The changeable/commutable salient-pole synchronous machine

For this configuration the rotor is supplied with direct-current (dc) current so that the rotor frequency is zero. Therefore the stator frequency is directly linked to the rotational speed by the relation:

$$f_{\mathrm{s}} = \frac{n \cdot p}{60} \tag{1.3}$$

As the stator frequency is fixed by the network frequency, changing speed can only be done by changing the number of poles. The poles of a synchronous machine are connected in series, and the polarity is reversed between adjacent poles. By changing the connections, i.e. the polarities, different numbers of poles can be obtained. Figure 1.10 shows a simple change of connection in order to half the number of poles, and the corresponding airgap magnetic field. Finally two different numbers of poles are obtained and consequently two different speeds.

In hydraulic applications, identical or different rotor-pole shapes can be used. In order to reduce design complexity and keep acceptable performance (vibrations, losses) only two types of poles are chosen, and only two different number of poles are available. The first configuration in Figure 1.11, shows a ten-pole rotor with two different pole configurations, ten and height poles, and the corresponding airgap magnetic field. Changing connections modifies the distribution of the air-gap flux density and consequently affects the harmonic content. Using two different poles shape makes it possible to reduce the parasitic harmonics. In one case, all the poles are magnetized (second configuration), in the other case (third configuration) two poles are deactivated. The stator winding also needs to be modified. The number of stator poles must always be equal to the number of rotor poles. One solution is to install two independent stator windings, each with a different number of poles. Also, each stator phase could be separated into different sections and a different number of stator poles obtained by changing the connections [Xua76]. To operate as a pump, the machine needs to be started and taken to the operating speed. This can be done by several means: [Cha80; Can67]

- Back-to-back start: The stator of the main machine is connected to the stator of a secondary machine. The rotors of both machines are excited by dc current, and the secondary

machine is taken to the operating speed by increasing gradually its turbine mechanical speed. The main machine accelerates in motor mode to the operational speed in synchronism with the secondary machine.

- Asynchronous start: Salient-pole synchronous machines are normally equipped with a damper-bar cage. This cage damps airgap harmonics responsible for losses and parasitic forces. It damps electromagnetic-torque oscillations and small speed variations. The damper winding can also be used for asynchronous start, but it needs to be designed specifically for this application.
- Variable frequency start: This is similar to back-to-back start, the difference being that the stator winding is supplied by a static frequency converter instead of the secondary machine. By increasing the stator frequency, the machine is progressively taken to synchronous speed.

Pole-changing technology gives the possibility to run at two different speeds. The disadvantages are clearly the complexity of the rotor and stator designs. One must also pay attention to the parasitic field harmonics created by the stator and rotor windings which lead to extra-losses on the stator, heating on the rotor surface and parasitic electromagnetic forces which cause noise and vibrations.

1.3.2 The salient-pole synchronous machine connected to a static converter

If the number of poles is constant, and supplied with dc current, modifying the rotor mechanical speed requires that the stator/terminal frequency be changed. However, the terminal frequency must equal the network frequency. In order to satisfy this rule, a frequency converter makes the interface between the machine and the network. An example of configuration is shown in Figure 1.12:

Such installations are mainly reserved for 50 MVA and smaller applications as the size and price of the converter depend on the exchanged power. When designing such machines, one must consider the current harmonics due to the converter. On the machine side these could lead to additional losses and electromagnetic forces causing vibrations and noise. On the grid side, these could result in pollution of the network, leading to additional losses in the transmission lines or perturbation of other connected elements (transformers, generators etc...). However such technology does not require any major design changes of the standard synchronous machine. Furthermore, technical improvement and cost decreases of power-electronic converter should lead to a rapid development of such technology.

1.3.3 The Brushless-Double-Fed Induction Machine

The main principle is to couple mechanically and electrically two induction machines by the rotor. One stator is connected to the network (power winding) and the other is connected to the network via a converter (command winding). This technology, also called tandem machine, requires a lot of place, and a condensed version using only one induction machine has been proposed.

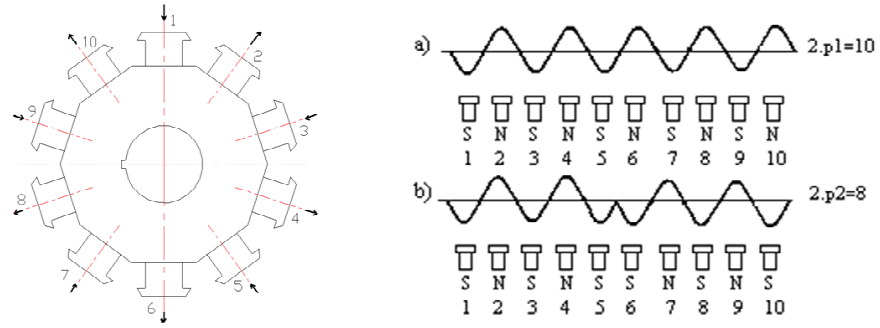

(a) Commutable SP machines: Configuration 1

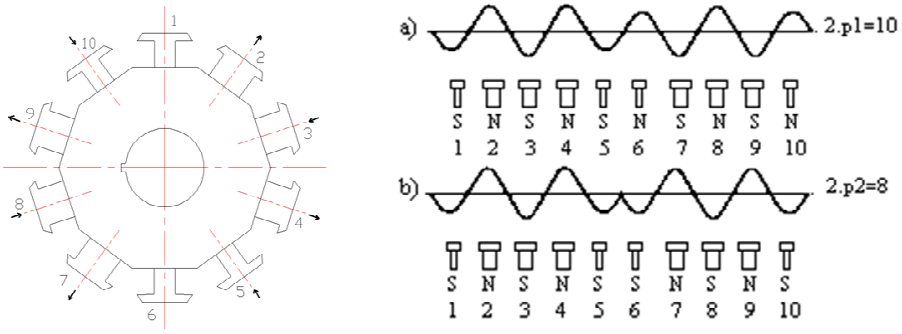

(b) Commutable SP machines: Configuration 2

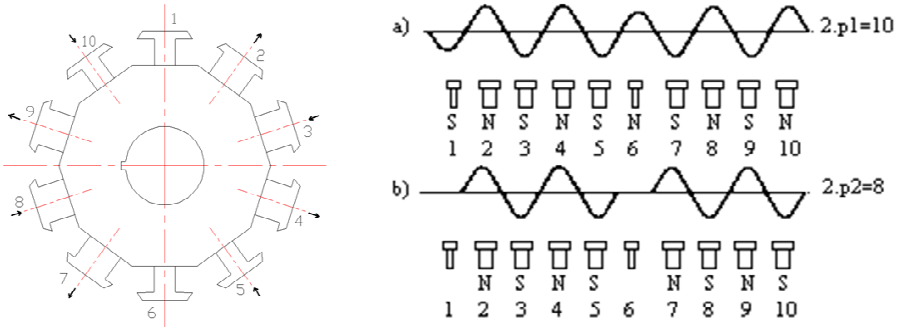

(c) Commutable SP machines: Configuration 3

Figure 1.11: Commutable SP: Three possible configurations [Sch]

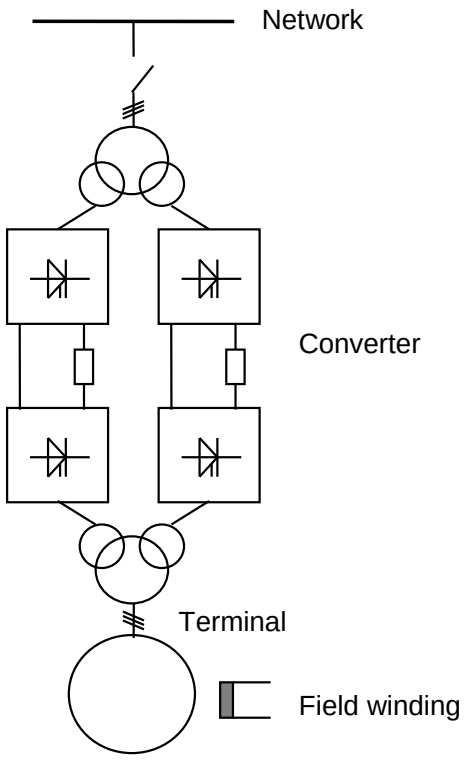

Figure 1.12: Salient poles synchronous machine with converter [Sch06]

The rotor has a squirrel-cage and the stator has two decoupled windings, one connected to the network (power winding) and one connected to the network via a converter (command winding). Brushless Double-Fed Induction Machine (BDFIM) is more and more debated in the literature. Liao [Lia96] presents the technology and compares this machine to the traditional squirrel-cage machine and makes from it a serious alternative to DFIM (see next section) for variable speed applications. Williamson [SFW97; SF97] presents the principles of modeling of the machine as well as design rules and explains how to choose the characteristics of the stator and rotor windings. Pozza [Poz+02] presents the principles of construction of an analytical model based on the extended model of the induction machine, details a control strategy and validates the model via measurements. Carlson [Car+06; McM+06] compares a BDFIM to a DFIM machine of same power. The losses are higher in the BDFIM. Although the rotor technology appears easier and cheaper than for the DFIM, the stator is more complex. This is due to the fact that two independent windings might have to share the same slots, which lead to higher slot dimensions, harmonics or insulation problems. Furthermore the efficiency of the machine might be lower due to the losses in the squirrel-cage rotor. One advantage of this technology is the absence of slip-rings which reduces periodic maintenance. Starting of the machine can be done by using the existing converter. The main disadvantage of the technology is the absence of industrial tests. For the moment such technology is limited to small power units such as small wind generators.

1.3.4 The Double-Fed Induction Machine

For this configuration, the stator is similar to that of a conventional synchronous machine and directly connected to the network. The rotor is equipped with a three-phase winding connected to the network via a converter. As opposed to the technology described in section 1.3.2, the converter of DFIM must only be designed for a fraction of the nominal power. This amount of power is directly linked to the admissible speed range of the machine, which is generally about $\pm 10\%$ of the synchronous speed. DFIM have been mainly used until now with cyclo-converters, as shown in Figure 1.13. Disadvantages of cyclo-converters are due to the fact that because of the use of thyristors the converter can only absorb reactive power and that the output frequency cannot be more than one third of the input frequency. This prevents the use of the converter for start-up in pump operation. An additional converter is therefore needed. Technical improvements of power electronics made possible a new generation of high-power converter Voltage Switched Inverter (VSI) as shown in Figure 1.14. Such technology corrects most of the disadvantages of cyclo-converter technology by enabling start, control of the reactive power on the rotor side, a strong reduction of parasitic current harmonics and a reduction of the needed installation volume (only one transformer for example).

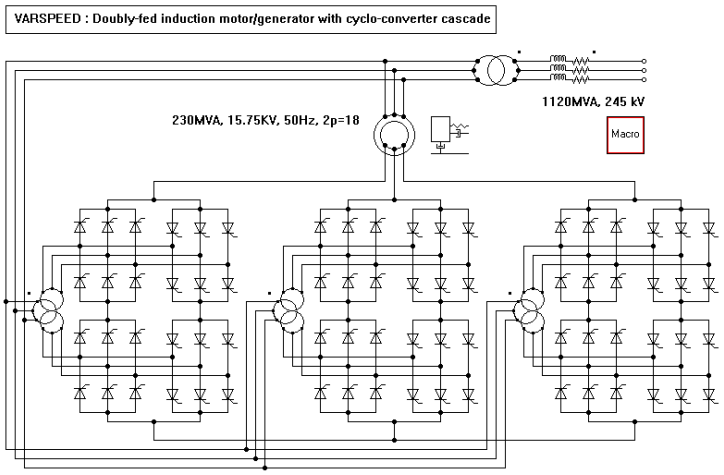

Figure 1.13: DFIM with cyclo-converter [Sch+05]

Figure (1.15) and Figure (1.16) compare a conventional synchronous machine with a DFIM. One can observe the non-negligible place covered by the slip ring system in the case of the DFIM. Note that in the presented case, both machines present similar dimensions. However the DFIM will usually be larger than an equivalently rated salient-pole synchronous machine. More details about DFIM dimensioning are given in Chapter 6.

The main challenge of this technology is the complexity of the rotor due to mechanical and insulation issues as explained by the following points.

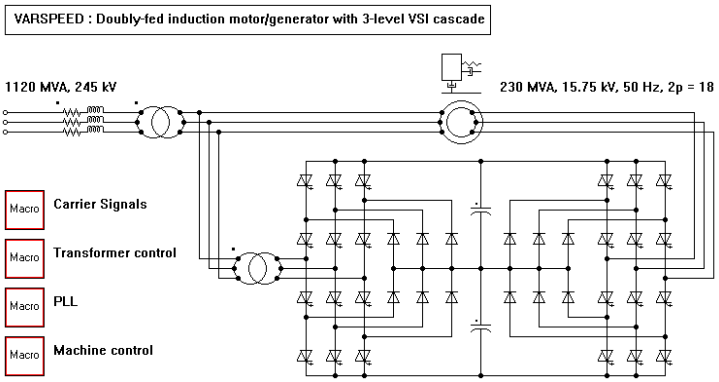

Figure 1.14: DFIM with VSI converter [Sch+05]

I. The rotor winding overhang

The rotor bars are similar to stator bars, one part installed in the core and the other part extending outside both ends of the core. In the core part, the bars are maintained in the slot by the slot wedges. Because of centrifugal forces during normal operation or worse in the case of over-speed, the overhang requires particular attention. Furthermore, in the case of faults such as short-circuits, the bars are subjected to very large forces. The overhang must always withstand such faults in order to avoid deformation or breaking. Several technologies exist to carry out this task, the most common being the use of glass tape epoxy to secure the overhang conductors. Although this solution is effective, it makes it difficult for maintenance operations such as inspection or replacement of bars. Another solution consists of using bolts [SV96].

II. The rotor bar insulation system

As described previously, the rotor is supplied by a frequency converter. Because of the Pulse Width Modulation (PWM) command, the output voltage contains high frequency (1 kHz) pulses. Depending on the impedance of the cable between the converter and the rotor terminals and of the rotor-winding, an over-voltage can appear at the rotor terminals. Furthermore, each pulse produces a high variation of voltage with time or high $\mathrm{d}V/\mathrm{d}t$. These parasitic behaviors can lead to significant stresses of the winding insulation. Consequently the rotor bar insulation system must be designed to withstand these dielectric stresses.

III. Rotor lamination power losses

The rotor is composed of laminated steel which may be subjected to significant power losses. In synchronous operation, the main magnetic field in the rotor does not oscillate. The induced power losses in the lamination are essentially due to the harmonics created by the stator winding and by the airgap permeance harmonics and these losses are generally small. When not at synchronous speed, the rotor magnetic field is traveling with respect to the rotor. Therefore, in addition to the latter losses, other larger losses due to the flux varying at the slip frequency

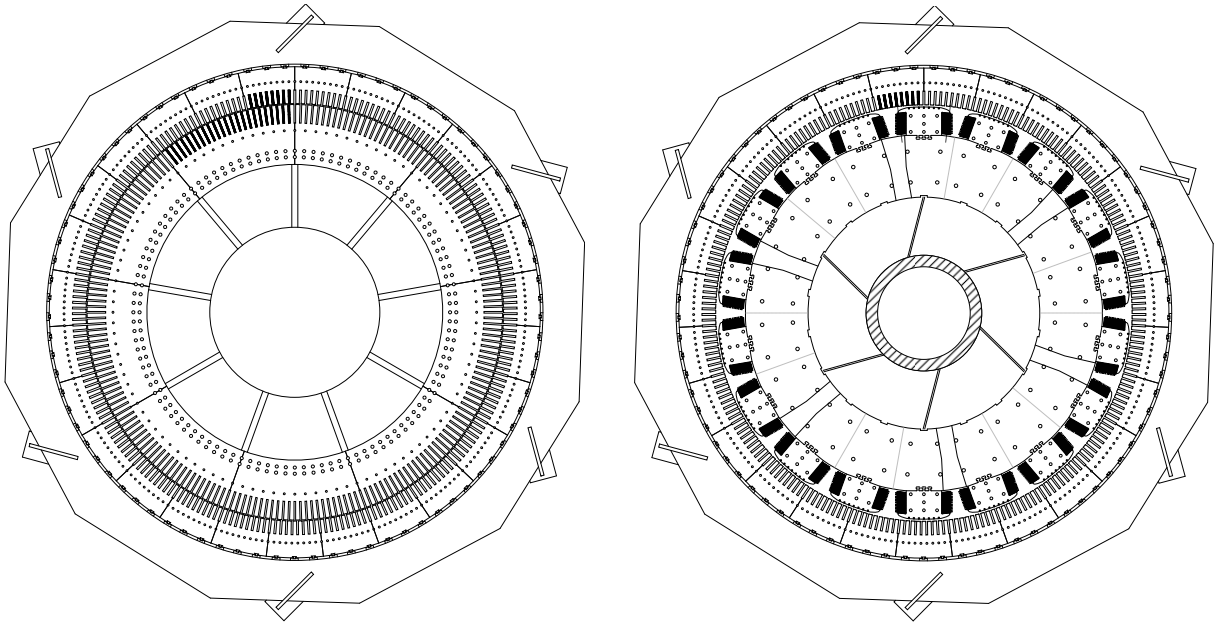

(a) Double-Fed Induction Machine (b) Salient Pole Synchronous Machine

Figure 1.15: Cross section of the two machines (from Alstom design tool)

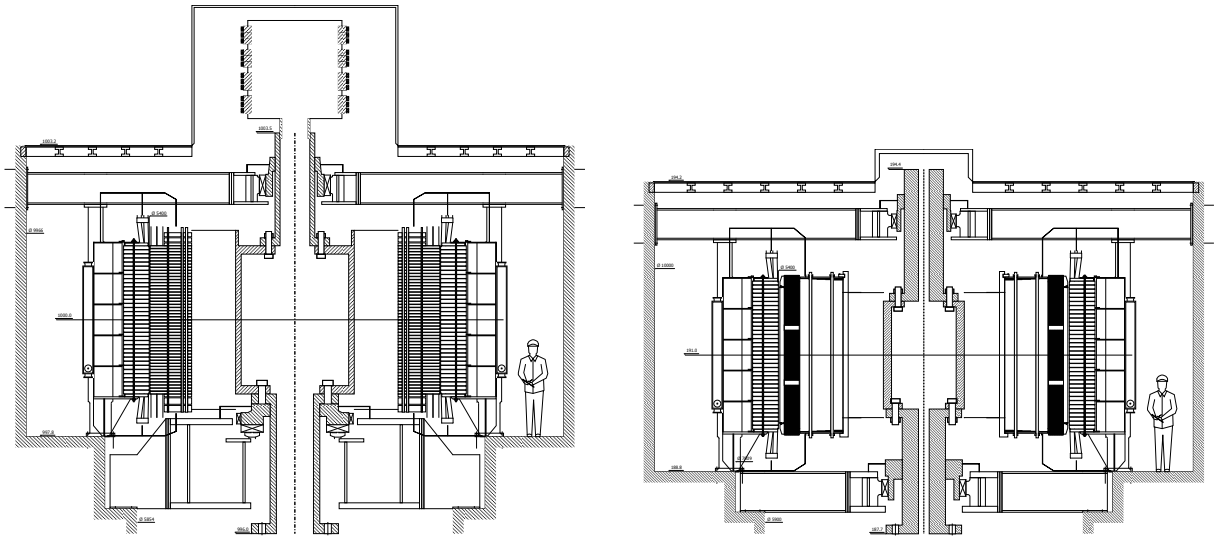

(a) Double-Fed Induction Machine (b) Salient Pole Synchronous Machine

Figure 1.16: Longitudinal section of the two machines (from Alstom design tool)

($f_s - f_m$) occur in the laminations. Normally, the lamination steel in the rotor is chosen to withstand the high mechanical stress. This choice cannot be done without a degradation of the material magnetic characteristics. Consequently the rotor lamination material has a larger specific loss than the stator lamination material. This must be considered when evaluating the losses and the cooling requirements of rotor.

IV. The rotor slip-ring and brushes

The slip-ring and carbon-brush systems are the interface between the converter and the three-phase winding of the rotor. The carbon-brush wear is strongly dependent on temperature and humidity and is subject to periodic maintenance.

1.3.5 Summary

Nevertheless knowledge acquired in the development of large conventional alternators i.e. 10 MVA to 800 MVA make it possible to overcome the previously listed difficulties. Large installations using DFIM have already been commissioned; the first one in 1987 by the Kansai Electric Power Company of Osaka Japan - a 18.5 MW motor-generator from Toshiba Corporation, then larger ones in 1993 (2×400 MW) from Hitachi were installed in Ohkawachi for commercial applications [Gre94; NK88]. Since then the interest for such technology has been growing gradually due to the major breakthrough in the power electronics. In 2003 one of the largest European hydro power plant (4×265 MW), Goldisthal, was commisioned. Two of the four generators are DFIM and provided by Siemens was commissioned. In 2015 and 2017 ALSTOM Renewable Power will put into operation the power plants at Linth Limmern (4×250 MW) and Nant de Drance (6×157 MW) in Switzerland using VSI converters.

1.4 Description and motivation of the study

1.4.1 Restriction of the study domain

Previous part described the actual solutions for developing motors/generator units able to run at variable speed. All these technologies present advantages and disadvantages. In order to select the most appropriate solutions for PSP applications, it is important to list the today required criteria:

- power of converter should be reduced in order to limit its size and its price
- the output power is in the range 10 MVA to 500 MVA
- knowledge acquired in stator design of standard salient poles alternator should be applicable to the chosen machine
- a variation of $\pm 10\%$ of the reference speed should be accessible

Adjustable-pole machines can not be chosen because of the point 4. Although Synchronous machines with frequency converters satisfy the points 2, 3 and 4, the point 1 is not any more

respected when dealing with high output power alternators (more than 50 MVA). BDFIM and DFIM are the only machines able to respect the four rules. However BDFIM development remains today still limited and is mainly reserved for small power applications such as windmills. Furthermore DFIM has the advantage to have an identical stator to a conventional synchronous machine. This is particularly interesting during refurbishment of old PSP when considering the upgrade of a fixed-speed standard machine to a variable speed unit; in this case only the rotor needs to be changed. Finally the DFIM has been chosen and will be mainly analyzed in this thesis. The considered input/output power is in the range of 10 MVA to 500 MVA, the synchronous speed is in the range 200 rpm to 600 rpm.

1.4.2 Definition and motivation of the study

Motors/generators dedicated to hydraulic applications have long been studyied in the past. The available papers concern more particularly the synchronous machines and treat about their design and their optimization. The main analyzed subjects are the following:

- computation of equivalent circuit parameters [Can83; Ram03]
- Three-Dimensional Finite Element (3DFE) computation of end winding inductances and losses in the end regions [Tra03; Ric97; Sil94; ALP08]
- computation of iron losses [TA09; Ran+09]
- computation of losses in the damper bars [TLS10]
- computation of radial electromagnetic forces [WK60; TLU12]
- computation of stator voltage shape [KXS06; TSS03]
- computation of temperatures and cooling air-flow [TZS10]

Studies about the DFIM focus mainly on windmill generators and are often dedicated to control implementation and stability studies [Rob04; Pet05]. Regarding hydraulic applications the literature is also very rich in articles regarding control infrastructure and network studies. Schafer and Simond [SS97] compare the DFIM to the synchronous machine and show the benefits given in terms of network regulation and dynamic response. Hodder [Hod04] simulates the complete infrastructure of a hydraulic varspeed installation including the network and machine transformer and the converter. He shows the advantages of using a VSI instead of a cycloconverter because of the lower harmonic distortion and the possibility to control the reactive power via the rotor. The control is based on a two-axis modeling of the machine and a decoupling of the d and q axis in order to control the speed and the reactive power. Pannatier [Pan10] studies different control strategies and simulates the interaction of the machine with other components of the network such as thermal power plants or wind farms. He also presents a strategy to startup a DFIM and to synchronize it on the network. Besides control and stability topics, some studies [Lor97; Mil10] deal with the steady-state equations using the equivalent-scheme of the squirrel-cage induction motor in which a rotor voltage source is added. Lorenzen wrote several studies about the induction machine and the DFIM. In particular he worked on the magnetic-circuit modeling [Lor96a], the load-point characteristics determination [Lor98], the

iron-losses calculation [Lor96b] and describes with Herzog [LH93] the DFIM modeling principles. Witt [Wit98] worked also on the problem of the operation point determination considering the effect of saturation on the equivalent-circuit parameters. Furthermore Lorenzen wrote about the radial electromagnetic forces occurring in the DFIM [Lor09] and on the analytical determination of the stator core eigen-frequencies [Lor11]. The DFIM design tool used in Alstom is mainly based on the original tool *DASM* developed by Lorenzen. Muller-Feugga [Mul06] contributed to the validation of the design tool by carrying out 2DFE computations.

The object of this thesis is to review the principles of modeling and electromagnetic design of the DFIM dedicated to hydraulic applications.

Firstly, due to its topology, the design of DFIM requires special attention. Like any standard electrical machines, the total airgap magnetic field of a DFIM is the result of the interaction between stator and rotor magnetic fields. In addition to the main or working field, several parasitic harmonics are superimposed. These harmonics are due to the distribution of the rotor and stator conductors in the slots. Furthermore the airgap of the DFIM is constant but modulated by the stator and rotor teeth which lead to extra harmonics called airgap permeance harmomics; this is even more crucial since the airgap of such machine is in general small. These harmonics are responsible in one hand for additional power losses on the stator and rotor magnetic core which must be considered when designing the cooling system of the machine. On the other hand, they create parasitic radial or tangential electromagnetic forces which by interacting with the stator or the shaft eigen-frequencies may create noise and vibration.

Secondly, due to fact that the speed can be varied the evaluation of the machine performance has to be done for the full range of speed. Change of speed leads to a shift of some of the rotor field harmonics frequencies. Consequently electromagnetic forces component frequencies can slip so that the risk to match an eigen-frequency from the stator or the shaft line becomes more important. Furthermore as explained in part 1.3.4, out of the synchronous speed, the rotor sees an alternating magnetic flux which is accountable for non negligible power losses.

Thirdly, the rotor winding of a DFIM is supplied with a VSI converter piloted by PWM command. Such command is generally responsible for extra harmonics in the rotor currents and consequently on the air gap field. It is important to quantify the effect of such modulation on the performance of the machine.

Finally, all these elements lead to the necessity to develop models to better understand the electromagnetic behavior of the DFIM. We will use for this the existing Alstom tool on which we propose improvements based on new modeling techniques and validations with Finite Element (FE) simulations. Such model will help to evaluate and finally to optimize the design of such machines.

1.4.3 Structure of the thesis

Chapter 2 presents the magnetic modeling of the DFIM based on a simple magnetic permeance network. The obtained simplified magnetic network is validated by carrying out 2DFE simulation. The developed model makes it possible to consider later the electromagnetic behavior on

the performance of the machine.

Chapter 3 defines an equivalent model of the machine for steady-state operation studies. Parameters of the model are obtained from analytical calculations based on the geometry of the machine. In particular the calculation of the stator and rotor leakage inductance is described according to the existing studies in the literature. 2DFE and 3DFE are used to validate the obtained results. The effect of magnetic saturation on the values of the circuit parameters is obtained by applying the results of the magnetic permeance model described in Chapter 2. Finally the load-point calculation is described and the results are validated by carrying out magneto-harmonic and time-stepping FE simulations. So as to efficiently perform these latter computations, an approach based on the regulation of the DFIM is described. It makes it possible to simulate any steady-state load conditions of the machine and also allows to either model the rotor power supply by standard sinusoidal voltage sources or by a simplified VSI. The developed method can be used to compute parasitic radial forces, dynamic torques or iron losses as it is shown in Chapter 5.

Chapter 4 deals with the problem of airgap flux density harmonics. Although Chapter 3 presents an accurate modeling of the DFIM, it considers that the airgap magnetic field varies sinusoidally. FE computations results have shown the necessity to complete this simplified approach by including additional harmonics such as the winding and the airgap permeance harmonics. The main originality is to use a modeling based on the BEM in order to consider efficiently the double-slotted airgap. The effect of saturation is included by applying a modulation of the airgap permeance based on the results of Chapter 3. This simplified approach makes it possible to deal with the saturation of the magnetic circuit on the main harmonics such as the fundamental wave and the third harmonic wave. However it does not make it possible to describe accurately its effect on other harmonics. A proposal for improvement for the future suggests to combine a simplified discretization of the stator and rotor cores using a magnetic permeance network and the accurate Boundary Element (BE) model of the air gap.

Chapter 5 uses the results of the previous chapters to study the behavior of different quantities such as the stator voltage harmonics, the radial electromagnetic forces, the dynamic electromagnetic torques and the iron losses. The developed algorithms are validated with FE simulations. We discuss in particular the impact of the saturation on the performance of the machine and the impact on the radial forces when using fractional slot windings. For the latter subject, we propose an original method (at the knowledge of the author) making it possible to optimize a winding in order to decrease the risk of vibration by exchanging some winding connections.

Chapter 6 reviews the design principles of the DFIM. Subjects such as the choice of rated parameters, the airgap length and the stator and rotor slots numbers are discussed. Furthermore it is shown how the dimensioning of the machine can be formulated as an optimization problem having some constraints and an objective function. In particular we study the transformation of an existing salient-pole synchronous machine into a DFIM changing first only the rotor then both the stator and the rotor. The method appears very efficient to find the main dimensions of the machine.

2 Magnetic circuit model

2.1 Introduction

Designing a rotating electrical machine requires the correct modeling of its magnetic circuit. The stator and rotor cores are made of magnetic iron sheets facing magnetic saturation. The magnetizing current which creates the magnetic flux is linked to the state of saturation so that a wrong assessment of the latter has a dramatic effect on the losses and consequently on the overall efficiency.

First part exposes a simplified analytical magnetic model of the DFIM based on the well-known Ampere-Maxwell theorem, applying a piecewise integration of the magnetic field strength along a chosen magnetic path. The magnetic potential drop calculation along the airgap as well as the different magnetic regions are described; a 2DFE calculation is used to accurately quantify the impact of the magnetic saturation on some design coefficients such as the pole enclosure coefficient and the airgap form factor. Finally the result of the magnetic integration makes it possible to compute the required magnetizing current in order to drive the magnetic flux through the magnetic circuit.

Second part compares the results of the magnetic circuit calculation obtained from the simplified analytical magnetic model and from a 2DFE magneto-static computation. The comparison is made for various designs with regard to the magnetizing voltage and the stator and rotor teeth magnetic flux densities. This allows to certify the method for the full range of machines studied in this thesis.

2.2 The analytical magnetic model

2.2.1 The Ampere-Maxwell theorem

The chosen method is based on the application of the Ampere-Maxwell theorem. The integration of the magnetic field strength H over a closed path $\mathcal{C}$ also called mmf Θ_{w} is equal to the sum of all currents I crossing the domain enclosed by this path.

$$\Theta_{\mathrm{w}}(\mathcal{C}) = \oint_{\mathcal{C}} H \cdot \mathrm{d}l = \sum I \tag{2.1}$$

Figure 2.1 shows a simplified illustration of the DFIM magnetic circuit as well as the integration path C chosen in order to cover one magnetic pole pitch.

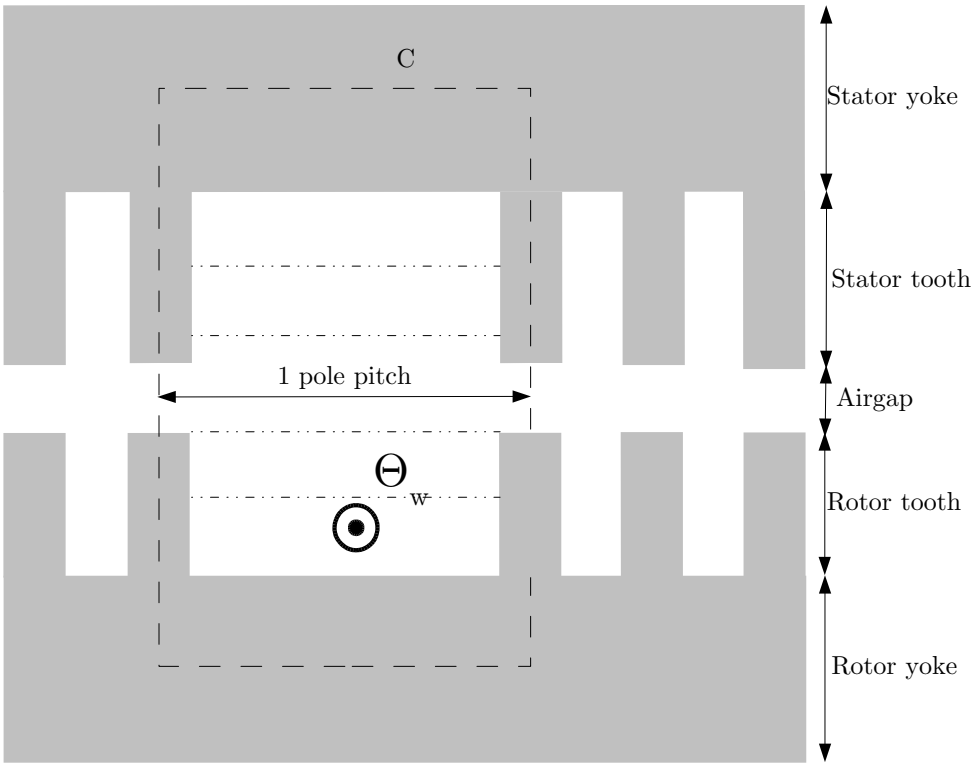

Figure 2.1: Magnetic circuit

Five regions can be identified: the airgap, the stator teeth, the stator yoke, the rotor teeth and the rotor yoke. Except for the airgap region, the magnetic permeability of all regions depends on the magnetic material characteristics and on the crossing magnetic field strength. The integration of the magnetic field on the path $\mathcal{C}$ consists of a piecewise integration of the magnetic strength on each identified region. Finally Equation (2.1) is expressed as Equation (2.2) where $\hat{U}_{\mathrm{m,ts}}$, $\hat{U}_{\mathrm{m,ys}}$, $\hat{U}_{\mathrm{m,tr}}$ and $\hat{U}_{\mathrm{m},\delta}$ are respectively the magnetic potential drops in the stator tooth, the stator yoke, the rotor tooth and the rotor yoke whereas $\hat{U}_{\mathrm{m},\delta}$ stands for the magnetic potential drop in the airgap.

$$\Theta_{\mathrm{w}}(\mathcal{C}) = \oint_{\mathcal{C}} H \cdot \mathrm{d}l = 2 \cdot \hat{U}_{\mathrm{m,ts}} + \hat{U}_{\mathrm{m,ys}} + 2 \cdot \hat{U}_{\mathrm{m,tr}} + \hat{U}_{\mathrm{m,yr}} + 2 \cdot \hat{U}_{\mathrm{m},\delta} \tag{2.2}$$

2.2.2 The magnetizing voltage and flux

Only the rotor winding is supplied. The purpose is to calculate the rotor current in order to induce a certain voltage V_{s} at the stator terminals. Note that at no-load V_{s} is later equivalent to the magnetizing voltage V_{μ}. V_{s} can be obtained from the induction's law:

$$V_{\mathrm{s}} = -\frac{\mathrm{d}\Phi_{\mathrm{f}}}{\mathrm{d}t} \tag{2.3}$$

where Φ_{f} is the fundamental magnetizing flux. One can show that the airgap flux density contains several harmonic components inducing voltages on the stator winding[1]. However only the fundamental part of the flux density takes part in the effective power generation. The Root Mean Squared (RMS) value of the fundamental stator line-to-line voltage U_s^{rms} is expressed as:

$$U_s^{\mathrm{rms}} = \sqrt{\frac{3}{2}} \cdot 2\pi f_{\mathrm{s}} \cdot \xi_{\mathrm{f,s}} N_{\mathrm{s,s}} \cdot \hat{\Phi}_{\mathrm{f}} \tag{2.4}$$

where $\xi_{\mathrm{f,s}}$ is the fundamental winding coefficient considering the winding configuration and $N_{\mathrm{s,s}}$ is the number of stator winding turns in series. The maximum fundamental magnetic flux $\hat{\Phi}_{\mathrm{f}}$ is obtained by integrating the fundamental airgap flux density $B_{\delta\,,\mathrm{f}}$ over the stator pole pitch $\tau_{\mathrm{p,s}}$ so that:

$$\hat{\Phi}_{\mathrm{f}} = l_{\mathrm{i}} \int_0^{\tau_{\mathrm{p,s}}} \hat{B}_{\delta\,,\mathrm{f}} \cdot \sin(x\pi/\tau_{\mathrm{p,s}}) \mathrm{d}x = \frac{2}{\pi} l_{\mathrm{s}} \tau_{\mathrm{p,s}} \cdot \hat{B}_{\delta\,,\mathrm{f}} \tag{2.5}$$

where l_{i} is the equivalent core length also called ideal length considering the presence of stator and rotor cooling air ducts[2]. Only the fundamental part of the magnetizing flux takes part in the effective power generation, however the magnetic state of the machine depends directly on the maximum value of the magnetizing flux Φ_m expressed as:

$$\hat{\Phi} = l_{\mathrm{i}} \int_0^{\tau_{\mathrm{p,s}}} B_{\delta}(x) \cdot \mathrm{d}x = l_{\mathrm{s}} \tau_{\mathrm{p,s}} \alpha_{\mathrm{i}} \cdot \hat{B}_{\delta} \tag{2.6}$$

where $B_{\delta}(x)$ describes the spatial evolution of the flux density along a path at the middle of the airgap, $\hat{B}_{\delta}$ is the maximum airgap flux density and α_{i} is the so-called pole enclosure coefficient. Figure 2.2 shows the evolution of the airgap magnetic flux density B_{δ} for three magnetizing currents ($3/4 \cdot I_{\mu,0},\ I_{\mu,0},\ 5/4 I_{\mu,0}$) computed by FE. Note that $I_{\mu,0}$ corresponds to the magnetizing current under rated no-load operation. The spatial variation of B_{δ} has been rebuilt in order to remove high order spatial harmonics due to the stator and rotor slots, furthermore for comparison purposes the evolution of the fundamental component $B_{\delta\,,\mathrm{f}}$ of the flux density is also displayed. One can see that the airgap flux density gets more and more flattened as the magnetizing current increases. Consequently α_{i} depends on the magnetizing current and finally on the magnetic state of the machine.

Finally Equation (2.3) can be rewritten as a function of $\hat{\Phi}$, α_{i} and the form factor coefficient $\mathrm{C}_1 = \hat{B}_{\delta\,,\mathrm{f}}/\hat{B}_{\delta}$ expressing the ratio between the fundamental airgap magnetic flux density and the maximum airgap magnetic flux density. One can identify an analogy with the salient-pole synchronous machine but in this case α_{i} and C_1 would mainly depend on the salient-pole geometry.

$$U_s^{\mathrm{rms}} = \sqrt{\frac{3}{2}} \cdot 2\pi f_{\mathrm{s}} \cdot \xi_{\mathrm{f,s}} N_{\mathrm{s,s}} \cdot \frac{2}{\pi} \cdot \hat{\Phi} \cdot \frac{\mathrm{C}_1}{\alpha_{\mathrm{i}}} \tag{2.7}$$

[1] See Chapter 4 for more details

[2] This ideal length l_{i} is defined in section 2.3

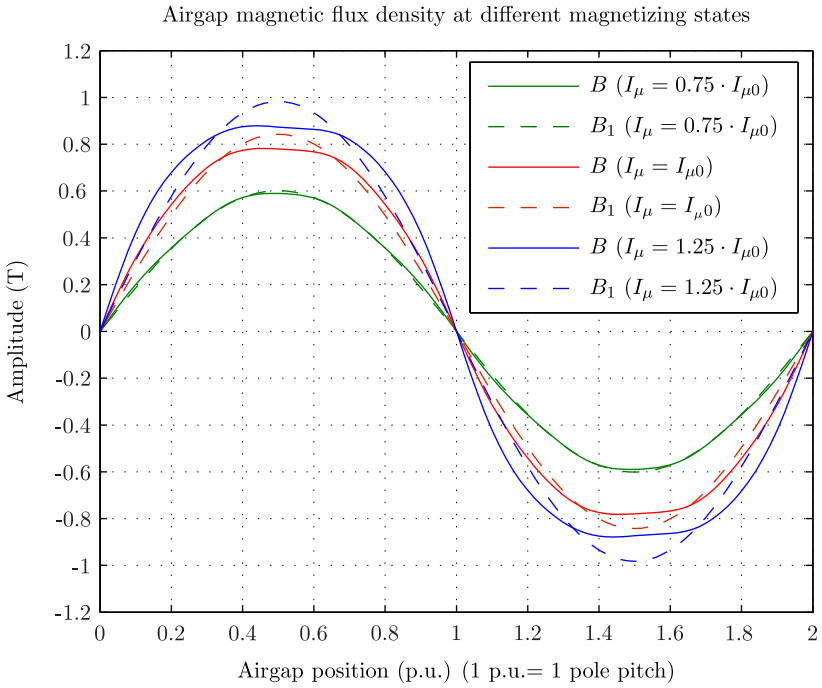

Figure 2.2: Airgap flux density at different magnetizing states

2.2.3 The magnetic saturation coefficient

In order to quantify the magnetic state of the machine, the magnetic saturation coefficient K_s is defined as:

$$K_s = \frac{2 \cdot \hat{U}_{m,ts} + \hat{U}_{m,ys} + 2 \cdot \hat{U}_{m,tr} + \hat{U}_{m,yr}}{2 \cdot \hat{U}_{m,\delta}} \tag{2.8}$$

When the magnetic circuit is not saturated, the magnetic drop in the iron regions is negligible compared to the magnetic drop in the airgap. Consequently K_s is equal to zero and as the airgap flux density contains mainly the fundamental component, the coefficients C_1 and α_i are respectively equal to one and $2/\pi$. When the magnetic circuit gets into saturation, the magnetic drop in the iron path is not any more negligible and the latter coefficients increase. The dependency law between the form coefficient C_1 and the saturation coefficient K_s can be computed by carrying out a 2DFE simulation. By using a magneto-static resolution, where the magnetic field is constant, the rotor winding is supplied with a three-phase current system: $\hat{I}_{r,a} = I_\mu$, $\hat{I}_{r,b} = -I_\mu/2$, $\hat{I}_{r,c} = -I_\mu/2$. The parameter I_μ is varied in the range from 0.1 to 5.0 p.u., where 1 p.u. corresponds to the value of the rotor current under rated no-load operation. Note that in reality the excitation current will never reach such high values during no-load operation as the machine will get very saturated. For each value of I_μ, the 2DFE simulation is solved. The flux density is computed over a path in the airgap and the values of the parameters $\hat{B}_\delta$ and $\hat{B}_{\delta,f}$ are extracted and with them the form factor coefficient C_1. Furthermore, the saturation coefficient K_s is obtained by rewriting Equation (2.8) in Equation

Quantity	min	max
Apparent power S (MVA)	150	400
Rated stator voltage U_{s} (kV)	15	18
Stator bore diameter $D_{\mathrm{b,s}}$ (mm)	4000	10000
Stator Core length l_{s} (mm)	2000	4000
Minimum airgap length δ_g (mm)	14	18
Number of pole pairs p (-)	6	8
Number of stator slots per pole/phase q_{s} (-)	4	8
Number of rotor slots per pole/phase q_{r} (-)	3	7
Stator yoke height/stator yoke pole pitch $h_{\mathrm{y,s}}/\tau_{\mathrm{y,s}}$ (-)	0.20	0.35
Rotor yoke height/rotor yoke pole pitch $h_{\mathrm{y,r}}/\tau_{\mathrm{y,r}}$ (-)	0.45	1.05
Stator tooth width/stator slot pitch $w_{\mathrm{t,s}}/\tau_{s,\mathrm{s}}$ (-)	0.3	0.5
Rotor tooth width/rotor slot pitch $w_{\mathrm{t,r}}/\tau_{s,\mathrm{r}}$ (-)	0.25	0.4

Table 2.1: Machine characteristics for magnetic coefficients calculation

(2.9) by considering Equation (2.2)

$$\mathrm{K_s} = \frac{\hat{\Theta}_{\mathrm{w}}(\mathcal{C}) - 2 \cdot \hat{U}_{\mathrm{m,\delta}}}{2 \cdot \hat{U}_{\mathrm{m,\delta}}} \tag{2.9}$$

where $\hat{\Theta}_{\mathrm{w}}(\mathcal{C})$ is the total mmf created by the rotor currents and $\hat{U}_{\mathrm{m,\delta}}$ is the magnetic drop in the airgap described further in this part by Equation (2.12). $\hat{\Theta}_{\mathrm{w}}(\mathcal{C})$ can be obtained from Equation (2.10) where θ represents the magnetic voltage created by the rotor currents, the scaling coefficient *2* comes from the fact that both pole positive and negative are crossed by the magnetic field. In the case of a three-phase winding and by considering only the fundamental component, $\hat{\theta}$ is obtained from Equation (2.11)[3].

$$\hat{\Theta}_{\mathrm{w}}(\mathcal{C}) = 2 \cdot \hat{\theta} \tag{2.10}$$

$$\hat{\theta} \approx \frac{6\sqrt{2}}{\pi} \cdot \frac{N_{\mathrm{s,r}} \xi_{\mathrm{f,r}}}{p} \cdot I_{\mathrm{r}}^{\mathrm{rms}} \tag{2.11}$$

where $N_{\mathrm{s,r}}$ is the number of rotor series turns, $\xi_{\mathrm{f,r}}$ is the fundamental rotor winding coefficient and $I_{\mathrm{r}}^{\mathrm{rms}}$ is the RMS value of the current in the rotor winding; here $I_{\mathrm{r}}^{\mathrm{rms}} = \hat{I}_{\mu}/\sqrt{2}$. These calculations are made for a wide range of machine designs provided in Table 2.1.

Figure 2.3 and Figure 2.4 show the corresponding variations of the coefficients $\mathrm{C_1}$ and α_{i}. There is a slight change in the variation of $\mathrm{C_1}$ and α_{i} from one design to another. However one can also identify a common trend as shown by the red line on both graphs. Note that during rated no-load or load operation $\mathrm{K_s} \in [0.2 \cdots 0.4]$.

Finally for a given value of the fundamental magnetizing voltage, one can express the corresponding maximum magnetic flux. The corresponding magnetic drops in all the sections previously defined can be computed as demonstrated in the next part.

[3]The mmf calculation is described in Chapter 4

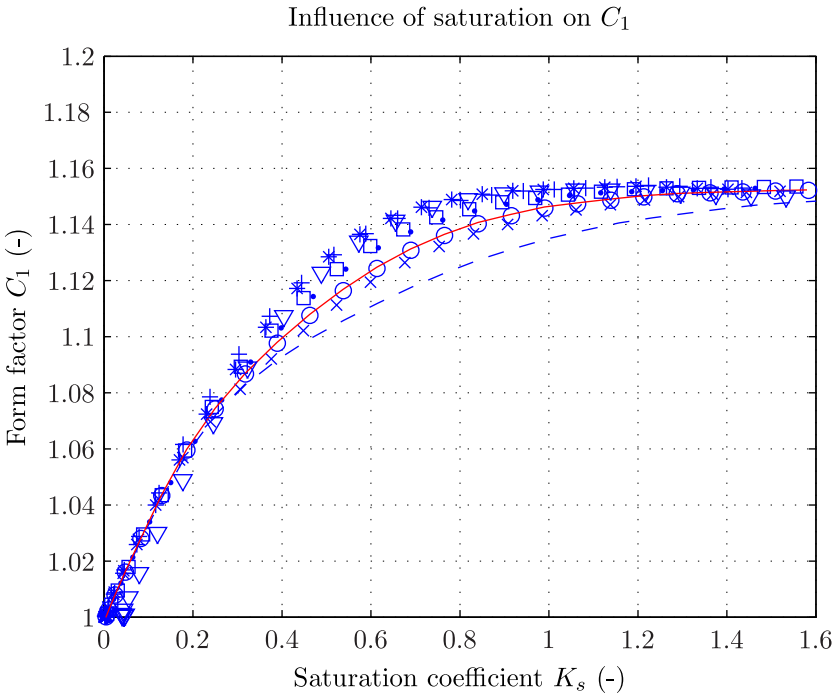

Figure 2.3: Form factor C_1

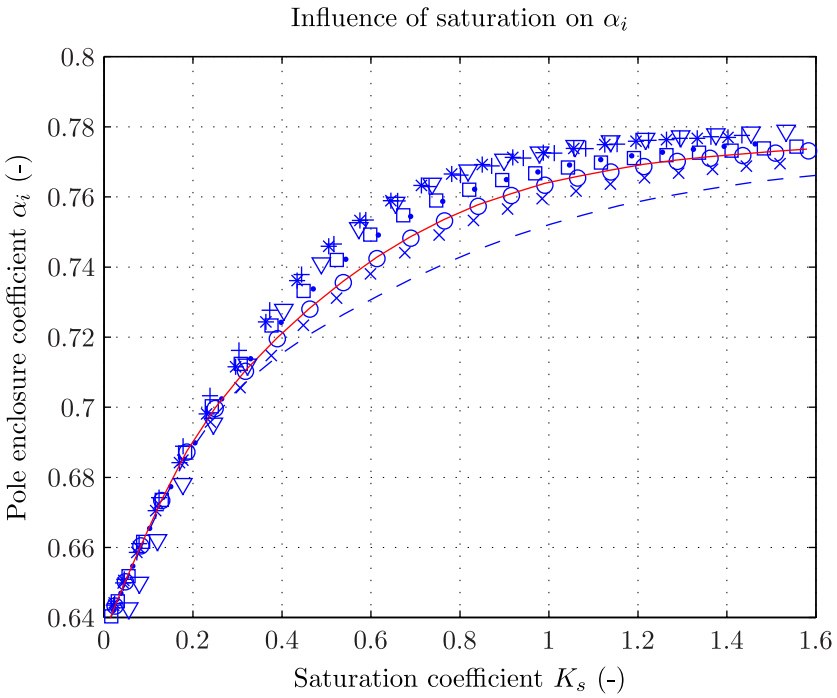

Figure 2.4: Pole enclosure coefficient α_i

2.2.4 The magnetic drop calculation

I. Magnetic drop in the airgap

In the air gap the magnetic potential drop is expressed as:

$$\hat{U}_{\mathrm{m},\delta} = \frac{\hat{B}_{\delta}}{\mu_0} \cdot \delta_{\mathrm{g}} k_{\mathrm{c}} \tag{2.12}$$

where μ_0 is the air permeability, δ_{g} is the value of the minimum airgap depth and k_{c} is the well-known Carter factor considering the fact that slots lead to a decrease of the magnetic flux density. In the studied machine, the airgap is slotted on both sides, this factor can be defined as $k_{\mathrm{c}} \approx k_{\mathrm{c,s}} \cdot k_{\mathrm{c,r}}$ where $k_{\mathrm{c,s}}$ and $k_{\mathrm{c,r}}$ express respectively the Carter coefficient considering the influence of stator and rotor slots. $k_{\mathrm{c,s}}$ is defined as:

$$k_{\mathrm{c,s}} = \frac{\tau_{s,\mathrm{s}}}{\tau_{s,\mathrm{s}} - \gamma_s \delta_g} \tag{2.13}$$

where $\tau_{s,\mathrm{s}}$ is the stator slot pitch and γ_{s} is a leakage coefficient defined as

$$\gamma_{\mathrm{s}} = \frac{\left(\frac{w_{\mathrm{s,s}}}{\delta_{\mathrm{g}}}\right)^2}{5 + \frac{w_{\mathrm{s,s}}}{\delta_{\mathrm{g}}}} \tag{2.14}$$

$k_{\mathrm{c,r}}$ is obtained from the same formula but considering the parameters of the rotor. The quantity $\delta_{\mathrm{g}} k_{\mathrm{c}}$ can be interpreted as a virtual larger airgap due to the lower permeance of the slots by comparison to the teeth. $\hat{B}_{\delta}$ is obtained from $\hat{\Phi}$ using Equation (2.6).

II. Magnetic drop in the stator tooth

The stator tooth flux density $\hat{B}_{\mathrm{t,s}}$ is obtained by considering first that all the magnetic flux is passing trough the teeth so that

$$\hat{B}_{\mathrm{t,s}} = \hat{B}_{\delta} \cdot \frac{\mathrm{S}_{\tau_{s,\mathrm{s}}}}{\mathrm{S}_{\mathrm{t,s}}} \tag{2.15}$$

$\mathrm{S}_{\tau_{s,\mathrm{s}}}$ is the cross section over one stator slot pitch and $\mathrm{S}_{\mathrm{t,s}}$ is the cross section over one stator tooth given as:

$$\mathrm{S}_{\mathrm{t,s}} = (\tau_{s,\mathrm{s}} - w_{\mathrm{s,s}}) \cdot l_{\mathrm{f,s}} \tag{2.16}$$

where $\tau_{s,\mathrm{s}}$ is the stator slot pitch, $w_{\mathrm{s,s}}$ is the stator slot width and $l_{\mathrm{f,s}} = \mathrm{k}_{\mathrm{f,s}} \cdot (l_{\mathrm{s}} - N_{\mathrm{d,s}} \cdot w_{\mathrm{d,s}})$ is the effective iron length of the stator. $l_{\mathrm{f,s}}$ takes into account the stacking factor $\mathrm{k}_{\mathrm{f,s}}$ and the presence of $N_{\mathrm{d,s}}$ cooling ducts whose width is equal to $w_{\mathrm{d,s}}$. However Equation (2.15) does not take into account that when the teeth get saturated a part of the magnetic flux passes into the slot. This can be written as

$$\hat{\Phi}_{\tau,\mathrm{s,s}} = \hat{\Phi}_{\mathrm{t,s}} + \hat{\Phi}_{\mathrm{s,s}} \tag{2.17}$$

where $\hat{\Phi}_{\tau,\mathrm{s,s}}$ is the magnetic flux per stator slot pitch, $\hat{\Phi}_{\mathrm{t,s}}$ is the effective flux passing through the stator tooth and $\hat{\Phi}_{\mathrm{s,s}}$ is the magnetic flux passing in the stator slot. By considering the

stator tooth cross section $S_{t,s}$, the stator slot cross section $S_{s,s} = S_{\tau_{s,s}} - S_{t,s}$ and by defining an equivalent flux density $\hat{B}'_{t,s}$ so that $\hat{\Phi}_{\tau,s,s} = \hat{B}'_{t,s} \cdot S_{t,s}$, Equation (2.17) leads to:

$$\hat{B}'_{t,s} = \hat{B}_{t,s} + \hat{B}_{s,s} \cdot \frac{S_{s,s}}{S_{t,s}} \tag{2.18}$$

In the slot we have $\hat{B}_{s,s} = \mu_0 \cdot \hat{H}_{s,s}$ where $\hat{H}_{s,s}$ is the magnetic field strength. As there is continuity of the magnetic field at the border between the slot and the tooth one can write: $\hat{H}_{s,s} = \hat{H}_{t,s}$, where $\hat{H}_{t,s}$ is the magnetic field strength in the stator tooth, finally Equation (2.18) becomes:

$$\hat{B}'_{t,s}\left(\hat{H}_{t,s}\right) = \hat{B}_{t,s}\left(\hat{H}_{t,s}\right) + \mu_0 \cdot \hat{H}_{t,s} \cdot \frac{S_{s,s}}{S_{t,s}} \tag{2.19}$$

$\hat{B}'_{t,s}(\hat{H}_{t,s})$ can be seen as an equivalent magnetic characteristic of the stator teeth region considering the presence of air as shown in Figure 2.5. The magnetic field $\hat{H}_{t,s}$ corresponding to the flux density $\hat{B}_{t,s}$ obtained from Equation (2.15) can be derived directly from this magnetic curve. Furthermore as shown in Figure 2.6, the stator teeth of an hydro-motor/generator can have different sections along the height, here five regions are identified. In order to consider such geometry, the tooth is divided in several regions i. For each region the magnetic field is computed at its minimum height $\hat{H}^{min}_{t,s,i}$, at its middle height $\hat{H}^{mid}_{t,s,i}$ and its maximum height $\hat{H}^{max}_{t,s,i}$. Finally the average magnetic field $\hat{H}^{av}_{t,s,i}$ in each stator tooth region i is obtained by applying the Simpson integration method:

$$\hat{H}^{av}_{t,s,i} = \frac{1}{6} \cdot (\hat{H}^{min}_{t,s,i} + 4\hat{H}^{mid}_{t,s,i} + \hat{H}^{max}_{t,s,i}) \tag{2.20}$$

The corresponding magnetic drop in the stator tooth is obtained by:

$$\hat{U}_{m,ts} = \sum_{i=1}^{5} \hat{H}^{av}_{t,s,i} \cdot l_{t,s,i} \tag{2.21}$$

where $l_{t,s,i}$ is the geometric height and also the magnetic path length of the stator tooth region i.

III. Magnetic drop in the stator yoke

In the stator yoke the magnetic voltage drop is expressed as:

$$\hat{U}_{m,ys} = \hat{H}_{y,s} \cdot l'_{y,s} \tag{2.22}$$

$l'_{y,s}$ represents the length of the equivalent magnetic path in the stator yoke. The main difficulty here is to find $l'_{y,s}$ because of the non-uniformity and non-linearity of the magnetic field in this region. Usually it is obtained by considering an equivalent line $l_{y,s}$, normally placed at the middle of the yoke and by defining the correction factor $k_{y,s}$ so that

$$l'_{y,s} = l_{y,s} \cdot k_{y,s} \tag{2.23}$$

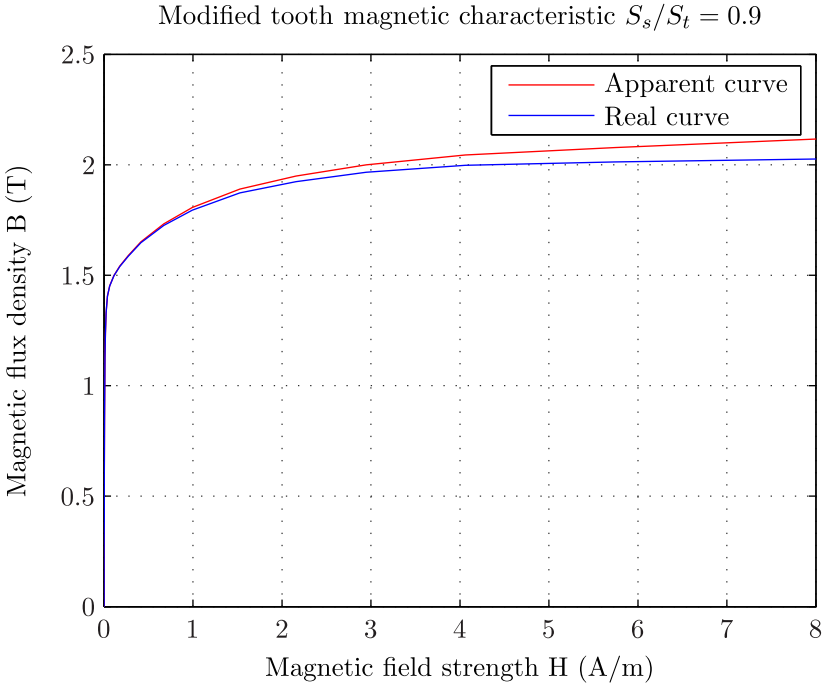

Figure 2.5: Modified magnetic characteristic curve in the teeth

with

$$\mathrm{l_{y,s}} = \frac{\pi}{2p}\left(D_{\mathrm{b,s}} + 2 \cdot h_{\mathrm{s,s}} + \frac{h_{\mathrm{y,s}}}{2}\right) \tag{2.24}$$

$h_{\mathrm{s,s}}$ is the stator slot height and $h_{\mathrm{y,s}}$ is the stator yoke height. The stator yoke magnetic field $\hat{H}_{\mathrm{y,s}}$ is obtained from the stator yoke magnetic flux density $\hat{B}_{\mathrm{y,s}}$ and the magnetic curve of the stator yoke material. $\hat{B}_{\mathrm{y,s}}$ is calculated from the maximum magnetic flux $\hat{\Phi}$ and considering the fact that the magnetic flux splits into two parts after entering the yoke so that:

$$\hat{B}_{\mathrm{y,s}} = \frac{\hat{\Phi}}{2 \cdot S_{\mathrm{y,s}}} \tag{2.25}$$

where $S_{\mathrm{y,s}} = h_{\mathrm{y,s}} \cdot l_{\mathrm{f,s}}$ is the area crossed by one half of the magnetic flux. The correction coefficient $\mathrm{k_{y,s}}$ can be obtained by calculating the average value of the magnetic field strength on the path $\mathrm{l_{y,s}}$ over one pole pitch and considering that the magnetic flux density is varying sinusoidally [PJH08; Wur96] over this path so that:

$$\mathrm{k_{y,s}} = \frac{\int_0^{\pi} H(B)d\alpha}{\hat{H}_{\mathrm{y,s}}} \tag{2.26}$$

where $B = \hat{B}_{\mathrm{y,s}} \sin(\alpha)$.

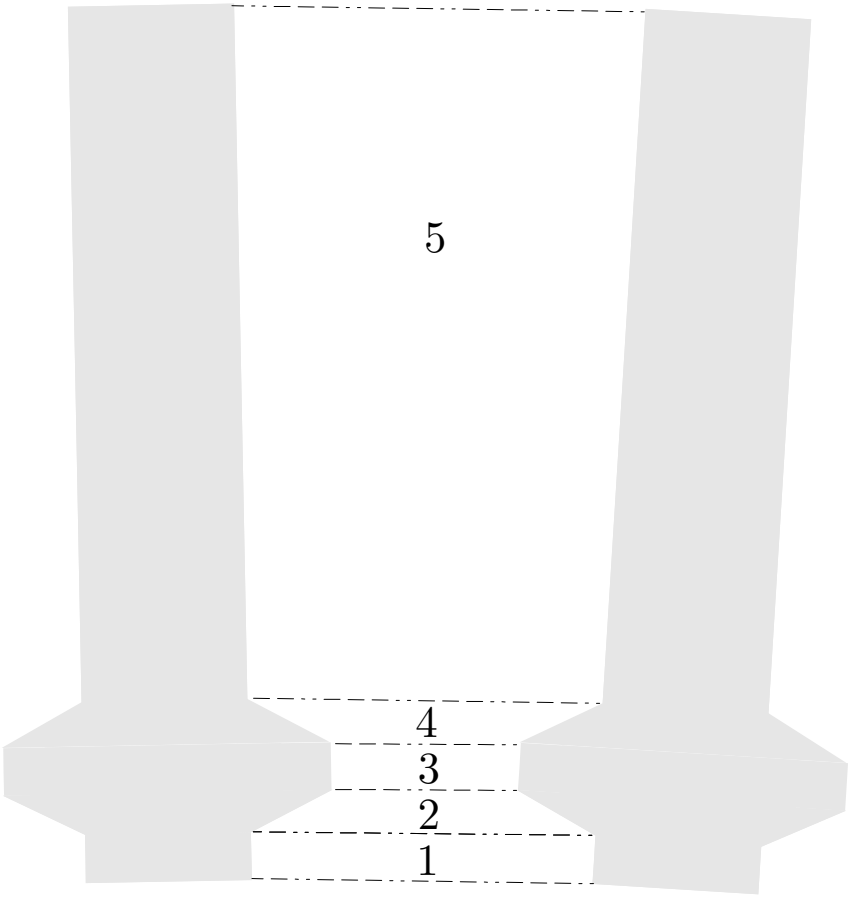

Figure 2.6: Stator slot geometry with different sections (not real proportions)

IV. Magnetic drop in the rotor tooth and yoke

As the rotor teeth and rotor yoke have a similar geometry compared to the stator, the same method can be applied for determining the rotor tooth and rotor yoke magnetic voltage drop.

2.2.5 Calculation of the no-load characteristics

The no-load characteristics calculation makes it possible to define the relation between the magnetizing voltage V_μ equivalent to the no-load stator voltage given by Equation (2.7) and the magnetizing current I_μ. I_μ is obtained by using the equivalence between the total mmf created by the magnetizing current and the sum of all magnetic voltage drops.

$$\hat{\Theta}_{\mathrm{w}}(\mathcal{C}) = 2 \cdot \hat{\theta} = 2 \cdot \hat{U}_{\mathrm{m},\delta} \cdot (\mathrm{K_s} + 1) \tag{2.27}$$

Using the definition of the magnetic voltage $\hat{\theta}$ obtained from Equation (2.10), the value of the required magnetizing current to drive the flux is given by

$$I_{\mu} = \hat{U}_{\mathrm{m},\delta} \cdot (\mathrm{K_s} + 1) \cdot \frac{\pi}{6} \cdot \frac{p}{N_{\mathrm{s,s}} \cdot \xi_{\mathrm{f,s}}} \tag{2.28}$$

For a particular value of the stator voltage U_s^{rms} and assuming at the beginning $\mathrm{K_s} = 0$ so that $\mathrm{C_1} = 1$ and $\alpha_i = 2/\pi$, one can find the maximum magnetic flux $\hat{\Phi}$ and consequently $\hat{B}_\delta$. From $\hat{B}_\delta$ one can derive the maximum flux density in the stator and rotor core regions and finally all the magnetic potential drops by applying the previous described method. From Equation (2.8) one can find the value of the saturation coefficient $\mathrm{K_s}$ and the corresponding values $\mathrm{C_1}$ and α_{i}. One has to repeat the process until convergence, i.e. until the coefficient $\mathrm{K_s}$ is not changing anymore. Finally one can find the value of I_{μ} by applying Equation (2.28).

2.3 Validation of the method

We use the presented method to compute the no-load magnetizing voltage and the flux densities in the stator and rotor teeth regions. The results are compared with those obtained when running a magneto-static 2DFE.

2.3.1 The Two-dimensional finite element model

Figure 2.7 shows an example of 2DFE model of a DFIM. Given the periodicity of the geometry and the stator and rotor winding configuration, only one pole needs to be modeled, the rest of the model is obtained by anti-cyclic periodicity. Furthermore the magnetic field is assumed to be well-driven by the stator and rotor yoke, so that tangential magnetic field boundary conditions are applied on the inner-rotor and the outer-stator border lines.

The stator and rotor core material magnetic behavior is modeled by a non-linear curve giving the dependency between the flux density B and the magnetic strength H. Furthermore both

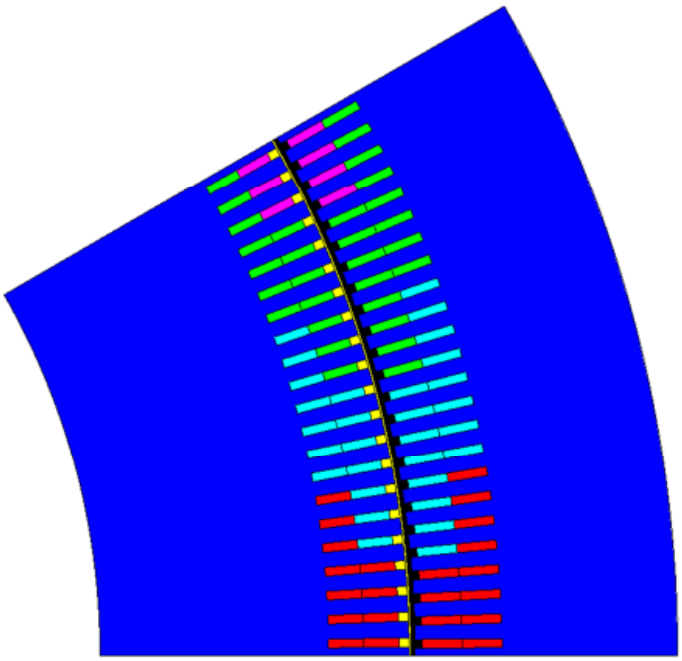

Figure 2.7: 2DFE model

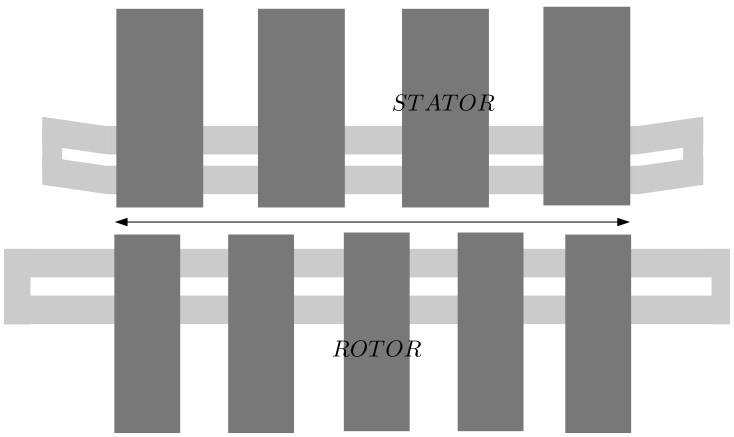

Figure 2.8: Axial overview of the stator and rotor air ducts

materials are assumed having isotropic properties. As already explained, hydro motor/generator units are often equipped with radial cooling air ducts as shown in Figure 2.8.

These ducts are responsible for a local diminution of the airgap flux density in front of themselves as well as a diminution of the iron length. In order to properly consider such three-dimensional effect in the model, one can use the equivalent length l_{i}, defined by Equation (2.29), as the axial length of the model. Note that usually, one adds the term $+2\delta_{\mathrm{g}}$ to l_{i} considering the end-effects [PJH08]. We did not take into account this effect which makes our calculation more conservative. Note that the stator and rotor core lengths, l_{s} and l_{r}, are equal to l.

$$l_{\mathrm{i}} \approx l - N_{\mathrm{d,s}} \frac{w_{\mathrm{d,s}}}{1 + 5\delta_{\mathrm{g}}/w_{\mathrm{d,s}}} - N_{\mathrm{d,r}} \frac{w_{\mathrm{d,r}}}{1 + 5\delta_{\mathrm{g}}/w_{\mathrm{d,r}}} \tag{2.29}$$

Furthermore one must also consider the reduced iron length leading to a different state of magnetic saturation[Ram03]. Indeed because of the magnetic flux conservation one can write for the stator:

$$\hat{\Phi}_{\tau,\mathrm{d,s}} = \hat{\Phi}_{\mathrm{i,s}} \tag{2.30}$$

where $\hat{\Phi}_{\tau,\mathrm{d,s}}$ is the magnetic flux per stator duct pitch and $\hat{\Phi}_{\mathrm{i,s}}$ is the flux going through one stator iron stack. Note that we assume that the flux is well-driven by the iron and no flux goes trough the air duct. Considering $\hat{B}_{\mathrm{i,s}}$ as the stator iron stack flux density one can write:

$$\hat{\Phi}_{\mathrm{i,s}} = \hat{B}_{\mathrm{i,s}} \cdot \frac{l_{\mathrm{f,s}}}{N_{\mathrm{d,s}}} \cdot \pi D_{\mathrm{b,s}} \tag{2.31}$$

One can define the equivalent stator iron stack flux density $\hat{B}'_{\mathrm{i,s}}$ so that:

$$\hat{\Phi}_{\tau,\mathrm{d,s}} = \hat{B}'_{\mathrm{i,s}} \frac{l_{\mathrm{i}}}{N_{\mathrm{d,s}}} \cdot \pi D_{\mathrm{b,s}} \tag{2.32}$$

We obtain:

$$\hat{B}'_{\mathrm{i,s}} = \hat{B}_{\mathrm{i,s}} \frac{l_{\mathrm{f,s}}}{l_{\mathrm{i}}} \tag{2.33}$$

In the same way one can write for the rotor:

$$\hat{B}'_{\mathrm{i,r}} = \hat{B}_{\mathrm{i,r}} \frac{l_{\mathrm{f,r}}}{l_{\mathrm{i}}} \tag{2.34}$$

Finally the three-dimensional stator and rotor core geometry with air ducts is modeled as a Two-Dimensional (2D) geometry with an axial length equal to the ideal length l_{i} and with corrected stator and rotor core material magnetic characteristics. Figure 2.9 shows, as example, the original and the modified magnetic characteristics of the stator core material. One should pay attention to the fact that the flux density values extracted from the 2DFE simulation will have to be rescaled in order to get the real values.[4]

[4]This is further discussed in Chapter 5 when dealing with iron losses in the stator and rotor core

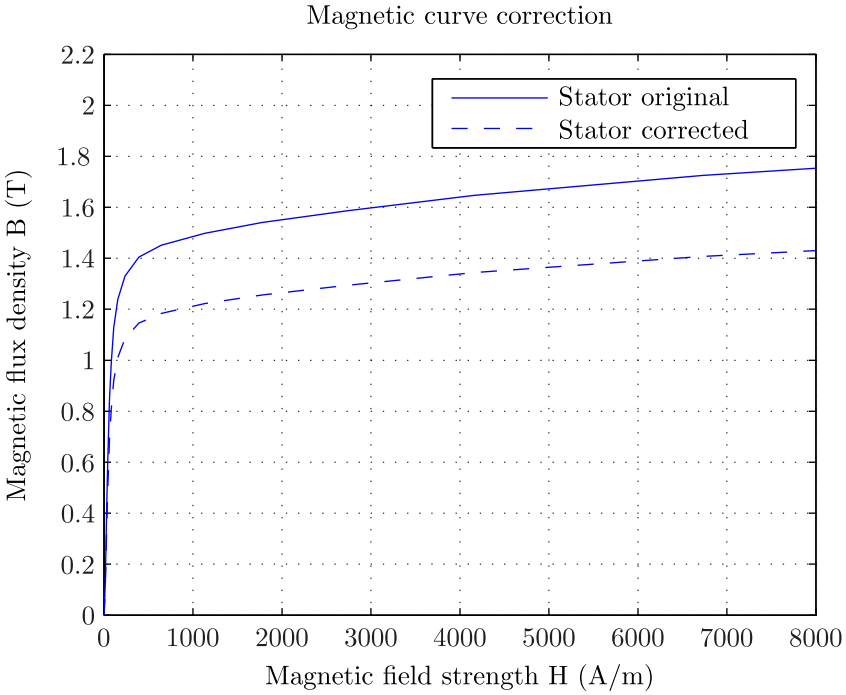

Figure 2.9: Correction of the material magnetic characteristic

2.3.2 Magnetizing voltage curve

Figures 2.10, 2.11 compare the magnetizing voltage curve obtained by using the analytical method and the FE method for two different designs. One can see a good agreement between both calculations.

2.3.3 Stator and rotor teeth flux density

In this part we compare for different designs the stator and rotor magnetic flux densities $\hat{B}_{\mathrm{t,s}}$ and $\hat{B}_{\mathrm{t,r}}$ obtained by using the analytical method and the FE method. The analytical method gives access to the maximum flux density over the tooth height and the average flux density. From the FE simulation results, we calculate the average flux density in the tooth where the passing flux is maximum.

Figures 2.12, 2.13, 2.14, 2.15 show the comparison for the same two designs as previously. Although one can observe some discrepancies, the results are satisfying.

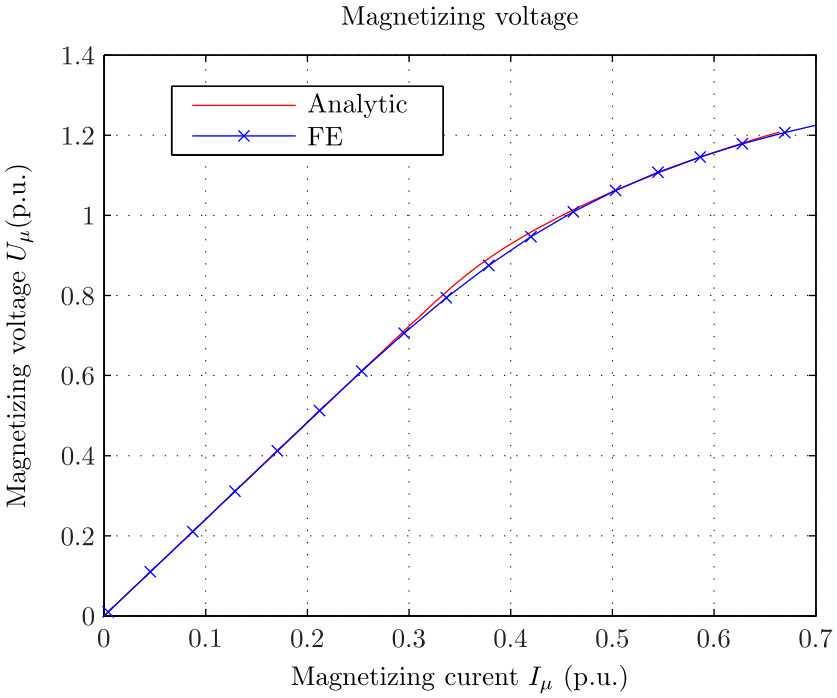

Figure 2.10: Magnetizing voltage: comparison between analytical method and FEM (design 1)

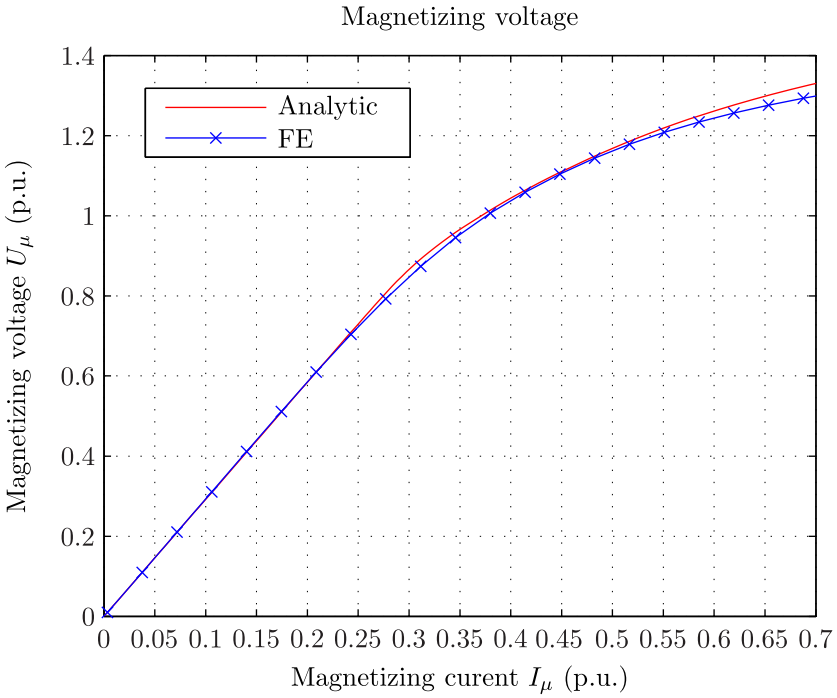

Figure 2.11: Magnetizing voltage: comparison between analytical method and FEM (design 2)

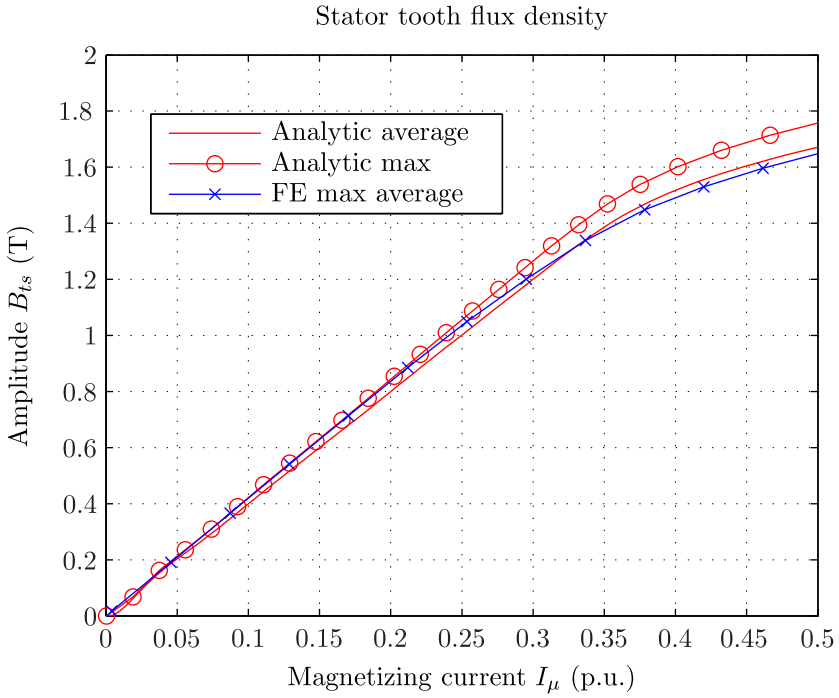

Figure 2.12: Stator flux density: comparison between analytical method and FEM (design 1)

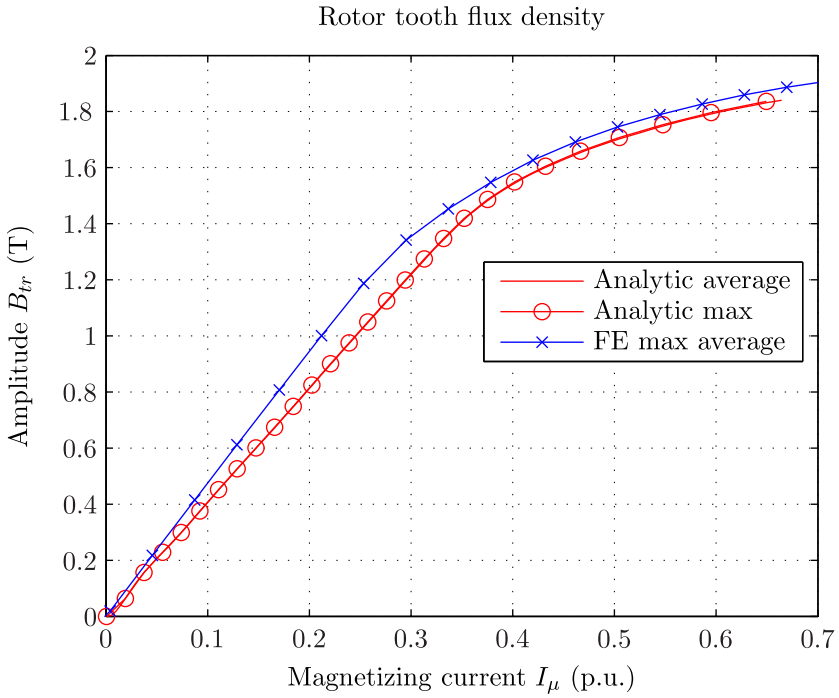

Figure 2.13: Rotor flux density: comparison between analytical method and FEM (design 1)

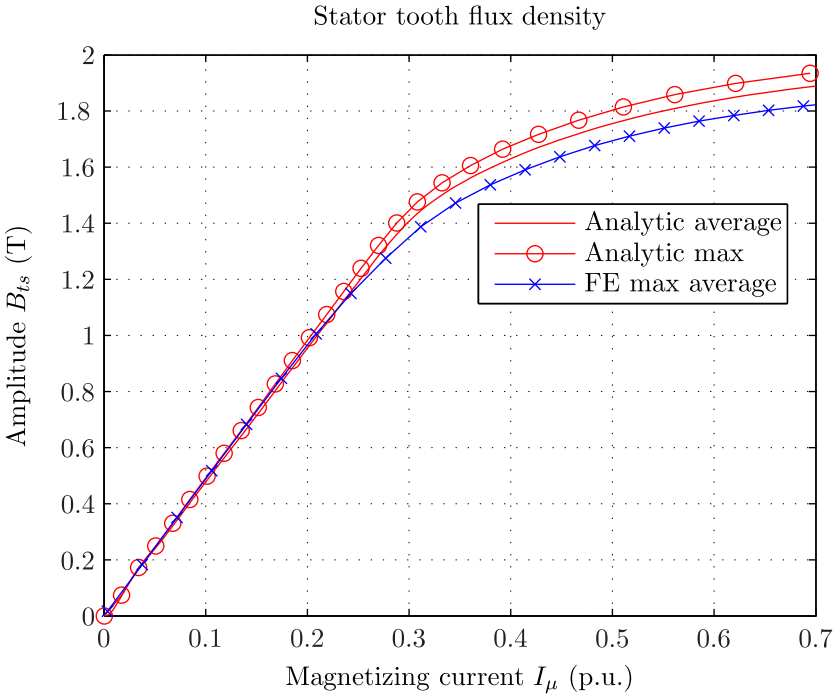

Figure 2.14: Stator flux density: comparison between analytical method and FEM (design 2)

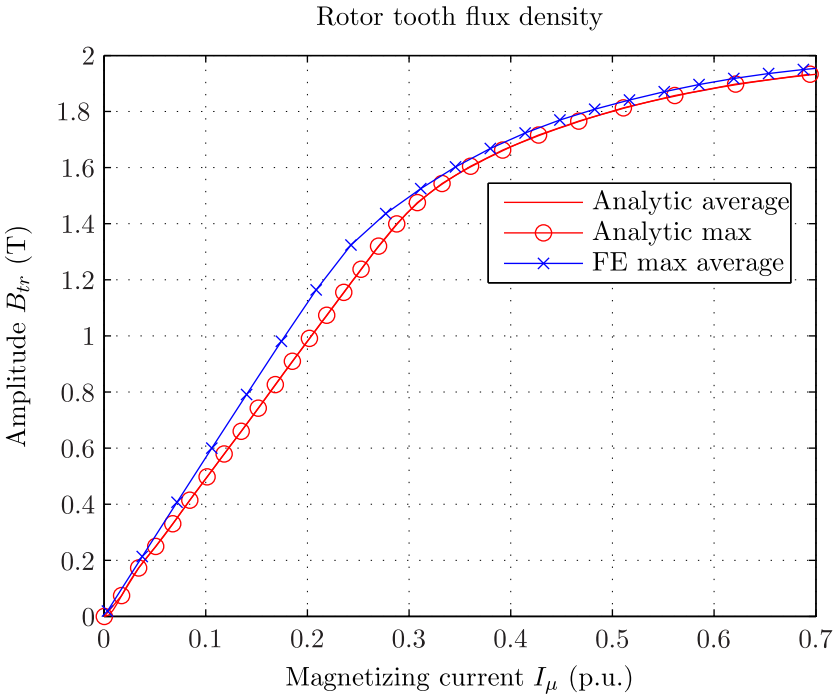

Figure 2.15: Rotor flux density: comparison between analytical method and FEM (design 2)

2.4 Conclusion

This chapter exposed a simplified analytical method in order to model efficiently and accurately the magnetic circuit behavior of the DFIM. This method defined and computed the magnetic voltage drop along a chosen magnetic path crossing the airgap, the stator core and the rotor core regions. The main geometric parameters of the machine were considered for the calculation as well as corrective factors such as the pole enclosure coefficient α_i, the form factor C_1 being able to better quantify the impact of the saturation on the magnetic circuit. Such coefficients were obtained by FE computations and average values were defined in order to cover the full range of studied machine designs. The analytical model was finally validated by carrying out a 2DFE magneto-static computation. We compared in particular the no-load characteristics and the stator and rotor flux densities in the teeth. The defined magnetic model can be used to study the steady-state operation of the machine. This is the object of the next chapter.

3 Steady-state model

3.1 Introduction

This chapter describes an equivalent scheme of the DFIM. The chosen equivalent scheme corresponds to the well-known transformer model of the standard induction machine with a short-circuited rotor. Given the long experience of application of this model and its good accuracy for steady-state analysis, it suits well to the studied type of machine.

The first part details the equivalent circuit structure as well as its corresponding parameters. It focuses more particularly on the definition of the leakage components and on the consideration of the effect of the magnetic circuit saturation on the parameters. 2DFE and 3DFE computations are used to validate the analytical calculation of these parameters.

Given the obtained definition of an equivalent circuit, the second part presents methods to calculate the steady-state load operation of the machine. A parametric calculation makes it possible to study the effect of the slip and the stator voltage amplitude and frequency on the operation of the machine. Operation limits are defined and presented in a capability diagram also known as P-Q diagram.

Finally the results are first validated with a 2DFE magneto-harmonic then with a 2DFE time stepping application. Given the non-negligible simulation time of the latter computation caused by a long initialization state, the validation is not immediate. So as to counter this issue, an efficient method based on the regulation model of the DFIM is carried out. Such time stepping simulations are used in Chapter 4 to evaluate the performances of the machine in particular the iron losses and the electromagnetic forces. Furthermore the developed methodology can be used to simulate transient states of the machine and in particular the start up as it will be shown later in Chapter 5 when dealing with dynamical torques components.

3.2 Structure of the equivalent scheme

The equivalent scheme used for studying the DFIM is defined in Figure 3.1. It corresponds to the equivalent transformer model of the induction machine with short-circuited rotor in which a voltage source on rotor side has been added. Lorenzen and Miller [Lor98; Mil10] use this definition. The scheme parameters are the following:

- the magnetizing inductance L_{h}
- the stator and rotor resistance R_{s} and R'_{r} (expressed in the stator frame)
- the stator and rotor leakage inductance $L_{\sigma,\mathrm{s}}$ and $L'_{\sigma,\mathrm{r}}$ (expressed in the stator frame)

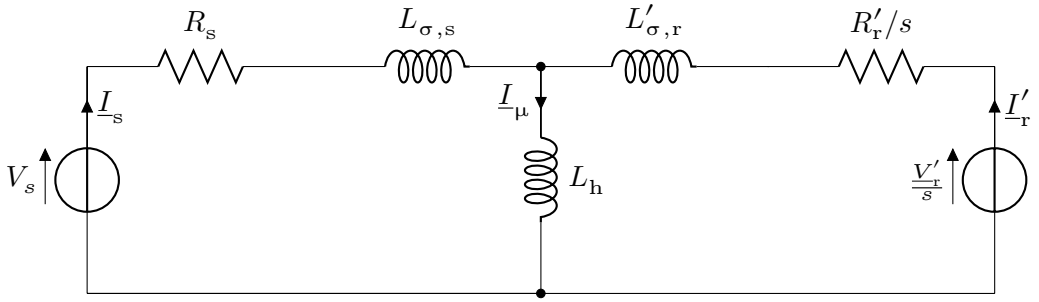

Figure 3.1: Equivalent scheme of the DFIM

In this scheme the rotor quantities (voltage, current, resistance, leakage inductance) are expressed in the stator frame using the transformation ratio $u_t = (\xi_{f,s}N_{s,s}/\xi_{f,r}N_{s,r})$ so that: $\underline{I}'_r = \underline{I}_r/u_t$, $\underline{V}'_r = \underline{V}_r \cdot u_t$, $R'_r = R_r \cdot u_t^2$, $L'_{\sigma,r} = L_{\sigma,r} \cdot u_t^2$.

Following part derives analytical expressions for all the equivalent circuit parameters. The different magnetic leakage components are presented as well as the different analytical methods available in the literature. Last part computes numerically in two steps the different components of leakages; firstly the leakages in the active part with a 2DFE simulation and secondly the leakages in the end part by using a 3DFE model.

3.2.1 The magnetizing inductance

In absence of saturation the magnetizing inductance of a three-phase winding is defined as:

$$L_h = \mu_0 \cdot (N_{s,s}\xi_{f,s})^2 \cdot \frac{6}{\pi^2}\frac{l_i \tau_{p,s}}{p\delta_g} \tag{3.1}$$

By using the results of the magnetic model developed in Chapter 2, the relation between the maximum magnetizing voltage $\hat{V}_\mu$ and the maximum magnetizing current $\hat{I}_\mu$ i.e $\left|\underline{V}_\mu\right| = 2\pi f_s \cdot L_h \left|\underline{I}_\mu\right|$ one can consider the effect of saturation on the magnetizing inductance [1]. Figure 3.2 shows the magnetizing inductance for different magnetizing currents and compares with the results obtained from a 2DFE simulation. It is expressed on the graph in p.u. of the stator reference impedance $Z_{ref} = U_s^2/S$. One can observe a good agreement between both computations.

3.2.2 The stator and rotor resistances

The stator and rotor windings are double-layer windings, this means that each stator and rotor slot counts one top and one bottom copper conductor. Figure 3.3-left describes a typical stator and rotor slot with its two conductors. The stator winding is fed with currents alternating at the network frequency i.e. $f_s = 50\,\text{Hz}$ or $f_s = 60\,\text{Hz}$. In order to decrease eddy-current losses in

[1] The magnetizing of Chapter 2 is divided by u_t so as to express it in the stator reference frame

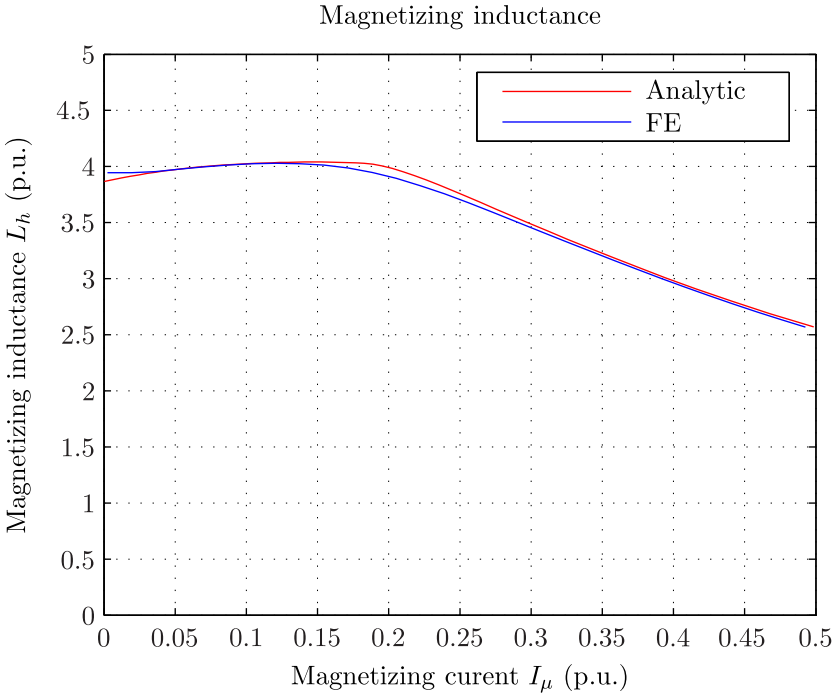

Figure 3.2: Effect of saturation of magnetizing inductance

the stator bars due to skin effect, it is necessary to split each bar in several copper strands as shown in Figure 3.3-right.

At the rotor, the frequency of the rotor currents f_r is linked to the slip by the relation $f_r = s \cdot f_s$. The studied machines run at a speed in the range 90 % to 110 % of the synchronism speed i.e. at a slip in the range $\pm 10\%$, consequently the rotor currents frequency remains low in normal operation i.e less than 6 Hz. However during the start for pumping operation, the stator winding is short circuited while the amplitude and the frequency of the rotor currents are controlled in order to drive the machine to the synchronous speed. Figure 3.4 shows the evolution of the rotor frequency during such operation. One can observe that the rotor frequency reaches higher values i.e. close to the rated frequency of the stator currents. Consequently the rotor bars are also divided in several strands. However as the rotor frequency is small in normal operation, the rotor bar strands can be larger than the stator strands.

Figure 3.5 shows the non-uniform distribution of the magnetic field in a slot when the slot conductor carries an alternative current.[2] A different voltage is induced on each strand and because the strands of a bar are connected in parallel, the induced voltages lead to circulating currents between strands and consequently additional copper losses.

In order to limit the circulating currents between the strands, the Roebel technology is used for both the stator and the rotor windings. Such technology is based on a special transposition of the strands within the portion of the bar belonging to the magnetic core as shown in Figure

[2]Note that only one conductor is placed here in the slot for simplification reasons, normally two-layers windings are used

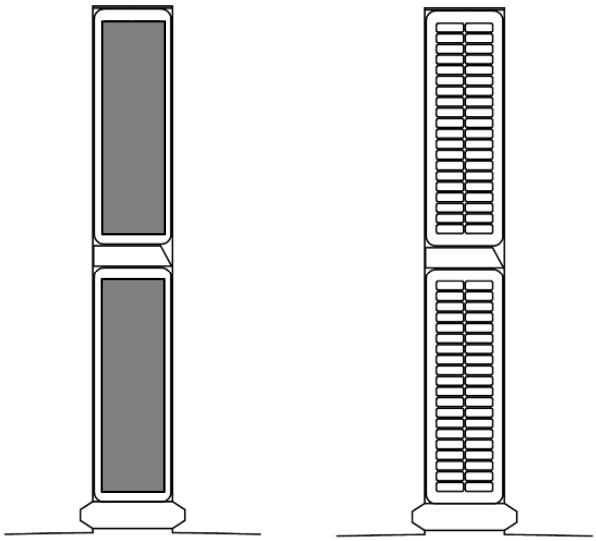

Figure 3.3: Slot with full bars (left) and subdivided bars (right)

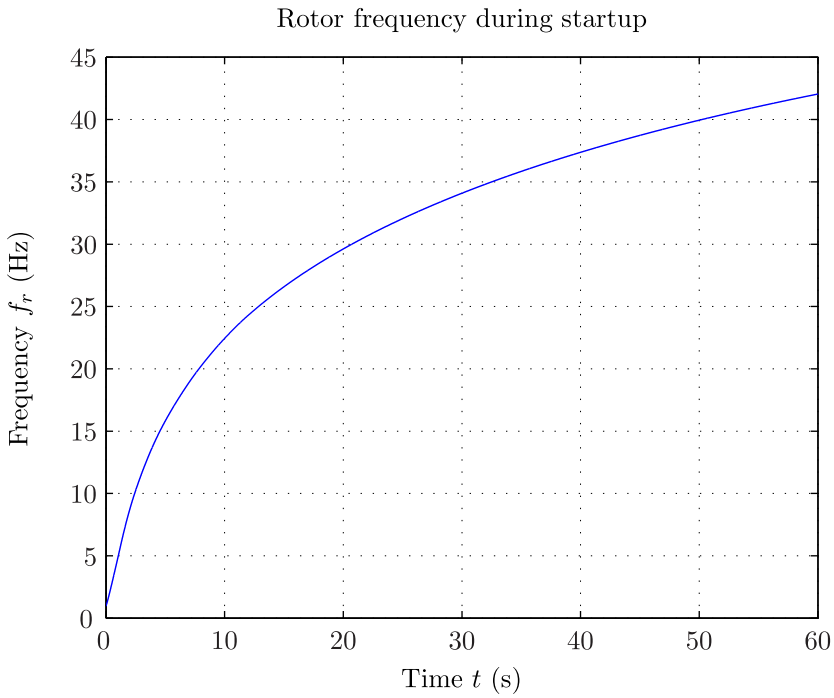

Figure 3.4: Rotor electrical frequency during startup

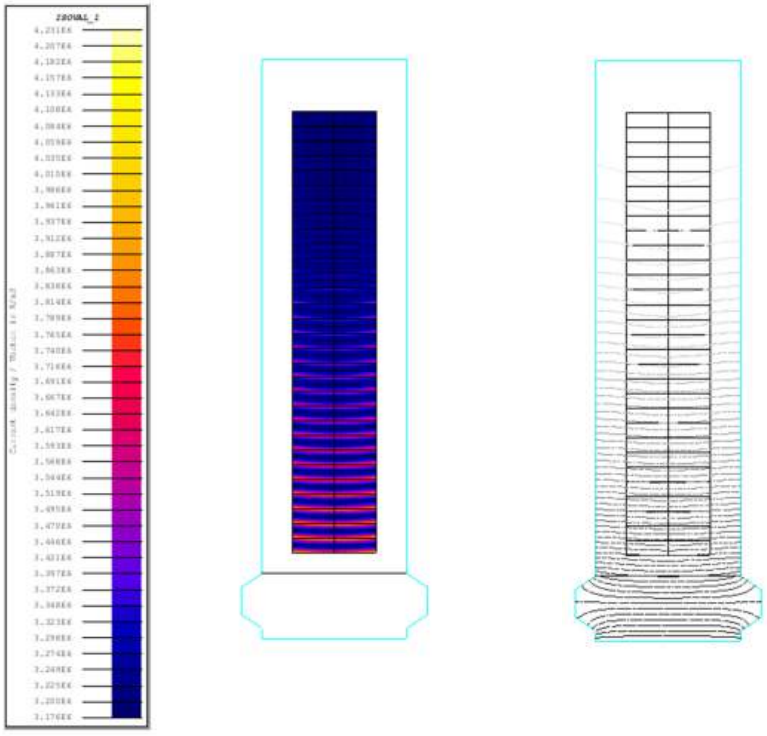

Figure 3.5: Current density (left) and magnetic field (right) in a slot

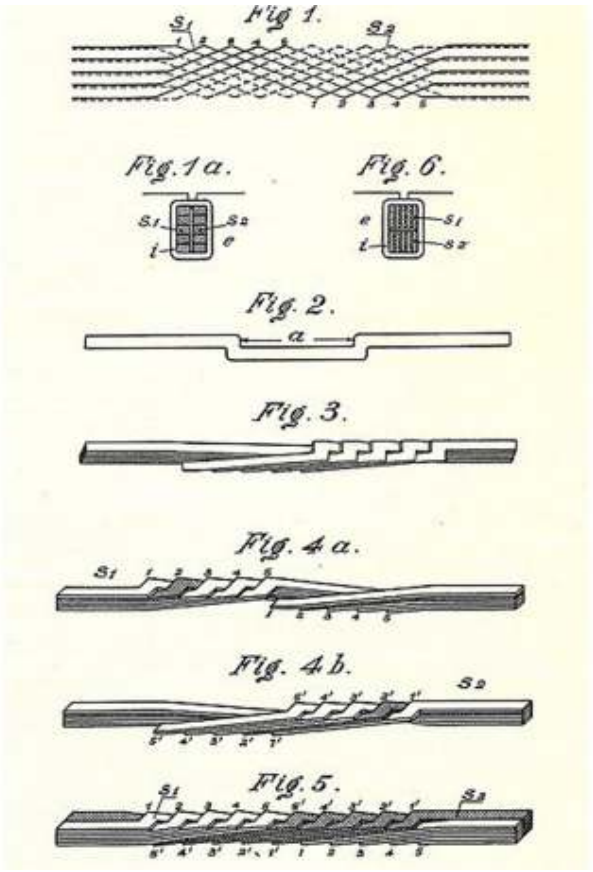

Figure 3.6: Roebel bar technology (patent: Ludwig Roebel 1912)

3.6. One can see that each strand will occupy all the positions. This prevents the circulation of current between each strand of a bar and consequently reduces the losses. Note that the parasitic end-winding fields can also lead to circulating currents and eddy-currents, this is not considered in this study. More details on this can be found in [Tra03].

Figure 3.5-right shows that the magnetic field is higher in the top of the slot than in the bottom of the slot. One can also see the non-uniform distribution of the current density within the slot. Additional eddy-current losses need to be considered when calculating the total losses in the stator and rotor winding by using eddy-current coefficients. Finally the stator and rotor bar resistances, $R_{\mathrm{b,s}}$ and $R_{\mathrm{b,r}}$ are obtained by the following formula:

$$\begin{aligned} R_{\mathrm{b,s}} &= R_{\mathrm{b,dc,s}} + R_{\mathrm{b,ac,s}} \\ R_{\mathrm{b,r}} &= R_{\mathrm{b,dc,r}} + R_{\mathrm{b,ac,r}} \end{aligned} \tag{3.2}$$

The stator term $R_{\mathrm{b,dc,s}}$ is given by:

$$R_{\mathrm{b,dc,s}} = \frac{1}{\kappa_{cu}} \cdot \frac{l_{\mathrm{b,s}}}{2 \cdot N_{\mathrm{st,s}} S_{\mathrm{st,s}}} \tag{3.3}$$

where $N_{\mathrm{st,s}}$ is the number of vertical stator strands per bar $S_{\mathrm{st,s}} = h_{\mathrm{st,s}} \cdot w_{\mathrm{st,s}}$ is the area of

one stator strand, with $h_{\mathrm{st,s}}$ the stator strand height and $w_{\mathrm{st,s}}$ the stator strand width, $l_{\mathrm{b,s}}$ is the total length of one stator bar including the length of the bar placed in the slot and the end-winding part and finally κ_{cu} is the copper electrical conductivity calculated at a temperature of 75 °C as it is normally done for such machines. The stator term $R_{\mathrm{b,ac,s}}$ corresponds to an additional resistance due to eddy-current losses defined as:

$$R_{\mathrm{b,ac,s}} = \left(1 - \mathrm{k}_{\mathrm{m,s}}\left(\xi_{\mathrm{st,s}}\right)\right) R_{\mathrm{b,dc,s}} \tag{3.4}$$

where $\mathrm{k}_{\mathrm{m,s}}$ is the mean eddy-current loss coefficient over the whole stator winding defined as:

$$\mathrm{k}_{\mathrm{m,s}}\left(\xi_{\mathrm{st,s}}\right) = \left(k_{\mathrm{r,s}}\left(\xi_{\mathrm{st,s}}\right) - 1\right) \frac{l_{\mathrm{f,s}}}{l_{\mathrm{b,s}}} + 1 \tag{3.5}$$

where $k_{\mathrm{r,s}}(\xi_{\mathrm{st,s}})$ is the mean eddy-current loss coefficient over all stator strands given by Equation (3.6):

$$k_{\mathrm{r,s}}(\xi_{\mathrm{st,s}}) = \Phi(\xi_{\mathrm{st,s}}) + \frac{\left(2 \cdot N_{\mathrm{st,s}}\right)^2 - 1}{3} \Psi(\xi_{\mathrm{st,s}}) \tag{3.6}$$

where Φ and Ψ are two field functions defined by as a function of the reduced height $\xi_{\mathrm{st,s}}$:

$$\Phi(\xi_{\mathrm{st,s}}) = \xi_{\mathrm{st,s}} \frac{\sinh(2\xi_{\mathrm{st,s}}) + \sin(2\xi_{\mathrm{st,s}})}{\cos(2\xi_{\mathrm{st,s}}) - \cos(2\xi_{\mathrm{st,s}})} \tag{3.7}$$

$$\Psi(\xi_{\mathrm{st,s}}) = 2\xi_{\mathrm{st,s}} \frac{\sinh(\xi_{\mathrm{st,s}}) - \sin(\xi_{\mathrm{st,s}})}{\cos(\xi_{\mathrm{st,s}}) + \cos(\xi_{\mathrm{st,s}})} \tag{3.8}$$

$\xi_{\mathrm{st,s}}$ is given by Equation (3.9).

$$\xi_{\mathrm{st,s}} = h_{\mathrm{st,s}} \cdot \sqrt{\frac{2\pi f_{\mathrm{s}} \cdot \mu_0 \kappa_{\mathrm{cu}}}{2} \cdot \frac{2 \cdot w_{\mathrm{st,s}}}{w_{\mathrm{s,s}}}} \tag{3.9}$$

Note that $k_{\mathrm{r,s}}\left(\xi_{\mathrm{st,s}}\right)$ is applied only for the portion of the stator bar belonging to the core. $R_{\mathrm{b,dc,r}}$ and $R_{\mathrm{b,ac,r}}$ are based on the same formula but depend on the rotor dimensions, $S_{\mathrm{st,r}}$, $N_{\mathrm{st,r}}$ and $l_{\mathrm{b,r}}$. Finally the total rotor and stator phase winding resistance, R_{s} and R_{r} are given by:

$$R_{\mathrm{s}} = 2 \cdot N_{\mathrm{s,s}} \cdot R_{\mathrm{b,s}} \tag{3.10}$$

$$R_{\mathrm{r}} = 2 \cdot N_{\mathrm{s,r}} \cdot R_{\mathrm{b,r}} \tag{3.11}$$

The coefficient 2 comes from the fact that a turn is made of two bars connected in series.

3.2.3 The stator and rotor winding leakage inductance

This part defines and computes the stator and rotor leakage inductances. The correct assessment of these elements is important since it will impact on the magnetizing current amplitude and consequently on the losses. Furthermore the leakage inductance will set the maximum values of the currents and torque during faults such as short-circuits or faulty synchronization. Three main components compose the winding leakage inductance:

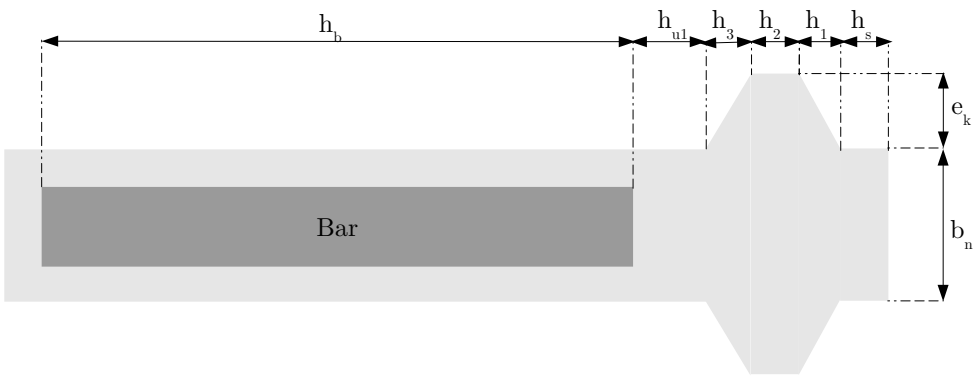

Figure 3.7: Detailed slot geometry with only one conductor (not real proportions)

- the slot leakage inductance
- the airgap leakage inductance
- the end-winding leakage inductance

I. The slot leakage inductance

Figure 3.5-right shows the repartition of the magnetic flux lines created by one conductor inside a slot. A part of the flux does not cross the airgap and closes itself inside the slot; this flux stands for the slot leakage flux. The stator leakage inductance is expressed as:

$$L_{\sigma,\mathrm{sl,s}} = \frac{2\mu_0 l_\mathrm{i} N_\mathrm{s,s}^2}{q_\mathrm{s} \cdot p} \cdot \lambda_{1,\mathrm{s}} \tag{3.12}$$

where q_s is the number of stator slots per pole and phase, $\lambda_{1,\mathrm{s}}$ is a well known coefficient [LW61]depending on the slot geometry characteristics detailed in Figure 3.7. It is given by Equation (3.13).

$$\lambda_{1,\mathrm{s}} = \frac{h_\mathrm{b,s}}{3w_\mathrm{s,s}} + \frac{h_{\mathrm{u}_1,\mathrm{s}}}{w_\mathrm{s,s}} + \frac{h_\mathrm{3,s}}{w_\mathrm{s,s} + \mathrm{e_{k,s}}} + \frac{h_\mathrm{2,s}}{w_\mathrm{s,s} + 2\mathrm{e_{k,s}}} + \frac{h_\mathrm{1,s}}{w_\mathrm{s,s} + \mathrm{e_{k,s}}} + \frac{h_\mathrm{p,s}}{w_\mathrm{s,s}} \tag{3.13}$$

Equation (3.13) is always valid when there is only one bar per slot. As seen previously in the studied machines two bars occupy each slot and do not necessary belong to the same phase. Depending on the phase shift between both currents, the leakage inductance is not the same. Table 3.1 shows an example of a three-phase winding, one can see that the slot number 1 carries two conductors of the phase a so that the corresponding current phase shift $\gamma_\mathrm{k,s}$ equals 0°. The slot number 2 carries one conductor of the phase a and one conductor of the phase c in opposite direction so that the corresponding phase shift $\gamma_\mathrm{k,s}$ equals 60°. The general method consists in considering the top and bottom bar inductance coefficients $\lambda_{2,\mathrm{t,s}}$ and $\lambda_{2,\mathrm{b,s}}$ defined as [LW61]:

$$\lambda_{2,\mathrm{b,s}} = \frac{h_\mathrm{bb,s}}{3 \cdot w_\mathrm{s,s}} + \frac{h_{\mathrm{u}_2,\mathrm{s}}}{w_\mathrm{s,s}} + \frac{h_\mathrm{tb,s}}{w_\mathrm{s}} + \frac{h_{\mathrm{u}_1,\mathrm{s}}}{w_\mathrm{s,s}} + \frac{h_\mathrm{3,s}}{w_\mathrm{s} + \mathrm{e_{k,s}}} + \frac{h_\mathrm{2,s}}{w_\mathrm{s} + 2 \cdot \mathrm{e_{k,s}}} + \frac{h_\mathrm{1,s}}{w_\mathrm{s} + \mathrm{e_{k,s}}} + \frac{h_\mathrm{p,s}}{w_\mathrm{s}} \tag{3.14}$$

Slot index	1	2	3	4	5	6	7	8	9	10	11	12	13	14	15	16	17	18
Top	a	a	a	-c	-c	-c	b	b	b	-a	-a	-a	c	c	c	-b	-b	-b
Bottom	a	-c	-c	-c	b	b	b	-a	-a	-a	c	c	c	-b	-b	-b	a	a

Table 3.1: Winding configuration example over two poles: $q = 3$, $Y_1 = 7$

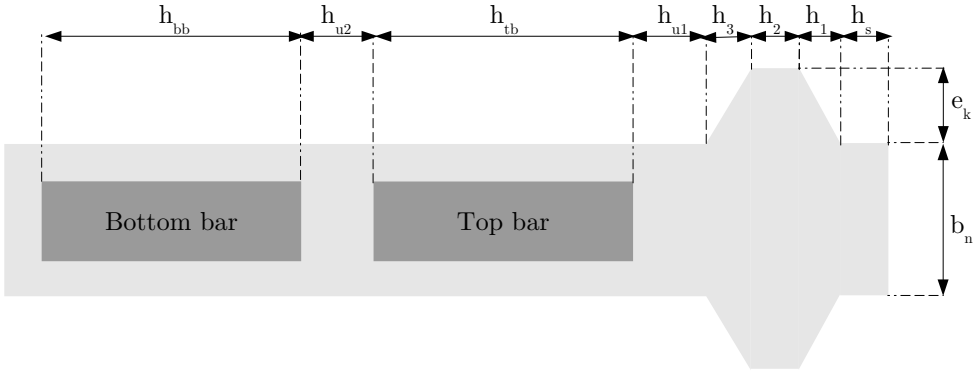

Figure 3.8: Detailed slot geometry with two conductors (not real proportions)

$$\lambda_{2,\mathrm{t,s}} = \frac{h_{\mathrm{tb,s}}}{3 \cdot w_{\mathrm{s}}} + \frac{h_{\mathrm{u_1,s}}}{w_{\mathrm{s,s}}} + \frac{h_{3,\mathrm{s}}}{w_{\mathrm{s,s}} + \mathrm{e_{k,s}}} + \frac{h_{2,\mathrm{s}}}{w_{\mathrm{s,s}} + 2 \cdot \mathrm{e_{k,s}}} + \frac{h_{1,\mathrm{s}}}{w_{\mathrm{s,s}} + \mathrm{e_{k,s}}} + \frac{h_{\mathrm{p,s}}}{w_{\mathrm{s,s}}} \tag{3.15}$$

Furthermore an additional coefficient representing the mutual effect from the top and bottom conductors is expressed as:

$$\lambda_{2,\mathrm{tb,s}} = \sum_{k=1}^{N_{\mathrm{z,s}}} \frac{\cos(\gamma_{\mathrm{k,s}})}{N_{\mathrm{z,s}}} \frac{h_{\mathrm{tb,s}}}{2 \cdot w_{\mathrm{s,s}}} + \frac{h_{\mathrm{u_1,s}}}{w_{\mathrm{s,s}}} + \frac{h_{3,\mathrm{s}}}{w_{\mathrm{s,s}} + \mathrm{e_{k,s}}} + \frac{h_{2,\mathrm{s}}}{w_{\mathrm{s,s}} + 2 \cdot \mathrm{e_{k,s}}} + \frac{h_{1,\mathrm{s}}}{w_{\mathrm{s,s}} + \mathrm{e_{k,s}}} + \frac{h_{\mathrm{p,s}}}{w_{\mathrm{s,s}}} \tag{3.16}$$

where $N_{\mathrm{z,s}}$ is the number of stator slots. Finally the leakage coefficient $\lambda_{2,\mathrm{s}}$ is expressed as:

$$\lambda_{2,\mathrm{s}} = \frac{1}{4}(\lambda_{2,\mathrm{b,s}} + \lambda_{2,\mathrm{t,s}} + 2 \cdot \lambda_{2,\mathrm{tb,s}}) \tag{3.17}$$

Equation (3.18) and (3.19) make it possible to compute the stator slot leakage inductance $L_{\sigma,\mathrm{sl,s}}$ when two bars are placed in each slot:

$$L_{\sigma,\mathrm{sl,s}} = \frac{2\mu_0 l_{\mathrm{i}} N_{\mathrm{s,s}}^2}{q_{\mathrm{s}} \cdot p} \cdot \lambda_{2,\mathrm{s}} \tag{3.18}$$

In the same way one can find the rotor slot leakage inductance $L_{\sigma,\mathrm{sl,r}}$:

$$L_{\sigma,\mathrm{sl,r}} = \frac{2\mu_0 l_{\mathrm{i}} N_{\mathrm{s,r}}^2}{q_{\mathrm{r}} \cdot p} \cdot \lambda_{2,\mathrm{r}} \tag{3.19}$$

where q_{r} is the number of rotor slots per pole and phase. Note that this calculation considers an infinite iron magnetic permeability. In reality as seen in Chapter 2, the rotor and stator magnetic circuits and more particularly the teeth regions are affected by magnetic saturation.

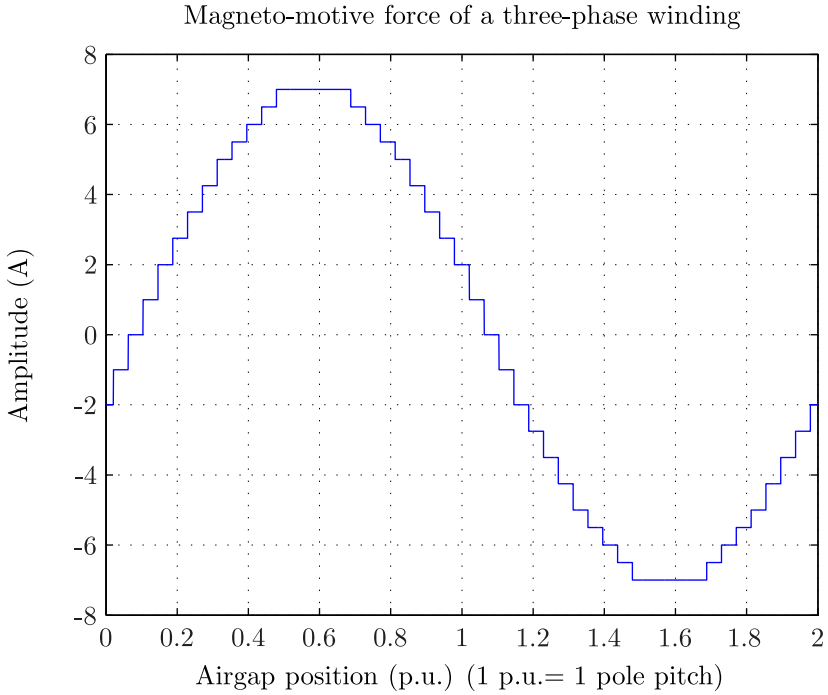

Figure 3.9: mmf distribution of a three-phase winding

For example the magnetic saturation of the tooth tips will lead to a virtual increase of the slot opening and consequently a decrease of the slot leakage inductance. Note that one could also take into account the effect of eddy-current which will lead to a slight decrease of the slot leakage inductance; this can been here neglected given the frequency of the stator and rotor currents.

II. The airgap leakage inductance

The rotor and stator windings of the studied machine are placed in slots. Figure 3.9 shows the resulting mmf of a three-phase winding supplied with a three-phase balanced current source[3]. One can see that the field wave is not purely sinusoidal but consists of several steps. The airgap leakage flux is usually decomposed into two terms. Firstly there is the phase belt leakage flux which is equal to the area between an ideal sinusoidal mmf and the mmf obtained if the number of slots were infinite. Secondly there is the zigzag leakage flux which is equal to the area between the mmf obtained with an infinite number of slots and the real stepped mmf [Fog99].

In order to better visualize the behavior of the leakage flux in the airgap, we carry out a 2DFE simulation. We use the model of Chapter 2 and supply the stator winding and the rotor winding in a way that the stator magnetic field compensates the rotor magnetic field. In this case the fundamental flux is reduced to zero whereas the harmonic flux components are still present. Figure 3.10 shows the corresponding simulation results and more particularly the iso-flux lines. Some flux lines travel on one side from one tooth to another tooth, these are

[3]More details on mmf calculation are given in Chapter 4

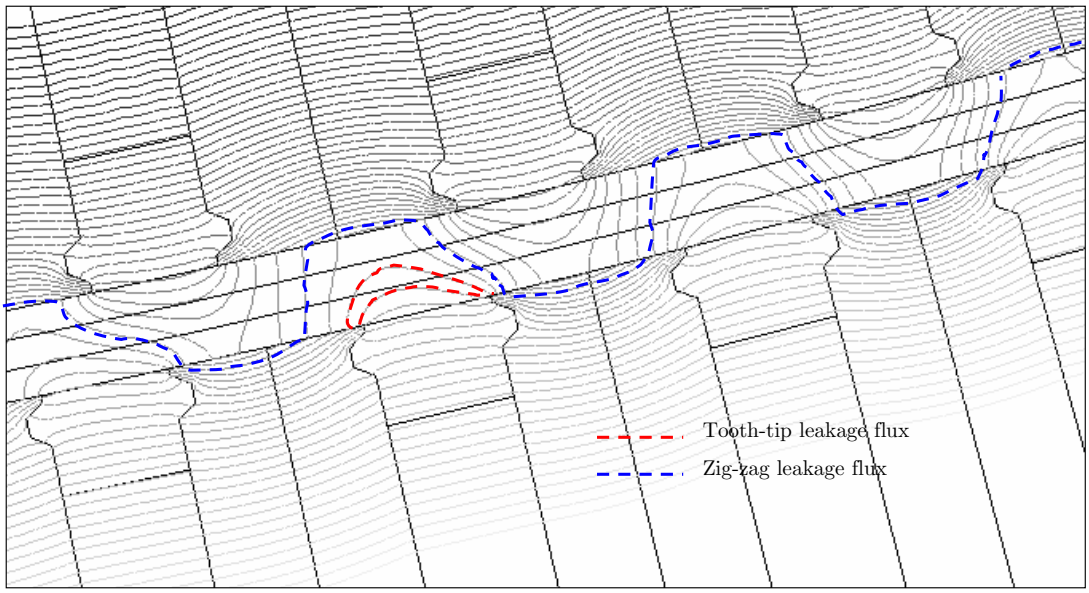

Figure 3.10: Airgap flux leakage example

usually called tooth-tip leakage fluxes, some flux lines alternate between the stator teeth and the rotor teeth, these are called zig-zag leakage fluxes. When the airgap is large as it is the case for hydraulic salient-pole synchronous machines, the airgap leakage flux mainly behaves as the tooth-tip leakage flux. In the case of the induction which have a smaller airgap, the airgap leakage flux mainly behaves in a zig-zag way.

One can find in the literature several articles and books dealing with the calculation of airgap leakage flux leakage inductance. Belot [Bel82] proposes to decompose this flux into three elements: the tooth tip leakage inductance $L^{\mathrm{B}}_{\sigma,\mathrm{tt}}$ given by Equation (3.20), the phase belt leakage inductance $L_{\sigma,\mathrm{diff}}$ given by Equation (3.21) and the zig-zag leakage inductance $L_{\sigma,\mathrm{zz}}$ given by Equation (3.22). If the airgap is doubly slotted, as it is the case here, Belot suggests to multiply by two the tooth tip leakage inductance.

$$L^{\mathrm{B}}_{\sigma,\mathrm{tt}} = \frac{2\mu_0 l_{\mathrm{i}} N^2_{\mathrm{s,s}}}{q_{\mathrm{s}} \cdot p} \frac{5\delta_{\mathrm{g}}}{5w_{\mathrm{s,s}} + 4\delta_{\mathrm{g}}} \tag{3.20}$$

$$L^{\mathrm{B}}_{\sigma,\mathrm{diff}} = \frac{2\mu_0 l_{\mathrm{i}} N^2_{\mathrm{s,s}}}{q_{\mathrm{s}} \cdot p} \frac{\tau^2_{\mathrm{p,s}}}{\pi^2 \cdot \delta_{\mathrm{g}} \tau_{ss}} \cdot 0.0025 \tag{3.21}$$

$$L^{\mathrm{B}}_{\sigma,\mathrm{zz}} = \frac{2\mu_0 l_{\mathrm{i}} N^2_{\mathrm{s,s}}}{q_{\mathrm{s}} \cdot p} \frac{(\tau_{s,\mathrm{s}} - w_{\mathrm{s,s}})^2}{8\delta_{\mathrm{g}} \tau_{s,\mathrm{s}}} \tag{3.22}$$

Note that this considers both the rotor and the stator. Foggia [Fog99] proposes similar equations for the phase belt leakage and zig-zag leakage inductances while the tooth tip leakage inductance is not treated. Alger [Alg51] does not mention as well the tooth-tip leakage inductance but gives two other formula for the phase-belt and zig-zag leakage inductances. Firstly the total belt-leakage inductance is the sum of all the harmonic magnetizing inductance of a winding. For

the stator it is derived from Equation (3.23). The formula is the same for the rotor but with the winding coefficient ξ_ν of the rotor winding mmf.

$$L^{\mathrm{A}}_{\sigma,\nu,s} = \frac{L_{\mathrm{h}}}{\xi^2_{\mathrm{f,s}}} \cdot \sum_{\substack{\nu=1 \\ \nu \neq p}}^{+\infty} \left(\frac{\xi_{\nu,s}}{\nu/p} \right)^2 \tag{3.23}$$

Note that this sum does not consider the third and its multiple harmonics as well as the fundamental component. Besides this, each winding harmonic induces voltages and consequently circulating currents on the other winding, which should lead to a damping effect of the leakage flux and consequently to a reduction of the total leakage inductance. This effect would be very strong in case of an induction with squirrel cage rotor; for the studied machine this effect is not so strong and will be neglected.

Secondly, the zig-zag leakage inductance is splitted between the stator Equation (3.24) and the rotor Equation (3.25)

$$L^{\mathrm{A}}_{\sigma,\mathrm{zz,s}} = \frac{\pi^2 \cdot L_{\mathrm{h}}}{12 \cdot (3q_{\mathrm{s}})^2} \cdot \left(1 - \frac{\frac{w_{\mathrm{t,s}}}{\tau_{s,\mathrm{s}}} \cdot (1 + \frac{w_{\mathrm{t,s}}}{\tau_{s,\mathrm{s}}})(1 - \frac{1}{k_{\mathrm{c}}})}{2 \cdot \frac{1}{k_{\mathrm{c}}}} \right) \tag{3.24}$$

$$L^{\mathrm{A}}_{\sigma,\mathrm{zz,r}} = \frac{\pi^2 \cdot L_{\mathrm{h}}}{12} \cdot \left(\frac{1}{(3q_{\mathrm{r}})^2} - \frac{\frac{w_{\mathrm{t,s}}}{\tau_{s,\mathrm{s}}} \cdot (1 + \frac{w_{\mathrm{t,s}}}{\tau_{s,\mathrm{s}}})(1 - \frac{1}{k_{\mathrm{c}}})}{2 \cdot \frac{1}{k_{\mathrm{c}}} \cdot (3q_{\mathrm{s}})^2} \right) \tag{3.25}$$

Pyrhonen [PJH08] considers the tooth tip leakage inductance in the same way as Belot and identifies the airgap leakage inductance as the sum of all the main inductance created by each harmonic of the winding which is similar as Equation (3.23). The zig-zag inductance is not explicitly treated. The evaluation of all these methods will be done in next section when comparing with FE simulation results.

IV. Computation of the overhang leakage inductance

The overhang leakage inductance is due to the leakage flux in the end-winding regions. Because of the Three-Dimensional (3D) configuration of the rotor and stator end-windings, an accurate analytical calculation of corresponding leakage inductance is difficult. Some analytical formula exist based on the geometry and the spatial disposition of the windings. One formula is used by Belot [Bel82], Foggia [Fog99] based on the work of Alger and given by Equation (3.26)

$$L^{\mathrm{A}}_{\sigma,\mathrm{end,s}} = \mu_0 \cdot \frac{3 \cdot N^2_{\mathrm{s,s}} \cdot D_{\mathrm{b,s}}}{p^2} \cdot f(\gamma_{\mathrm{s}}) \tag{3.26}$$

where $f(\gamma)$ is expressed as:

$$f(\gamma_{\mathrm{s}}) = \frac{\gamma_{\mathrm{s}} \cdot \tan(\chi_{\mathrm{ov,s}})}{4} \left(1 - \frac{\sin(\gamma_{\mathrm{s}} \cdot \pi)}{\gamma_{\mathrm{s}} \cdot \pi} \right) + \frac{\xi^2_{\mathrm{f,s}}}{6} \cdot (1 + 0.12 \cdot \gamma^2_{\mathrm{s}}) \tag{3.27}$$

$\gamma_{\mathrm{s}} = \mathrm{Y}_{1,\mathrm{s}}/(3q_{\mathrm{s}})$ is linked to the coil opening and $\chi_{\mathrm{ov,s}}$ is the inclination angle of the bar. The formula from Liwschitz and Kostenko [Ric97; Sil94] are also available and given by Equations

(3.28) and (3.29).

$$L^{\mathrm{L}}_{\sigma,\mathrm{end,s}} = 2 \cdot \frac{N^2_{\mathrm{s,s}}}{p} \cdot \lambda^{L}_{\mathrm{ov,s}} \tag{3.28}$$

$\lambda^{\mathrm{L}}_{\mathrm{ov,s}} = 0.43\mu_0 \cdot l_{\mathrm{ov,s}} \cdot \gamma^2_{\mathrm{s}}$ is a permeance factor with $l_{\mathrm{ov,s}}$ being the length of one overhang.

$$L^{\mathrm{K}}_{\sigma,\mathrm{end,s}} = 2 \cdot \frac{N^2_{\mathrm{s,s}}}{p} \cdot \lambda^{K}_{\mathrm{ov,s}} \tag{3.29}$$

$\lambda^{\mathrm{K}}_{\mathrm{ov,s}} = 0.57 \cdot \tau_{\mathrm{p,s}} \cdot (3 \cdot \gamma_{\mathrm{s}} - 1)/2$ is a permeance factor. The previous formula are also valid for the rotor winding. However the number of series turns $N_{\mathrm{s,s}}$ has to be replaced by $N_{\mathrm{s,r}}$, and the permeance factor have to be evaluated according to the rotor end-winding geometry. All these formula are checked in the next section by carrying out a 3DFE study.

3.2.4 Validation with FE method

I. Leakages in the active part

Firstly we consider the leakage inductance in the active part, i.e the slot leakage inductance and the airgap leakage inductance. The corresponding components are computed by 2DFE by applying the standard tests:

- the no load test: The stator is supplied by a voltage source. The machine is running at the synchronous speed so that the slip is equal to zero. This test makes it possible to determine the stator total inductance defined as: $L_{\mathrm{s}} = L_{\mathrm{h}} + L_{\sigma,\mathrm{s}}$
- the short-circuit test: The stator is supplied by a voltage source and the rotor is short-circuited. The machine is at stand-still so that the slip is equal to one. This test makes it possible to define the quantity $L_{\sigma,\mathrm{s}} + L'_{\sigma,\mathrm{r}}$.

These two tests are carried out by using the 2DFE model from Chapter 2 and a magneto-harmonic application. In such application, the rotation of the rotor is not considered and all magnetic quantities are assumed varying sinusoidally and represented as complex quantities. The stator winding is supplied with a voltage source at a reduced amplitude in order to avoid magnetic saturation. The stator and rotor resistance are known and defined using Equations (3.10) and (3.11). At no load i.e. when the slip is equal to zero, the stator current is equal to the magnetizing current and limited by the stator winding impedance $\underline{Z}^{\mathrm{nl}}$ given by Equation (3.30).

$$\underline{Z}^{\mathrm{nl}} = R_{\mathrm{s}} + \mathrm{i} \cdot 2\pi f_{\mathrm{s}} \cdot L_{\mathrm{s}} \tag{3.30}$$

One can first compute the total apparent power S^{nl} expressed by Equation (3.31) where $\underline{V}_{\mathrm{a,s}}$, $\underline{V}_{\mathrm{b,s}}$ and $\underline{V}_{\mathrm{c,s}}$ are the stator phase voltages and $\underline{I}_{\mathrm{a,s}}$, $\underline{I}_{\mathrm{b,s}}$ and $\underline{I}_{\mathrm{c,s}}$ are the stator phase currents at no-load. Note that we use here the complex notation.

$$\underline{S}^{\mathrm{nl}} = \frac{1}{2} \cdot (\underline{V}_{\mathrm{a,s}} \cdot \underline{I}^*_{\mathrm{a,s}} + \underline{V}_{\mathrm{b,s}} \cdot \underline{I}^*_{\mathrm{b,s}} + \underline{V}_{\mathrm{c,s}} \cdot \underline{I}^*_{\mathrm{c,s}}) \tag{3.31}$$

Quantity	M_1	M_2	M_3	M_4	M_5	M_6
$L_{\sigma,\mathrm{sl,s}}$	0.0911	0.0691	0.1044	0.1547	0.1049	0.0586
$L_{\sigma,\mathrm{sl,r}}$	0.1040	0.0994	0.1450	0.2145	0.1641	0.0589
$L^{\mathrm{B,P}}_{\sigma,\mathrm{tt}}$	0.0242	0.0208	0.0342	0.0448	0.0352	0.0152
$L^{\mathrm{B}}_{\sigma,\mathrm{diff}}$	0.0145	0.0081	0.0080	0.0100	0.0060	0.0039
$L^{\mathrm{A,P}}_{\sigma,\nu,s}$	0.0034	0.0028	0.0033	0.0055	0.0061	0.0030
$L^{\mathrm{A,P}}_{\sigma,\nu,r}$	0.0051	0.0051	0.0058	0.0086	0.0128	0.0019
$L^{\mathrm{B,F}}_{\sigma,\mathrm{zz}}$	0.0045	0.0034	0.0050	0.0075	0.0105	0.0043
$L^{\mathrm{A}}_{\sigma,\mathrm{zz,s}}$	0.0054	0.0042	0.0057	0.0098	0.0097	0.0041
$L^{\mathrm{A}}_{\sigma,\mathrm{zz,r}}$	0.0072	0.0058	0.0084	0.0158	0.0178	0.0028

Table 3.2: Stator and rotor leakage inductance elements (p.u.)

From $\underline{S}^{\mathrm{nl}}$ and the RMS stator phase current I_{s} one obtains the value of Z_{nl} as shown in Equation (3.32).

$$\underline{Z}^{\mathrm{nl}} = \frac{\underline{S}^{\mathrm{nl}}}{3 \cdot \underline{I}^{\mathrm{nl}}_{\mathrm{s}}} \tag{3.32}$$

The total stator inductance is finally derived by using Equation (3.33).

$$L_{\mathrm{s}} = \frac{\Im\left(\underline{Z}^{\mathrm{nl}}\right)}{2\pi f_{\mathrm{s}}} \tag{3.33}$$

Under short-circuit conditions the slip is equal to one. The magnetizing current can be neglected in front of the rotor current and the approximated impedance $\underline{Z}^{\mathrm{sc}}$ seen from the stator terminal is given by:

$$\underline{Z}^{\mathrm{sc}} \approx 2\pi f_{\mathrm{s}} \cdot (L_{\sigma,\mathrm{s}} + L'_{\sigma,\mathrm{r}}) \tag{3.34}$$

By applying the same method, one can get the value of $L_{\sigma,\mathrm{s}} + L'_{\sigma,\mathrm{r}}$. As we can see, these two tests alone do not make it possible to separate the stator leakage inductance from the rotor leakage inductance. Taghezout [TD08] suggests to calculate at no-load the airgap flux density, to derive from it its fundamental value and finally the corresponding fundamental magnetizing flux. After calculating the stator current, he extracts the magnetizing inductance. This method makes it possible to derive the stator leakage inductance from the first test and the rotor leakage inductance from the second test.

Table 3.2 details the leakage inductance analytical calculation results made for several designs whose characteristics were presented in Chapter 2 in Table 2.1. As we have seen before, the equations calculating the airgap flux leakage inductance are different from one author to another, so we decided to evaluate and compare all the presented methods. Note that each inductance is expressed in p.u. of the stator reference impedance Z_{ref}.

Table 3.3 compares the total leakage inductance (stator and rotor), according to the different authors, with the results of the 2DFE represented by $L^{\mathrm{FE}}_{\mathrm{s+r}}$. One can see that all the methods give results in accordance with the FE simulation. However it appears that the methods from Foggia

Quantity	M_1	M_2	M_3	M_4	M_5	M_6
L^{B}_{s+r}	0.238	0.200	0.296	0.431	0.320	0.141
L^{F}_{s+r}	0.214	0.179	0.262	0.386	0.285	0.126
L^{A}_{s+r}	0.216	0.186	0.272	0.409	0.315	0.129
L^{P}_{s+r}	0.232	0.199	0.297	0.439	0.331	0.139
L^{FE}_{s+r}	0.214	0.186	0.278	0.408	0.305	0.129

Table 3.3: Total leakage inductances (p.u.)

and Alger give the closest values. The common point between Alger and Foggia methods is that the tooth-tip leakage inductance is not explicitly considered. Firstly, the tooth tip leakage flux is difficult to assess since the airgap of our machine is doubly-slotted. Secondly it is difficult to split it from the other phenomena such as zig-zag flux especially because the airgap is small. This may explain why the other methods give higher values than the 2DFE method.

II. Leakages in the end-winding part

Secondly we deal with the end-winding leakage inductance by using a 3DFE computation. This subject has already been treated by several authors. Taieb [Bra92] for example computed the end-winding leakage inductance of a squirrel cage induction machine while Silva [Sil94] and Richard [Ric97] worked on a synchronous generator. More recently Arshad [ALP08] compares the leakage inductance computed with 3DFE on several synchronous generators with measurements. All these authors extract the end-leakage inductance after solving a magneto-static simulation and computing the magnetic energy stored in the air surroundings the end-windings. Taghezout [Tag11] computes the rotor and stator end-winding leakage inductances of a DFIM by solving a magneto-harmonic application. We detail here this method and its results as it applies directly to our studied machine.

Figure 3.11 shows an example of 3D end-winding coils and Figure 3.12a shows the complete rotor and stator end-winding geometry. Note that according to the symmetries, only one pole needs to be modeled. In case of fractional slot windings, one would have to model the smallest winding repetition period.[4] Furthermore the model is encapsulated in the so-called *infinite box* which makes it possible to delimit the air domain surrounding the windings as shown in Figure 3.12b. Note that the active part of the generator is not physically modeled but replaced by a boundary condition considering that due to the larger permeability of the iron compared to the air, the end-magnetic field enters perpendicularly into the magnetic core.

Figure 3.13 shows the electrical circuit coupled to the FE model. Each coil or single bar is associated with a conductor in the circuit and the different conductors are regrouped per phase according to the winding configuration. The current is injected by supplying each circuit, stator and rotor, with a balanced three-phase current source. The simulation is done in two steps, firstly by feeding only the stator winding and then the rotor winding. This makes it possible

[4]More detailed about such windings are given in Chapter 4 and Chapter 5

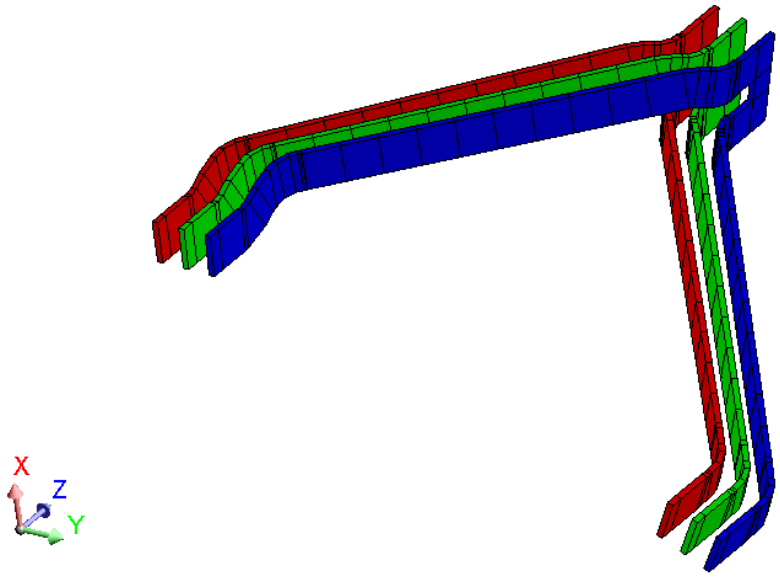

Figure 3.11: Example of end-winding coils

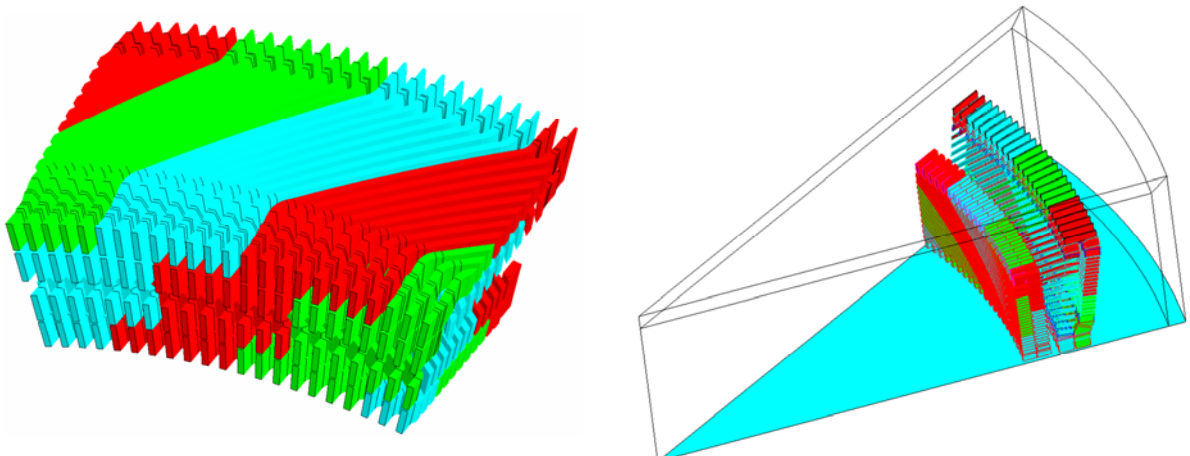

(a) 3d winding geometry (seen from the last iron sheet)

(b) 3d model with infinite box

Figure 3.12: Three-dimensional finite element end-winding model [Tag11]

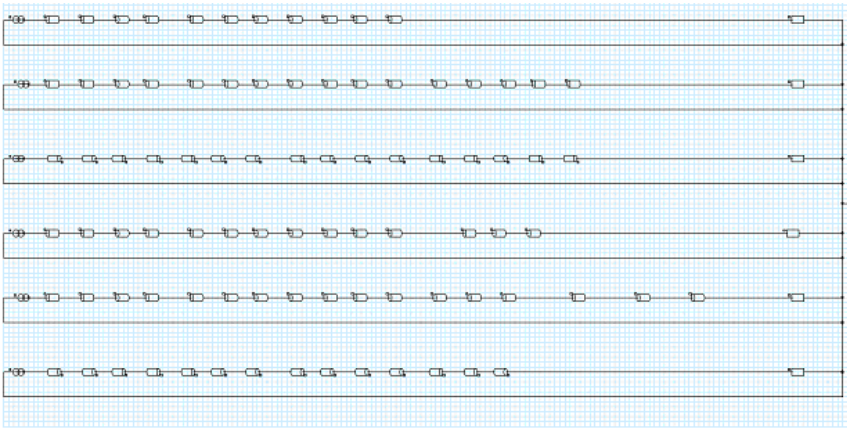

Figure 3.13: Electrical circuit for end-winding inductance calculation [Tag11]

	$L^{\mathrm{FE}}_{\sigma,\mathrm{end}}$	$L^{\mathrm{A}}_{\sigma,\mathrm{end}}$	$L^{\mathrm{K}}_{\sigma,\mathrm{end}}$	$L^{\mathrm{L}}_{\sigma,\mathrm{end}}$
Rotor	0.028	0.028	0.038	0.026
Stator	0.0269	0.029	0.040	0.019

Table 3.4: End-winding leakage inductance (p.u.)

to dissociate the stator end-winding leakage inductance from the rotor end-winding leakage inductance. The calculation of the inductance is similar to what was done previously in this part for the 2DFE computation. Indeed the total stator and rotor supplied apparent power is computed and finally the stator and rotor end-winding impedance so that one can find the corresponding stator and rotor end-winding leakage inductances. The obtained results are then multiplied by 2 since both sides of the machine contribute to the end-leakage flux.

Finally Table 3.4 lists the computed FE values. $L^{\mathrm{FE}}_{\sigma,\mathrm{end}}$, as well as the analytical values obtained from the formula of Alger, Kotsenko and Liwschitz. One can notice that the results from Alger's formula agree very well with the FE computation while the two other formula lead to larger discrepancies. The total end-winding leakage inductance (stator and rotor) represents in this example about 20% of the total leakage inductance which is not negligible. Indeed, during faults the maximum values of the current and the torque are inversely proportional to the total leakage inductance; consequently this shows the necessity to assess correctly this component. Although the Alger's formula leads to the best results, we recommend for the future a deeper study with different designs in order to fully conclude on its reliability.

3.2.5 Summary

An equivalent circuit for modeling the DFIM has been described. The model is similar to the one normally used for standard induction machines. The components of the equivalent circuit have been defined and formulas depending mainly on geometry characteristics have been given. Difficulties arose especially when dealing with the airgap leakage inductances. A 2DFE

analysis has been used in order to compare the available methods in the literature and shows that the formula from Alger gave the best match. End-winding leakage inductances have been assessed by applying analytical formulations and compared with a 3DFE analysis modeling the complete geometry of the stator and rotor windings. The analytical calculation, given Alger's formula, agreed very well with the FE results. Although this is satisfying, a deeper study with different designs appears relevant for the future in order to conclude on the full validity of this formula. Indeed a wrong assessment of this component could be problematic as it controls the maximum amplitude of currents and torque during faults such as short-circuits. After defining and validating the modeling of the DFIM, the steady-state operation can be studied. This is the object of the second part.

3.3 Steady-state study

While the literature regarding the study of the induction machine with short-circuited rotor is very rich [Alg51; Cha80], the steady-state operation of the DFIM is rarely discussed. From the equivalent scheme previously described, we first define the exchanges of power between the machine and the network. Second part explains the computation of load operation points, considering the power factor and either the mechanical power available on the shaft or the active power at the terminals. In all discussions, the stator voltage as well as the stator frequency are assumed constant and imposed by the network and the mechanical speed is constant. Only the rotor voltage amplitude and relative phase compared to stator voltage can be changed in order to modify the operating point of the machine. The rotor frequency is also constant and depends directly on the mechanical speed and the stator frequency. Third part investigates the influence of the slip on the power exchanges and on the rotor voltage but also the impact of a shift in stator voltage and frequency. These parametric studies make it possible to define the capability diagram of the machine.

3.3.1 Power balance

In the case of a DFIM the total active power P_{net} at the interconnection point with the network corresponds to the sum of the stator active power P_{s} and rotor active power P_{r}.

$$P_{\text{net}} = P_{\text{s}} + P_{\text{r}} \tag{3.35}$$

Similarly the reactive power at the interconnection point with the network is expressed as:

$$Q_{\text{net}} = Q_{\text{s}} + Q_{\text{c}} \tag{3.36}$$

Depending on the topology of the rotor converter, VSI or cycloconverter, the definition of the rotor reactive power Q_{c} is different. Figure 3.14 shows a simplified overview comparing the power exchanges for both configurations.[5] Contrarily to the cycloconverter, when using a VSI

[5]More details about the converter topology can be found in Chapter 1 in Figures 1.13 and 1.14

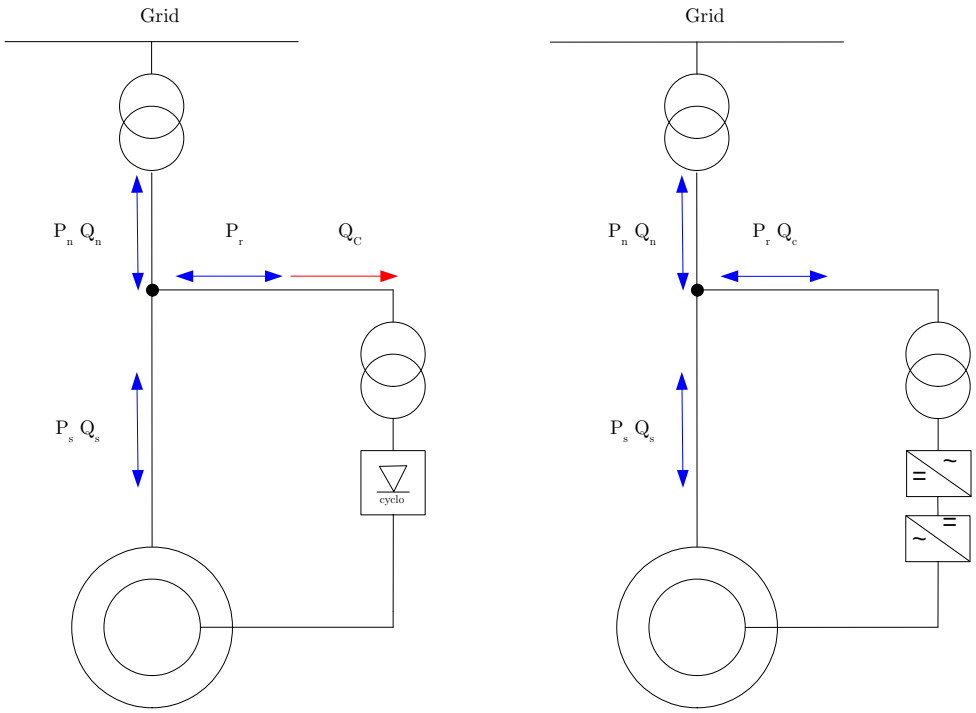

Figure 3.14: Power exchange for Cyclo-converters (left) and VSI (right) topologies

converter, the reactive power at the rotor terminal Q_r does not show up in the final power balance since a dc bus decouples the machine rotor side from the network side. However by controlling properly the VSI converter, it is possible to regulate the amount of reactive power at the rotor transformer side. This amount depends directly on the circulating rotor active power and the nominal apparent power of the rotor transformer. Assuming that the active power is always smaller than the rotor transformer nominal power $S_{\mathrm{t,r}}$, the theoretical maximal quantity of reactive power $Q_\mathrm{c}^\mathrm{VSI}$ transmitted or absorbed by the VSI can be expressed as:

$$Q_\mathrm{c}^\mathrm{VSI} = \sqrt{S_{\mathrm{t,r}}^2 - P_\mathrm{r}^2} \tag{3.37}$$

As the rotor active power is slip dependent, the quantity $Q_\mathrm{c}^\mathrm{VSI}$ will also depend on the slip. Modern DFIM are fed via a VSI. In this study we decide that only the stator reactive power intervenes in the total reactive power i.e. that the VSI does not inject or consume reactive power on network side so that $Q_\mathrm{c} = 0$. In this case the magnetizing current will be higher and the design of the machine has to be done in consequence. It corresponds to a more conservative use of the machine but it is a safer design.

The network power factor is expressed as:

$$\cos\varphi_\mathrm{n} = \arccos\left(\frac{P_\mathrm{net}}{S_\mathrm{net}}\right) \tag{3.38}$$

where S_net is the apparent network power expressed as

$$S_\mathrm{net} = \sqrt{P_\mathrm{net}^2 + S_\mathrm{net}^2} \tag{3.39}$$

The active and reactive stator and rotor active power are given by the following expressions:

$$P_{\mathrm{s}} = 3 \cdot \left|\underline{V}_{\mathrm{s}}\right| \left|\underline{I}_{\mathrm{s}}\right| \cdot \cos(\varphi_{\mathrm{s}}) \tag{3.40}$$

$$Q_{\mathrm{s}} = 3 \cdot \left|\underline{V}_{\mathrm{s}}\right| \left|\underline{I}_{\mathrm{s}}\right| \cdot \sin(\varphi_{\mathrm{s}}) \tag{3.41}$$

$$P_{\mathrm{r}} = 3 \cdot \left|\underline{V}_{\mathrm{r}}\right| \left|\underline{I}_{\mathrm{r}}\right| \cdot \cos(\varphi_{\mathrm{r}}) \tag{3.42}$$

where φ_{s} and φ_{r} are respectively the phase shifts between the stator voltage and the stator current and between the rotor voltage and the rotor current. The mechanical power P_{mec} is given by:

$$P_{\mathrm{mec}} = P_{\mathrm{shaft}} + p_{\mathrm{mec}} \tag{3.43}$$

where P_{shaft} is the shaft power available from the turbine or for the pump and p_{mec} represents the mechanical losses including bearing and friction losses. By convention p_{mec} is always positive and P_{shaft} is negative in generator mode. Consequently, in generator mode the shaft power is greater than the transmitted mechanical power whereas in motor mode, the shaft power is smaller than the mechanical power. The mechanical power is also linked to the airgap power P_{δ} by the relation:

$$P_{\mathrm{mec}} = P_{\delta} \cdot (1 - s) \tag{3.44}$$

Note that the stator frequency f_{s} and rotor frequency f_{r} are linked through the slip s by the expression:

$$f_{\mathrm{r}} = s \cdot f_{\mathrm{r}} \tag{3.45}$$

The stator power is given by:

$$P_{\mathrm{s}} = P_{\delta} + \mathrm{p}_{\mathrm{c,s}} + \mathrm{p}_{\mathrm{i,s}} \tag{3.46}$$

The rotor power is linked to the airgap power by:

$$P_{\mathrm{r}} + \mathrm{p}_{\mathrm{c,r}} + \mathrm{p}_{\mathrm{i,r}} = -s \cdot P_{\delta} \tag{3.47}$$

where $\mathrm{p}_{\mathrm{c,s}}$ and $\mathrm{p}_{\mathrm{c,r}}$ are the stator and rotor winding copper losses defined by Equations (3.48) and (3.49). The calculation of stator and rotor iron losses, $\mathrm{p}_{\mathrm{i,s}}$ and $\mathrm{p}_{\mathrm{i,r}}$, is described in Chapter 5.

$$\mathrm{p}_{\mathrm{c,s}} = 3R_{\mathrm{s}} \left|\underline{I}_{\mathrm{s}}\right|^2 \tag{3.48}$$

$$\mathrm{p}_{\mathrm{c,r}} = 3R_{\mathrm{r}} \left|\underline{I}_{\mathrm{r}}\right|^2 \tag{3.49}$$

In the next part we explain how to compute any load operation point of a DFIM.

3.3.2 Calculation of a load operation point

Any load operation point can be defined either by the mechanical power P_{mec} and the network active power factor $\cos\varphi_{\mathrm{n}}$ or by the apparent network power S_{net} and the network active power factor $\cos\varphi_{\mathrm{n}}$. Depending on the analyzed operation mode (motor or generator) one method is more relevant than the other. Whatever the chosen definition the stator voltage and the speed are assumed constant.

I. Definition from the apparent power, the power factor, the stator voltage and the speed

Four parameters define the load operation point, the apparent network power S_{net}, the active power factor at the network connection $\cos\varphi_{\text{n}}$, the stator phase-to-neutral voltage $\left|\underline{V}_{\text{s}}\right|$ and the mechanical speed n. As the rotor is fed via a VSI converter and deciding that it does not inject or consume reactive power, one can write:

$$Q_{\text{s}} = Q_{\text{net}} \tag{3.50}$$

When neglecting the copper and iron losses we obtain:

$$P_{\text{s}} = P_{\text{net}} - P_{\text{r}} \approx \frac{P_{\text{net}}}{1-s} \tag{3.51}$$

Furthermore, by considering the stator and the network power factor one can write:

$$\begin{aligned} Q_{\text{s}} &= P_{\text{s}} \cdot \tan\varphi_{\text{s}} \\ Q_{\text{net}} &= P_{\text{net}} \cdot \tan\varphi_{\text{n}} \end{aligned} \tag{3.52}$$

Using Equations (3.50), (3.51) and (3.52), one can define the stator phase shift φ_{s}:

$$\varphi_{\text{s}} = \arctan\left((1-s)\cdot\tan\varphi_{\text{n}}\right) \tag{3.53}$$

Taking the stator voltage phasor as the reference, φ_{s} is the phase shift of the stator current. Furthermore, from Equations (3.42) and (3.53) one can find the amplitude of the stator current $\left|\underline{I}_{\text{s}}\right|$:

$$\left|\underline{I}_{\text{s}}\right| = \frac{Q_{\text{s}}}{3\left|\underline{V}_{\text{s}}\right|\sin\varphi_{\text{s}}} \tag{3.54}$$

By using the equivalent scheme previously presented and using complex notations, the following equations can be derived in order to find the rotor current and the rotor voltage:

$$\underline{V}_{\mu} = \underline{V}_{\text{s}} - R_{\text{s}}\underline{I}_{\text{s}} - \text{i}X'_{\sigma,\text{s}}\underline{I}_{\text{s}} \tag{3.55}$$

$$\underline{I}'_{\text{r}} = \frac{\underline{V}_{\mu}}{\text{i}X_{\text{h}}} - \underline{I}_{\text{s}} \tag{3.56}$$

$$\underline{V}'_{\text{r}} = s\left(\left(\text{i}X'_{\sigma,\text{r}} + \text{i}X_{\text{h}} + \frac{R'_{\text{r}}}{s}\right)\underline{I}'_{\text{r}} + \text{i}X_{\text{h}}\underline{I}_{\text{s}}\right) \tag{3.57}$$

Where $X'_{\sigma,\text{s}} = 2\pi f_{\text{s}} L_{\sigma,\text{s}}$, $X'_{\sigma,\text{r}} = 2\pi f_{\text{s}} L'_{\sigma,\text{r}}$ and $X_{\text{h}} = 2\pi f_{\text{s}} L_{\text{h}}$. By using Equation (3.58) and combining Equations (3.55), (3.56) and (3.57) one can find the rotor active power as a function of the stator voltage, the stator current and the equivalent scheme parameters.

$$P_{\text{r}} = 3\cdot\Re(\underline{V}'_{\text{r}}\cdot\underline{I}'_{\text{r}}*) \tag{3.58}$$

However the value obtained from Equation (3.58) stands on the fact that the stator active power was obtained by neglecting the losses (Equation (3.51)). It is therefore necessary to iterate on the value of P_{s} as described in Figure 3.15. Note that as L_{h} depends on the magnetizing current $\left|\underline{I}_{\mu}\right|$, an additional iterations loop is necessary.

This algorithm makes it possible to find the stator and rotor current, rotor voltage for any load point defined by the network apparent power, the power factor and the speed.

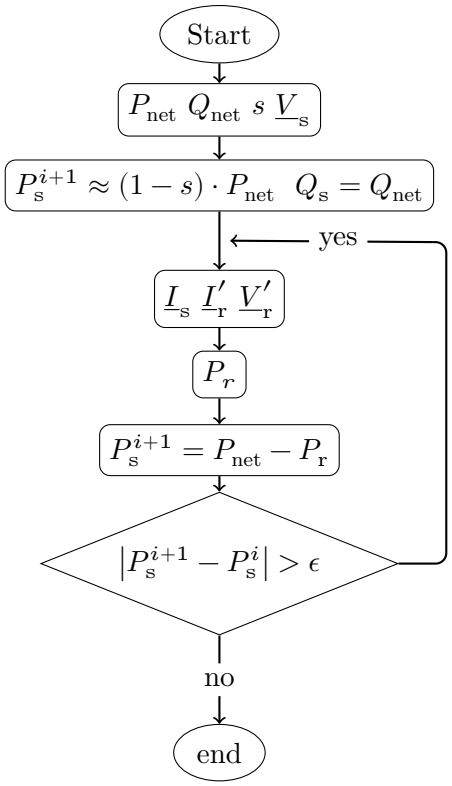

Figure 3.15: Load point calculation algorithm 1

II. Definition from the mechanical power, the power factor, the stator voltage and the speed

The load operation point is defined by four parameters: the mechanical power P_{mec}, the active power factor at the network connection $\cos\varphi_{\mathrm{n}}$, the stator voltage $\left|\underline{V}_{\mathrm{s}}\right|$ and the mechanical speed n. Lorenzen [Lor97] uses this definition. The load point resolution is based on the definition of the electromagnetic torque Γ_{em}; this one is due to the interaction of the stator magnetic field with the rotor magnetic field and can be written as:

$$\Gamma_{\mathrm{em}} = -3pL_{\mathrm{h}}\Im(\underline{I}_{\mathrm{s}} \cdot \underline{I}'_{\mathrm{r}}*) \tag{3.59}$$

By using the equivalent scheme previously defined, one can express the stator and rotor current as functions of the stator and rotor voltage and calculate the corresponding electromagnetic torque given by Equation (3.60):

$$\Gamma_{\mathrm{em}} = \Gamma_{\mathrm{s}} + \Gamma_{\mathrm{r}} + \Gamma_{\mathrm{sr}} \tag{3.60}$$

where Γ_{s}, Γ_{r} and Γ_{sr} are obtained from Equations (3.61), (3.62), (3.63).

$$\Gamma_{\mathrm{s}} = \frac{3pL_{\mathrm{h}}}{\Delta^2} \cdot sX_{\mathrm{h}}R'_{\mathrm{r}} \cdot \left|\underline{V}_{\mathrm{s}}\right|^2 \tag{3.61}$$

$$\Gamma_{\mathrm{r}} = -\frac{3pL_{\mathrm{h}}}{\Delta^2} \cdot R_{\mathrm{s}}X_{\mathrm{h}} \cdot \left|\underline{V}'_{\mathrm{r}}\right|^2 \tag{3.62}$$

$$\Gamma_{\mathrm{sr}} = -\frac{3pL_{\mathrm{h}}}{\Delta^2} \cdot ((-sX_{\mathrm{h}}^2 + R_{\mathrm{s}}R'_{\mathrm{r}} + sX_{\mathrm{s}}X'_{\mathrm{r}}) \cdot \sin(\varphi_{\mathrm{m}}) + (-R_{\mathrm{s}}sX'_{\mathrm{r}} + X_{\mathrm{s}}R'_{\mathrm{r}}) \cdot \cos(\varphi_{\mathrm{m}})) \cdot \left|\underline{V}_{\mathrm{s}}\right| \left|\underline{V}'_{\mathrm{r}}\right| \tag{3.63}$$

Δ depends on the circuit parameters and is expressed as:

$$\Delta = \left|Z_{\mathrm{s}}Z'_{\mathrm{r}} + s \cdot X_{\mathrm{h}}^2\right|^2 \tag{3.64}$$

where $Z_{\mathrm{s}} = R_{\mathrm{s}}+\mathrm{i}\cdot(X'_{\sigma,\mathrm{s}}+X_{\mathrm{h}})$ and $Z'_{\mathrm{r}} = R'_{\mathrm{r}}+\mathrm{i}\cdot s(X'_{\sigma,\mathrm{r}}+X_{\mathrm{h}})$. As one can see, the electromagnetic torque in a DFIM is composed of three terms:

- Γ_{s} corresponds to the induction torque of a motor with short-circuited stator
- Γ_{r} corresponds to the induction torque of a motor with short-circuited rotor
- Γ_{sr}corresponds to the synchronous torque

φ_{m} is the phase shift between the stator and the rotor voltage. Considering the stator voltage phasor as the reference, φ_{m} is equal to the rotor voltage phase shift. The method proposed by [LH93] is the following: assuming a mechanical power P_{mec} and a constant speed N the corresponding electromagnetic torque Γ_{em} is defined as:

$$\Gamma_{\mathrm{em}} = \frac{P_{\mathrm{mec}}}{n \cdot \frac{2\pi}{60}} \tag{3.65}$$

Considering the stator voltage $\left|\underline{V}_{\mathrm{s}}\right|$, the active power factor $\cos\varphi_{\mathrm{n}}$ and a certain rotor phase voltage φ_{m}, Equation (3.60) can be organized as a second order polynomial equation whose unknown is the absolute value of the rotor voltage:

$$\mathrm{A}\left|\underline{V}'_{\mathrm{r}}\right|^2 + \mathrm{B}\left|\underline{V}'_{\mathrm{r}}\right| + \mathrm{C} = 0 \tag{3.66}$$

where A,B,C are real coefficients obtained from Equations (3.61), (3.62) and (3.63). The phase shift angle φ_{m} can initially be obtained by applying the same method as before i.e. by neglecting the losses so one can write:

$$P_{\mathrm{net}} \approx P_{\mathrm{mec}} \tag{3.67}$$

From Equation (3.67) and applying Equations (3.54), (3.55), (3.57) one can get the value of the rotor voltage and finally the rotor voltage phase shift angle φ_{m} defined as:

$$\varphi_{\mathrm{m}} = \arg\left(\underline{V}'_{\mathrm{r}}\right) \tag{3.68}$$

From the phase shift angle φ_{m} and the load operation point characteristics (P_m, V_s, s) Equation (3.66) can be solved. Depending on the values of the couple of coefficients $[\mathrm{A}, \mathrm{B}, \mathrm{C}]$ one or two solutions can be found, the constraint is that any found solution has to be greater than zero. In case of two possible solutions the smallest value of $\left|\underline{V}'_{\mathrm{r}}\right|$ is kept. From the found $\left|\underline{V}'_{\mathrm{r}}\right|$ the values of $\underline{I}_{\mathrm{s}}$ and $\underline{I}'_{\mathrm{r}}$ can be computed. This leads to the evaluation of the power factor $\cos\varphi_{\mathrm{n}}$ which can be compared with the target value.

The value of $\cos\varphi_{\mathrm{n}}$ will be directly linked to the initial value of $\varphi_{\mathrm{m}} = \varphi_{\mathrm{m},0}$ which was obtained by neglecting the losses. An iteration process on the value of φ_{m} is therefore necessary. This is solved by defining the interval $[\varphi_{\mathrm{m},0} - \Delta\varphi_{\mathrm{m}} \cdots \varphi_{\mathrm{m},0} + \Delta\varphi_{\mathrm{m}}]$ where $\Delta\varphi_{\mathrm{m}}$ is a small variation angle. For each value of φ_{m} on the interval, one applies the previously described process and extract the power factor $\cos\varphi_{\mathrm{n}}$. The angle φ_{m} which makes it possible to reach the target power factor is kept. If no solution is found $\Delta\varphi_{\mathrm{m}}$ can be increased in order to enlarge the interval. From φ_{m}, one can identify the value of the rotor voltage and finally the rotor and stator currents. As previously, an additional iteration loop has to be included to manage the non-linearity of L_{h}.

III. Vector diagrams

The previously described procedure is applied to compute several load points. Figure 3.16 shows the vector diagrams obtained for four operation points in generator mode. For each case, the mechanical power, the power factor, the stator voltage and the stator frequency are the same. However the slip is either minimum and maximum and the reactive power is either provided (over-excited) or absorbed (under-excited) by the machine. Figure 3.17 shows the same vector diagrams but in motor mode. One can observe the different arrangements of the vectors, especially when changing the excitation modes ($\underline{V}_{\mu}$ is longer in over-excited mode) or when commuting from generator mode to motor mode (the angles are opposite).

3.3.3 Parametric study

In this part we use the algorithms previously described to study the effect of the slip on the rotor voltage and on the exchange of active and reactive power. The machine is running in generator mode which means that the stator active power is negative.

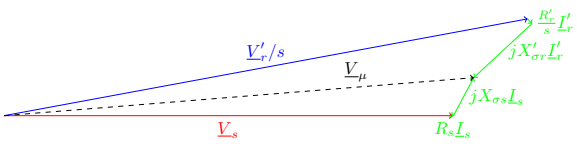

(a) $s = -10\%$, over-excited

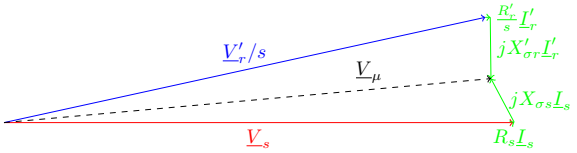

(b) $s = -10\%$, under-excited

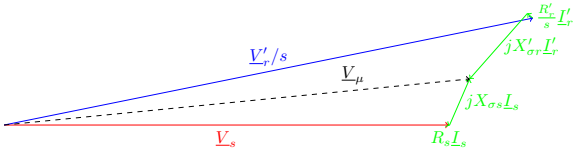

(c) $s = 10\%$, over-excited

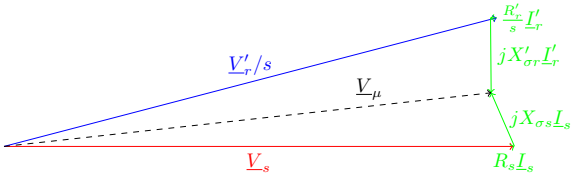

(d) $s = 10\%$, under-excited

Figure 3.16: Vector diagrams in generator mode

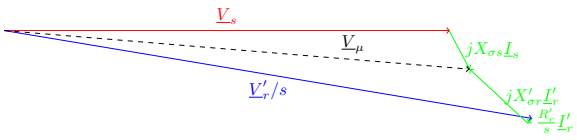

(a) $s = -10\%$, over-excited

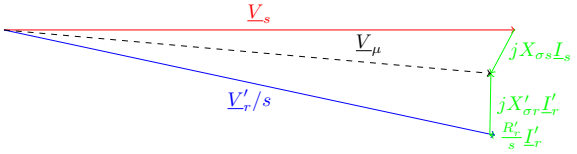

(b) $s = -10\%$, under-excited

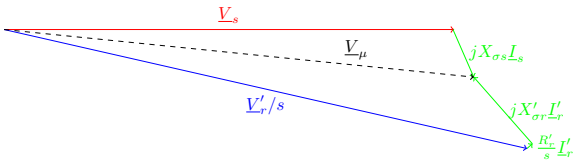

(c) $s = 10\%$, over-excited

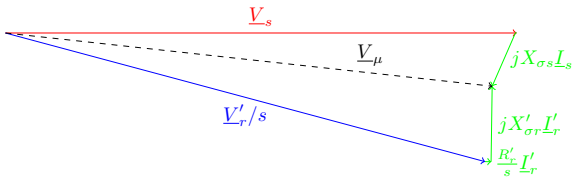

(d) $s = 10\%$, under-excited

Figure 3.17: Vector diagrams in motor mode

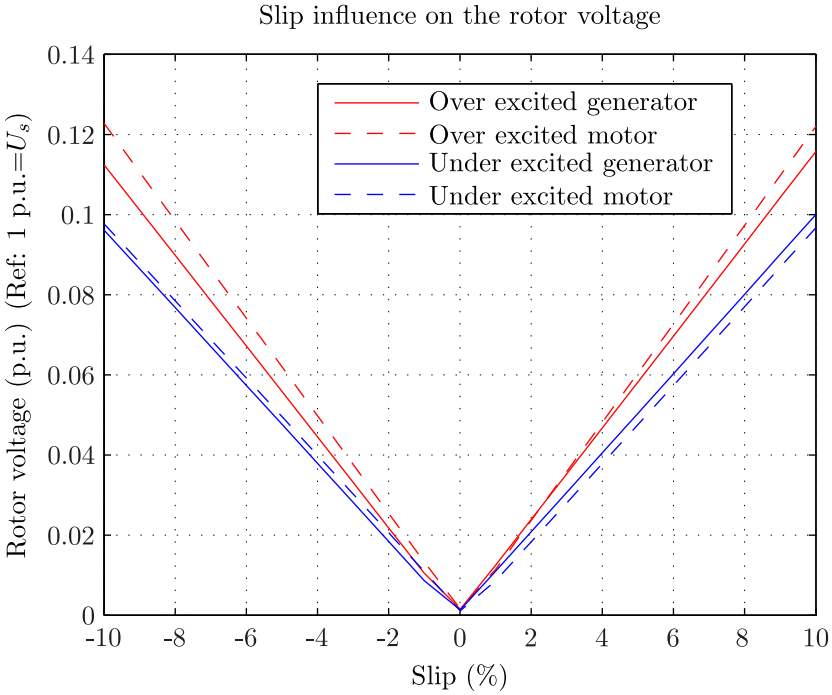

Figure 3.18: Influence of the slip on rotor voltage

I. Effect of slip on rotor voltage and powers

The mechanical power as well as the network power factor are kept constant. Figure 3.18 describes the impact of the slip on the rotor voltage considering that the machine absorbs reactive power from the network (under-excited mode) or delivers reactive power on the network (over-excited mode). Figure 3.19 shows the evolution of the stator and rotor active power in generator operation and motor operation. When the slip is positive, the machine runs in hypo-synchronous mode. In such condition the rotor rotates slower than the stator magnetic field and the stator carries the additional rotor power. When the slip is negative the rotor rotates faster than the stator magnetic field, the stator active power is reduced and the rotor delivers active power on the network. Contrarily to the conventional synchronous machine, the stator of DFIM has to be designed to sustain the extra flowing power in hypo-synchronous mode. The further from the synchronous speed, the higher the rotor voltage will be. Consequently the rotor converter has to be dimensioned in order to supply the rotor voltage at the maximum and minimum speed. Furthermore the transformer on rotor side has to be able to sustain the rotor active power at any allowed speed.

II. Effect of network voltage and frequency variation

Even on a strong network, small variations of the frequency $\pm 5\%$ and voltage $\pm 10\%$ may happen. In case of such variation the machine must not be disconnected from the grid and be able to generate under its nominal power [Swi09]. We study here this phemonena, by keeping the

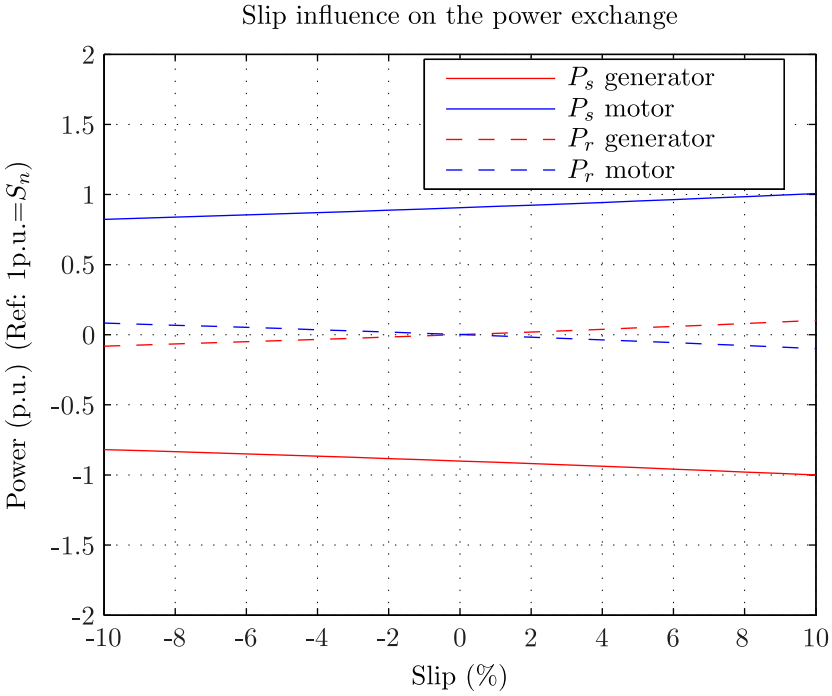

Figure 3.19: Influence of the slip on power exchange

network apparent power and power factor constant while the network voltage and frequency are changed according to Figure 3.20.

Figure 3.21 shows the corresponding variation of the rotor voltage at different speeds. As expected, one can observe a shift between each curves. This is explained by the fact that if the speed is constant, and the stator frequency is changed, the relative speed of the stator magnetic field compared to the rotor magnetic field is also changed. Because of the converter the rotor voltage is constrained to a certain limit displayed as $U_{\mathrm{r,max}}$, depending on the frequency and network voltage the maximal range of speed variation should be adapted. Figure 3.22 shows the variation of the magnetizing current at different speeds. As expected one can see that when the stator voltage increases, i.e. the cases $(U+, f+)$ and $(U+, f-)$, the magnetizing current increases. As the flux density depends directly on the magnetizing current, this may lead to a saturation in the rotor and stator core regions. Figure (3.23) and (3.24) show the variation of the stator current and rotor current at different speeds. One can see that case $(U-, f+)$ is the worst case as the stator and rotor current are maximum. Such cases should be checked carefully especially in terms of losses and temperatures.

III. Computation of the capability diagram

A hydro-motor/generator has to work under different operation modes: generator or motor mode, over-excited (capacitive) or under-excited (inductive) mode . The allowed area of operation is usually given as a diagram P (active power) v.s Q (reactive power). The knowledge of this

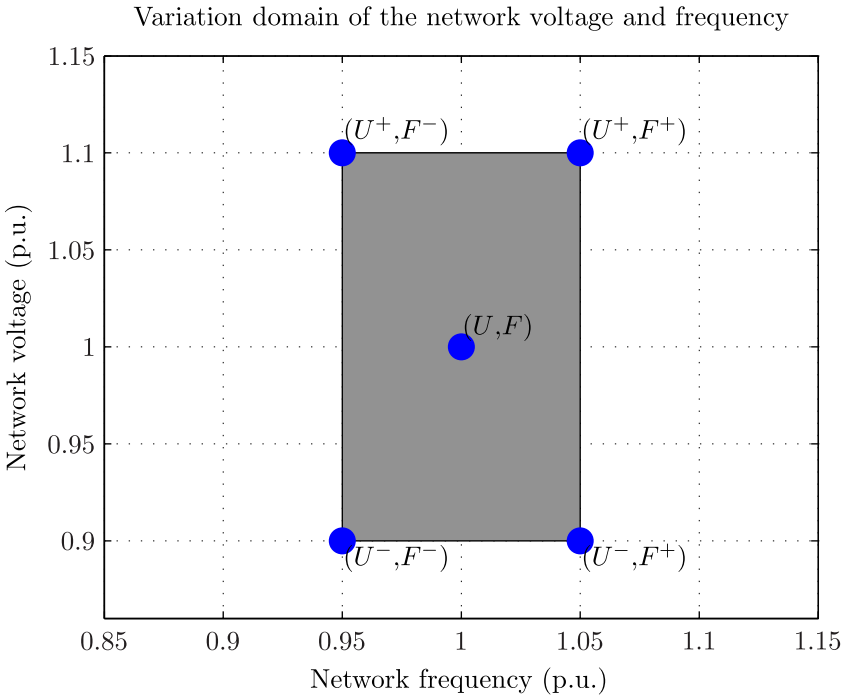

Figure 3.20: Network Frequency and voltage domain

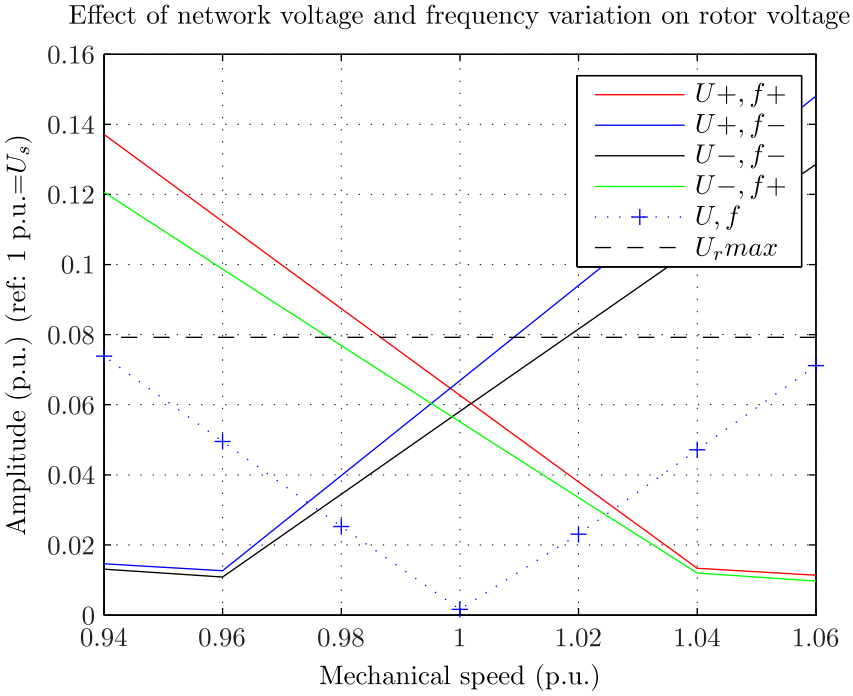

Figure 3.21: Effect of stator voltage and frequency on rotor voltage

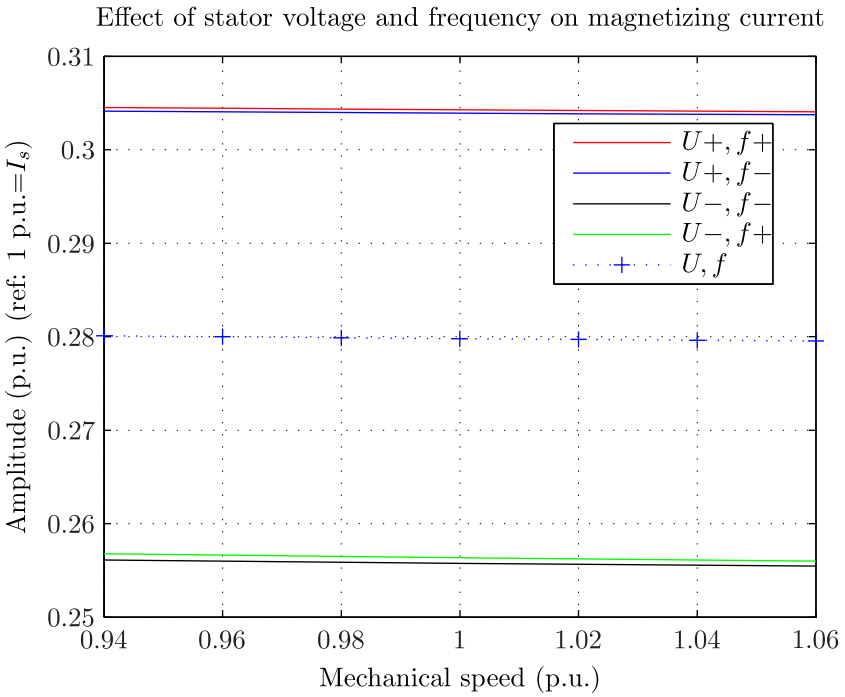

Figure 3.22: Effect of stator voltage and frequency on magnetizing current

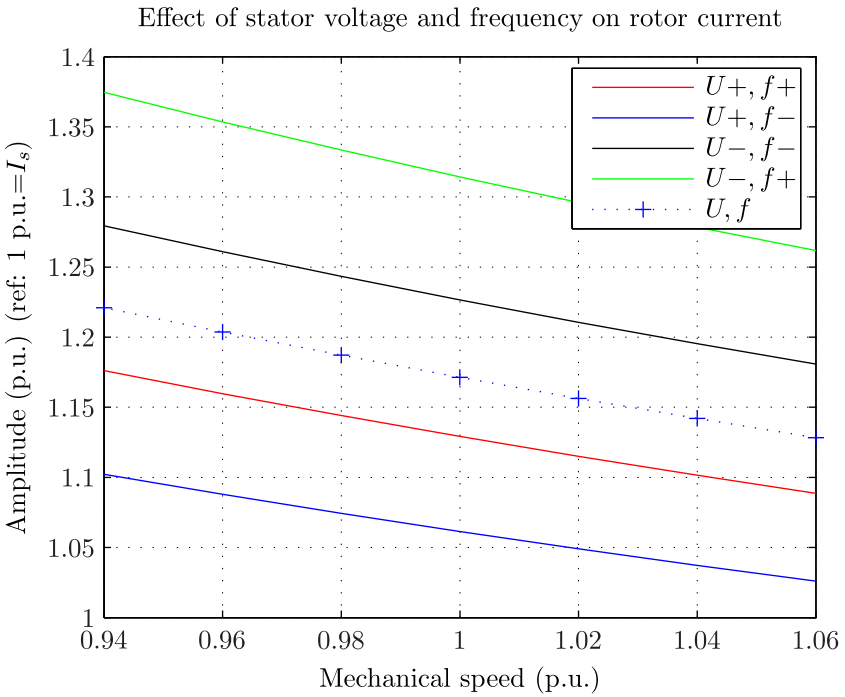

Figure 3.23: Effect of stator voltage and frequency on rotor current

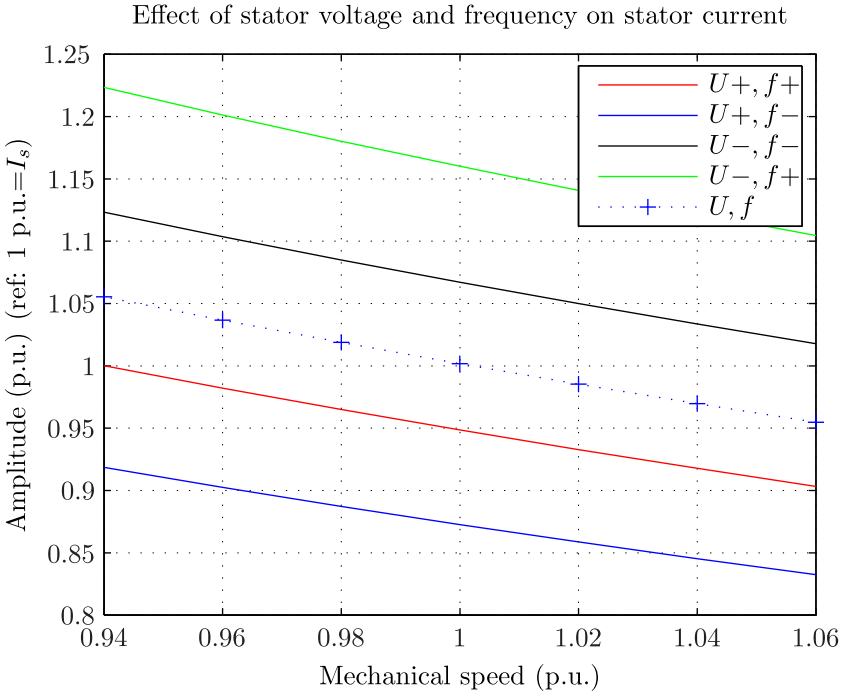

Figure 3.24: Effect of stator voltage and frequency on stator current

diagram is necessary since it defines the operation limits of the machine. The limits given for a DFIM are the following:

- Stator current: The stator winding is designed to work under a certain temperature limit.
- Rotor current: The rotor winding is designed to work under a certain temperature limit.
- Rotor voltage: The output converter voltage is limited. Depending on the slip, stator frequency the operation can be limited.
- Magnetizing current: Depending on the operation point, the magnetizing current varies. The flux density in the teeth and in the yoke depend directly on its value and consequently the iron losses. In order to limit these components, a constraint can be set on this component.

For standard synchronous machines, a constraint is also set on the minimal excitation current because of stability issue. This is irrelevant for the DFIM since the problem of stability is solved with an adapted control.

Figure 3.25 shows the capability diagram considering the different limits. One can see that each limit sets a certain operation area. The intersection of all the zones defines the allowed operation zone (in green on the diagram). A positive active power corresponds to a generator mode and a positive reactive power stands for the over-excited mode. Such graph should be computed for each mechanical speed of the operation range, considering or not a shift in network voltage and/or frequency. The presented graph shows the results obtained at the lowest mechanical speed, in over network voltage and under network frequency mode. One can see that

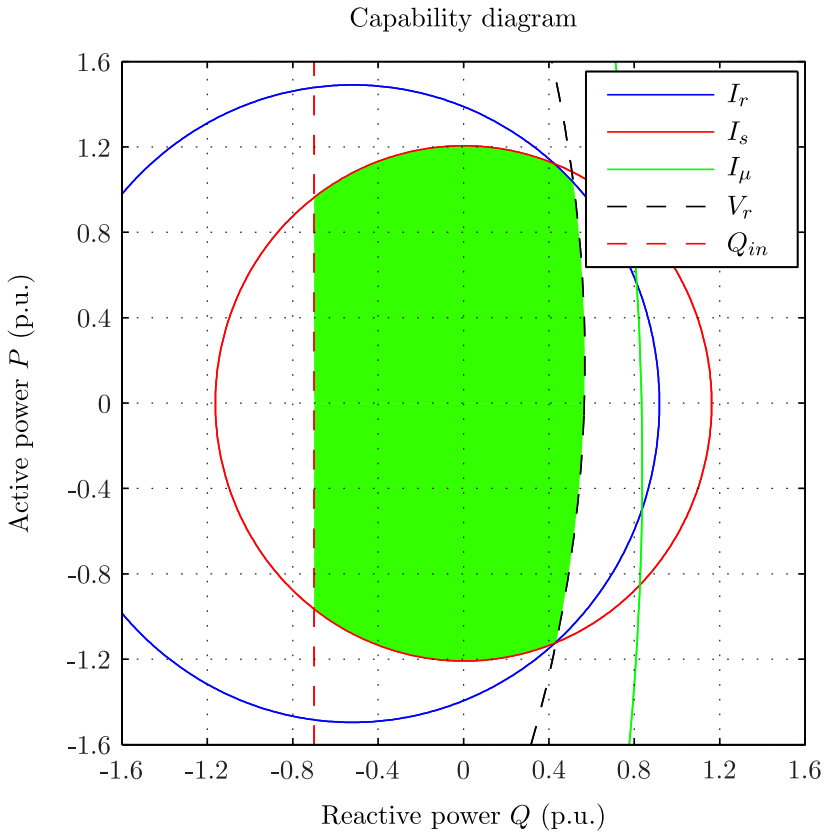

Figure 3.25: Capability diagram example: over-voltage and under-frequency

the constraint on the rotor voltage limits the amount of reactive power in over-excited mode. One can also notice a limit set on the absorbed reactive power Q_{in} placed on the left side of the graph, i.e. in under-excited mode. Because of the axial component of the magnetic flux density, power losses occur in the end-parts of the machine, i.e in the last iron stack, in the clamping plates and fingers (see Figure 3.26). In under-excited mode, these losses increase [CJ00; Kuc]. Finally the maximal absorbed reactive power may also have to be limited in this area in order to limit heating in the end-parts. Note that the defined limit on the present graph is purely arbitrary and depends on the machine characteristics.

Each curve of the graph is obtained by using the equivalent circuit parameters and its characteristic equations. Considering for example the maximum limit on the stator current $I_{\text{s,m}}$, one can define the phasor: $\underline{I}_{\text{s}} = I_{\text{s,m}} \cdot e^{i \cdot \varphi_{I_{\text{s}}}}$ where $\varphi_{I_{\text{s}}}$ is the phase shift of the current. Note that the stator voltage is assumed constant and its phase shift is taken as reference. The stator frequency and the speed are as well assumed constant. First the stator active P_{s} and reactive Q_{s} powers can be found. Then using the equivalent circuit parameters and Equations (3.55), (3.56) and (3.57) one can derive the corresponding rotor current phasor $\underline{I}'_{\text{r}}$ and rotor voltage phasor $\underline{V}'_{\text{r}}$. The rotor active power P_{r} is extracted by applying Equation (3.58). Finally one can find the values of the network active and reactive powers from Equations (3.35) and (3.36) by

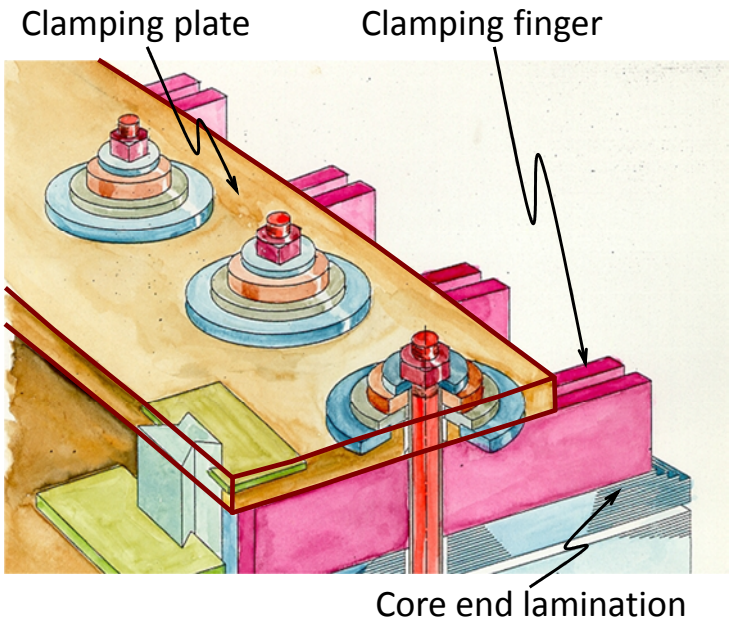

Figure 3.26: End-regions details [STS06]

setting $Q_c = 0$. By varying the value of φ_{I_s}, one describes the geometric locus (Q_{net}, P_{net}). The same method can be applied for the other limits.

One can show by neglecting the stator and resistive terms and the influence of magnetic saturation, that all these loci describe an ellipse. Indeed, in the case of the stator current limit, $I_{s,m}$, the corresponding ellipse is centered in $c_1 \approx (0, 0)$ whose major axis length is a_1 and minor axis length is b_1. The coefficient 3 comes from the fact that there are three phases.

$$\begin{aligned} a_1 &\approx 3 \left|\underline{V}_s\right| I_{s,m} \\ b_1 &\approx 3 \left|\underline{V}_s\right| I_{s,m}(1-s) \end{aligned} \tag{3.69}$$

The geometric locus corresponding to the rotor current limit, $I_{r,m}$, is also an ellipse centered in c_2 whose coordinates are c_{2x} and c_{2y} and whose major axis length is a_2 and minor axis length is b_2.

$$\begin{aligned} c_{2x} &\approx -\frac{3\left|\underline{V}_s\right|^2}{X_h + X'_{\sigma,s}} \\ c_{2y} &\approx 0 \\ a_2 &\approx 3\left|\underline{V}_s\right| \left(\frac{I_{r,m}}{u_t}\right) \frac{X_h}{X_h + X'_{\sigma,s}} \\ b_2 &\approx 3\left|\underline{V}_s\right| \left(\frac{I_{r,m}}{u_t}\right) \frac{X_h}{X_h + X'_{\sigma,s}}(1-s) \end{aligned} \tag{3.70}$$

The geometric locus corresponding to the rotor voltage limit, $V_{r,m}$, is as well an ellipse centered in c_3 whose coordinates are c_{3x} and c_{3y} and whose major axis length is a_3 and minor axis length

is b_3.

$$\begin{aligned}
\mathrm{c}_{3\mathrm{x}} &\approx -3\left|\underline{V}_{\mathrm{s}}\right|^2 \frac{X_{\mathrm{h}} + X'_{\sigma,\mathrm{r}}}{((X'_{\sigma,\mathrm{s}} + X'_{\sigma,\mathrm{r}})X_{\mathrm{h}} + X'_{\sigma,\mathrm{s}}X'_{\sigma,\mathrm{r}})} \\
\mathrm{c}_{3\mathrm{x}} &\approx 0 \\
\mathrm{a}_3 &\approx 3\left|\underline{V}_{\mathrm{s}}\right|(V_{\mathrm{r,m}}\mathrm{u}_{\mathrm{t}})\frac{X_{\mathrm{h}}}{X_{\mathrm{h}} + X'_{\sigma,\mathrm{s}}}\frac{1-s}{s} \\
\mathrm{b}_3 &\approx 3\left|\underline{V}_{\mathrm{s}}\right|(V_{\mathrm{r,m}}\mathrm{u}_{\mathrm{t}})\frac{X_{\mathrm{h}}}{X_{\mathrm{h}} + X'_{\sigma,\mathrm{s}}}\frac{1}{s}
\end{aligned} \tag{3.71}$$

Finally the geometric locus corresponding to the magnetizing current limit, $I_{\mu,\mathrm{m}}$, describes also an ellipse centered in c_4 whose coordinates are $\mathrm{c}_{4\mathrm{x}}$ and $\mathrm{c}_{4\mathrm{y}}$ and whose major axis length is a_4 and minor axis length is b_4.

$$\begin{aligned}
\mathrm{c}_{4\mathrm{x}} &\approx \frac{-3\left|\underline{V}_{\mathrm{s}}\right|^2}{X'_{\sigma,\mathrm{s}}} \\
\mathrm{c}_{4\mathrm{y}} &\approx 0 \\
\mathrm{a}_4 &\approx 3\left|\underline{V}_{\mathrm{s}}\right| I_{\mu,\mathrm{m}}\frac{X_{\mathrm{h}}}{X'_{\sigma,\mathrm{s}}}(1-s) \\
\mathrm{b}_4 &\approx 3\left|\underline{V}_{\mathrm{s}}\right| I_{\mu,\mathrm{m}}\frac{X_{\mathrm{h}}}{X'_{\sigma,\mathrm{s}}}
\end{aligned} \tag{3.72}$$

Note that neglecting the effect of saturation and resistive terms leads to higher inaccuracies when dealing with the rotor voltage and magnetizing current limits. However these approximated geometric loci are sufficient to understand the impact of the limits on the operation domain of the machine.

3.4 Validation by finite element computations

In order to validate the results of the analytical model, load points are calculated using the FE method. The 2D geometry model is similar to the one used in Chapter 2 for the magnetic circuit validation. The simulations are first done using a magneto-harmonic application and then a time-stepping magnetic application. The rotor and stator electrical currents are introduced in the model by using the circuit defined in Figure 3.27. The network is modeled with an ideal three-phase voltage source VNET and a short circuit impedance ZNET. The rotor converter is modeled with an ideal three-phase voltage source VCONV[6]. The previously computed end-winding leakages are introduced in the 2DFE by adding inductances LEND in series with the rotor and stator phases coils in the electrical circuit.

First section describes the simulation using a magneto-harmonic application. An iterative process is carried out in order to consider the effect of the non-linear magnetic material. The main advantage of such application is to quickly obtain results, the main drawback comes from the fact that the rotation effect is not considered and that the saturation management is approximated. Second section describes the simulation using a time-stepping application. In such

[6]A more advanced converter model is shown in Chapter 5 when dealing with the no-load stator voltage harmonics

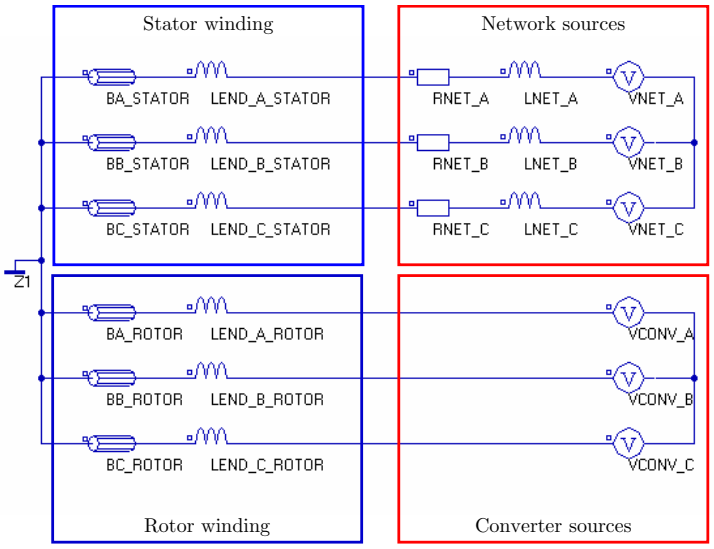

Figure 3.27: FEM: Coupling electrical circuit

application, the saturation and rotor position are correctly considered. However the simulation time is non-negligible especially because of the long initialization state of the rotor and stator currents. In order to counter this issue a method based on the regulation process of the DFIM is implemented. Last section compares the results of both FE simulations to the analytical results.

3.4.1 Modeling using a magneto-harmonic application

The problem is solved by using a magneto-harmonic application. It corresponds to a sinusoidal steady-state where the frequency is equal to the network frequency. This kind of application is very interesting as it is very fast, however it stands on some approximations. Firstly magneto-harmonic applications use an approximate method to consider the non linear behavior of the magnetic material. Indeed this application considers that all quantities are sinusoidally varying at the given frequency. Yet because of magnetic saturation, the magnetic field and the magnetic flux density can not be set sinusoidal at the same time as shown in Figure 3.28. The method exposed by some authors [Gue94] and included in the software *Flux* is to define an equivalent $B(H)$ law based on the energetic equivalence method [Ced13].

Secondly the impact of the rotor position is not considered in this kind of simulation. However as shown in Figure 3.29 the impact on the electromagnetic torque is not negligible especially because of the changing interaction of the stator and rotor teeth. One can observe a relative variation of about $\pm 1\%$. This simulation was performed by setting the stator and rotor voltage amplitude corresponding to a certain operation point. The stator voltage phase angle was defined as the reference while the rotor voltage phase angle φ_m was set according to the following equation:

$$\varphi_\mathrm{m} = \varphi_{\mathrm{m},0} - p \cdot \theta_\mathrm{m} \tag{3.73}$$

where $\varphi_{\mathrm{m},0}$ is the relative phase shift between the rotor voltage and the stator voltage corre-

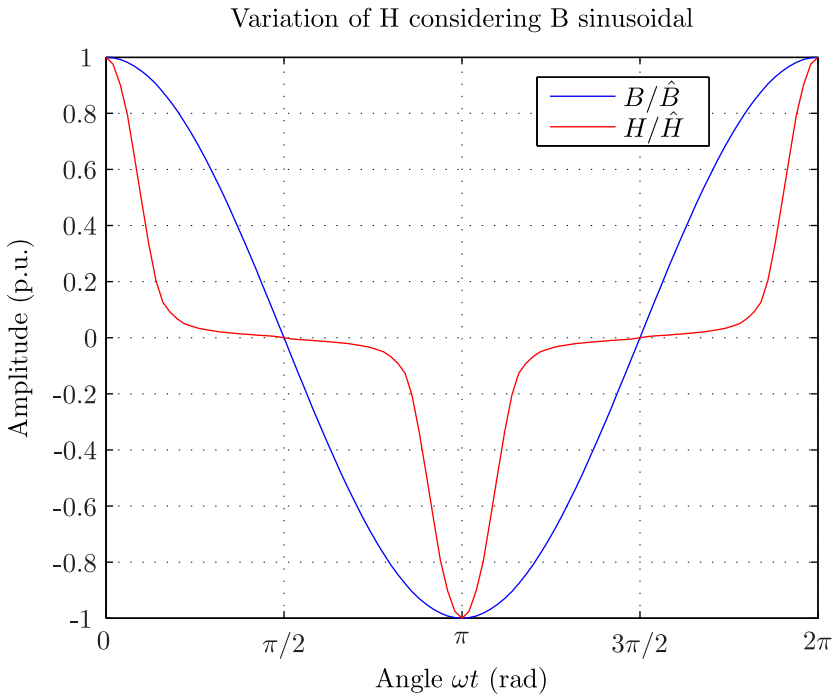

Figure 3.28: Variation of H considering B sinusoidal and magnetic saturation

sponding to the studied operation point and θ_{m} is the mechanical rotor position. Such definition makes it possible to keep constant the phase shift between the rotor and the stator magnetic fields although the mechanical rotor position is changing. The angular position was shifted within a range corresponding to a complete pole step i.e. π/p and the electromagnetic torque was extracted for each position. One can see that the signal repeats each third of the pole step, i.e. q_{s} stator slot pitches or q_{r} rotor slot pitches [7].

Taking these two elements into consideration, we now expose the magneto-harmonic load-point computation. The load point is defined in generator mode i.e from the apparent power and the power factor. It corresponds to the first definition of the load-point described in the previous part. The stator voltage is constant and the speed is set by modifying the slip. The rotor voltage has to be set in amplitude and phase in order to obtain the correct active and reactive power. The analytical algorithm described previously makes it possible to define the rotor voltage amplitude and phase shift corresponding to any load operation point. However as the analytical method stands on approximations, equivalent circuit parameters, saturation management, these quantities may have to be refined. Petrichenko [Pet08] proposes an iterative process in order to define the load point characteristics of a synchronous machine for turbo applications. The process presented here stands on the same principles but is adapted to the DFIM.

The apparent power and the power factor make it possible to define the reference network active power $P_{\mathrm{net}}^{\mathrm{ref}}$ and reactive power $Q_{\mathrm{net}}^{\mathrm{ref}}$. For each couple $[V_{\mathrm{r}}, \varphi_{\mathrm{m}}]$ one can extract the ro-

[7] Note that this might be different when dealing with fractional slot windings

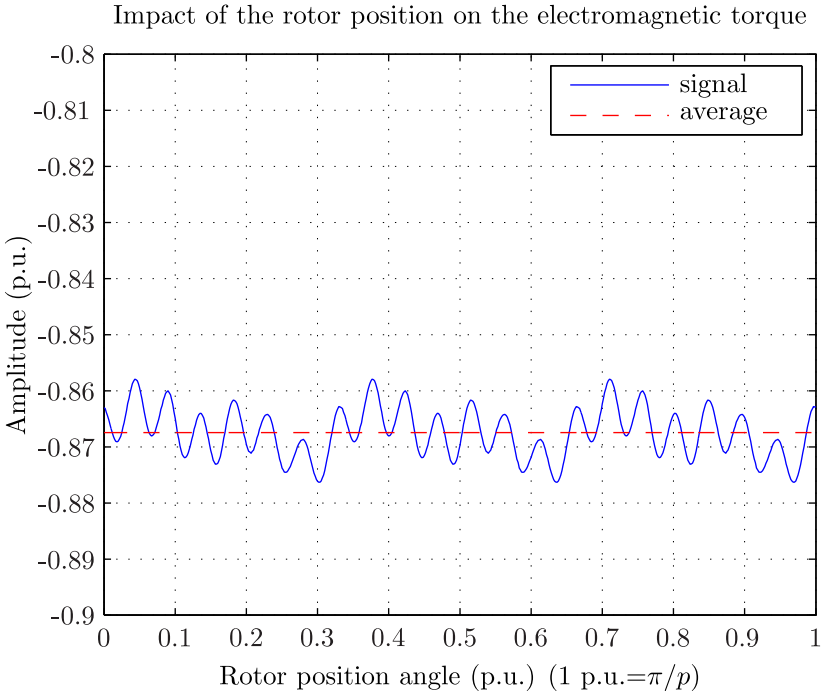

Figure 3.29: Impact of the rotor position on the electromagnetic torque

tor and stator, voltages and currents from the magneto-harmonic simulation and derive the corresponding active and reactive stator and rotor powers.

$$\begin{aligned} P_{\mathrm{s}} &= \Re\left(\underline{V}_{\mathrm{VnetA}} \cdot \underline{I}^{*}_{\mathrm{VnetA}}\right) + \Re\left(\underline{V}_{\mathrm{VnetB}} \cdot \underline{I}^{*}_{\mathrm{VnetB}}\right) + \Re\left(\underline{V}_{\mathrm{VnetC}} \cdot \underline{I}^{*}_{\mathrm{VnetC}}\right) \\ Q_{\mathrm{s}} &= \Im\left(\underline{V}_{\mathrm{VnetA}} \cdot \underline{I}^{*}_{VnetA}\right) + \Im\left(\underline{V}_{\mathrm{VnetB}} \cdot \underline{I}^{*}_{\mathrm{VnetB}}\right) + \Im\left(\underline{V}_{VnetC} \cdot \underline{I}^{*}_{\mathrm{VnetC}}\right) \\ P_{\mathrm{r}} &= \Re\left(\underline{V}_{\mathrm{VconvA}} \cdot \underline{I}^{*}_{VconvA}\right) + \Re\left(\underline{V}_{\mathrm{VconvB}} \cdot \underline{I}^{*}_{\mathrm{VconvB}}\right) + \Re\left(\underline{V}_{\mathrm{VconvC}} \cdot \underline{I}^{*}_{\mathrm{VconvC}}\right) \end{aligned} \tag{3.74}$$

Finally the network active and reactive powers obtained from the FE simulation are given by:

$$\begin{aligned} P^{\mathrm{fem}}_{\mathrm{net}} &= P_{\mathrm{s}} + P_{\mathrm{r}} \\ Q^{\mathrm{fem}}_{\mathrm{net}} &= Q_{\mathrm{s}} \end{aligned} \tag{3.75}$$

Let us define the vector function F whose variable X is the couple $[V_{\mathrm{r}}, \varphi_{\mathrm{m}}]$.

$$F(X) = \begin{bmatrix} F_1 \\ F_2 \end{bmatrix} = \begin{bmatrix} P^{\mathrm{fem}}_{\mathrm{net}} - P^{\mathrm{ref}}_{\mathrm{net}} \\ Q^{\mathrm{fem}}_{\mathrm{net}} - Q^{\mathrm{ref}}_{\mathrm{net}} \end{bmatrix} \tag{3.76}$$

The objective of the computation is to find X so that $F[X] = 0$. As F is a non-linear function, the Newton Raphson method is used. The Jacobian J of F is defined as:

$$\mathrm{J}(X) = \begin{bmatrix} \frac{\partial F_1}{\partial V_{\mathrm{r}}} & \frac{\partial F_1}{\partial \varphi_{\mathrm{m}}} \\ \\ \frac{\partial F_2}{\partial V_{\mathrm{r}}} & \frac{\partial F_2}{\partial \varphi_{\mathrm{m}}} \end{bmatrix} \tag{3.77}$$

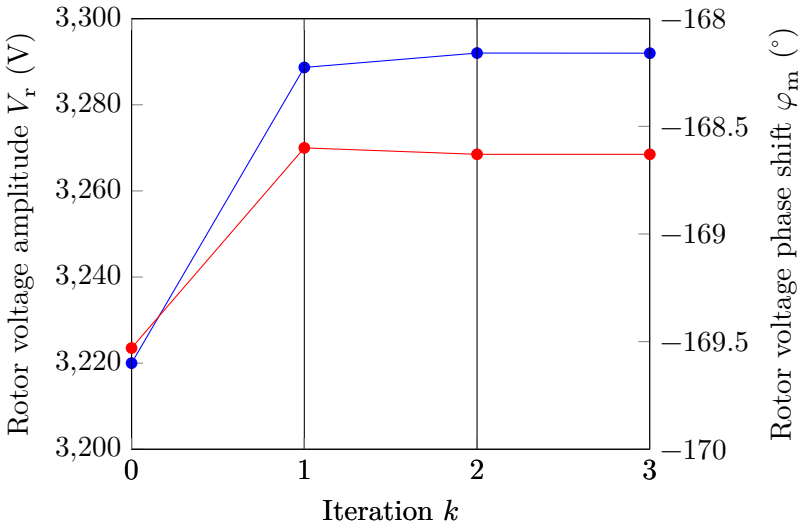

Figure 3.30: Evolution example of the rotor voltage amplitude V_r (—●—) and phase shift φ_m (—●—) during iteration process

The values of the partial derivatives ∂ are approximated considering small variations h so that for example:

$$\frac{\partial f(a)}{\partial x} \approx \frac{f(a+h) - f(a)}{h} \tag{3.78}$$

At the first iteration $k = 0$, the vector X is initialized to the vector $X^0 = [V_r, \varphi_m]$ obtained from the analytical tool and then updated along the iterative process according to the Equation (3.79). When $F\left(X^k\right) < \epsilon$, where ϵ is the admissible error, the rotor voltage and angle have been determined. Figure 3.30 shows an example of resolution for a given load-point, one can observe the evolution of V_r and φ_m. Such method is very efficient as it makes it possible to define rapidly any operation point of the machine.

$$X^{k+1} = X^k - J(X^k)^{-1} \cdot F\left(X^k\right) \tag{3.79}$$

3.4.2 Modeling using a time stepping application

As explained previously, magneto-harmonic applications do not consider the rotation of the rotor and approximate the magnetic behavior of non-linear magnetic materials. This part computes the load operation of the machine by using a magnetic time-stepping simulation. The same geometry and electrical circuits are used. Such simulation makes it possible latter to study the harmonic content of the stator and rotor current, the electromagnetic forces and to compute the iron losses in the stator and the rotor core. The main problem when using time-stepping applications is the long transient state. Indeed at the beginning of the simulation, all the circuit variables i.e. stator and rotor currents are set to zero, which given high winding time constants

requires non negligible time before stabilization. Two methods can be used in order to accelerate the initialization.

I. Initialization using a magneto-harmonic calculation

One solution is to use the results from the magneto-harmonic so as to initialize the transient application, however the results will directly depend on the rotor voltage found in the magneto-harmonic simulation which may not lead to exactly the same steady-state operation point.

II. Initialization using the control of the machine

The method proposed here implements the control of the machine. Note that Kanerva [Kan05] already studied the interest of integrating a control procedure into a FE simulation tool. He more particularly developed a coupling between Matlab-Simulink and a FE tool and studied the example of the DFIM. Contrarily to [Kan05], here the control is directly implemented inside the FE tool without using an external software. General equations of the DFIM in the synchronous frame and using p.u. notation are given by the followings [Cha80]:

$$\begin{aligned}
\underline{u}_{\mathrm{s}} &= r_{\mathrm{s}}\underline{i}_{\mathrm{s}} + \frac{1}{\omega_{\mathrm{n}}}\frac{\mathrm{d}\underline{\psi}_{\mathrm{s}}}{\mathrm{d}t} + \mathrm{i}\omega_{\mathrm{s}}\underline{\psi}_{\mathrm{s}} \\
\underline{u}_{\mathrm{r}} &= r_{\mathrm{r}}\underline{i}_{\mathrm{r}} + \frac{1}{\omega_{\mathrm{n}}}\frac{\mathrm{d}\underline{\psi}_{\mathrm{r}}}{\mathrm{d}t} + \mathrm{i}(\omega_{\mathrm{s}} - \omega_{\mathrm{m}})\underline{\psi}_{\mathrm{r}} \\
\underline{\psi}_{\mathrm{s}} &= l_{\mathrm{s}}\underline{i}_{\mathrm{s}} + l_{\mathrm{s,r}}\underline{i}_{\mathrm{r}} \\
\underline{\psi}_{\mathrm{r}} &= l_{\mathrm{r}}\underline{i}_{\mathrm{r}} + l_{\mathrm{s,r}}\underline{i}_{\mathrm{s}} \\
\Gamma_{\mathrm{em}} &= \Im(\underline{\psi}_{\mathrm{s}} \cdot \underline{i}_{\mathrm{s}})
\end{aligned} \tag{3.80}$$

$\underline{\psi}_{\mathrm{s}}$ and $\underline{\psi}_{\mathrm{r}}$ are the stator and rotor magnetic fluxes. ω_s and ω_{m} are the stator and mechanical angular frequency while ω_{n} is the reference angular frequency. l_{s}, l_{r} are the stator and rotor inductances while $l_{\mathrm{s,r}}$ is the mutual inductance between stator and rotor. Note that all the variable are expressed in p.u. except ω_{n}.

The command of the DFIM stands on a two-axis Park transformation of the stator and rotor

currents, voltages and flux so that the equations defined by (3.80) become:

$$\begin{aligned}
u_{\mathrm{d,s}} &= r_{\mathrm{s}} i_{\mathrm{d,s}} + \frac{1}{\omega_n}\frac{\mathrm{d}\psi_{\mathrm{d,s}}}{\mathrm{d}t} - \omega_{\mathrm{s}}\psi_{\mathrm{q,s}} \\
u_{\mathrm{q,s}} &= r_{\mathrm{s}} i_{\mathrm{q,s}} + \frac{1}{\omega_n}\frac{\mathrm{d}\psi_{\mathrm{q,s}}}{\mathrm{d}t} + \omega_{\mathrm{s}}\psi_{\mathrm{d,s}} \\
u_{\mathrm{d,r}} &= r_{\mathrm{r}} i_{\mathrm{d,r}} + \frac{1}{\omega_n}\frac{\mathrm{d}\psi_{\mathrm{d,r}}}{\mathrm{d}t} - (\omega_{\mathrm{s}} - \omega_{\mathrm{m}})\psi_{\mathrm{q,r}} \\
u_{\mathrm{q,r}} &= r_{\mathrm{r}} i_{\mathrm{d,r}} + \frac{1}{\omega_n}\frac{\mathrm{d}\psi_{\mathrm{q,r}}}{\mathrm{d}t} + (\omega_{\mathrm{s}} - \omega_{\mathrm{m}})\psi_{\mathrm{d,r}} \\
\Gamma_{\mathrm{em}} &= \psi_{\mathrm{d,s}} i_{\mathrm{q,s}} - \psi_{\mathrm{q,s}} i_{\mathrm{d,s}} \\
\psi_{\mathrm{d,s}} &= l_{\mathrm{s}} i_{\mathrm{d,s}} + l_{\mathrm{s,r}} i_{\mathrm{d,r}} \\
\psi_{\mathrm{q,s}} &= l_{\mathrm{s}} i_{\mathrm{q,s}} + l_{\mathrm{s,r}} i_{\mathrm{q,r}} \\
\psi_{\mathrm{d,r}} &= l_{\mathrm{r}} i_{\mathrm{d,r}} + l_{\mathrm{s,r}} i_{\mathrm{d,s}} \\
\psi_{\mathrm{q,r}} &= l_{\mathrm{r}} i_{\mathrm{q,r}} + l_{\mathrm{s,r}} i_{\mathrm{q,s}}
\end{aligned} \tag{3.81}$$

The regulation is based on a stator voltage oriented control. The stator voltage is therefore set on the d-stator axis. Consequently the torque is controlled by regulating the d-axis stator current and the stator reactive power is controlled by acting on the q-axis stator current. The torque and the speed are linked by the mechanical equation, $J\mathrm{d}\Omega/\mathrm{d}t = \Gamma_{\mathrm{em}} - \Gamma_{\mathrm{turbine}}$, where $\Omega = n \cdot 2\pi/60$ and $\Gamma_{\mathrm{turbine}}$ is the torque from the turbine. Consequently controlling the d-axis stator current makes it possible to control the speed.

Figure 3.31 shows one possible structure of speed and powers control in pump and turbine mode. The Park transformer block $\mathrm{Pi_s}$ and $\mathrm{Pi_r}$ transform the stator and rotor phase currents in their equivalent d and q axis components considering the electrical angles θ_{s} and $\theta_{\mathrm{r}} = \theta_{\mathrm{s}} - p \cdot \theta_{\mathrm{m}}$. The inverse Park transformer block $\mathrm{Pv_r}$ transforms the d and q axis rotor voltage components into its equivalent phase components. The blocks $\mathrm{K_n}$ and $\mathrm{K_q}$ give the consign on the stator current regarding the speed and the stator reactive power. The blocks $\mathrm{K_{Isd}}$, $\mathrm{K_{Isq}}$, $\mathrm{K_{Ird}}$ set the consign on the rotor current regarding the stator current and the blocks $\mathrm{K_{Ird}}$, $\mathrm{K_{Irq}}$ set the d and q axis component of the rotor voltage. All the regulation blocks are proportional integrators regulators, for more details about the control of a DFIM and the synthesis of the regulators one can refer to [Hod04].

The scheme shown in Figure 3.31 has been translated in a *Python* program. The module *multi-physics* available in the FE software *Flux* from Cedrat has been used in order to integrate the *Python* program within the FE solving process. Figure 3.32 shows the main principles of the coupled simulation. The 2DFE simulation is solved and at each time step the values of the rotor voltage sources are updated given the consigns of the regulators. The advantage of such application is the possibility to automatize easily the calculation of a load-point in order to compute for any load conditions the efficiency and in particularly the electromagnetic forces or the iron losses (see Chapter 5). Furthermore this makes it possible to study later the behavior of the machine under transient states such as short circuit or start-up (see Chapter 5).

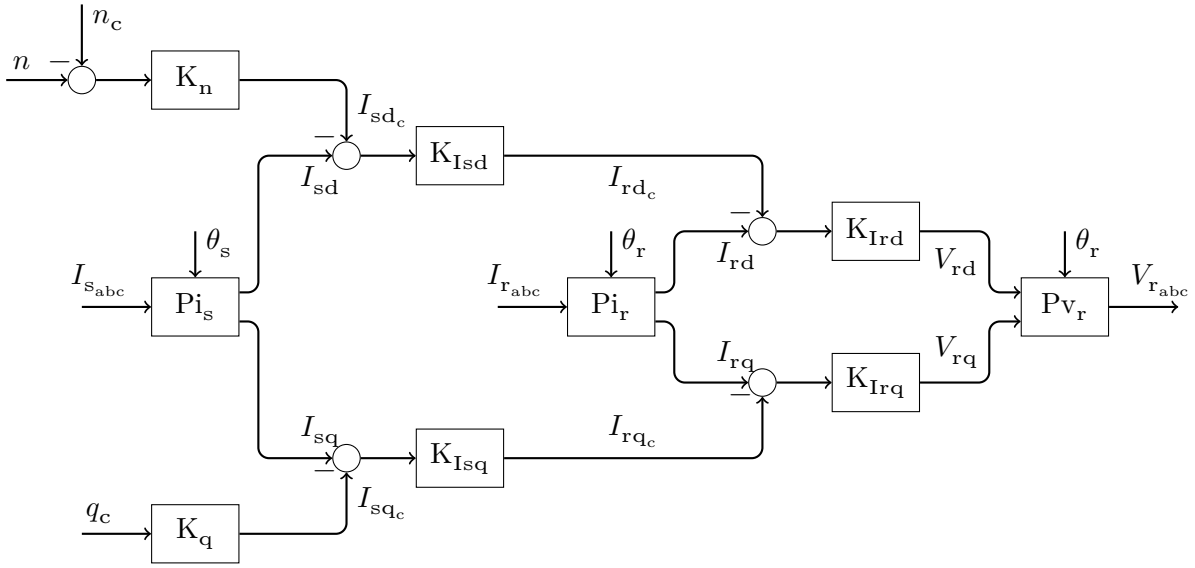

Figure 3.31: Control Structure for load operation

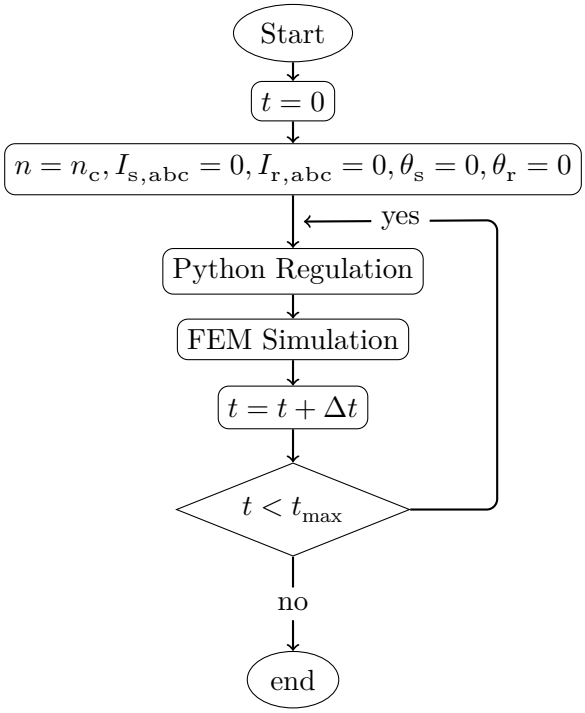

Figure 3.32: Coupled FEM-Python simulation

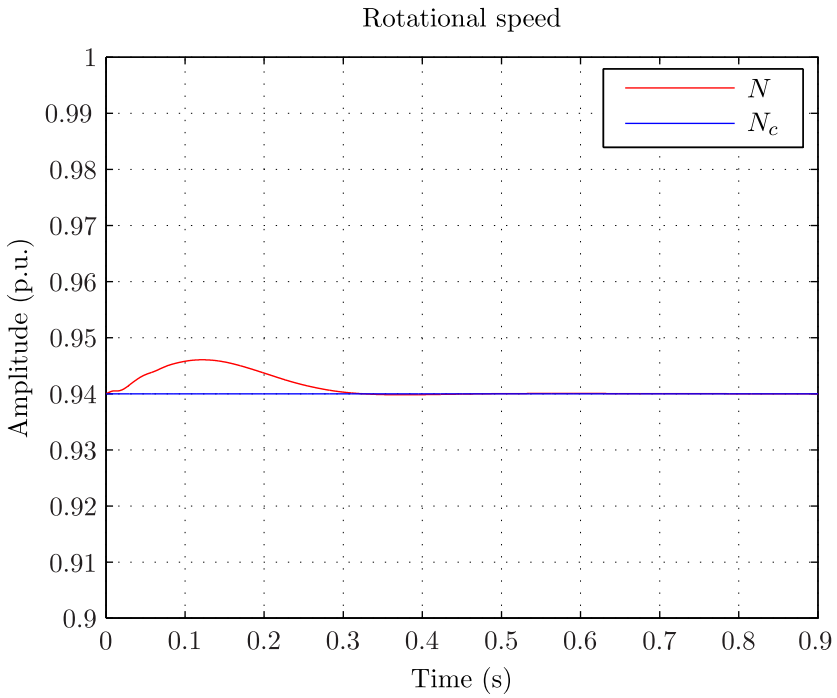

Figure 3.33: Controlled Simulation: Rotational speed

Figures 3.33, 3.34, 3.35, 3.36, 3.37 and 3.38 show the evolution of the speed, torque and rotor currents and stator currents. We set as consigns: 0.8 p.u. for the active power, 0.2 p.u. for the reactive power and 0.94p.u. for the speed. One can see that the simulation converges fast to the steady state. The next part compares the results from the analytical calculation to the magneto-harmonic and time stepping simulation ones.

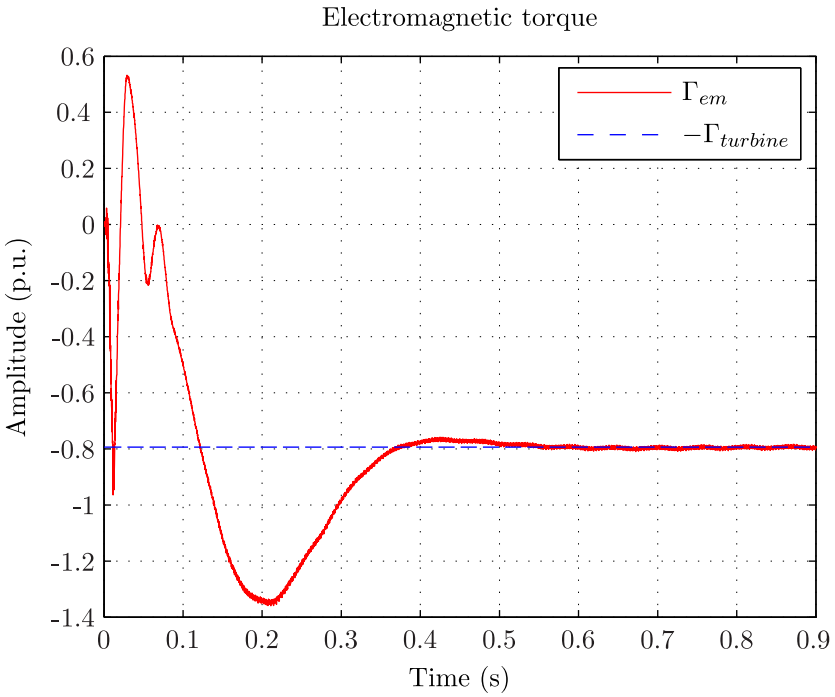

Figure 3.34: Controlled Simulation: Electromagnetic torque

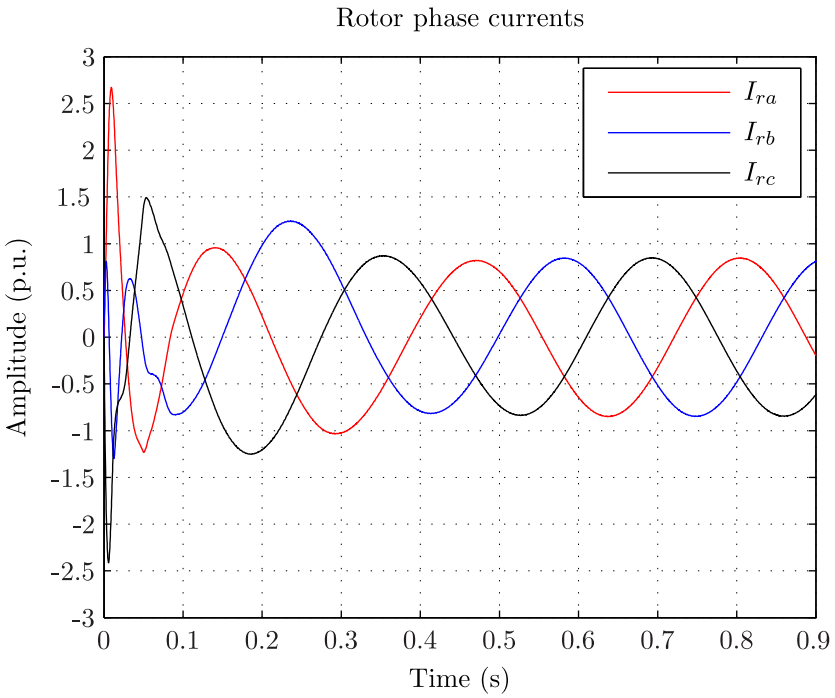

Figure 3.35: Controlled Simulation: Rotor currents

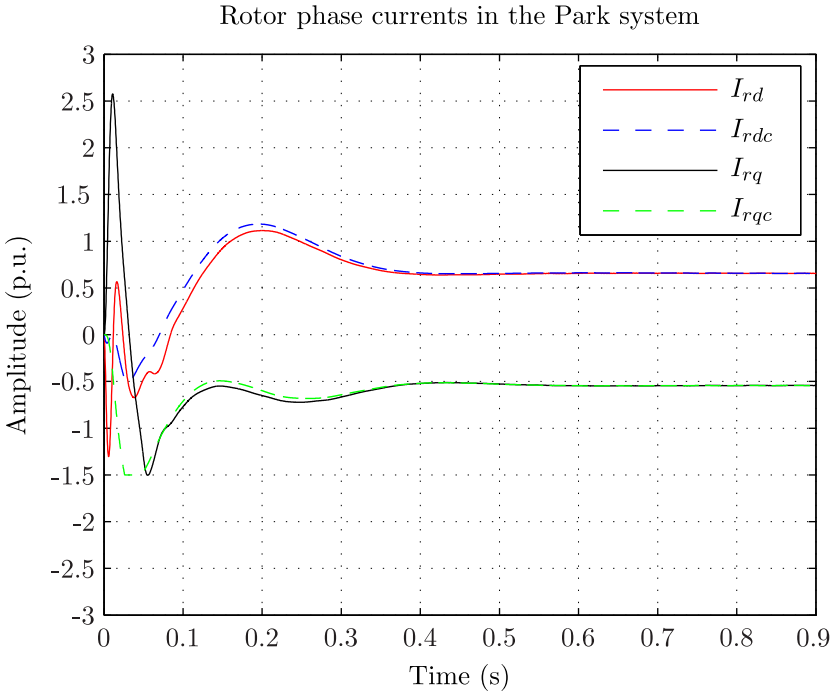

Figure 3.36: Controlled Simulation: Rotor currents in Park system

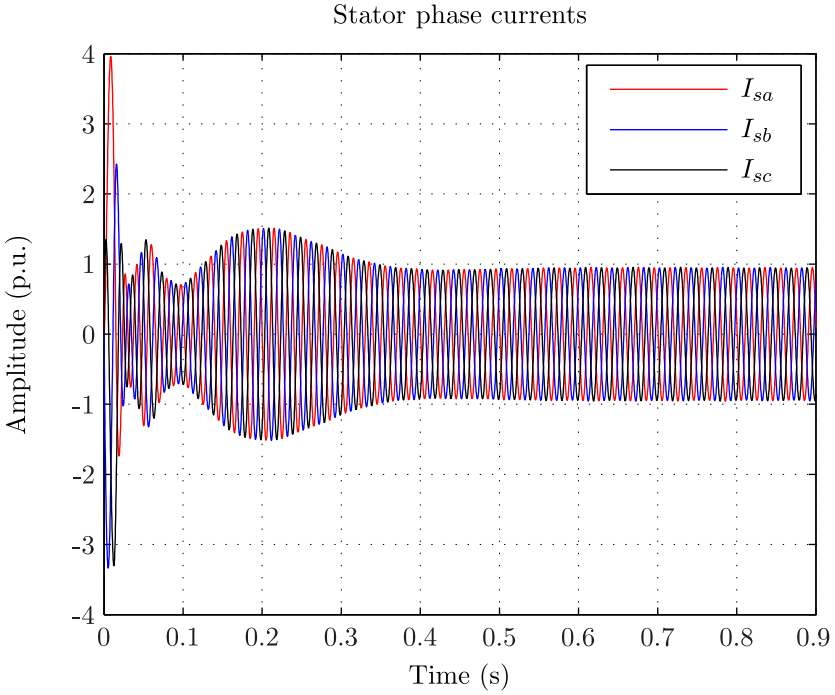

Figure 3.37: Controlled Simulation: Stator currents

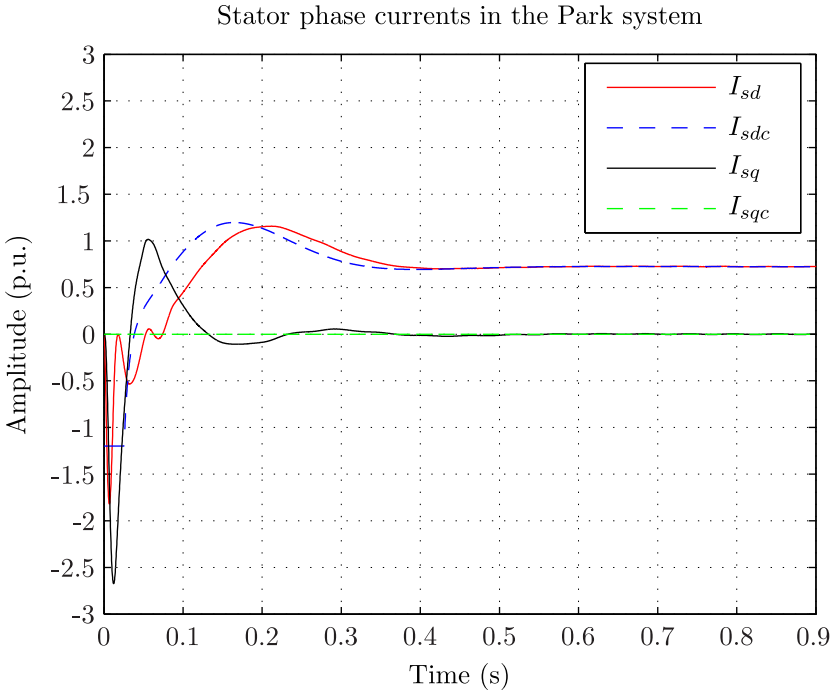

Figure 3.38: Controlled Simulation: Stator currents in Park system

3.4.3 Comparison of results

Table 3.5 compares the analytical and the FE computations. The operation point characteristics used for the comparisons are described in Table 3.6. When taking the time stepping FE simulation as reference, one can see that all methods give very close results. Differences between analytical and FE might be explained by some inaccuracies in the equivalent scheme components or regarding the consideration of the magnetic circuit saturation. However the results are very satisfying and prove that the analytical model is correct.

Quantity	Analytic	FE AC application	FE TS application
U_{r}	3793	3831	3838
I_{r}	5776	5803	5869
I_{s}	8313	8281	8279

Table 3.5: Validation of a steady-state operation point

OP	P_{mec} (MW)	U_{s} (kV)	$\cos\varphi_{\mathrm{n}}$ (−)	s (%)	mode (−)
1	255.6	18	0.9	−10	over-excited

Table 3.6: Load points characteristics for validation

3.5 Conclusion

This chapter exposed and validated the modeling of the DFIM in steady state operation. An equivalent circuit is presented and its corresponding parameters were validated by FE computations. Although leakage component such as slot leakage inductance or harmonic leakage inductance are well known, difficulties arise when defining special components such as the *zig-zag* leakage inductance or the end-leakage inductance.

Based on the developed equivalent scheme, load-point calculation algorithms were exposed and made it possible to define any steady-state load operation as well as the limits of operation of the machine.

Two FE methods were described in order to validate the analytical model. It was shown that these two FE simulations were not immediate, the magneto-harmonic due to saturation management approximation and the time stepping simulation due to the long simulation time. The latter was solved by developing a controlled FE simulation based on the regulation of the DFIM.

The comparison of the analytical method results with FE results demonstrated a good agreement. The time stepping analysis proved the presence of harmonics on the rotor voltages, on rotor currents as well as on the electromagnetic torque. All these elements showed the necessity to develop and to add a harmonic model to the current steady-state equivalent formulation; this is the object of the next chapter.

4 Airgap harmonics model

4.1 Introduction

Chapter 3 described the equivalent scheme used for studying the steady-state load operation of the DFIM. The developed model assumed that the magnetic field varies sinusoidally. This chapter completes the simplified modeling of Chapter 3 by considering additional harmonics existing in reality such as the following:

- the conductors are placed in stator and rotor slots. This leads to a non-sinusoidal mmf and consequently to winding harmonics.
- the stator and rotor slots modulate the airgap causing airgap permeance harmonics.
- the magnetic saturation of the stator and rotor magnetic circuits virtually enlarges the airgap and physically modifies the permeance harmonics.

First part defines the stator and rotor mmf standing on their respective winding configurations. The resulting airgap flux density is obtained by combining the rotor and stator mmf considering their phase shift and by assuming a constant airgap. The effect of the slip on the harmonic frequency content is explained.

Second part corrects the constant airgap used in the first part by considering the presence of the stator and rotor slots. The double-slotted airgap permeance is derived by using the BEM. The results are compared to the ones obtained from the analytical formula existing in the literature [Bru97].

Third part computes the resulting airgap flux density by modulating the airgap flux density obtained in the first part by the real airgap permeance function. The impact of the magnetic saturation on the airgap flux density harmonics is integrated by correcting the airgap permeance using the results of the developed magnetic model developed in Chapter 3. The results are validated by carrying out a 2DFE computation.

Fourth part proposes an option for improvement of the current modeling method which makes it possible to deal with the saturation of the magnetic circuit on the fundamental wave, but does not make it possible to describe accurately its effect on other harmonics. The proposal for improvement suggests to combine a simplified discretization of the stator and rotor cores using magnetic resistances with an accurate BE model of the air gap. Results are compared with FE results and demonstrate a good potential of improvement for the future.

Combined with the steady-state operation scheme presented in Chapter 3, the developed harmonic model will make it possible later in Chapter 5 to deal accurately with the problem of electromagnetic forces, stator voltage harmonics and iron losses for any steady-state load

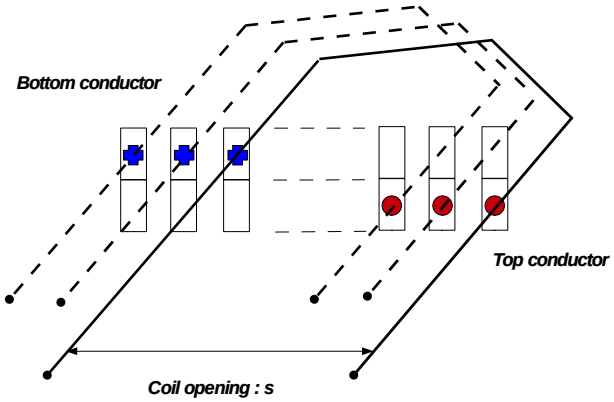

Figure 4.1: Two-layer winding and coil opening

conditions.

4.2 Rotor and stator flux density with a constant airgap

4.2.1 Definition of the mmf of a three-phase winding

As seen in Chapter 3 the stator and rotor windings of the studied DFIM are double-layer windings. Each slot counts one top and one bottom conductor. In the following we call it a turn the association of one top conductor with one bottom conductor as shown in Figure 4.1. One can see that the distance between both conductors is equal to s also called winding pitch. When the winding pitch s is equal to the pole pitch τ_{p} the winding is called full pitch winding. However in order to reduce certain harmonic winding coefficients, the winding pitch s is often chosen different from the pole pitch i.e $s = (\mathrm{Y}_1/3 \cdot q) \cdot \tau_{\mathrm{p}}$ with q the number of slots per pole and phase and Y_1 is the number of slot pitches $\tau_s = 2 \cdot \pi / N_{\mathrm{z}}$ in one coil opening. Figure 4.2 shows an example of magnetic field created by one turn. The mmf $\theta_{t_{\mathrm{i}}}$ of one turn t_i can be written as a sum of Fourier series as shown by Equation (4.1) where α_i is the angular position of the top conductor.

$$\theta_{t_{\mathrm{i}}}(\alpha, \alpha_i) = \sum_{\nu=1}^{+\infty} \theta_{t_{\mathrm{i}},\nu} \sin(\nu(\alpha - \alpha_i) + \varphi_\nu) \tag{4.1}$$

The stator and rotor windings of the studied machine count three phases disphased of an electrical degree equal to 120°. Each phase can be splitted into N_{a} parallel paths and each parallel path consists of the connection of N_{s} turns in series. In the studied machine, all parallel paths are assumed identical which means that for the same current they will create the same magnetic field. Consequently one can study the magnetic field created by each phase by considering the N_{a} parallel circuits as a surrogate circuit with N_{s} turns in series. Table 4.1 shows an example of a three-phase winding configuration having four slots per pole and phase and a coil opening equal to ten. A $\pm$ indicates the orientation of the conductor.

In the studied case the winding is periodic every two poles which is the smallest possible period.

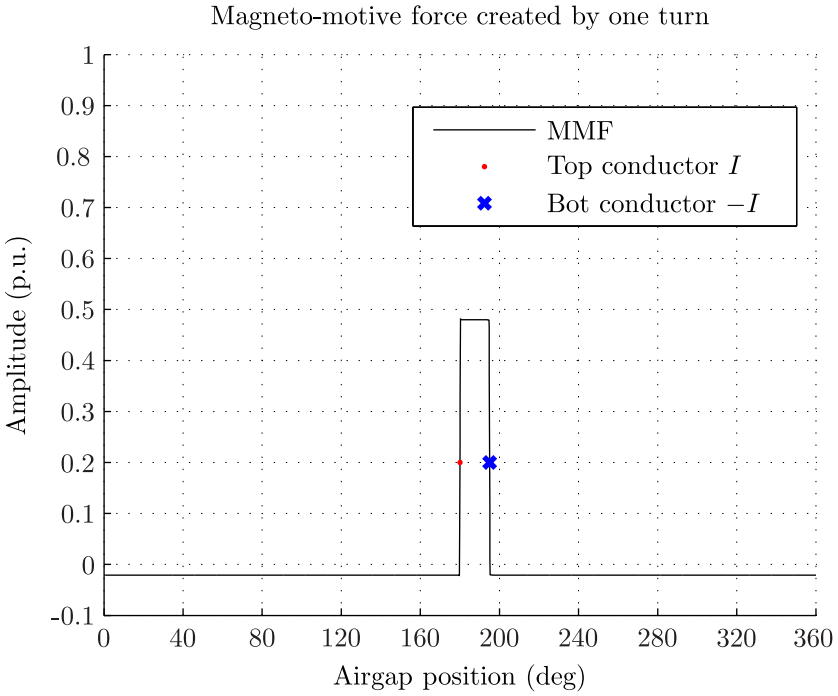

Figure 4.2: Magneto-motive force created by one turn

Slot index	1	2	3	4	5	6	7	8	9	10	11	12
Top	a	a	a	a	-c	-c	-c	-c	b	b	b	b
Bottom	a	a	-c	-c	-c	-c	b	b	b	b	-a	-a

(a) First pole

Slot index	13	14	15	16	17	18	19	20	21	22	23	24
Top	-a	-a	-a	-a	c	c	c	c	-b	-b	-b	-b
Bottom	-a	-a	c	c	c	c	-b	-b	-b	-b	a	a

(b) Second pole

Table 4.1: Winding configuration example over two poles: $q = 4$, $Y_1 = 10$

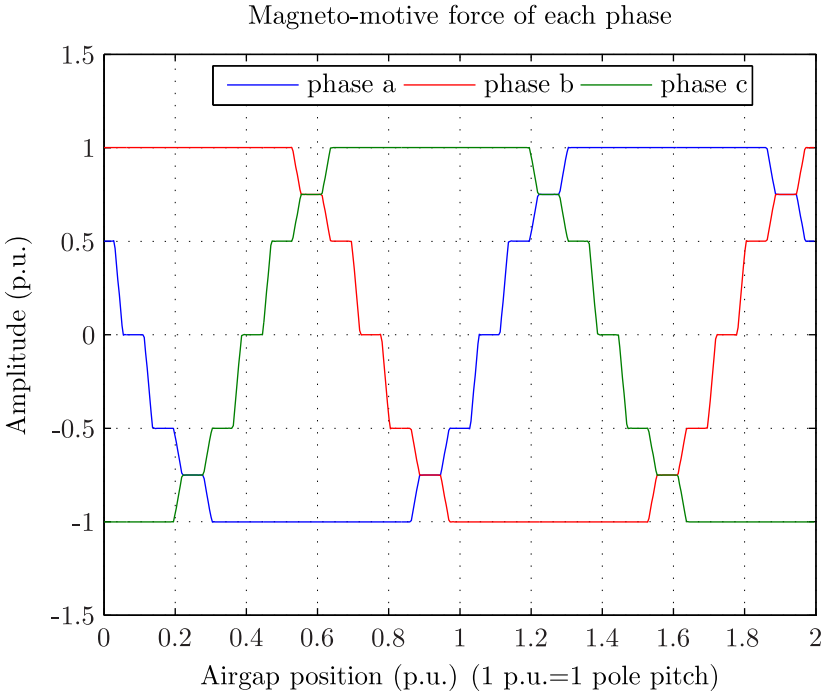

Figure 4.3: Magneto-motive-force distribution of each phase

It is not always the case and in particular when dealing with fractional slot windings.[1] Each phase winding mmf Θ_{j} is obtained by superposing all the single mmf $\Theta_{t_{\mathrm{i,j}}}$ of turns belonging to the same phase j as given by Equation (4.2).

$$\Theta_{\mathrm{j}}(\alpha) = \sum_{i=1}^{2pq} \sigma_i \cdot \frac{I}{N_{\mathrm{a}}} \cdot \Theta_{t_{\mathrm{i,j}}}(\alpha, \alpha_i) \tag{4.2}$$

As the considered windings are balanced, there are $2p \cdot q$ single mmf per phase; $\sigma_i = \pm 1$ is the sign of the top conductor i, and I is the amplitude of the total current flowing in the phase j. Figure 4.3 shows the magnetic field created by each phase when supplied with the same current. One can clearly see the steps due to the distribution of the conductors in the slots. Figure 4.4 shows the harmonic content of the mmf created by one phase. In this graph, the reference of the harmonics is chosen so that the fundamental i.e the field with p pole-pairs is the first harmonic. One can see the presence of main harmonics such as the third harmonic and its multiples as well as the $\nu = 5$ and $\nu = 7$ harmonics and the slot harmonics $\nu = 6q \pm 1 = 23..25$.

Equation 4.1 can be expressed as sum of Fourier series. When the phase j is supplied with a current I, a general expression is given by Equation (4.3)

$$\Theta_j(\alpha) = \sum_{\nu=1}^{+\infty} \Theta_\nu I \sin(\nu\alpha + \varphi_\nu) \tag{4.3}$$

[1] Fractional slot windings are detailed in Chapter 5 when dealing with parasitic forces calculation

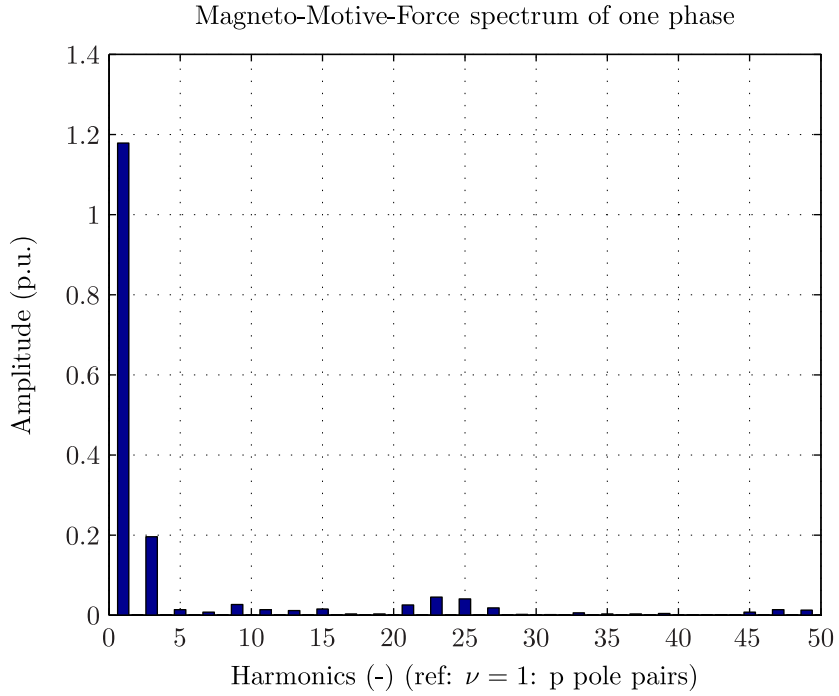

Figure 4.4: Magneto-motive-force spectrum of one phase

where ν is the harmonic number, Θ_ν is the amplitude of the ν^{th} mmf harmonic considering a maximum current equal to 1 A, φ_ν is the phase shift of the ν^{th} mmf harmonic and α is the angular position in the airgap. Note that for the fundamental wave we have $\nu = p$. We consider now that the three phases are supplied by a three-phase balanced system of currents according to:

$$\begin{aligned} I_{\text{a}} &= \hat{I}\cos\left(2\pi f \cdot t + \varphi_0\right) \\ I_{\text{b}} &= \hat{I}\cos\left(2\pi f \cdot t + \varphi_0 - \frac{2\pi}{3}\right) \\ I_{\text{c}} &= \hat{I}\cos\left(2\pi f \cdot t + \varphi_0 - \frac{4\pi}{3}\right) \end{aligned} \tag{4.4}$$

where $\hat{I}$ is the maximum value of the current and φ_0 is the initial phase shift of the currents. Finally the mmf created by each phase j is given by Equation (4.5).

$$\begin{aligned} \Theta_{\phi_a}(\alpha, t) &= \sum_{\nu=1}^{+\infty} \Theta_\nu \hat{I}\sin\left(\nu\alpha + \varphi_\nu\right)\cos\left(2\pi f \cdot t + \varphi_0\right) \\ \Theta_{\phi_b}(\alpha, t) &= \sum_{\nu=1}^{+\infty} \Theta_\nu \hat{I}\sin\left(\nu\left(\alpha - \frac{2\pi}{3p}\right) + \varphi_\nu\right)\cos\left(2\pi f \cdot t + \varphi_0 - \frac{2\pi}{3}\right) \\ \Theta_{\phi_c}(\alpha, t) &= \sum_{\nu=1}^{+\infty} \Theta_\nu \hat{I}\sin\left(\nu\left(\alpha - \frac{4\pi}{3p}\right) + \varphi_\nu\right)\cos\left(2\pi f \cdot t + \varphi_0 - \frac{4\pi}{3}\right) \end{aligned} \tag{4.5}$$

One can see that each phase creates a pulsating magnetic field. The superposition of the three

mmf leads to a rotational mmf expressed as:

$$\Theta_{\mathrm{abc}}(\alpha,t)=\frac{3}{2}\sum_{\nu=1}^{+\infty}\sigma_{\nu}\Theta_{\nu}\hat{I}\sin\left(\sigma_{\nu}\nu\cdot\alpha+\sigma_{\nu}\phi_{\nu}-2\pi f\cdot t-\varphi_{0}\right) \tag{4.6}$$

where σ_{ν} is the harmonic wave direction. For the third harmonic and multiples we have $\sigma_{\nu}=0$ and for the others $\sigma_{\nu}=\pm1$. For example the fundamental wave $\nu=p$, the harmonic $\nu=7p$ and $\nu=13p$ rotate in the same direction. The harmonics $\nu=5p$ and $\nu=11p$ rotate in an opposite direction. Note that Equation (4.6) is only valid when the three-phase system is balanced.

4.2.2 Definition of the stator and rotor magneto-motive-forces

The stator winding when supplied with a balanced three-phase system of currents of frequency f_{s}, maximum value $\hat{I}_{\mathrm{s}}$ and initial phase shift $\varphi_{I_{\mathrm{s}}}$ creates a rotating mmf given by:

$$\Theta_{\mathrm{s}_{\mathrm{abc}}}(\alpha_{\mathrm{s}},t)=\frac{3}{2}\sum_{\nu=1}^{+\infty}\sigma_{\nu,\mathrm{s}}\Theta_{\nu,\mathrm{s}}\sin\left(\sigma_{\nu}\nu\cdot\alpha_{\mathrm{s}}+\sigma_{\nu,\mathrm{s}}\phi_{\nu,\mathrm{s}}-2\pi f_{\mathrm{s}}\cdot t-\varphi_{I_{\mathrm{s}}}\right) \tag{4.7}$$

where α_{s} is an angular position in the airgap in the stator reference frame. The rotor winding when supplied with a balanced three-phase system of currents of frequency f_{r}, maximum value $\hat{I}_{\mathrm{r}}$ and initial phase shift $\varphi_{I_{\mathrm{r}}}$ creates a rotating mmf given by:

$$\Theta_{\mathrm{r}_{\mathrm{abc}}}(\alpha_{\mathrm{r}},t)=\frac{3}{2}\sum_{\nu=1}^{+\infty}\sigma_{\nu,\mathrm{r}}\Theta_{\nu,\mathrm{r}}\sin\left(\sigma_{\nu}\nu\cdot\alpha_{\mathrm{r}}+\sigma_{\nu,\mathrm{r}}\varphi_{\nu,\mathrm{r}}-2\pi f_{\mathrm{r}}\cdot t-\varphi_{I_{\mathrm{r}}}\right) \tag{4.8}$$

where α_{r} is an angular position in the airgap in the rotor frame. As the rotor is rotating at the mechanical speed Ω_{m}, the rotor mmf can be expressed in the stator frame by using the following relation:

$$\alpha_{\mathrm{s}}=\alpha_{\mathrm{r}}+\Omega_{\mathrm{m}}t+\theta_{0} \tag{4.9}$$

where θ_0 is the initial mechanical angle between the magnetic fields created by the rotor and stator phases a. Finally the rotor mmf in the stator frame is given by:

$$\Theta_{r\phi_{abc}}(\alpha_{\mathrm{s}},t)=\frac{3}{2}\sum_{\nu=1}^{+\infty}\sigma_{\nu,\mathrm{r}}\Theta_{\nu,\mathrm{r}}\sin\left(\sigma_{\nu}\nu\cdot\alpha_{\mathrm{s}}+\sigma_{\nu,\mathrm{r}}\varphi_{\nu,\mathrm{r}}-2\pi f_{\nu,\mathrm{r}}\cdot t-\varphi_{I_{\mathrm{r}}}-\sigma_{\nu}\nu\cdot\theta_{0}\right) \tag{4.10}$$

where $f_{\nu,\mathrm{r}}=f_{\mathrm{r}}+\sigma_{\nu,\mathrm{r}}\nu\Omega_{\mathrm{m}}$ is the frequency of the currents induced by the rotor field in the stator winding. If the speed relation $f_{\mathrm{s}}=f_{\mathrm{r}}+f_{\mathrm{m}}$ ($f_{\mathrm{m}}=p\cdot\Omega_{m}/(2\pi)$) is verified and $f_{\mathrm{r}}=s\cdot f_{\mathrm{s}}$, the rotor frequency in the stator frame $f_{\mathrm{r},\nu}$ can be written as:

$$f_{\nu,\mathrm{r}}=f_{\mathrm{s}}\cdot(s+(1-s)\frac{\sigma_{\nu,\mathrm{r}}\nu}{p}) \tag{4.11}$$

One can see that the fundamental of the rotor field i.e $\sigma_{\nu,\mathrm{r}}\nu=+p$ induces stator voltages with a frequency equal to f_{s}. When the machine runs at the synchronous speed, i.e the slip s equals zero, rotor field harmonics induce voltages at the stator with a frequency equal to $(\nu/p)\cdot f_{\mathrm{s}}$.

Quantity	Value
Apparent power S (MVA)	290
Razed voltage U (KV)	18
Number of poles $2 \cdot p$ (-)	12
Number of stator parallel paths $N_{\mathrm{a,s}}$ (-)	4
Number of stator slots per pole/phase q_{s} (-)	8
Stator coil opening $\mathrm{Y}_{1,\mathrm{s}}$ (-)	20
Number of rotor parallel paths $N_{\mathrm{a,r}}$ (-)	2
Number of rotor slots per pole/phase q_{r} (-)	7
Rotor coil opening $\mathrm{Y}_{1,\mathrm{r}}$ (-)	18
Airgap length δ_{g} (mm)	14

Table 4.2: Machine characteristics rotor and stator mmf calculation

Out of the synchronous speed, the rotor fields harmonics induce voltages at the stator with a frequency depending on the slip as shown by Equation (4.11). Considering a constant airgap corrected by the Carter coefficient k_{c} and neglecting the magnetic drop in the stator and rotor core, the stator and rotor airgap magnetic flux densities $B_{\delta,\mathrm{s},0}$ and $B_{\delta,\mathrm{r},0}$ in the stator frame are given by:

$$\begin{aligned} B_{\delta,\mathrm{s},0}(\alpha_{\mathrm{s}},t) &= \Lambda_0 \cdot \Theta_{\mathrm{s}_{\mathrm{abc}}}(\alpha_{\mathrm{s}},t) \\ B_{\delta,\mathrm{r},0}(\alpha_{\mathrm{s}},t) &= \Lambda_0 \cdot \Theta_{\mathrm{r}_{\mathrm{abc}}}(\alpha_{\mathrm{s}},t) \end{aligned} \tag{4.12}$$

where Λ_0 is the airgap permeance given by:

$$\Lambda_0 = \frac{\mu_0}{k_{\mathrm{c}} \cdot \delta_{\mathrm{g}}} \tag{4.13}$$

The total airgap flux density $B_{\delta,0}$, with a constant airgap corrected by the Carter coefficient, can be found by superimposing the stator and rotor magnetic flux density such as:

$$B_{\delta,0}(\alpha_s,t) = B_{\delta,\mathrm{s},0}(\alpha_{\mathrm{s}},t) + B_{\delta,\mathrm{r},0}(\alpha_{\mathrm{s}},t) \tag{4.14}$$

The method developed in Chapter 3 is used to determine the values of the stator and rotor current maximum values and initial phase shift for any operation point. For a given load point, the stator and rotor winding are supplied with the following currents:

$$\begin{aligned} \hat{I}_{\mathrm{s}} &= 8978 \text{ A} \quad & \varphi_{I_{\mathrm{s}}} &= 155.6^\circ \\ \hat{I}_{\mathrm{r}} &= 6099 \text{ A} \quad & \varphi_{I_{\mathrm{r}}} &= -38.34^\circ \\ \theta_0 &= -0.357^\circ \end{aligned} \tag{4.15}$$

Table 4.2 gives the parameters of the machine design used for the calculation. Figure 4.5 shows at one instant along two pole pitches the evolution of the stator and rotor flux density as well as the resulting flux density when considering a constant airgap.

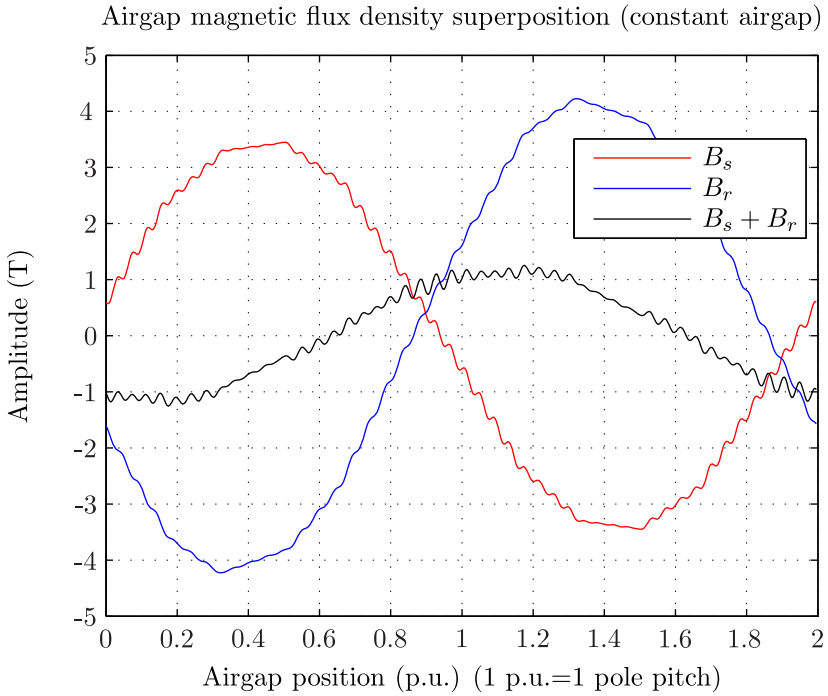

Figure 4.5: Stator and rotor airgap flux density superimposition for a constant airgap

4.3 Calculation of the airgap permeance function

4.3.1 Definition of the airgap permeance

The airgap permeance is inversely proportional to the length of the airgap:

$$\Lambda = \frac{\mu_0}{\delta_{\mathrm{g}}} \tag{4.16}$$

Last section considered a constant airgap corrected by the Carter coefficient. However in a DFIM the air gap is not constant but modulated by the rotor and the stator teeth which leads to additional airgap harmonics. It is important to consider the effect of tooth ripples on the performance of the machine which can lead to parasitic forces [TLU12].

4.3.2 The slot ripple harmonics

In a hydro-motor/generator the conductors are placed in slots. For manufacturing reasons i.e. to introduce the bar in the slot, these slots are opened. The bars are mechanically maintained inside the slot by using a non-magnetic wedge[2]. The opening of the slots creates local variations of the airgap permeance. The general expression of the airgap permeance $\Lambda^{\mathcal{B}r}$ of an induction

[2]In Chapter 5 we study the impact of magnetic-wedges

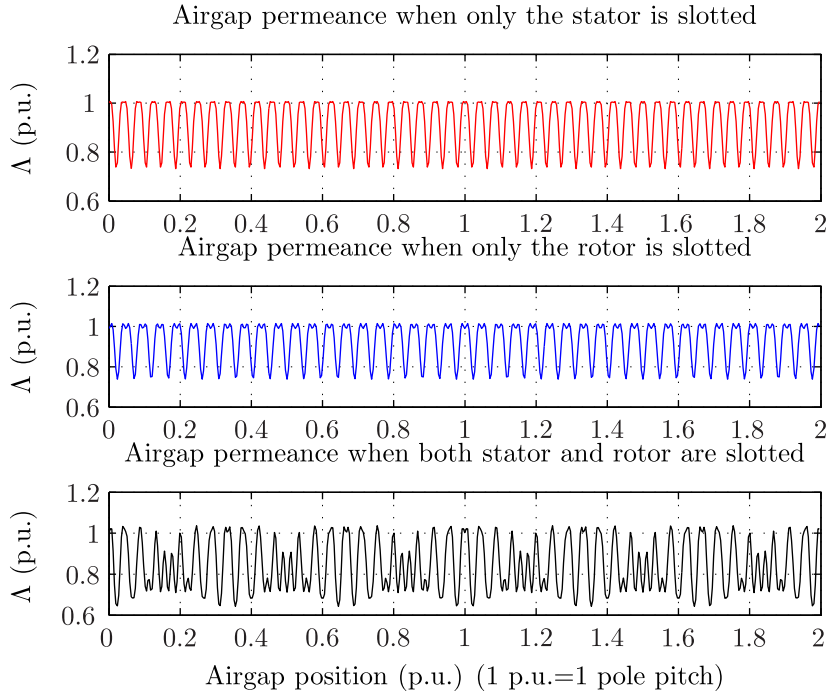

Figure 4.6: Airgap permeance variation at one instant along two pole-pitches

machine with a doubly slotted airgap is the following [Bru97]:

$$\begin{aligned}\Lambda^{\mathcal{B}r}(\alpha_\mathrm{s},t) = \Lambda_0 &+ \sum_{k_\mathrm{s}=1}^{\infty} \Lambda_{\mathrm{s},k_\mathrm{s}} \cos\left(k_\mathrm{s} N_{\mathrm{z,s}} \alpha_\mathrm{s}\right) \\ &+ \sum_{k_\mathrm{r}=1}^{\infty} \Lambda_{\mathrm{r},k_\mathrm{r}} \cos\left(k_\mathrm{r} N_{\mathrm{z,r}} \alpha_\mathrm{s} - k_\mathrm{r} N_{\mathrm{z,r}} \Omega_\mathrm{m} t - k_\mathrm{r} N_{\mathrm{z,r}} \theta_0\right) \\ &+ \sum_{k_\mathrm{s}=1}^{\infty} \sum_{k_\mathrm{r}=1}^{\infty} \Lambda_{\mathrm{s,r},k_\mathrm{s},k_\mathrm{r}} \cdot (\cos((k_\mathrm{s} N_{\mathrm{z,s}} - k_\mathrm{r} N_{\mathrm{z,r}})\alpha_\mathrm{s} + k_\mathrm{r} N_{\mathrm{z,r}} \Omega_\mathrm{m} t + k_\mathrm{r} N_{\mathrm{z,r}} \theta_0) \\ &\qquad + \cos((k_\mathrm{s} N_{\mathrm{z,s}} + k_\mathrm{r} N_{\mathrm{z,r}})\alpha_\mathrm{s} - k_\mathrm{r} N_{\mathrm{z,r}} \Omega_\mathrm{m} t - k_\mathrm{r} N_{\mathrm{z,r}} \theta_0))\end{aligned} \tag{4.17}$$

One can notice the presence of four terms. The first term is constant and is inversely proportional to the minimum airgap length. The second term is due to the presence of the stator slots and based on the number of stator slots. The third term is due to the rotor slots and based on the number of rotor slots. The fourth term is created by the interaction of the stator slots with the rotor slots. The different coefficients $\Lambda_{\mathrm{s},k_\mathrm{s}}$, $\Lambda_{\mathrm{r},k_\mathrm{r}}$ and $\Lambda_{\mathrm{s,r},k_\mathrm{s},k_\mathrm{r}}$ depend on the airgap length and on the dimensions of the stator and rotor slots. Figure 4.6 shows the variation of $\Lambda/\Lambda_\mathrm{c}$ considering a slotted airgap on stator side, on rotor side or on both sides. $\Lambda_\mathrm{c} = \mu_0/\delta_\mathrm{g}$ is the constant permeance.

Kron [Kro31] and Brudny [Bru97] propose analytical expressions for each terms which give relative good agreement with FE computation. In the next part we propose a fast numerical

method to compute accurately the airgap permeance of a DFIM. The developed method makes it possible to express the airgap flux density at different radial positions in the airgap which is not the case of the existing method.

4.3.3 Numerical computation of the permeance

The computation of the double-slotted airgap permeance is done by using a BE formulation. The BEM is a mathematical tool based on the solving in a domain of linear partial differential equations formulated as integral equations. In opposite to FE where the full domain has to be meshed, BEM requires only the discretization of the borders i.e the lines for a 2D domain and the faces for a 3D domain. The main advantage of the method is the speed of the resolution and the lower complexity of the mesh. The main drawback is that the obtained matrices are full in opposite to the sparse matrices of the FE. Consequently the time of computation increases sharply when the size of the problem increases. In order to counter this issue researchers have been working on fast multi-pole algorithms [Liu09]. This study only considers a standard algorithm although the implementation of the fast-multi-pole algorithm might accelerate the resolution. The BEM code used in this thesis is based on [BD92].

In magneto-static when there is no source of current one can write:

$$\vec{rot}\vec{H} = \vec{0} \tag{4.18}$$

Equation (4.18) shows that $\vec{H}$ derives from a potential which is here the scalar magnetic potential ϕ given as:

$$\vec{H} = -\vec{grad}\phi \tag{4.19}$$

One can express the relation between the flux density B and the magnetic field H in a domain with a magnetic permeability equal to μ.

$$\vec{B} = \mu \cdot \vec{H} \tag{4.20}$$

Furthermore the local Maxwell equation gives:

$$div\vec{B} = 0 \tag{4.21}$$

Finally by combining Equations (4.19), (4.20) and (4.21) we obtain:

$$div(\mu\vec{grad}\phi) = 0 \tag{4.22}$$

In the studied case the domain, which is the airgap, is linear and homogeneous. Consequently Equation (4.22) can be reformulated as the Poisson equation with no source i.e. the Laplace Equation.

$$\Delta\phi = 0 \tag{4.23}$$

The BEM is used to solve Equation (4.23). The domain is limited by the border Γ along which the following boundary conditions can be applied:

- Constant potential ϕ
- Normal derivation of the potential $\mathrm{d}\phi/\mathrm{d}n$

The BEM consists of a system of linear equations defined in terms of integrals over the border Γ. Given the type of boundary conditions the unknown is either the magnetic potential ϕ or the normal derivation of the potential $\mathrm{d}\phi/\mathrm{d}n$. When all the unknowns of the border are found, the potential and its derivative can be calculated for any point inside the domain.

Figure (4.7) shows as example the BE model of a slot and an aigrap. The stator and rotor magnetic material permeability is assumed infinite, so that the flux lines enter normally into the surfaces of the stator (green border) and the rotor (blue border). This boundary condition is satisfied by applying a constant magnetic voltage on the stator and rotor borders. On the contrary the magnetic field is assumed tangential to the edge. This is done by setting the component $\mathrm{d}\phi/\mathrm{d}n$ equal to zero. The BEM makes it possible to find the value of the magnetic potential ϕ and its derivative in any point of the domain limited by the slot and in particular on a path at the middle of the airgap (red line). The normal H_{n} and tangential H_{t} components of the magnetic field on the path correspond here to the H_{y} and H_{x} components of the magnetic field and are obtained by using directly Equation (4.19). In a Cartesian coordinate system one can write:

$$\begin{aligned} H_{\mathrm{x}} &= -\partial\phi/\partial x \\ H_{\mathrm{y}} &= -\partial\phi/\partial y \end{aligned} \tag{4.24}$$

Figure (4.8) shows the corresponding results. One can observe the drop of the normal magnetic field as well as the rotation of the magnetic field in front of the slot.

Figure (4.9) shows a typical DFIM airgap geometry along one pole pitch as well as a calculation path (red line) at the middle of the airgap. The same principles are applied here for setting the boundary conditions. Here the values of the H_{x} and H_{y} magnetic field components cannot be directly used to calculate the radial and tangential components H_{n} and H_{t} on the path. We use the following relations:

$$\begin{aligned} H_{\mathrm{n}}(\theta) &= H_{\mathrm{x}}(\theta)\cos(\theta) + H_{\mathrm{y}}(\theta)\sin(\theta) \\ H_{\mathrm{t}}(\theta) &= H_{\mathrm{x}}(\theta)\sin(\theta) - H_{\mathrm{y}}(\theta)\cos(\theta) \end{aligned} \tag{4.25}$$

where θ is the angular position of a point in the computation path. Figure (4.10) shows the corresponding results. As we applied a potential difference equal to one, the corresponding airgap permeance is simply given by:

$$\Lambda = \frac{\mu_0}{\delta_{\mathrm{g}}} H_{\mathrm{n}} \tag{4.26}$$

The airgap geometry is changing as the rotor rotates, so that one has to compute the corresponding permeance for each position; this could lead to a heavy computation. In order to reduce the computation time, the geometry is simplified and only a few slots are modeled. Figure 4.11 shows the corresponding simplified model. The boundary conditions are the following:

- a different constant magnetic potential is applied on the stator and the rotor borders.
- the derivative of the flux is set to zero on the edges of the airgap. This forces a tangential field.

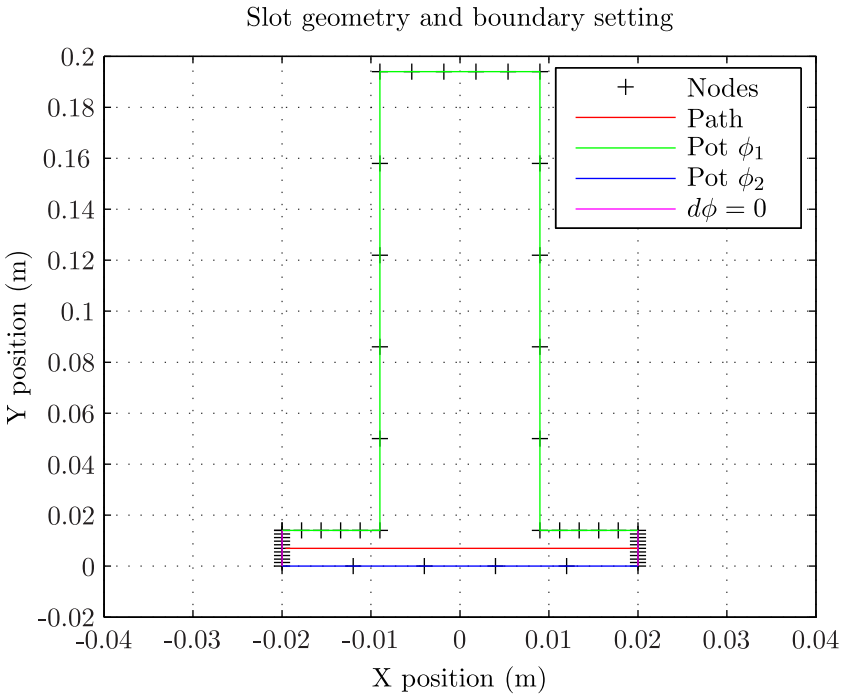

Figure 4.7: Single slot BEM model

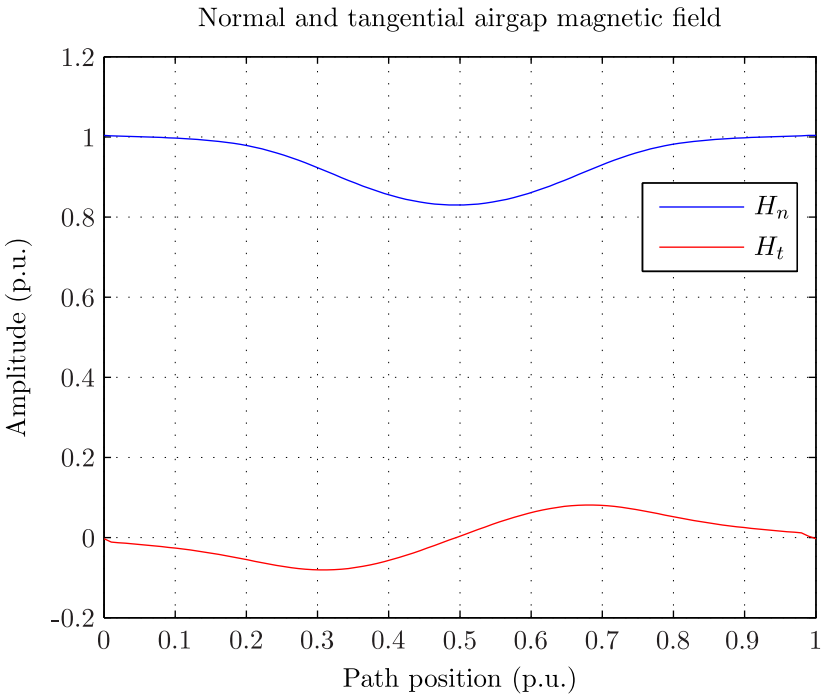

Figure 4.8: Single slot BEM results

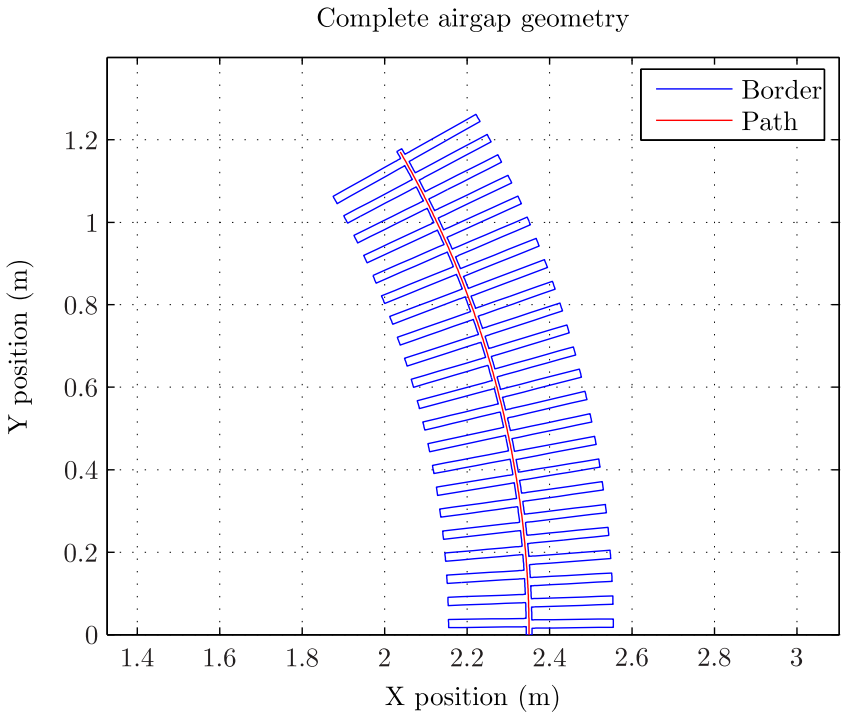

Figure 4.9: Double slotted airgap BEM model

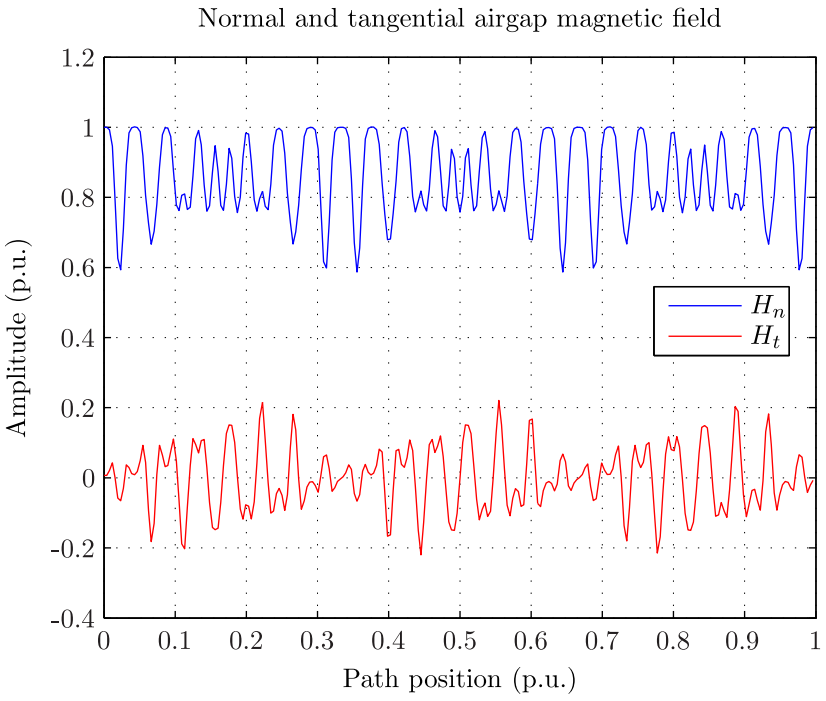

Figure 4.10: Double slotted airgap BEM results

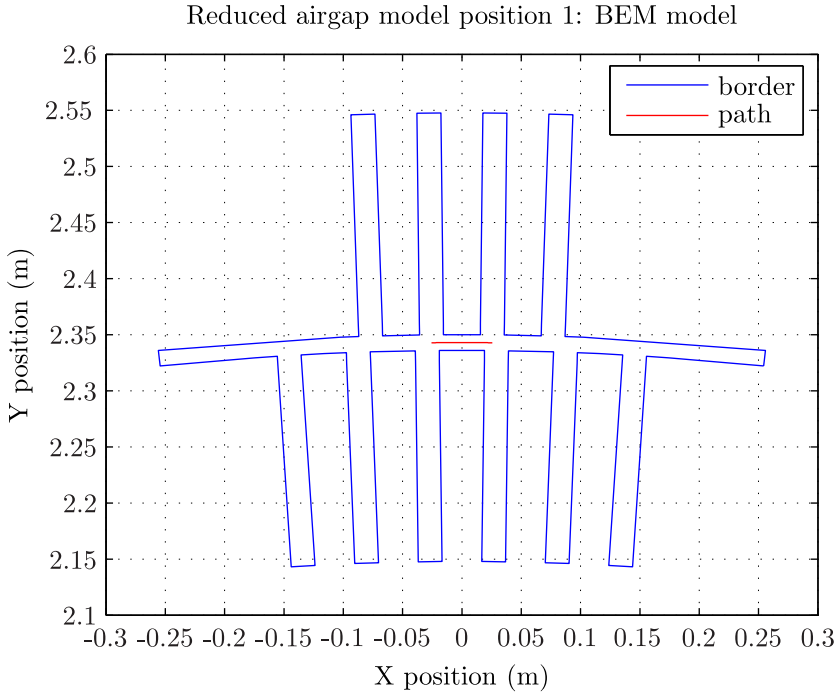

Figure 4.11: Permeance calculation model-position 1

Considering the simplified model the last boundary condition might be incorrect, since the complete geometry is not modeled. However the computation of the field is carried out on a reduced path far from the edges, as described in Figure 4.11, so that the error remains negligible. For different positions of the reference rotor tooth regarding the stator reference tooth, the airgap permeance is calculated on the path. For example Figure 4.11 shows the BE model of the reduced airgap when one stator tooth and one rotor tooth are in line. Figure 4.12 shows the corresponding variation of the normal magnetic field measured on the path. The field and consequently the permeance is maximal in front of the teeth. Figure 4.13 shows the BE model of the reduced airgap when one stator tooth and one rotor slot are in line and Figure 4.14 shows the corresponding variation of the normal magnetic field measured on the path. The field and consequently the permeance drop down in front of the slot.

Considering the full geometry and the position of the rotor relative to the stator, the complete airgap permeance is obtained by connecting all the permeances from the single reduced model calculations. Figure 4.15 shows the result of the reassembling for a given position of the rotor. Different colors highlight the different spatial segments of permeance. Figure 4.16 compares the results obtained from the assembled model to the one using the full model. One can see that the results are satisfying.

By applying this method one can compute the airgap permeance spatial evolution under one pole pair and its variation when changing the rotor position. Finally the airgap permeance Λ can be expressed as a Fourier series whose terms are obtained by carrying out a 2D Fourier

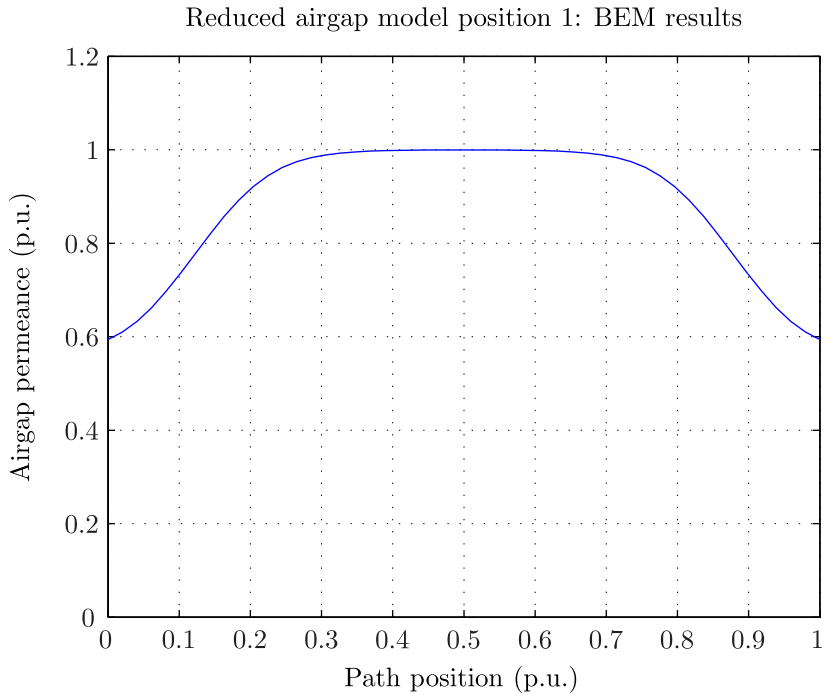

Figure 4.12: Permeance calculation results-position 1

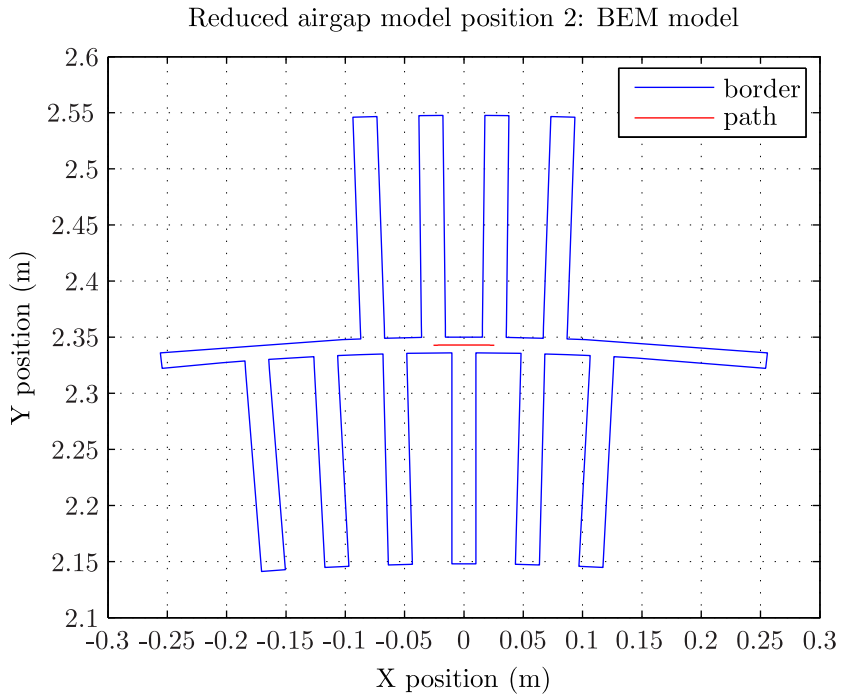

Figure 4.13: Permeance calculation model-position 2

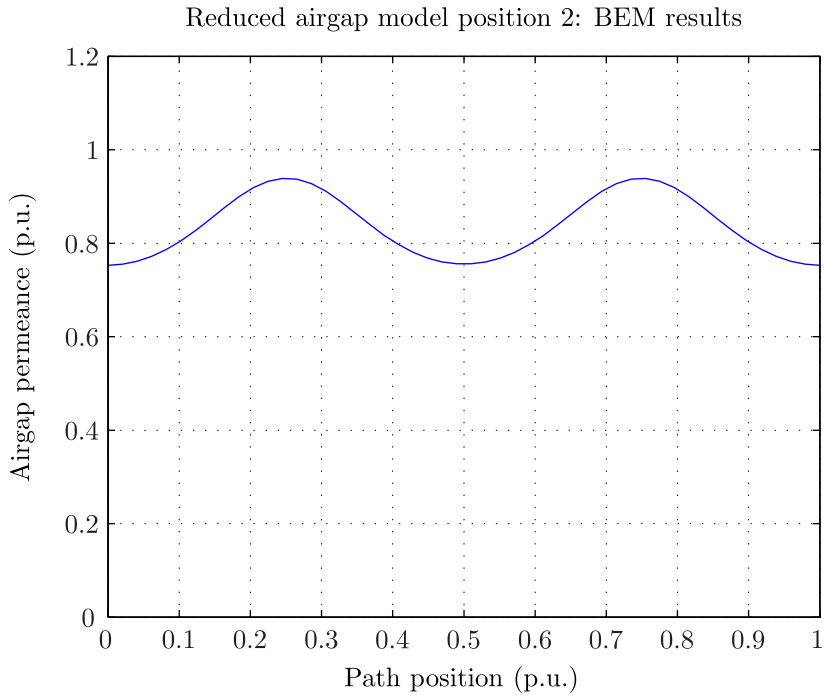

Figure 4.14: Permeance calculation results-position 2

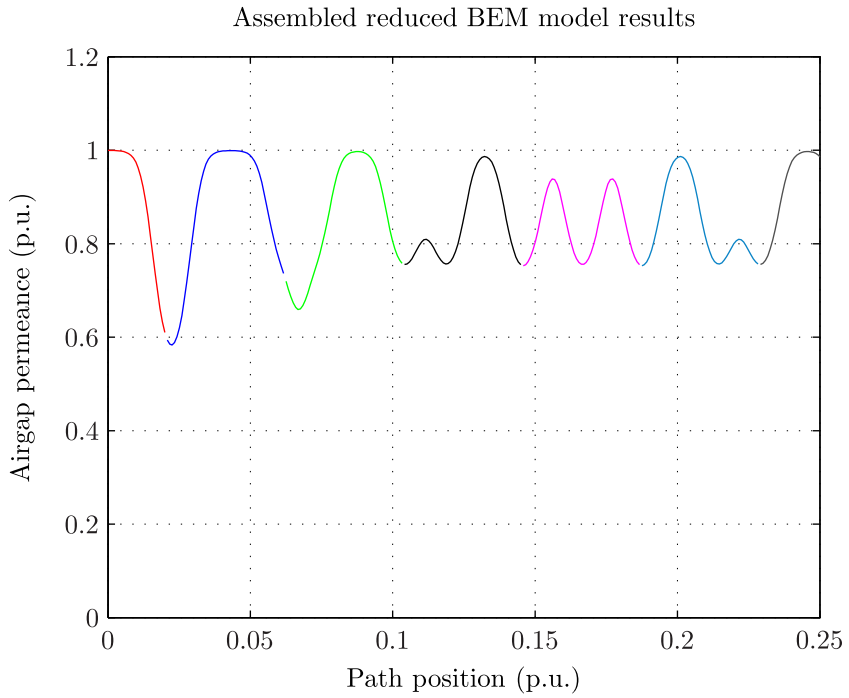

Figure 4.15: Multi-assembled reduced permeances

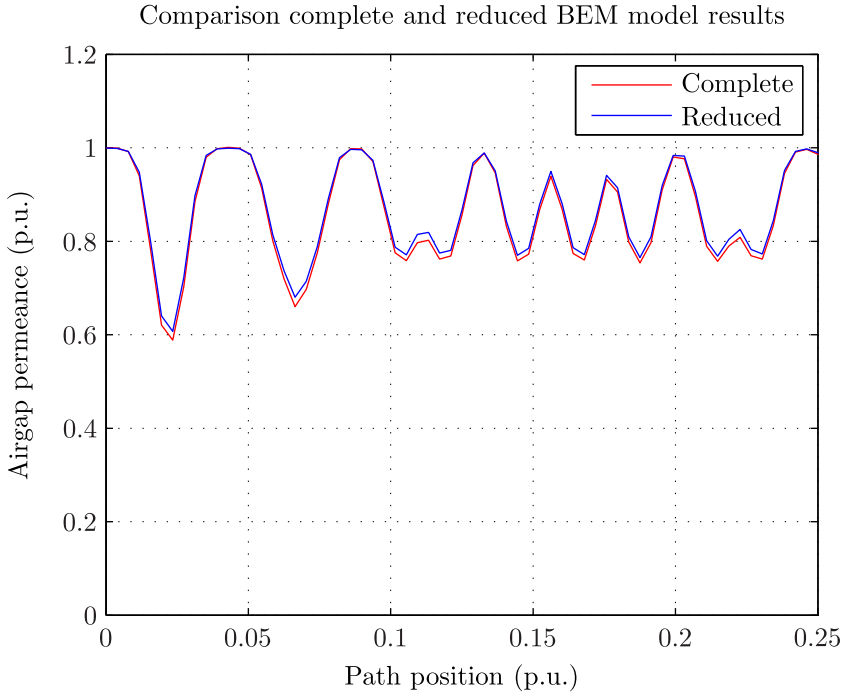

Figure 4.16: Validation between the reduced and the complete models

analysis on its airgap spatial and rotor position variations

$$\Lambda\left(\alpha_{\mathrm{s}}, \theta_{r}\right)=\sum_{\nu=1}^{\infty} \Lambda_{\nu} \cos\left(P_{\nu} \alpha_{\mathrm{s}}+F_{\nu}^{\prime} \theta_{\mathrm{r}}+C_{\nu}\right) \tag{4.27}$$

where $\theta_{\mathrm{r}}=\Omega_{\mathrm{m}} \cdot t$ is the rotor position which can be expressed as a function of the time t and the mechanical speed Ω_{m}. Λ_{ν} is the amplitude of the ν^{th} permeance harmonic expressed in p.u.. P_{ν} is the spatial order of the ν^{th} harmonic while $F_{\nu}^{\prime}$ is the frequency order of the ν^{th} harmonic. C_{ν} is the phase shift of the ν^{th} harmonic. Equation (4.27) can be rewritten as a function of t and the mechanical speed Ω_{m}. Furthermore considering $\Omega_{\mathrm{m}}=2\pi \cdot(1-s) \cdot f_{\mathrm{s}} / p$ we obtain:

$$\Lambda\left(\alpha_{\mathrm{s}}, t\right)=\sum_{\nu=1}^{\infty} \Lambda_{\nu} \cos\left(P_{\nu} \alpha_{\mathrm{s}}+2 \pi F_{\nu} \cdot t+C_{\nu}\right) \tag{4.28}$$

where $F_{\nu}=\left(F_{\nu}^{\prime} / p\right)(1-s) f_{\mathrm{s}}$. The method is applied on a machine whose characteristics are given in Table 4.3.

Table 4.4 gives the value of the main obtained components $\Lambda_{\nu} / \Lambda_{\mathrm{c}}$, considering $s=0$. The fist component $\nu=0$ corresponds to the average permeance. The components $\nu=1$ to $\nu=3$ correspond to the first, second and third stator slot permeance harmonics while the components $\nu=4$ to $\nu=6$ correspond to the first, second and third rotor slot permeance harmonics. The components $\nu=7$ and $\nu=8$ correspond to interaction between stator and rotor slots permeance. The computation was done for three different positions of the path in the airgap i.e close to the rotor slots $\Lambda^{\mathcal{R}}$, at the middle of the airgap Λ and close to the stator slots $\Lambda^{\mathcal{S}}$. It appears that

Quantity	Value
Number of pole pairs p (-)	6
Airgap length δ_{g} (mm)	14
Number of stator slots per pole/phase q_{s} (-)	8
Number of rotot slots per pole/phase q_{r} (-)	7

Table 4.3: Machine characteristics for airgap permeance calculation

ν	P_ν/p	F_ν/f_{s}	$\Lambda_\nu^{\mathcal{R}}/\Lambda_{\mathrm{c}}$	$\Lambda_\nu/\Lambda_{\mathrm{c}}$	$\Lambda_\nu^{\mathcal{S}}/\Lambda_{\mathrm{c}}$	$\Lambda_\nu^{\mathcal{B}r}/\Lambda_{\mathrm{c}}$
0	0	0	0.859	0.857	0.855	0.845
1	48	0	0.075	0.110	0.207	0.117
2	96	0	0.014	0.043	0.183	0.038
3	144	0	0.001	0.004	0.073	0.022
4	42	−42	0.170	0.100	0.073	0.107
5	84	−84	0.180	0.051	0.020	0.049
6	126	−126	0.087	0.013	0.002	0.0048
7	6	42	0.010	0.010	0.010	0.027
8	90	−42	0.011	0.005	0.012	0.027

Table 4.4: Airgap permeance calculation result

some terms almost disappear. Indeed when computing the permeance close to stator the effect of the rotor is decreased and vice versa. The fundamental term stays almost constant which is normal since the quantity of flux passing from the rotor to the stator remains the same. The small difference may be explained by a not enough fine discretization. We also compare the results to the ones obtained by applying the formula given by Brudny [Bru97] $\Lambda^{\mathcal{B}r}$. One can see a good agreement when considering the permeance calculated at the middle of the airgap.

Such computation makes also possible to recompute the equivalent Carter factor $k_{\mathrm{c}} = 1/(\Lambda_0/\Lambda_{\mathrm{c}})$ where Λ_0 is the aperiodic component of the permeance. As seen in Chapter 2, the Carter factor for a double-slotted airgap is given by $k_{\mathrm{c}} \approx k_{\mathrm{c,s}} \cdot k_{\mathrm{c,r}}$ where $k_{\mathrm{c,s}}$ is the Carter factor of an airgap with stator slots only and $k_{\mathrm{c,r}}$ only with rotor slots. Apply to the last example $k_{\mathrm{c,s}} = 1.097$ and $k_{\mathrm{c,r}} = 1.083$ which gives a Carter factor equal to $k_{\mathrm{c}} \approx 1.18$. From the BEM we have $k_{\mathrm{c}} \approx 1.17$ which is very close.

4.4 Computation of the airgap flux density

4.4.1 Definition of the airgap flux density

The mmf and the airgap permeance allow to compute the final airgap magnetic flux density by superposing the stator and rotor fields. The total magnetic flux density expressed in the stator

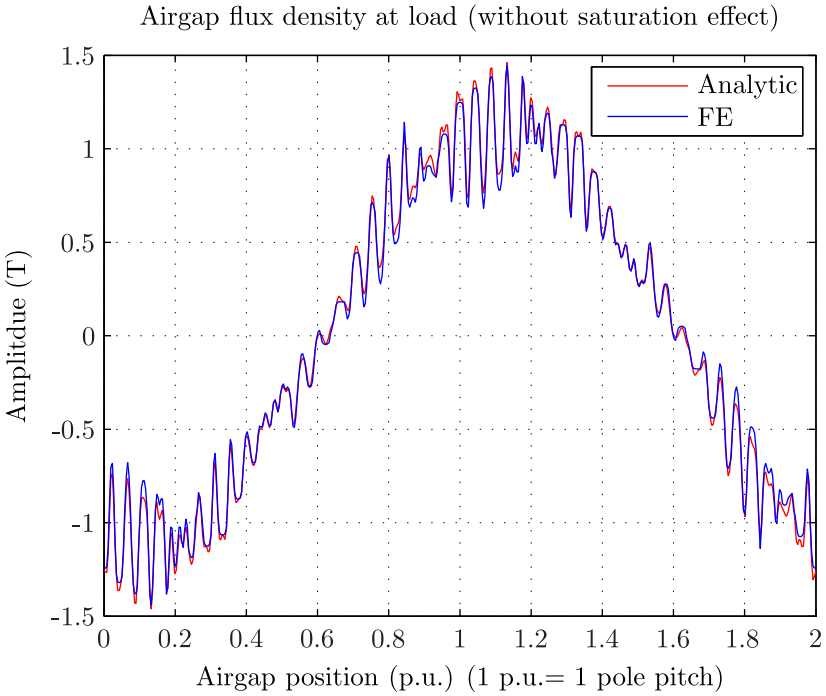

Figure 4.17: Airgap flux density at load without saturation

frame is given by:

$$B_{\delta}\left(\alpha_{s},t\right)=\left(B_{\delta,s,0}\left(\alpha_{s},t\right)+B_{\delta,r,0}\left(\alpha_{s},t\right)\right)\cdot\frac{\Lambda\left(\alpha_{s},t\right)}{\Lambda_{0}} \tag{4.29}$$

Λ is the airgap permeance defined previously. Figure 4.17 compares the obtained results with the ones extracted from a FE computation. One can observe the presence of large ripples due to the presence of stator and rotor slots. Figure 4.18 shows the corresponding harmonic content. One can see a good agreement between both calculations. Note that the fundamental flux density is for this case very high, about 1.16 T, this is because the magnetic saturation was not considered. It is the object of the next part.

4.4.2 Impact of magnetic saturation

Chapter 2 highlighted the impact of the magnetic saturation on the airgap flux density harmonics. The more the magnetic circuit is saturated, the more the airgap flux density is flattened. Figure 4.19 shows the variation of K_{sat} which is the ratio between the airgap flux density at no-load computed considering the impact of magnetic saturation B_{δ}^{sat} and without considering the saturation B_{δ}^{lin}.

$$K_{\text{sat}}\left(\alpha_{s}\right)=\frac{B_{\delta}^{\text{sat}}\left(\alpha_{s}\right)}{B_{\delta}^{\text{lin}}\left(\alpha_{s}\right)} \tag{4.30}$$

The computation is done for five magnetic states $1/4{\cdot}I_{\mu,0}\cdots1/2{\cdot}I_{\mu,0}\cdots3/4{\cdot}I_{\mu,0}\cdots I_{\mu,0}\cdots5/4{\cdot}I_{\mu,0}$ where $I_{\mu,0}$ is the magnetizing current at rated no-load operation. One can observe that magnetic

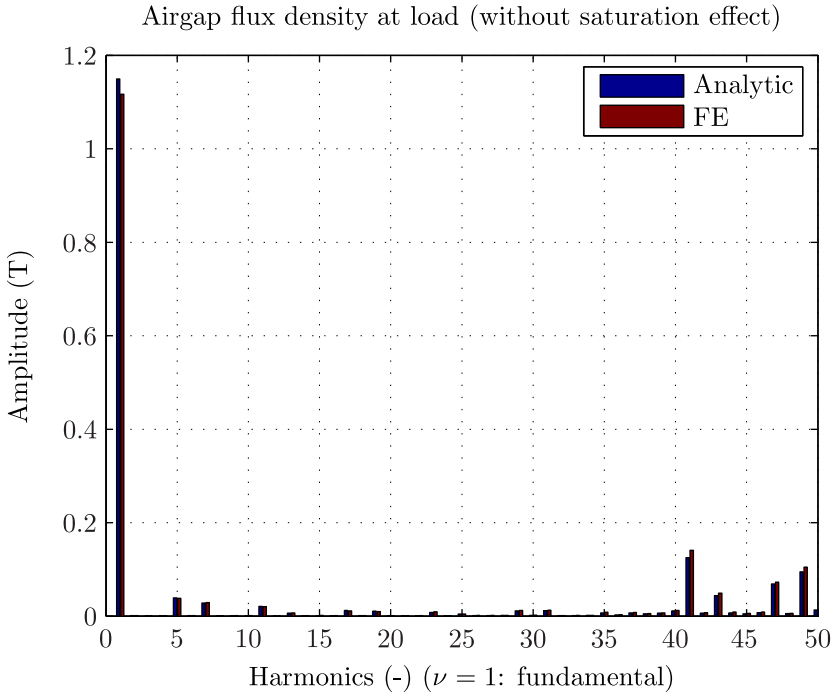

Figure 4.18: Airgap flux density spectrum at load without saturation

saturation leads to a modification of the function K_{sat}. A Fourier analysis of K_{sat} over two pole pitches shows mainly the presence of a constant component and a second and fourth harmonic. Figure 4.20 shows the evolution of the amplitudes of these three components as functions of the saturation factor K_s.

The effect of saturation, represented by K_{sat}, can be seen as a modulation of the airgap permeance moving at the same speed as the fundamental field. Finally the function K_{sat} can be approximated by the sum of a constant and two rotating components.

$$K_{\text{sat}}\left(\alpha_{\text{s}}, t\right) \approx K_0 + K_1 \cos\left(2p \cdot \alpha_{\text{s}} - 2 \cdot 2\pi f_{\text{s}} \cdot t\right) + K_2 \cos\left(4p \cdot \alpha_{\text{s}} - 4 \cdot 2\pi f_{\text{s}} \cdot t\right) \tag{4.31}$$

When considering the effect of saturation, Equation (4.29) can be rewritten as:

$$B_\delta\left(\alpha_{\text{s}}, t\right) = \left(B_{\delta,\text{s},0}\left(\alpha_{\text{s}}, t\right) + B_{\delta,\text{r},0}\left(\alpha_s, t\right)\right) \cdot \frac{\Lambda(\alpha_{\text{s}}, t)}{\Lambda_0} \cdot K_{\text{sat}}\left(\alpha_{\text{s}}, t\right) \tag{4.32}$$

The main difficulty consists in calculating the value of the parameters K_0, K_1 and K_2. The magnetic circuit model developed in Chapter 2 makes it possible to express the ratio $\text{C}_1 = \hat{B}_{\delta,\text{f}}/\hat{B}_\delta$ as well as $\text{C}_\text{f} = \hat{B}_{\delta,\text{f}}/\hat{B}^{\text{lin}}_{\delta,\text{f}}$, where $\hat{B}^{\text{lin}}_{\delta,\text{f}}$ is the amplitude of the fundamental flux density when the saturation is not considered. By only considering the fundamental component of the stator and rotor mmf and by neglecting the slots permeance terms and the term K_2 we can write:

$$B_\delta\left(\alpha_{\text{s}}, t\right) \approx \hat{B}^{\text{lin}}_{\delta,\text{f}} \cos\left(p \cdot \alpha_s - 2\pi f_{\text{s}} \cdot t\right) \cdot \left(K_0 + K_1 \cos\left(2p \cdot \alpha_{\text{s}} - 2 \cdot 2\pi f_{\text{s}} \cdot t\right)\right) \tag{4.33}$$

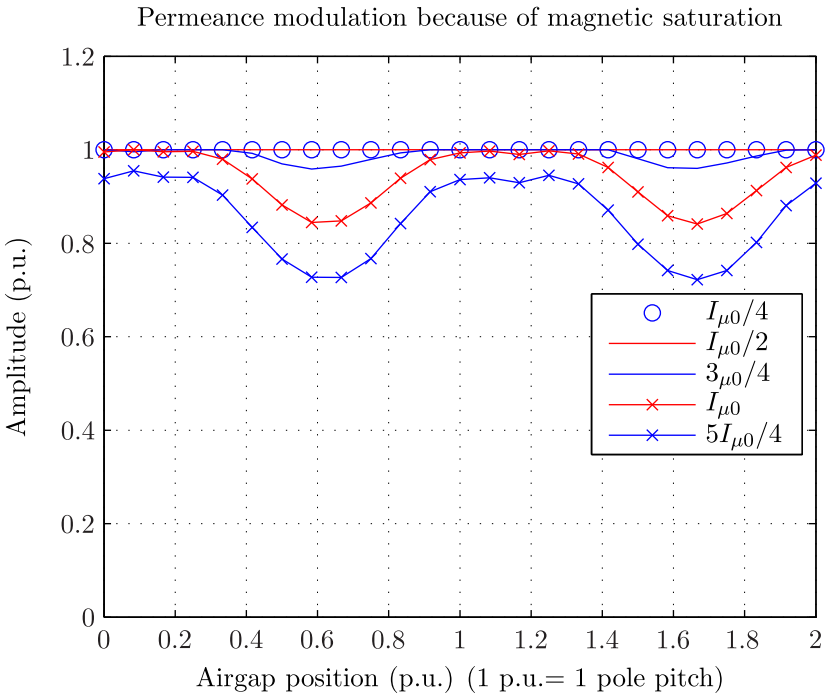

Figure 4.19: Saturated permeance

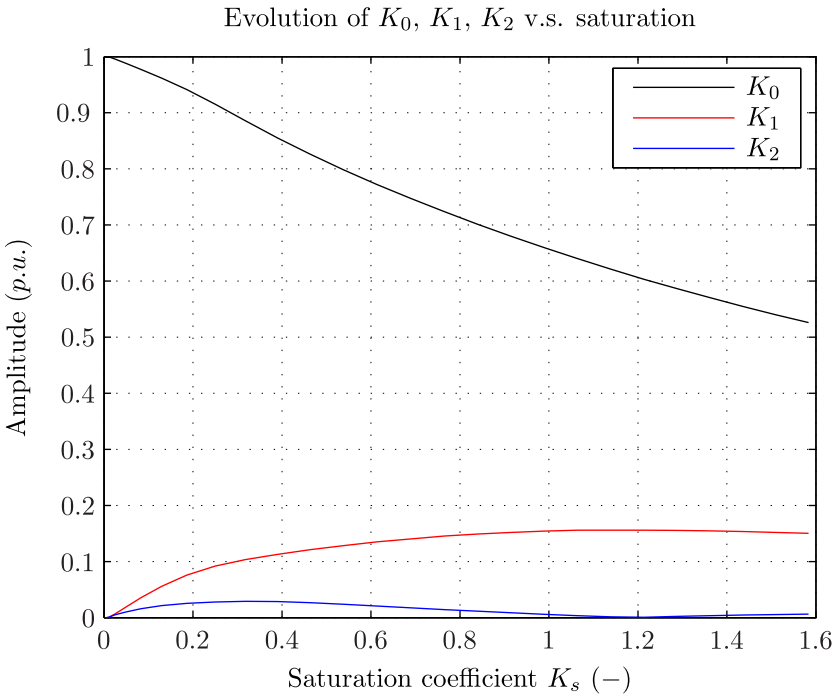

Figure 4.20: Saturated permeance main coefficients

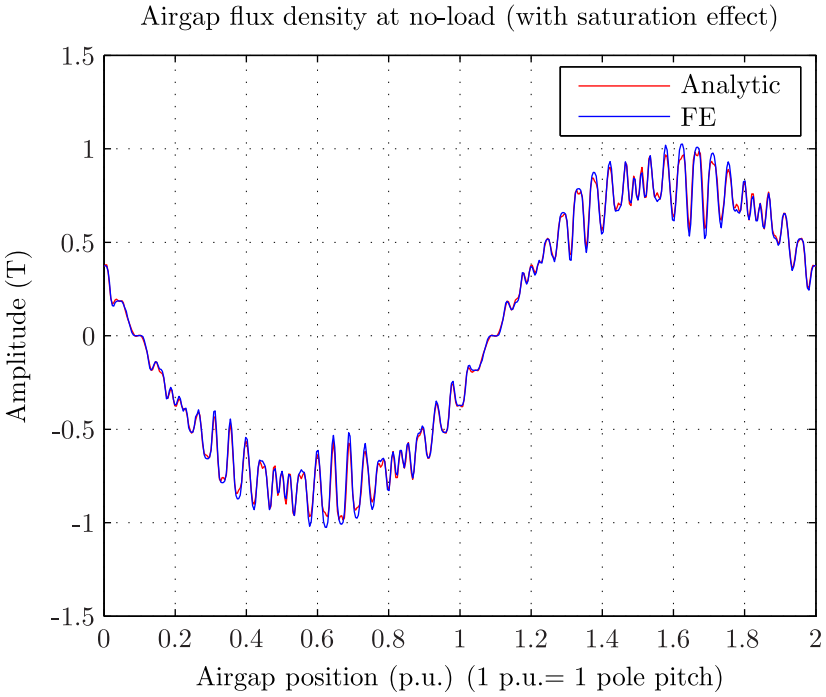

Figure 4.21: Airgap flux density at no-load with saturation

After analytical developments, we obtain:

$$B_\delta\left(\alpha_s, t\right) \approx \hat{B}^{\text{lin}}_{\delta,\text{f}}\left(K_0 + K_1/2\right)\cos\left(p\cdot\alpha_s - 2\pi f_s\cdot t\right) + \hat{B}^{\text{lin}}_{\delta,\text{f}}(K_1/2)\cos\left(3p\cdot\alpha_s - 3\cdot 2\pi f_s\cdot t\right) \tag{4.34}$$

One can see the presence of a third harmonic component. Finally the new fundamental value and the maximal value of $B_\delta(\alpha_s, t)$ are: $\hat{B}_{\delta,\text{f}} = \hat{B}^{\text{lin}}_{\delta,\text{f}}\cdot(K_0 + K_1/2)$ and $\hat{B}_\delta = \hat{B}^{\text{lin}}_{\delta,\text{f}}\cdot(K_0 + K_1)$. By using the definition of C_1 and C_f we finally obtain:

$$K_0 = \text{C}_\text{f}\left(2 - \frac{1}{\text{C}_1}\right) \tag{4.35}$$

$$K_1 = 2\text{C}_\text{f}\left(\frac{1}{\text{C}_1} - 1\right) \tag{4.36}$$

Given Figure 4.20 the term K_2 can be approximated as $K_2 \approx K_1/4$ in the operational saturation range i.e. $K_s = 0.2\cdots 0.4$. Finally one can compute the coefficients K_0, K_1 and K_2 as a function of the magnetizing current by using the magnetic model developed in Chapter 2.

Figures 4.21 and 4.23 show the variation of the airgap flux density under no-load and load operation using this simplified approach and a FE simulation. The corresponding harmonic content is obtained by carrying out a Fourier analysis as shown in Figures 4.22 and 4.24. One can observe a good agreement between both methods. When comparing Figure 4.24 and Figure 4.18 one can see the emergence of the triple harmonics and the reduction of the fundamental component.

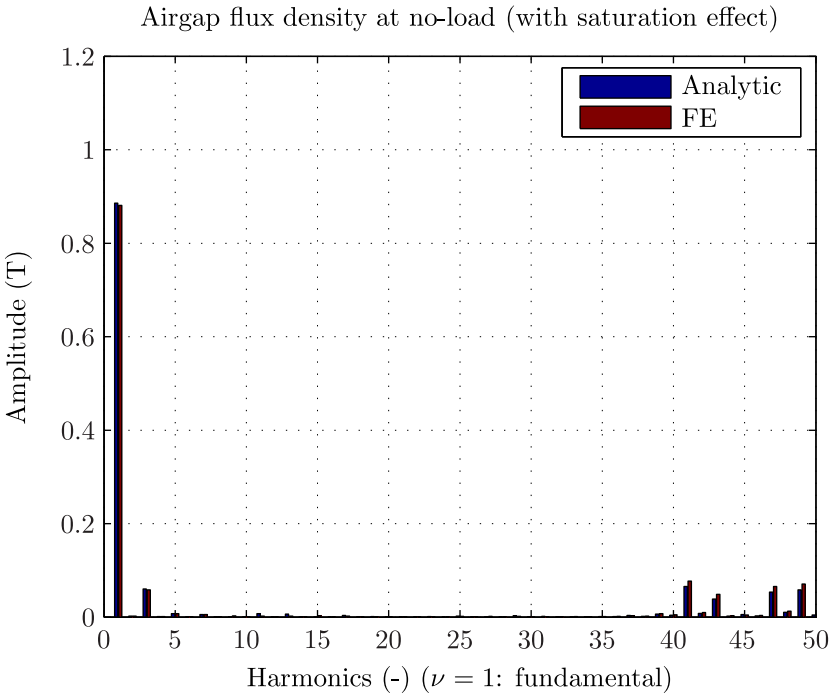

Figure 4.22: Airgap flux density spectrum at no-load with saturation

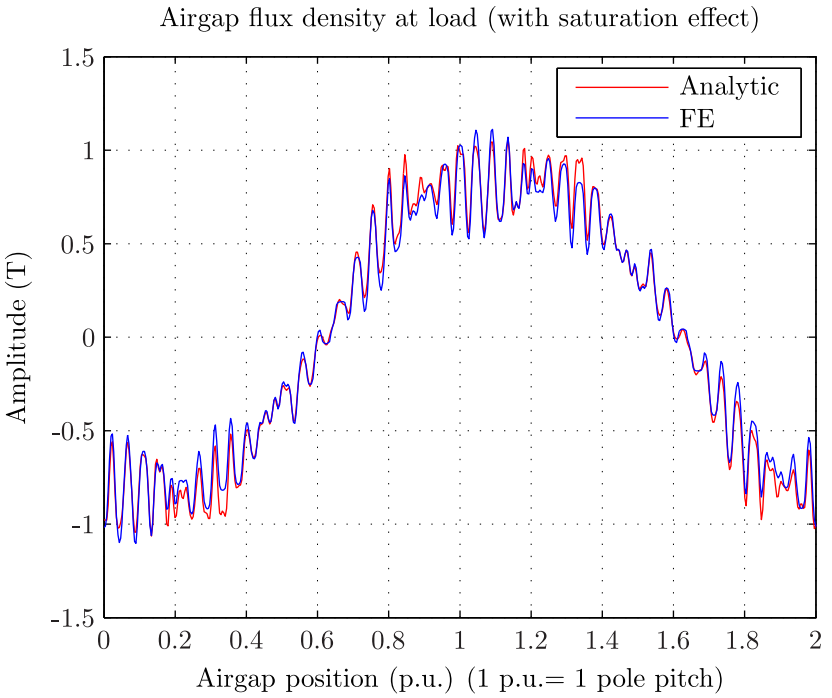

Figure 4.23: Airgap flux density at load with saturation

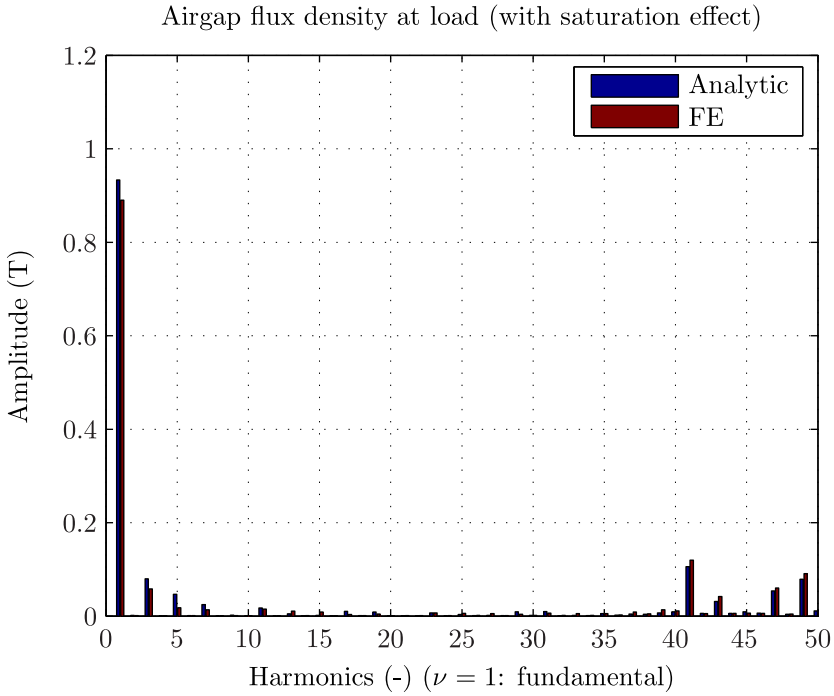

Figure 4.24: Airgap flux density spectrum at load with saturation

In the following we rewrite Equation (4.32) as:

$$B_{\delta}\left(\alpha_{\mathrm{s}}, t\right) = \sum_{\nu=1}^{\infty} \hat{B}_{\delta,\nu} \cos\left(P_{\nu}\alpha_{\mathrm{s}} + 2\pi F_{\nu} t + C_{\nu}\right) \tag{4.37}$$

where $\hat{B}_{\delta,\nu}$ is the amplitude of the ν^{th} airgap flux density harmonic, P_{ν} is the spatial order, F_{ν} is the frequency order and C_{ν} is the phase shift.

4.4.3 Airgap transformation factor and airgap flux density at the bore diameter

Until now, we considered that all the field wave harmonics generated by the rotor winding and the ones due to the stator winding cross completely the airgap. In reality, depending on its wave length, a field wave can never reach the opposite surface (stator or rotor). Traxler-Samek [TSS03; TLS10] considers this effect by using the airgap transformation factor $\mathrm{f}_{\mathrm{g},\nu}$ defined by Equation (4.38).

$$\mathrm{f}_{\mathrm{g},\nu}^{\mathcal{J}} = \frac{\hat{B}_{\delta,\nu}^{\mathcal{J}}}{\hat{B}_{\delta,\nu}^{\mathcal{J}}} = \frac{1}{\cosh(k_{\nu}\delta_{\mathrm{g}})} \tag{4.38}$$

$\hat{B}_{\delta,\nu}^{\mathcal{J}}$ is the radial airgap flux density harmonic on the side where the field wave is generated and $\hat{B}_{\delta,\nu}^{\mathcal{J}}$ is the corresponding component on the opposite side. k_{ν} (m) is the wave number of the field wave harmonic defined as $k_{\nu} = (P_{\nu}/p) \cdot \pi/\tau_{\mathrm{p}}$. Figure 4.25 shows the variation of $\mathrm{f}_{\mathrm{g},\nu}$ applied to the field wave harmonics generated by the stator winding of the machine of Table 4.2.

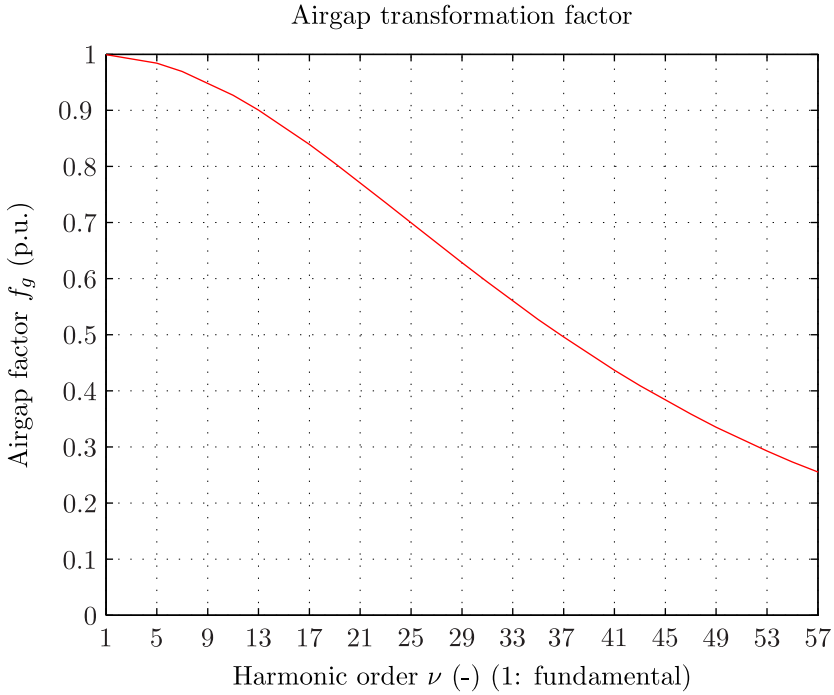

Figure 4.25: Airgap transformation factor example

One can see that the reduction is not at all negligible. Consequently using this factor, we can express the airgap flux density applied on the stator bore diameter $B_\delta^{\mathcal{S}}$ and the one applied on the rotor outer border $B_\delta^{\mathcal{R}}$ as shown by Equations (4.39) and (4.40). $\Theta_{\mathrm{s},\nu_\mathrm{s}}$ and $\Theta_{\mathrm{r},\nu_\mathrm{r}}$ are the mmf harmonics created respectively by the stator and by the rotor.

$$B_\delta^{\mathcal{S}}(\alpha_\mathrm{s},t) = \left(\sum_{\nu_\mathrm{s}=1}^{\infty}\Theta_{\mathrm{s},\nu_\mathrm{s}}(\alpha_\mathrm{s},t) + \sum_{\nu_\mathrm{r}=1}^{\infty}\Theta_{\mathrm{r},\nu_\mathrm{r}}(\alpha_\mathrm{s},t)\cdot \mathrm{f}_{\mathrm{g},\nu_\mathrm{r}}^{\mathcal{R}}\right)\cdot\Lambda^{\mathcal{S}}(\alpha_\mathrm{s},t)\cdot K_{\mathrm{sat}}(\alpha_\mathrm{s},t) \tag{4.39}$$

$$B_\delta^{\mathcal{R}}(\alpha_\mathrm{s},t) = \left(\sum_{\nu_\mathrm{s}=1}^{\infty}\Theta_{\mathrm{s},\nu_\mathrm{s}}(\alpha_\mathrm{s},t)\cdot \mathrm{f}_{\mathrm{g},\nu_\mathrm{s}}^{\mathcal{S}} + \sum_{\nu_\mathrm{r}=1}^{\infty}\Theta_{\mathrm{r},\nu_\mathrm{r}}(\alpha_\mathrm{s},t)\right)\cdot\Lambda^{\mathcal{R}}(\alpha_\mathrm{s},t)\cdot K_{\mathrm{sat}}(\alpha_\mathrm{s},t) \tag{4.40}$$

Note that $\Lambda^{\mathcal{S}}$ and $\Lambda^{\mathcal{R}}$ are the airgap permeances computed respectively close to the stator inner side and close to the rotor outer side. $\mathrm{f}_{\mathrm{g},\nu_\mathrm{r}}^{\mathcal{R}}$ is the airgap transformation factor applied only on the rotor field wave harmonics while $\mathrm{f}_{\mathrm{g},\nu_\mathrm{s}}^{\mathcal{S}}$ is applied only for the stator field wave harmonics.

Figure 4.26 and 4.27 compare the variations $B_\delta^{\mathcal{S}}(\alpha_\mathrm{s},t)$ and $B_\delta^{\mathcal{R}}(\alpha_\mathrm{s},t)$ at one instant, obtained from the analytical formula and from a FE simulation. One can see a good agreement between both methods. $B_\delta^{\mathcal{S}}(\alpha_\mathrm{s},t)$ and $B_\delta^{\mathcal{R}}(\alpha_s,t)$ are used in Chapter 5 when dealing with the stator voltage harmonics, the radial electromagnetic forces and the iron losses.

This section completed the sinusoidal model developed in Chapter 3 by considering the parasitic harmonics due to the stator and rotor windings the airgap permeance and the magnetic saturation. Although the developed method gives satisfying results, it has the disadvantage

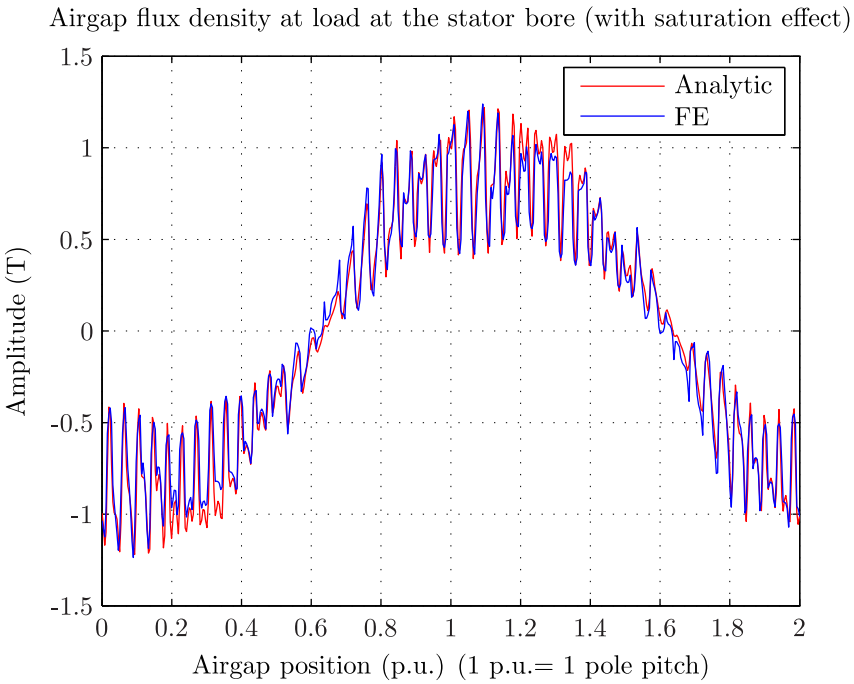

Figure 4.26: Airgap flux density at load with saturation at the stator bore

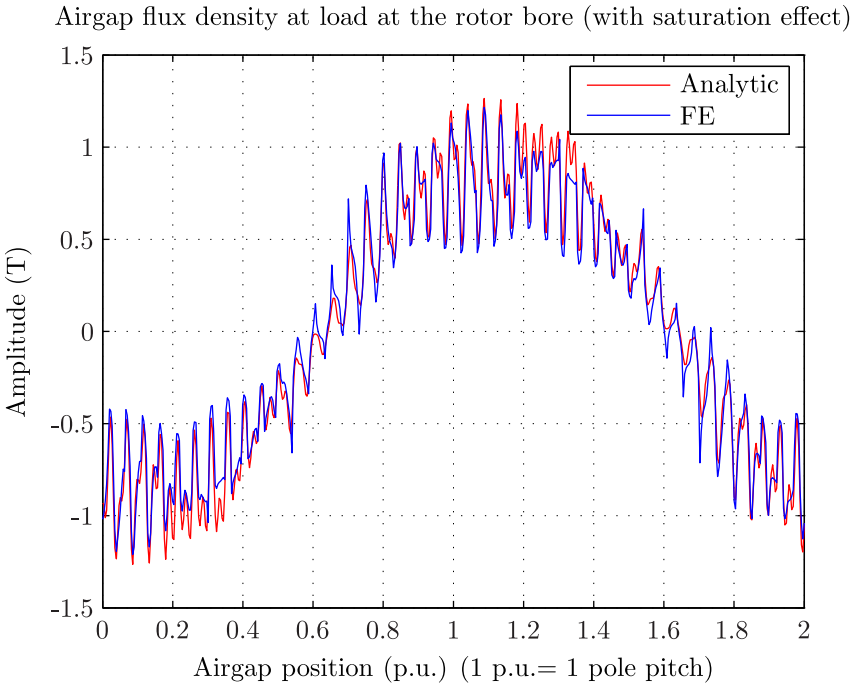

Figure 4.27: Airgap flux density at load with saturation at the rotor bore

to approximate our accurate model of the airgap because of the simplified magnetic saturation model. One could think of another approach being able to better use the developed BE model for the airgap and to consider the magnetic saturation. This is the object of the next section.

4.5 Potential improvement of the method

Last section computed the airgap flux density based on the definition of the stator and the rotor mmf and a numerical computation of the airgap permeance. The impact of the magnetic saturation was considered by correcting the airgap permeance function by using the results of the reduced magnetic model developed in Chapter 2. The main drawback of this method is that the accurate numeric modeling of the airgap is finally approximated when considering the influence of the magnetic saturation. This section investigates a possible improvement of the calculation of the airgap flux density by developing an extended magnetic permeance network of the stator and the rotor core coupled through a BE model of the double-slotted airgap.

Modeling via a permeance network has been widely used in the last years by electrical engineers as an alternative to FE methods. The main purposes are the mutli-physics coupling (e.g with power electronics) or the optimization. Petrichenko [Pet08] proposes a detailed permeance network of a turbo generator in order to study its behaviors under no-load and load operation. As a validation he compares the no-load and short-circuit characteristics given by the program to experimental results for several machines in operation and obtains good agreements. Perho [Per02], after having detailed the basics of the modeling, proposes a permeance network of a squirrel cage machine in order to derive an equivalent scheme. The results are compared with measurements. DuPeloux [Pel06] creates a software *Reluctool* coupled with optimization tools such as *Cades* [Del+07] to easily model any electromagnetic devices. Phuong Do[DO10] continues the work of [Pel06] and proposes methods so as to include transient analysis and iron losses computations. The tool is used to study and optimize electromagnetic switches.

In the following we propose a modeling applied exclusively to the DFIM although the presented concepts could be extended to other applications. Two main parts are identified: the modeling of the iron parts i.e stator and rotor core and the modeling of the airgap.

4.5.1 Modeling of the stator and rotor core

I. Discretization of the stator and rotor cores

A magnetic circuit can be discretized into several magnetic elements called magnetic reluctances connected so as to create a magnetic network. The magnetic model developed in Chapter 2 can be represented as a magnetic network as shown in Figure 4.28.

One can see the presence of a mmf source $\Theta = NI$ equivalent to a voltage source, and resistive elements simulating the airgap and the rotor and stator yoke magnetic reluctances. The teeth are discretized in three elements in order to consider its non-constant geometry while the yoke is represented by only one element. The magnetic drop U over each magnetic reluctance is given

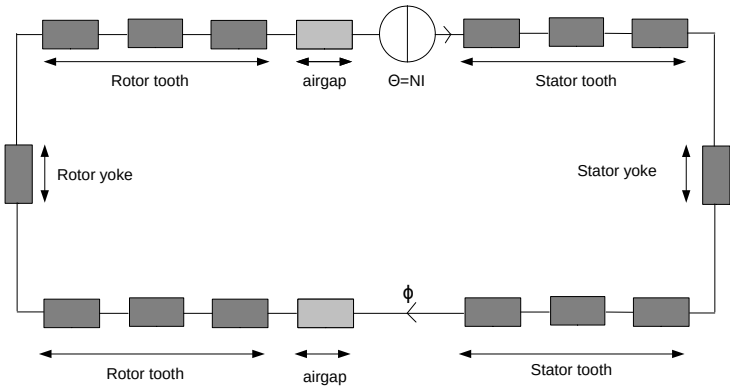

Figure 4.28: Simple magnetic network

by:

$$U = R \cdot \Phi \tag{4.41}$$

where Φ is the magnetic flux crossing the element and R is the magnetic reluctance of the element given by:

$$R = \gamma \cdot \mu \tag{4.42}$$

where γ is a parameter depending on the geometry of the element. Considering a simple rectangular shape element we have $\gamma = L_{\mathrm{p}}/S_{\mathrm{p}}$ whith L_{p} the length and S_{p} the crossed section. μ is the magnetic permeability depending on the magnetic properties of the material and the flux crossing the element.

The model shown in Figure 4.28 only simulates the main magnetic path where the magnetic flux is maximum but does not make it possible to model secondary magnetic paths such as for example the leakage paths which also contribute to magnetic saturation. This simplified magnetic network can be extended in order to include the complete geometry of the machine. Figure 4.29 shows a more detailed discretization of the stator core over one slot pitch including the teeth and the yoke [Per02]. One can see the presence of ten cells having two elements in normal and in tangential direction. Note that the number of discretization has been simplified here, its impact will be discussed in the next section. Figure 4.30 shows the magnetic model along one pole after connecting $3q_{\mathrm{s}}$ times the reduced slot pitch models (here $q_{\mathrm{s}} = 2$)[3]. One can see that the magnetic field is assumed to be tangential on the outer border of the yoke. As the rotor and the stator core geometries are similar, the same modeling can be used for both parts.

[3]In case of fractional slot winding, the model would have to be extended in order to cover a complete repetitive period of the winding

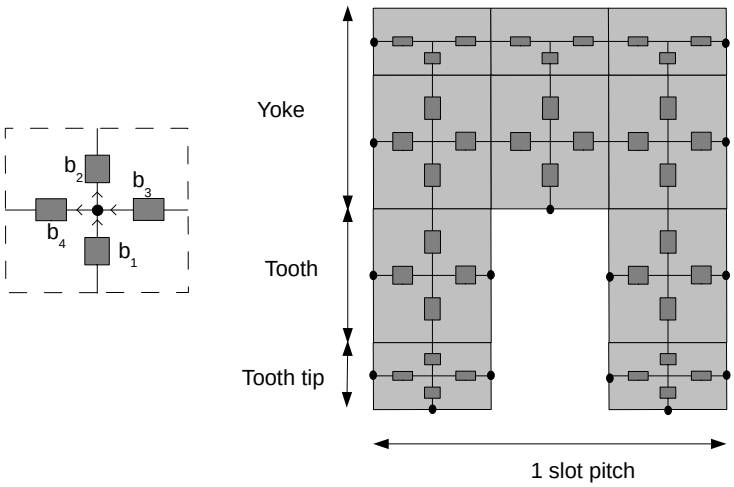

Figure 4.29: Permeance network: One slot pitch

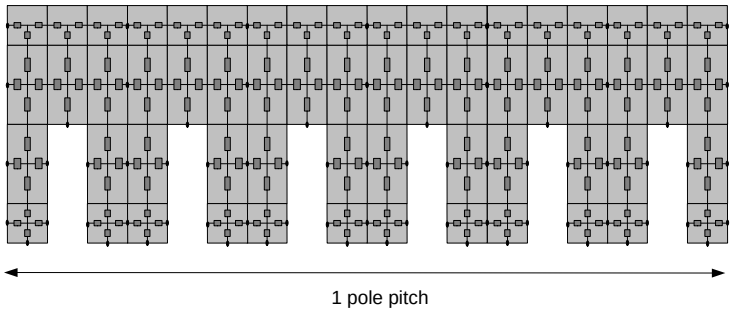

Figure 4.30: Permeance network: One pole pitch

II. Modeling of the magnetic materials

The magnetic materials of the stator and rotor core are modeled by using an approximated model of the magnetic characteristic $B(H)$ [Pel06; Ced13]

$$B(H) = \mu_0 H + J_\mathrm{s} \frac{H_\mathrm{s} + 1 - \sqrt{(H_\mathrm{s}+1)^2 - 4H_\mathrm{a}(1-\mathrm{a})}}{2(1-\mathrm{a})} \tag{4.43}$$

where $H_\mathrm{a} = \mu_0 H(\mu_\mathrm{r} - 1)/J_\mathrm{s}$, J_s is the magnetic polarization at saturation expressed in T, μ_r is the initial relative permeability of the material and a is an adjustment coefficient of the $B(H)$ curve [Ced13].

III. Assembly of the network

The assembly of the magnetic network as a matrix is done by applying general methods [Pet08; Per02; Pel06]. Figure 4.29 shows an example of a node at the intersection of four branches (b_1, b_2, b_3, $\mathrm{b}b_4$) containing a magnetic reluctance element. By applying the equivalent Kirchhoff law on this node, we obtain Equation (4.44) where $\Phi_{\mathrm{b},1}$, $\Phi_{\mathrm{b},2}$, $\Phi_{\mathrm{b},3}$ and $\Phi_{\mathrm{b},4}$ are the magnetic fluxes flowing in each branch.

$$\Phi_{\mathrm{b},1} - \Phi_{\mathrm{b},2} + \Phi_{\mathrm{b},3} - \Phi_{\mathrm{b},4} = 0 \tag{4.44}$$

Note that by convention when the flux is leaving the node, its orientation is negative and it is positive on the contrary. By applying this method to all the nodes of the network, one can write Equation (4.45) where $\boldsymbol{M}$ is the connection matrix also called nodes matrix of the magnetic network with a number of lines equal to the number of nodes N_n and the number of columns equal to the number of reluctance elements N_b. Φ_b is a vector containing the flux circulating in each branch. When dealing with the nodes on the right or left side of the model, one has to take into account of the periodic or anti-periodic properties of the model. When considering for example an odd number of poles, the flux Φ leaving from the left side of the model enters opposite by the right side. In case of an even number of poles, the flux enters positive.

$$\boldsymbol{M} \cdot \Phi_\mathrm{b} = \boldsymbol{0} \tag{4.45}$$

One can use the same connection matrix to express the relation between the voltage drop over each branch $\boldsymbol{U}_{\mathrm{m,b}}$ and each potential node $\boldsymbol{V}_\mathrm{n}$:

$$\boldsymbol{U}_{\mathrm{m,b}} = \boldsymbol{M}^\mathrm{t} \cdot \boldsymbol{V}_\mathrm{n} \tag{4.46}$$

were $\boldsymbol{M}^\mathrm{t}$ is the transposed matrix $\boldsymbol{M}$ while $\boldsymbol{U}_{\mathrm{m,b}}$ and $\boldsymbol{V}_\mathrm{n}$ are two vectors containing the voltage drop over each branch and the magnetic potential of each node. The flux circulating in each branch is linked to the magnetic potential drop $U_{\mathrm{m,p}}$ on each permeance element by Equation (4.47)

$$\Phi_\mathrm{b} = \boldsymbol{P}_\mathrm{b} \cdot \boldsymbol{U}_{\mathrm{m,p}} \tag{4.47}$$

where $\boldsymbol{U}_{\mathrm{m,p}}$ is a vector containing the potential over each permeance element of the network, and $\boldsymbol{P}_{\mathrm{b}}$ is a diagonal matrix whose diagonal terms equal the magnetic permeance of each branch. Note that the permeance is the inverse of the reluctance. Furthermore a mmf source according is included in the model in series with each magnetic element and regrouped in the vector $\boldsymbol{E}_{\mathrm{b}}$. The vector $\boldsymbol{E}_{\mathrm{b}}$ contains mainly zero values except for certain branches, i.e. the radial branches located along the teeth. These sources are set according to the current flowing into the stator and rotor conductors. For any branch b we can write:

$$U_{\mathrm{m,p}} = U_{\mathrm{m,b}} + E_{\mathrm{b}} \tag{4.48}$$

By using Equations (4.47), (4.48) and (4.46) one obtains Equation (4.49)

$$\Phi_{\mathrm{b}} = \boldsymbol{P}_{\mathrm{b}}\boldsymbol{M}^{\mathrm{t}}\boldsymbol{V}_{\mathrm{n}} + \boldsymbol{P}_{\mathrm{b}}\boldsymbol{E}_{\mathrm{b}} \tag{4.49}$$

Until now, the N_{c} flux Φ_{c} entering by the lower border were not yet included but need to be considered by modifying the Equation (4.45) which becomes:

$$\boldsymbol{M} \cdot \Phi_{\mathrm{b}} + \Phi_{\mathrm{add}} = \boldsymbol{0} \tag{4.50}$$

where $\Phi_{\mathrm{add}} = [\boldsymbol{0}, \Phi_{\mathrm{c}}]$ is a vector having a dimension equal to the number of nodes of the model and whose elements are zero except for its last N_{c} lines. Note that the matrix $\boldsymbol{M}$ is built so that its N_{c} last lines correspond to the N_{c} potential nodes of the lower border. By using Equation (4.49), Equation (4.50) leads to:

$$\boldsymbol{M}\boldsymbol{P}_{\mathrm{b}}\boldsymbol{M}^{\mathrm{t}}\boldsymbol{V}_{\mathrm{n}} + \boldsymbol{M}\boldsymbol{P}_{\mathrm{b}}\boldsymbol{E}_{\mathrm{b}} + \begin{bmatrix} \boldsymbol{0} \\ \Phi_{\mathrm{c}} \end{bmatrix} = \boldsymbol{0} \tag{4.51}$$

The vector $\boldsymbol{V}_{\mathrm{n}}$ is now splitted between the vector of potentials belonging to the lower border $\boldsymbol{V}_{\mathrm{c}}$ and the other potentials $\boldsymbol{V}_{\mathrm{m}}$. Finally Equation (4.51) can be rewritten as:

$$\begin{bmatrix} \boldsymbol{M}_1 & \boldsymbol{M}_2 & \boldsymbol{Z}_1 \\ \boldsymbol{M}_3 & \boldsymbol{M}_4 & \boldsymbol{I} \end{bmatrix} \begin{bmatrix} \boldsymbol{V}_{\mathrm{m}} \\ \boldsymbol{V}_{\mathrm{c}} \\ \Phi_{\mathrm{c}} \end{bmatrix} = \begin{bmatrix} \boldsymbol{Y}_1 \\ \boldsymbol{Y}_2 \end{bmatrix} \tag{4.52}$$

where $\boldsymbol{M}_1$, $\boldsymbol{M}_2$, $\boldsymbol{M}_3$ and $\boldsymbol{M}_4$ are the resulting matrices of the split of the matrix $\boldsymbol{M}\boldsymbol{P}_{\mathrm{b}}\boldsymbol{M}^{\mathrm{t}}$. $\boldsymbol{Z}_1$ is a zero matrix having $N_{\mathrm{n}} - N_{\mathrm{c}}$ lines and N_{c} columns, $\boldsymbol{I}$ is an identity matrix with a dimension equal to N_{c}. $\boldsymbol{Y}_1$ contains the $N_{\mathrm{n}} - N_{\mathrm{c}}$ first lines of the vector $\boldsymbol{M}\boldsymbol{P}_{\mathrm{b}}\boldsymbol{E}_{\mathrm{b}}$ while the vector $\boldsymbol{Y}_1$ contains its N_{c} last lines. When applying this procedure to the magnetic network of the stator and of the rotor core one obtains the system of Equation (4.53) where the unknown are the $N_{\mathrm{n,s}}$ and $N_{\mathrm{n,r}}$ magnetic potentials of the stator and rotor core and the $N_{\mathrm{c,s}}$ and $N_{\mathrm{c,r}}$ fluxes entering the stator and rotor border. In order to be able to solve such system we need $N_{\mathrm{c,s}} + N_{\mathrm{c,r}}$ additional equations defining the interaction between the stator and rotor core,

those are described in the following section.

$$\begin{bmatrix} \boldsymbol{M}_{1\mathrm{s}} & \boldsymbol{M}_{2,\mathrm{s}} & \boldsymbol{Z}_{1,\mathrm{s}} & \mathbf{0} & \mathbf{0} & \mathbf{0} \\ \boldsymbol{M}_{3\mathrm{s}} & \boldsymbol{M}_{4,\mathrm{s}} & \boldsymbol{I}_{\mathrm{s}} & \mathbf{0} & \mathbf{0} & \mathbf{0} \\ \mathbf{0} & \mathbf{0} & \mathbf{0} & \boldsymbol{M}_{1,\mathrm{r}} & \boldsymbol{M}_{2,\mathrm{r}} & \boldsymbol{Z}_{1,\mathrm{r}} \\ \mathbf{0} & \mathbf{0} & \mathbf{0} & \boldsymbol{M}_{3,\mathrm{r}} & \boldsymbol{M}_{4,\mathrm{r}} & \boldsymbol{I}_{\mathrm{r}} \end{bmatrix} \begin{bmatrix} \boldsymbol{V}_{\mathrm{m,s}} \\ \boldsymbol{V}_{\mathrm{c,s}} \\ \boldsymbol{\Phi}_{c,s} \\ \boldsymbol{V}_{\mathrm{m,r}} \\ \boldsymbol{V}_{\mathrm{c,r}} \\ \boldsymbol{\Phi}_{\mathrm{c,r}} \end{bmatrix} = \begin{bmatrix} \boldsymbol{Y}_{1,\mathrm{s}} \\ \boldsymbol{Y}_{2,\mathrm{s}} \\ \boldsymbol{Y}_{1,\mathrm{r}} \\ \boldsymbol{Y}_{2,\mathrm{r}} \end{bmatrix} \tag{4.53}$$

4.5.2 Connection of the stator and rotor core through the airgap

In order to connect the stator to the rotor we have to define the airgap permeances. As the airgap is slotted on both sides, it is difficult to define exactly all the fluxes linking the rotor teeth to the stator teeth. One solution proposed by [Per02] is to discretize in a fine way the airgap using similar elements to those used for the stator and rotor cores. This may lead to a very complicated model. Other authors compute analytically or numerically the permeance linking the teeth [Pet08; Yao06]. This method is interesting as it is easy to implement and gives good results. However it does not make it possible to consider accurately the fringing effect appearing at the base of the teeth. The method proposed here stands on the BEM already exposed in the first section. We use here the same method and dicretize the airgap border into several constant elements. The potential and its derivative are considered constant over each element which makes it possible to link on its border the scalar magnetic potential V_{c} and its derivative $Q_{\mathrm{c}} = \mathrm{d}V_{\mathrm{c}}/\mathrm{d}n$ by using the following equation [BD92]

$$\boldsymbol{G}\boldsymbol{V}_{\mathrm{c}} - \boldsymbol{H}\boldsymbol{Q}_{\mathrm{c}} = 0 \tag{4.54}$$

where $\boldsymbol{G}$ and $\boldsymbol{H}$ are interaction squared matrices whose coefficients depend on the geometry of the airgap. Their dimension is equal to $(N_{\mathrm{c,s}} + N_{\mathrm{c,r}} + N_{\mathrm{c,e}})$ where $N_{\mathrm{c,e}}$ is the number of elements on the edges of the airgap. In our case the vector $\boldsymbol{V}_{\mathrm{c}} = [\boldsymbol{V}_{\mathrm{c,s}} \;\; \boldsymbol{V}_{\mathrm{c,r}} \;\; \boldsymbol{V}_{\mathrm{c,e}}]$ contains the magnetic potentials of the stator and rotor inner borders as well as the potentials on the edges of the model. In the same way the vector $\boldsymbol{Q}_{\mathrm{c}} = [\boldsymbol{Q}_{\mathrm{c,s}} \;\; \boldsymbol{Q}_{\mathrm{c,r}} \;\; \boldsymbol{Q}_{\mathrm{c,e}}]$ contains the magnetic fields of the stator and rotor lower border as well as the magnetic fields on the edges of the model.

As the derivative $Q_{\mathrm{c}} = \mathrm{d}V_{\mathrm{c}}/\mathrm{d}n$ is equal to the magnetic field H_{c}, the flux $\Phi_{\mathrm{c,i}}$ crossing one border element i can be obtained by using the following equation:

$$\Phi_{\mathrm{c,i}} = \mu_0 \cdot S_{\mathrm{i}} \cdot H_{\mathrm{c,i}} = \mu_0 \cdot S_{\mathrm{i}} \cdot Q_{\mathrm{c,i}} \tag{4.55}$$

where S_{i} is the cross section of the border element i. The coefficients of the matrix $\boldsymbol{H}$ are rescaled so that we can write:

$$\boldsymbol{G}\boldsymbol{V}_{\mathrm{c}} - \boldsymbol{H}\boldsymbol{\Phi}_{\mathrm{c}} = \mathbf{0} \tag{4.56}$$

The vectors $\boldsymbol{V}_{\mathrm{c}}$ and $\boldsymbol{\Phi}_{\mathrm{c}}$ are splitted considering the stator, the rotor and the edges part so that Equation (4.56) leads to:

$$\begin{bmatrix} \boldsymbol{G}\mathrm{s} & \boldsymbol{G}_{\mathrm{r}} & \boldsymbol{G}_{\mathrm{e}} \end{bmatrix} \begin{bmatrix} \boldsymbol{V}_{\mathrm{c,s}} \\ \boldsymbol{V}_{\mathrm{c,r}} \\ \boldsymbol{V}_{\mathrm{c,e}} \end{bmatrix} - \begin{bmatrix} \boldsymbol{H}_{\mathrm{s}} & \boldsymbol{H}_{\mathrm{r}} & \boldsymbol{H}_{\mathrm{e}} \end{bmatrix} \begin{bmatrix} \boldsymbol{\Phi}_{\mathrm{c,s}} \\ \boldsymbol{\Phi}_{\mathrm{c,r}} \\ \boldsymbol{\Phi}_{\mathrm{c,e}} \end{bmatrix} = \mathbf{0} \tag{4.57}$$

By combining Equations (4.53) and (4.57) we obtain:

$$\begin{bmatrix} \boldsymbol{M}_{1,\mathrm{s}} & \mathbf{0} & \boldsymbol{M}_{2,\mathrm{s}} & \mathbf{0} & \mathbf{0} & \boldsymbol{Z}_{1,\mathrm{s}} & \mathbf{0} & \mathbf{0} \\ \boldsymbol{M}_{3,\mathrm{s}} & \mathbf{0} & \boldsymbol{M}_{4,\mathrm{s}} & \mathbf{0} & \mathbf{0} & \boldsymbol{I}_{\mathrm{s}} & \mathbf{0} & \mathbf{0} \\ \mathbf{0} & \boldsymbol{M}_{1,\mathrm{r}} & \mathbf{0} & \boldsymbol{M}_{2,\mathrm{r}} & \mathbf{0} & \mathbf{0} & \boldsymbol{Z}_{1,\mathrm{r}} & \mathbf{0} \\ \mathbf{0} & \boldsymbol{M}_{3,\mathrm{r}} & \mathbf{0} & \boldsymbol{M}_{4,\mathrm{r}} & \mathbf{0} & \mathbf{0} & \boldsymbol{I}_{\mathrm{r}} & \mathbf{0} \\ \mathbf{0} & \mathbf{0} & \boldsymbol{G}_{\mathrm{s}} & \boldsymbol{G}_{\mathrm{r}} & \boldsymbol{G}_{e} & -\boldsymbol{H}_{\mathrm{s}} & -\boldsymbol{H}_{\mathrm{r}} & -\boldsymbol{H}_{\mathrm{e}} \end{bmatrix} \begin{bmatrix} \boldsymbol{V}_{\mathrm{m,s}} \\ \boldsymbol{V}_{\mathrm{m,r}} \\ \boldsymbol{V}_{\mathrm{c,s}} \\ \boldsymbol{V}_{\mathrm{c,r}} \\ \boldsymbol{V}_{\mathrm{c,e}} \\ \boldsymbol{\Phi}_{\mathrm{c,s}} \\ \boldsymbol{\Phi}_{\mathrm{c,r}} \\ \boldsymbol{\Phi}_{\mathrm{c,e}} \end{bmatrix} = \begin{bmatrix} \boldsymbol{Y}_{1,\mathrm{s}} \\ \boldsymbol{Y}_{2,\mathrm{s}} \\ \boldsymbol{Y}_{1,\mathrm{r}} \\ \boldsymbol{Y}_{2,\mathrm{r}} \\ \mathbf{0} \end{bmatrix} \tag{4.58}$$

The system (4.58) counts now $N_{ns} + N_{nr} + N_{cs} + N_{cr} + N_{ce}$ equations. Its unknown are:

- $N_{\mathrm{n,s}}$ magnetic potentials of the stator core included the lower stator border potentials
- $N_{\mathrm{n,r}}$ magnetic potentials of the rotor core included the lower rotor border potentials
- $N_{\mathrm{c,e}}$ magnetic potentials on the edges of the airgap
- $N_{\mathrm{c,s}}$ magnetic fluxes crossing the stator lower border
- $N_{\mathrm{c,r}}$ magnetic fluxes crossing the rotor lower border
- $N_{\mathrm{c,e}}$ magnetic fluxes crossing the edges of the airgap

As we can see $N_{\mathrm{c,e}}$ equations are still missing; this is solved by adding boundary conditions on the magnetic flux crossing the edges of the airgap.

4.5.3 Solving of the system

The system of Equations (4.58) is ready to be solved and can be written as $\boldsymbol{M} \cdot \boldsymbol{X} = 0$ where $\boldsymbol{X} = [\boldsymbol{V}_{\mathrm{m,s}} \ \boldsymbol{V}_{\mathrm{m,r}} \ \boldsymbol{V}_{\mathrm{c,s}} \ \boldsymbol{V}_{\mathrm{c,r}} \ \boldsymbol{V}_{\mathrm{c,e}} \ \boldsymbol{\Phi}_{\mathrm{c,s}} \ \boldsymbol{\Phi}_{\mathrm{c,r}}]$. However the non-linearity of the stator and rotor core material characteristics leads to non-constant magnetic permeances.

The function F is defined so that $F(\boldsymbol{X}) = \boldsymbol{M} \cdot \boldsymbol{X}$. The purpose of the calculation is to find the vector $\boldsymbol{X}$ so that $F(\boldsymbol{X}) = \mathbf{0}$.

First we assume a constant permeability $\mu = \mu_0 \cdot \mu_{\mathrm{r}}$ in all the permeance elements. The system is solved which makes it possible to obtain the solution vector $\boldsymbol{X_i}$. Based on Equations (4.46) and (4.48), one can compute the magnetic drop U_{p} over each permeance element and finally the magnetic strength $H_{\mathrm{p}} = U_{\mathrm{p}}/l_{\mathrm{p}}$. From the characteristic $B(H)$ defined by Equation (4.43), one can derive the corresponding magnetic permeability μ.

Considering the new magnetic permeability of each permeance elements, the coefficients of the matrix M are updated and the residual $\boldsymbol{R} = F(\boldsymbol{X}_i)$ is defined. Depending on the magnetic state of the stator and rotor core, $\boldsymbol{R} = \mathbf{0}$ might not be satisfied and an iterative process is therefore needed; the Newton-Raphson method is used to perform this task. We define the Jacobian $\mathrm{d}\boldsymbol{M}$ of the matrix $\boldsymbol{M}$. Noticing that only permeance elements are affected by the magnetic saturation, the structure of $\mathrm{d}\boldsymbol{M}$ is the same as the matrix $\boldsymbol{M}$ except that the permeance coefficients $P = \mu/\gamma$ are replaced by $\mathrm{d}P = d\mu/\gamma$. $\mathrm{d}\mu = \mathrm{d}B/\mathrm{d}H$ corresponds to the derivative of Equation (4.43).

The equation $\mathrm{d}\boldsymbol{M} \cdot \mathrm{d}\boldsymbol{X} = -\boldsymbol{R}$ is solved which makes it possible to update the vector $\boldsymbol{X}_i$

Quantity	Value
Airgap length δ_{g} (mm)	17
Number of stator slots per pole/phase q_{s} (-)	4
Stator slot height $h_{\mathrm{s,s}}$ (mm)	180
Stator slot width $w_{\mathrm{s,s}}$ (mm)	23
Stator tooth width $w_{\mathrm{t,s}}$ (mm)	55
Stator yoke height $h_{\mathrm{y,s}}$ (mm)	300
Number of rotor slots per pole/phase q_{r} (-)	3
Rotor slot height $h_{\mathrm{s,r}}$ (mm)	180
Rotor slot width $w_{\mathrm{s,r}}$ (mm)	26
Rotor tooth width $w_{\mathrm{t,r}}$ (mm)	78
Rotor yoke height $h_{\mathrm{y,r}}$ (mm)	210

Table 4.5: Geometry characteristics for the BEM-Magnetic network calculation

so that $\boldsymbol{X}_{i+1} = \boldsymbol{X}_i + r \cdot \mathrm{d}\boldsymbol{X}$ where r is a scaling coefficient called relaxation coefficient less or equal to 1. The residual $\boldsymbol{R} = F(\boldsymbol{X}_{i+1})$ is then recomputed and the whole process carried on until convergence of the system which can be written as error $= \sum |R_{\mathrm{k}}| < \epsilon$ where R_{k} is the k^{th} element of the vector $\boldsymbol{R}$ and ϵ is the admissible error. Because of the strong non-linearity of the materials r is initially set to 0.1 and then to 1 during the iterative process when error is less than a certain value for example 10^{-3}.

4.5.4 Results

The presented method is applied on a simplified rectangular geometry of the DFIM as the one shown in Figure 4.31 where only one pole is modeled. The airgap boder is marked as a blue line. Table 4.5 describes the main parameters of the geometry.

The rotor winding is supplied with three different excitation currents corresponding to three different magnetic states. For each case, the airgap flux density is measured in the airgap at the beginning and after convergence of the non-linear iteration process.

Figure 4.32 shows the airgap flux density when supplying the rotor winding with a low current i.e setting a low saturation state. In this case the convergence is very fast and the flux density at the beginning and after convergence of the system are superposed.

Figure 4.33 shows the airgap flux density when increasing the rotor winding current by a factor 4. One can see now a slight impact of the magnetic saturation.

Figure 4.34 shows the airgap flux density when increasing the rotor winding current by a factor 6 . The impact of the magnetic saturation is this time very large. One can see that the computation remains stable even considering an high saturation state.

Figures 4.35 and 4.36 compare the BE output with a FE computation. Two cases are analyzed: one with a rough discretization of the airgap border and the other with a finer discretization. One can see that the second case gives very close results to the FE calculation. However one should

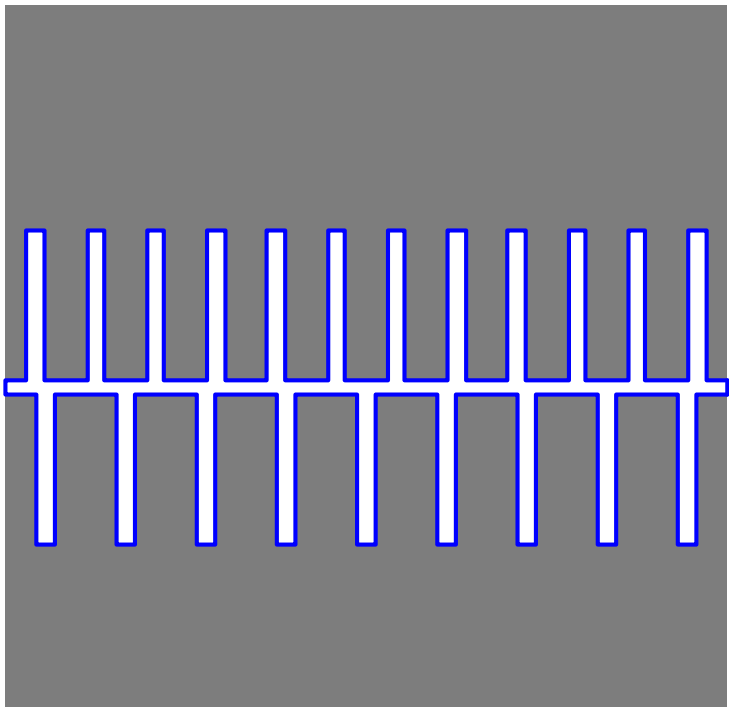

Figure 4.31: Simplified geometry for the BEM-Magnetic network calculation

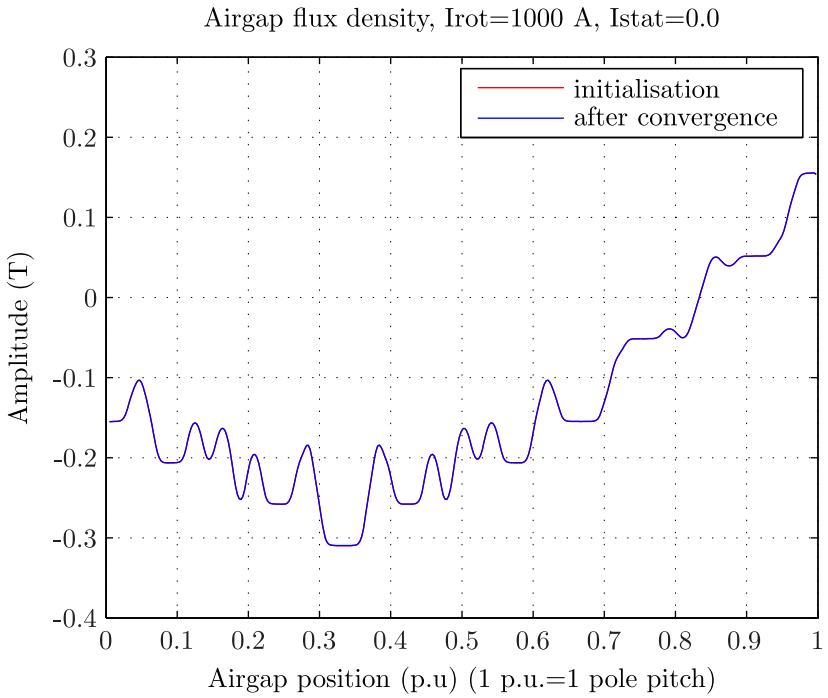

Figure 4.32: BEM-Magnetic network saturation state 1

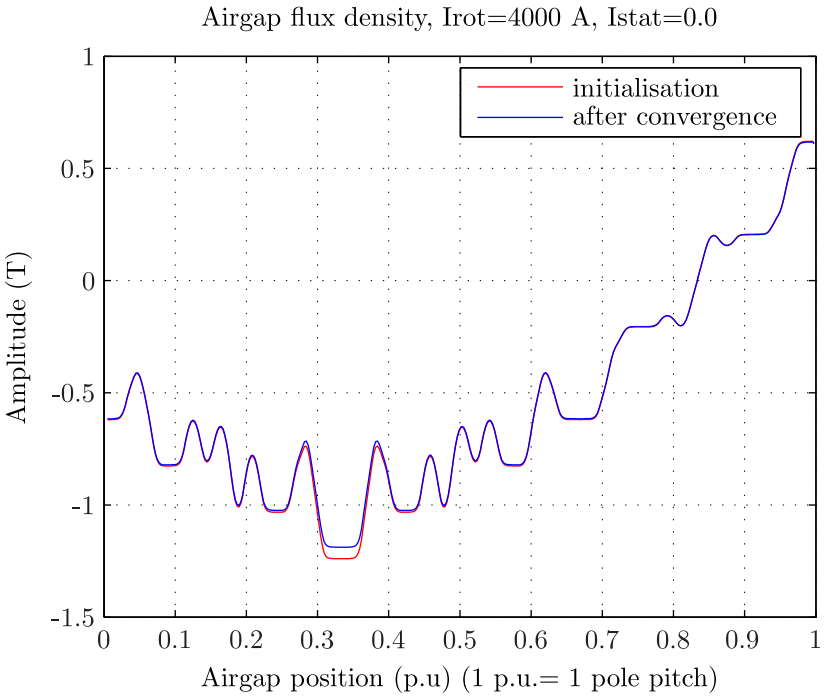

Figure 4.33: BEM-Magnetic network saturation state 2

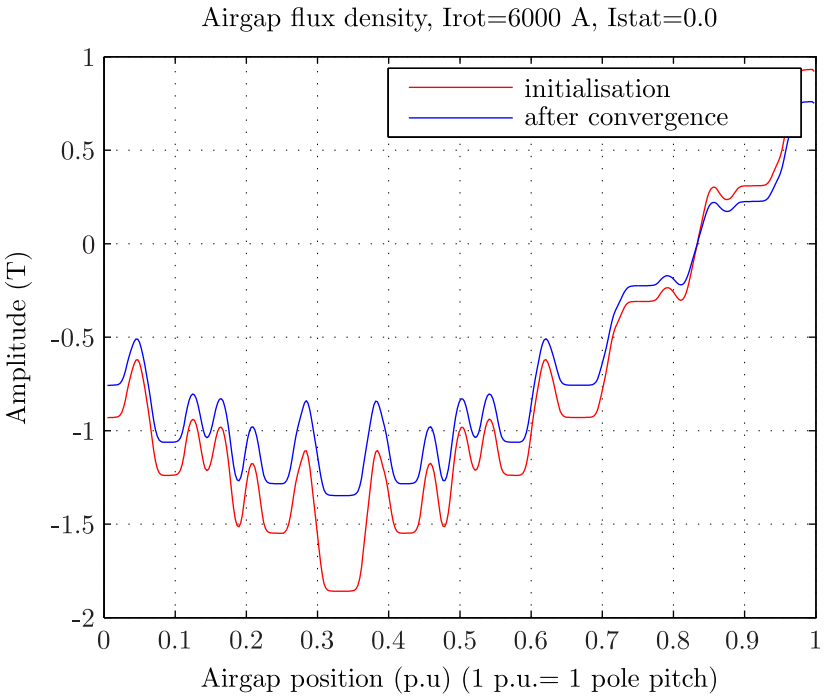

Figure 4.34: BEM-Magnetic network saturation state 3

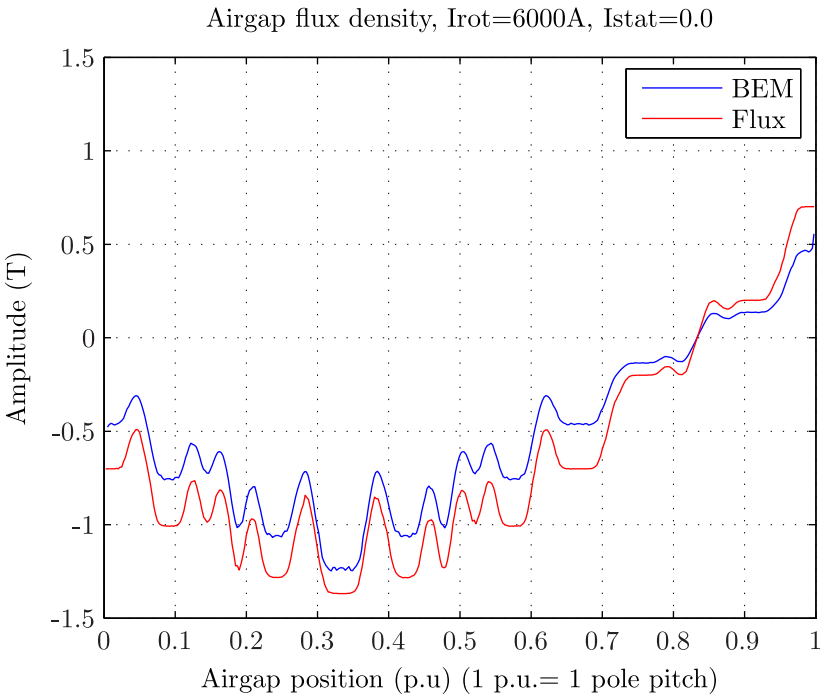

Figure 4.35: BEM-FE comparison with a rough discretization

add, that this finer discretization leads to an increase of the BEM matrix size and consequently of the calculation time. Figures 4.37 and 4.38 show both discretizations on a portion of the model. The nodes on the border are represented as dots.

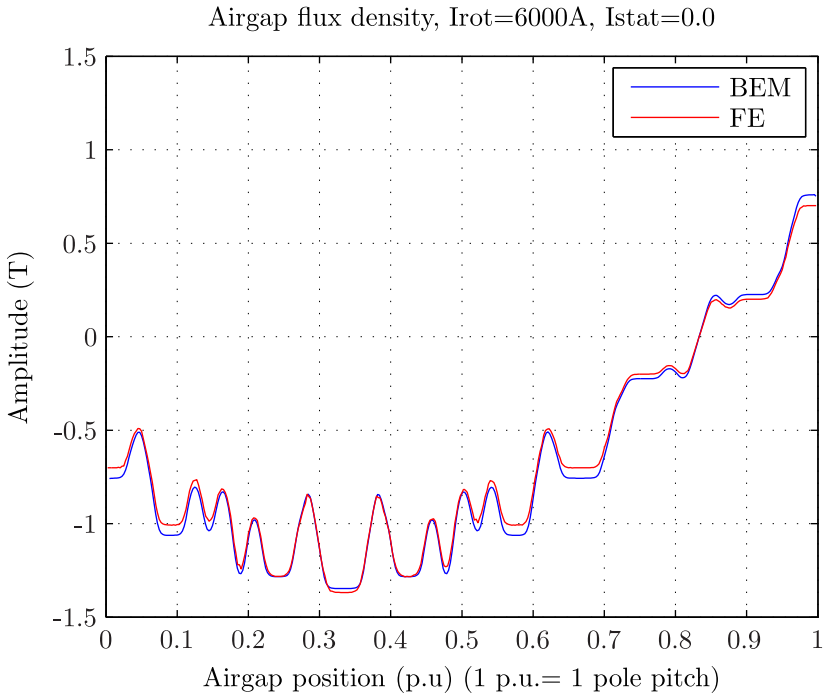

Figure 4.36: BEM-FE comparison with a fine discretization

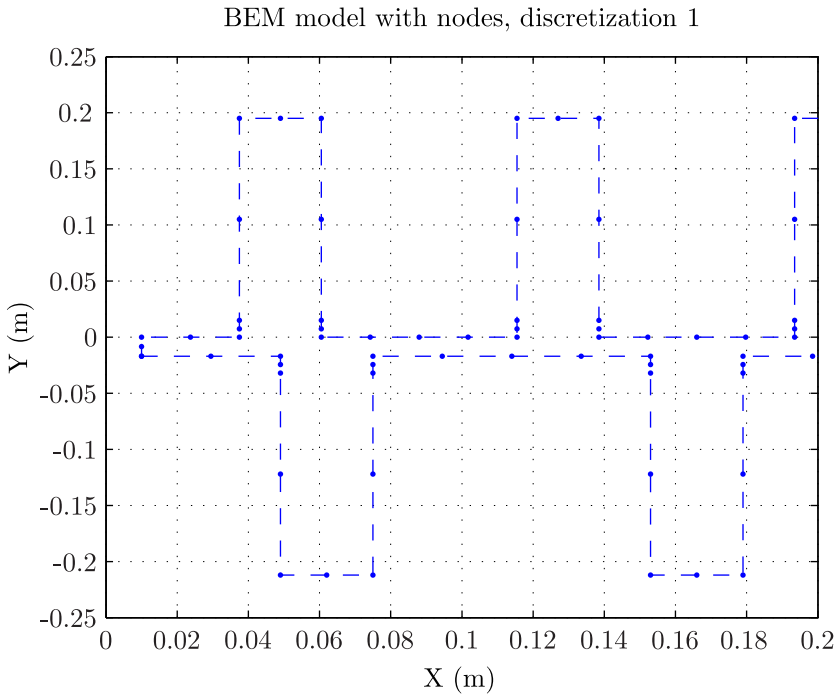

Figure 4.37: BE model: Rough discretization

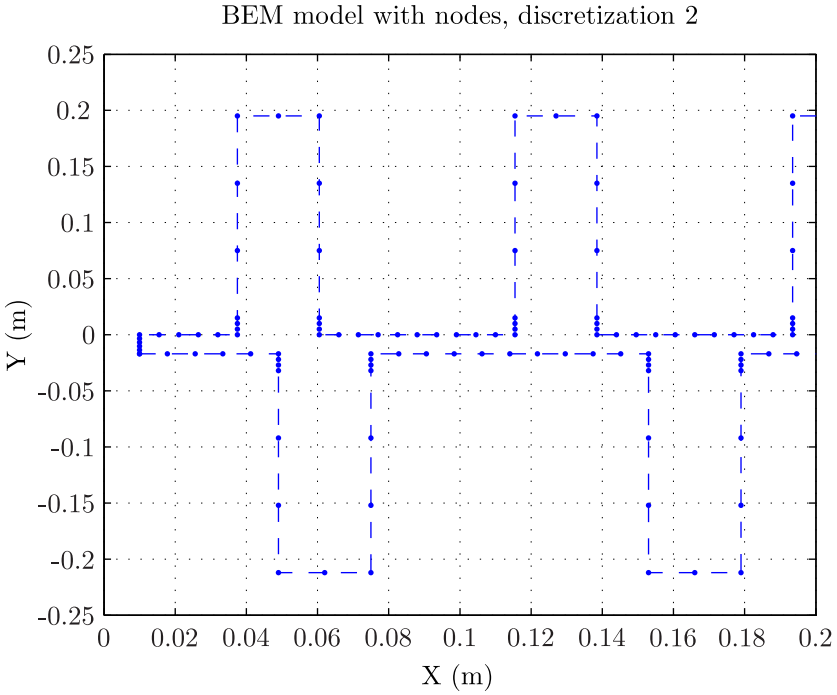

Figure 4.38: BE model: Fine discretization

4.6 Conclusion

This chapter completed the sinusoidal model developed in Chapter 3 by considering the parasitic harmonics due in one hand to the stator and rotor windings and in the other hand to the airgap permeance. The parasitic magnetic fields depending on the stator and rotor winding configuration were obtained by computing the corresponding mmf considering a constant airgap. The airgap permeance harmonics are mainly due to the interaction between the stator and rotor tooth. An original technique based on the BEM made it possible to calculate efficiently the harmonics of the airgap permeance. Finally the airgap flux density was obtained by multiplying the stator and rotor magneto-motive forces with the airgap permeance. The influence of the saturation was taken into account by applying a correction of the airgap permeance by using the results of the magnetic model developed in Chapter 2. The comparison of the obtained results with the ones obtained from FE showed a good agreement. The main disadvantage of this method is that the accurate numeric modeling of the airgap was approximated when considering the influence of the magnetic saturation. Therefore, a second method based on the coupling of the BE model of the airgap and a simplified magnetic network has been studied. This made it possible to profit from the efficient modeling of saturation occuring in the stator and rotor core with an accurate representation of the airgap. Comparison with FE has shown satisfying results and demonstrates that the method was stable even for high saturated case. This method has been tested until now only on a simplified linear geometry of the machine but could be extended to the real geometry. However, the large size of the BE matrix leads to

an heavy computation. This could be improved by using more efficient numeric tools such as the Fast Multipole Method [Liu09] which is more and more common when dealing with such problem. In the remainder of this thesis, only the first method is used i.e introducing airgap harmonics due to magnetic saturation based on the model developed in Chapter 2. However we believe that the coupled magnetic network and BEM represents a relevant way of improvement.

5 Applications to the study of the electromagnetic behavior

5.1 Introduction

Previous chapters developed and validated an analytical method being able to characterize the electromagnetic behavior of the DFIM considering magnetic saturation and parasitic airgap harmonics. The present chapter applies this model to four topics of interest for the electrical engineer.

First part calculates the stator-voltage harmonics. Connecting a hydro-generator on the network requires to satisfy some electromagnetic compatibility rules. The quality of its terminal voltage can be characterized by some factors: Telephone Harmonic Factor (THF), Telephone Harmonic Distortion (THD). The knowledge of the emitted harmonics is relevant in the design of hydro-motor/generator since it will determine whether the machine is allowed or not to be coupled on the grid. The harmonic content of the stator voltage is explained with regards to the winding configuration and the level of saturation.

Second part deals with the problem of the radial electromagnetic forces applied on the stator core. The knowledge of these components is necessary since they might excite an eigen-mode of the stator structure, leading to vibration and noise. The extraction of the radial forces from the airgap flux density harmonics is described and made, as example, for two machines, one with integer slot windings and one with a fractional slot winding at the stator. For the latter, we identify a dangerous component and correlate its amplitude with the measured vibration at various load conditions. Furthermore we describe a winding optimization method making it possible to rearrange a fractional winding in order to decrease the amplitude of a particular electromagnetic force.

Third part evaluates the dynamic electromagnetic torques. As for the radial forces the knowledge of these components is important. Indeed they can excite an eigen-mode of the shaft line composed by the turbine, the shaft and the motor-generator's rotor. The harmonic content of the torque is first obtained from time stepping 2DFE simulations of load operation points. The results are explained by using the analytical model. The eigen-frequencies of the shaft line are extracted by using a reduced three-mass model. The comparison of the eigen-frequencies and the exciting torque components make it possible to identify the dangerous components. The investigation is extended to the study of the machine behavior during start-up as a motor for pumping operations. The FE simulation process developed in Chapter 3 enables to simulate this transient operation and to extract the electromagnetic torque variations.

Fourth part calculates the power losses induced in the stator and rotor magnetic cores. These losses are expected to be higher than in a conventional synchronous machine. This is due to the fact that there are a high number of flux density harmonics and that the magnetic field is not necessarily fixed with respect to the rotor. The developed algorithm is based on the evaluation of the flux density harmonics in the teeth and yoke regions considering the airgap harmonics. The corresponding induced losses are obtained by applying the well-known Bertotti decomposition losses model and considering additional effects such as minor hysteresis cycles or bidirectional magnetic flux excitations.

5.2 The stator voltage harmonics

Following section computes the stator voltage shape of a DFIM, analyzes its harmonic content and proposes possible way of improvements. First part computes by a time-stepping 2DFE simulation the no-load stator voltage harmonics. The influence of the magnetic circuit saturation is investigated as well as the impact of rotor circulating currents. The computation is done first by considering an ideal sinusoidal voltage source at the rotor then a simplified VSI. A regulation method based on the approach developed in Chapter 3 for the time-stepping load computation is used here in order to perform efficiently the simulations. Second part uses the airgap harmonic model developed in Chapter 4 to compute analytically the stator voltage shape at no-load operation and to explain the results of the FE simulations. The impact of slip on the harmonic content is studied. Third part proposes improvements to optimize the stator voltage shape mainly by changing the stator and rotor winding configuration.

5.2.1 Finite Element studies

In a first stage, we perform 2DFE simulations in order to study the effect of the magnetic saturation, of the rotor voltage harmonics and of the slip on the stator voltage harmonic content. The FE model is the same as the one used in Chapter 3. The electrical circuit is also the same but its parameters are different:

- the rotational speed is imposed in order keep the stator frequency f_{s} constant.
- the network impedance is set to an infinite value in order to prevent any flow of stator current.

I. Harmonic content of the stator voltage

This part analyzes the stator line-to-line voltage induced at no-load operation. The simulations are done at the synchronization speed, in this case the rotor winding is supplied with a three-phase dc voltage system $V_{\mathrm{r,a}} = V_{\mathrm{r}}^{\mathrm{max}}$, $V_{\mathrm{r,b}} = -V_{\mathrm{r}}^{\mathrm{max}}/2$, $V_{\mathrm{r,c}} = -V_{\mathrm{r}}^{\mathrm{max}}/2$. V_r^{max} is the amplitude of the applied rotor voltage in order to generate the desired stator voltage. Furthermore the mechanical rotational speed is equal to the synchronous speed i.e. $f_{\mathrm{s}} \cdot 60/p$. The stator is connected on a very large resistive load. In order to accelerate the convergence of the compu-

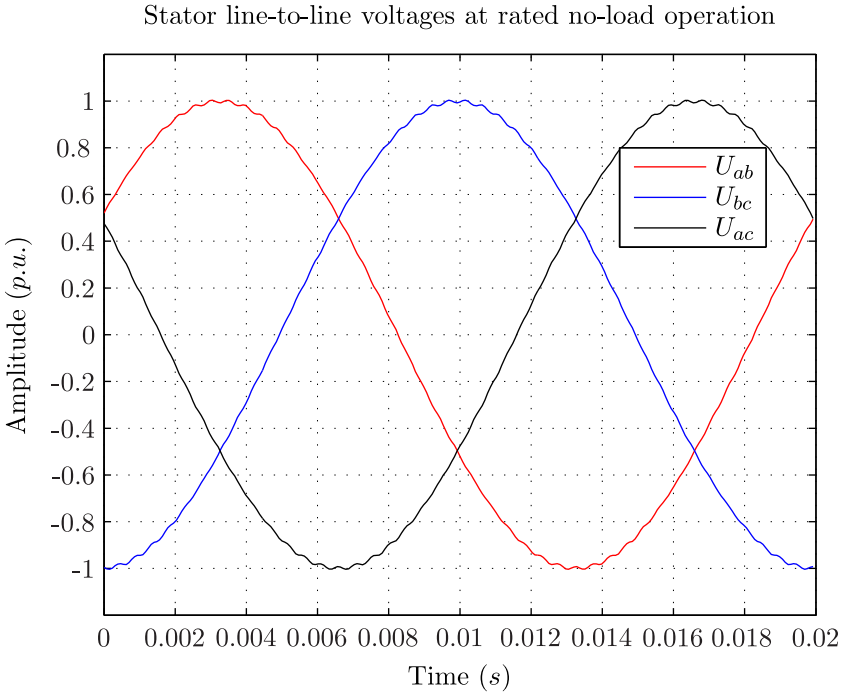

Figure 5.1: FEM: Stator line-to-line voltage at rated no-load operation

tation, the simulation is initialized by supplying the rotor winding with a three-phase current system: $I_{\mathrm{r,a}} = I_{\mathrm{r}}^{\max}$, $I_{\mathrm{r,b}} = -I_{\mathrm{r}}^{\max}/2$, $I_{\mathrm{r,c}} = -I_{\mathrm{r}}^{\max}/2$ where $I_{\mathrm{r}} = V_{\mathrm{r}}/R_{\mathrm{r}}$. The computation is done for a twelve-pole machine having $q_{\mathrm{s}} = 8$ stator slots per pole and phase and $q_{\mathrm{r}} = 7$ rotor slots per pole and phase.

Figure 5.1 shows the variation of the three stator line-to-line voltages at rated no-load operation. Figure 5.2 shows the corresponding harmonic spectrum obtained by Fourier analysis. One can see the presence of several harmonics and more particularly the winding harmonics at the ranks 5, 7, 11, 13 and the so-called slot harmonics whose ranks are equal to $6 \cdot q_{\mathrm{r}} \pm 1 = 41 \ldots 43$ and $6 \cdot q_{\mathrm{s}} \pm 1 = 47 \ldots 49$.

In order to characterize the quality of the stator voltage, the coefficients THF and THD given by Equations (5.1) and (5.2) can be used:

$$\mathrm{THF} = \sqrt{\sum_{\nu=1}^{100} w_\nu \cdot \frac{U_\nu}{U_1}} \tag{5.1}$$

$$\mathrm{THD} = \sqrt{\sum_{\nu=2}^{100} \frac{U_\nu}{U_1}} \tag{5.2}$$

where U_ν is the amplitude of the ν^{th} line-to line voltage harmonic, w_ν is the weighting coefficient of the ν^{th} voltage harmonic and U_1 is the amplitude of the fundamental line-to line voltage harmonic. Contrarily to the THD in which all the harmonics have the same weight, the THF gives more importance to certain harmonics. Figure 5.3 shows the weighting coefficients w_ν

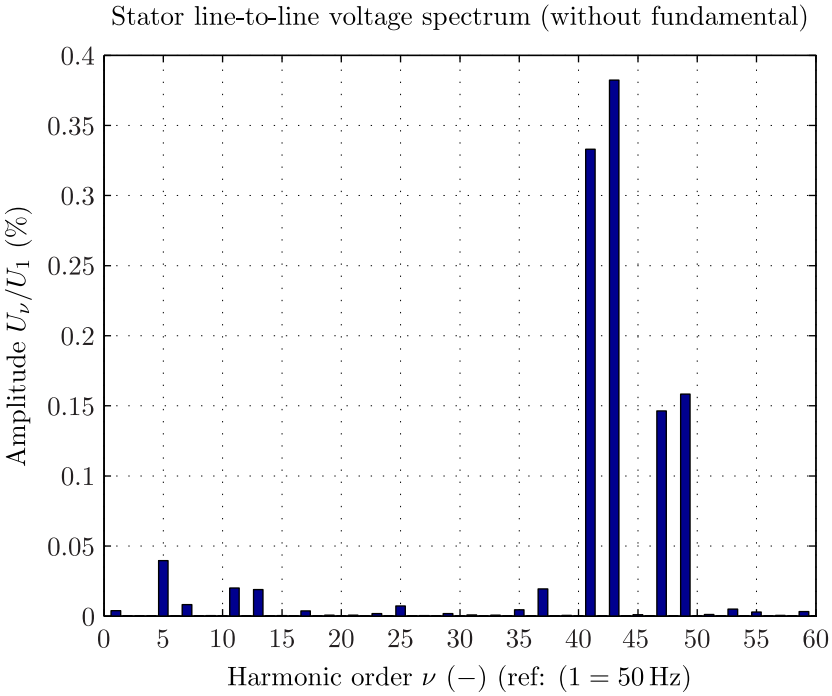

Figure 5.2: FEM: Stator line to line voltage spectrum at rated no-load operation (without fundamental)

used in the computation of the THF coefficient. One can see that harmonics in the rank $20-45$ (considering a reference frequency equal to 50 Hz) will be strongly reinforced. In our case these harmonics correspond to the slot harmonics. Generally for large hydro-generators the THD coefficient has to be less than 5% while the THF coefficient must be less than 1.5%. In the studied case, the THF equals 0.95% and the THD equals 0.55% which is within the acceptable limits. Furthermore maximal admissible values are set on each voltage harmonics. These limits depend on the class of the network on which the machine is connected. Figure 5.4 compares such limits as defined by the IEEE norm with the computed stator voltage harmonics of the studied machine. Note that the differences between class 1 and class 2 concern only the first harmonics. Most harmonics are below the limits of all classes, except the component $6 \cdot q_\mathrm{r} + 1$ which slightly overshoots the class 1 and class 2 limits. Following part studies more in details the slot harmonics and in particular the impact of the magnetic saturation and rotor circulating currents.

II. Impact of the magnetic circuit saturation and rotor circulating currents

In order to study more deeply the impact of magnetic saturation on the stator voltage harmonics and more particularly on the slots harmonics, the no-load operation is simulated for several states of magnetization i.e. from 0.1 to 1.2 p.u. of the rated stator voltage. Figure 5.5 shows the corresponding variations of the slot harmonics $\nu = 6 \cdot q_\mathrm{s} \pm 1$ and $\nu = 6 \cdot q_\mathrm{r} \pm 1$. In order to study

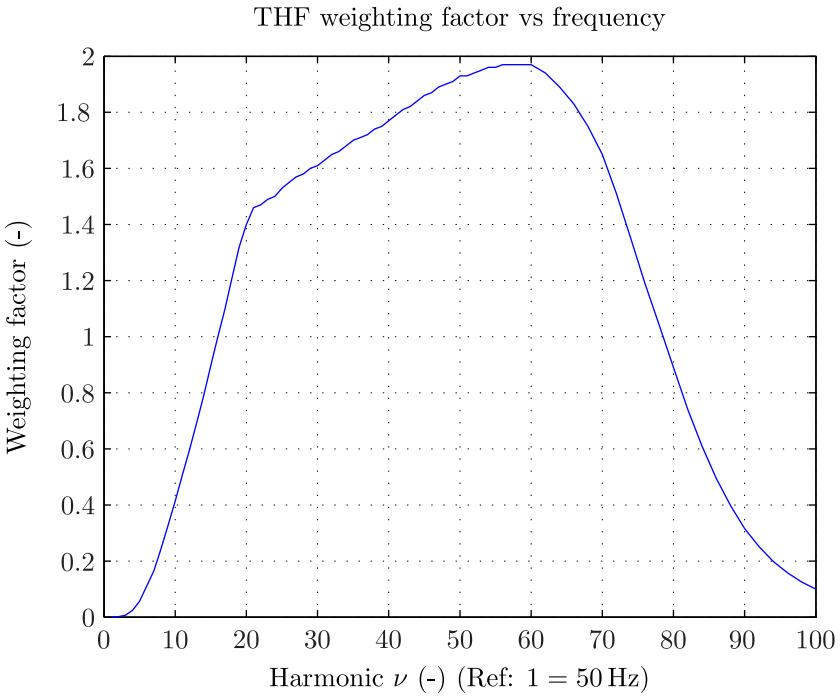

Figure 5.3: THF weighting factors

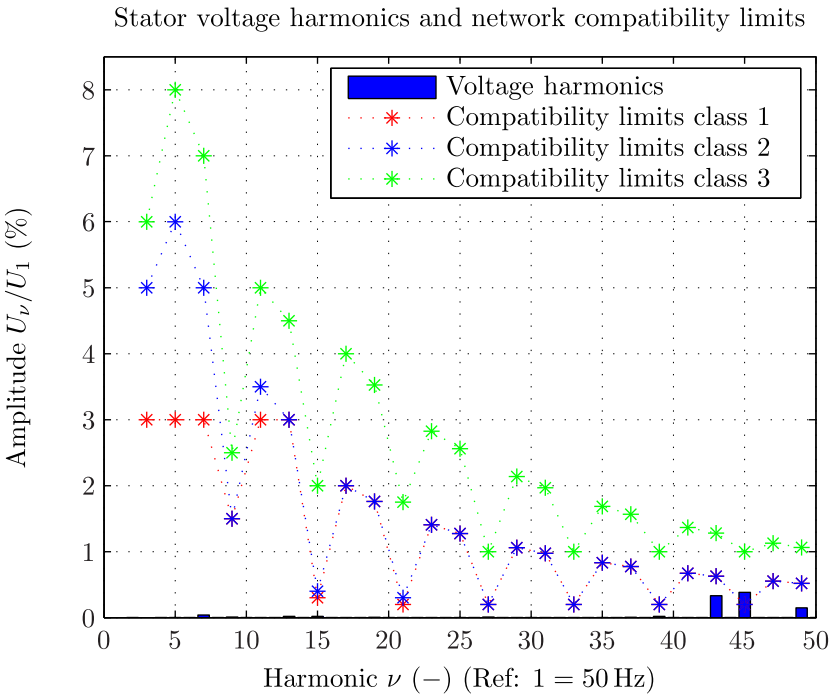

Figure 5.4: Voltage harmonic compatibility levels

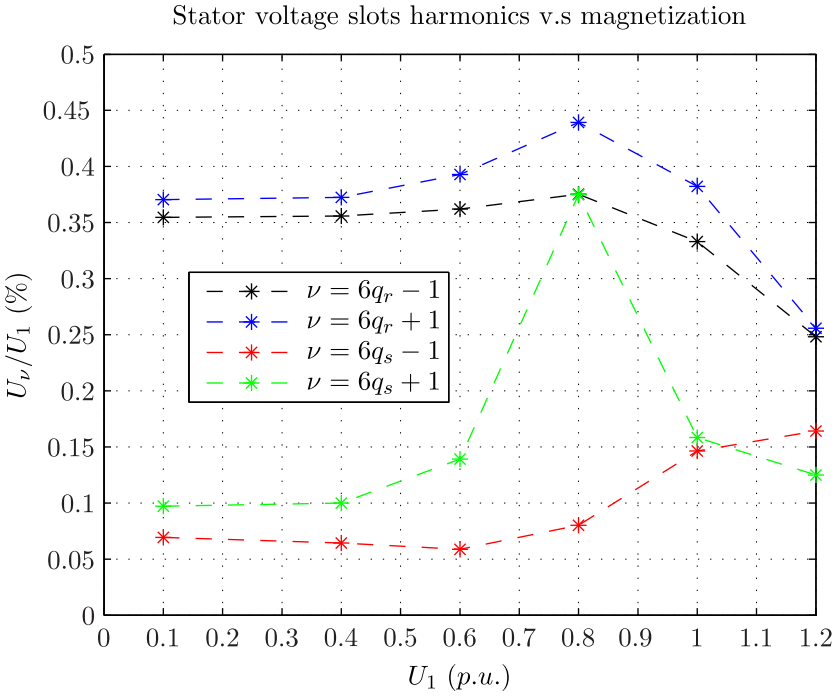

Figure 5.5: FEM: Effect of magnetization on slot harmonics

the effect of the magnetic saturation, the quantity U_ν/U_1 is calculated where U_ν is the amplitude of the ν^{th} slot harmonic and U_1 the amplitude of the fundamental component at the given state of magnetization. The variation of the slot harmonics is clearly not linear. This can be explained by the fact that the stator and rotor teeth get more and more saturated when increasing the magnetization which leads to a modification of the airgap permeance harmonics. In the studied case, the rotor winding is supplied with a three-phase dc voltage source. When studying the circulating current in one rotor phase as shown in Figure 5.6, one can see the presence of small ripples whose frequency is equal to the stator slot frequency i.e. $6q_{\text{s}}f_{\text{s}}$ Hz. Figure 5.7 shows the impact of magnetization on this particular rotor current harmonic. The displayed amplitude is expressed in percent of the rotor current dc component given the magnetization state. One can see that the rotor current harmonic is very sensitive to the state of magnetization. The more the magnetic circuit gets saturated, the larger the rotor current harmonic becomes.

So as to study the impact of the rotor circulating currents on the stator voltage harmonic content, two simulations are done one by applying voltage sources on the rotor winding and one by feeding directly the rotor winding with current sources. The second simulation consequently prevents the circulation of extra currents due to the slots harmonics.

Figure 5.8 compares the corresponding stator voltage spectrum for the rated no-load operation. It appears that the slots harmonics are much stronger, especially the component $6q_{\text{s}} - 1$ when the simulation is preventing the circulation of additional rotor current components. Although the rotor circulating current relative amplitude is small (Figure 5.7), its impact on the harmonic content of the stator voltage is very large. Such computations confirm firstly the strong de-

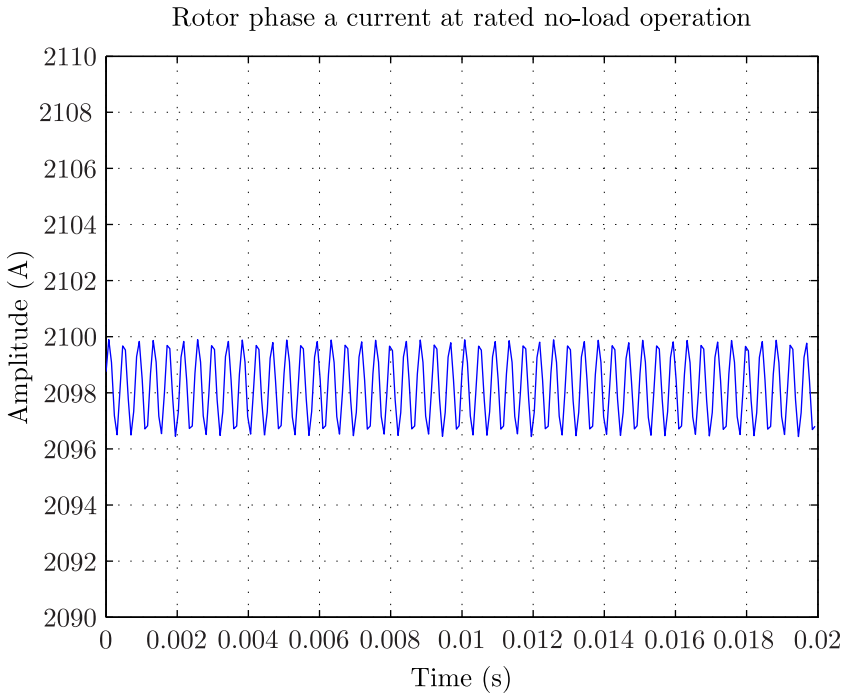

Figure 5.6: FEM: Rotor phase current at rated no-load operation

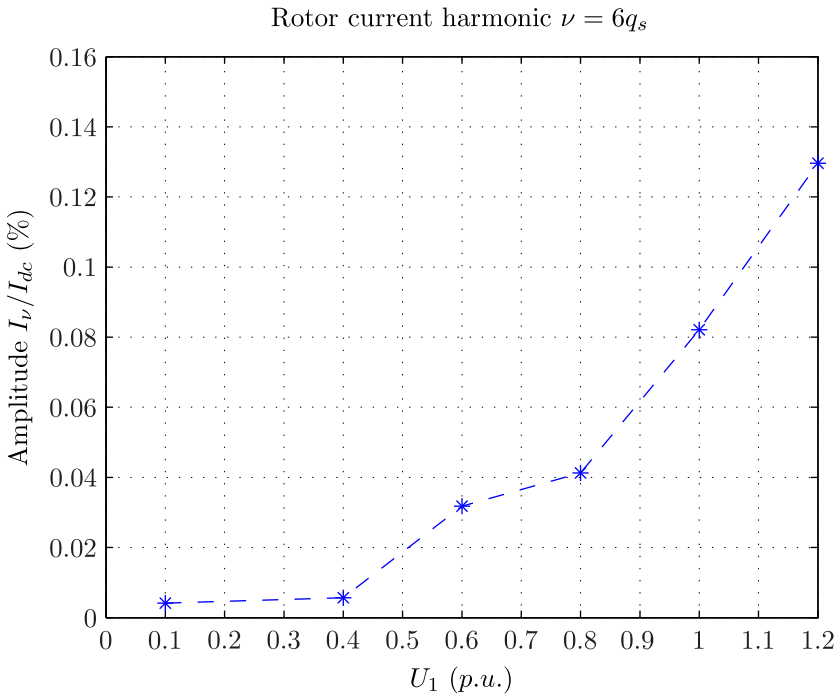

Figure 5.7: FEM: Effect of magnetization on slot harmonics

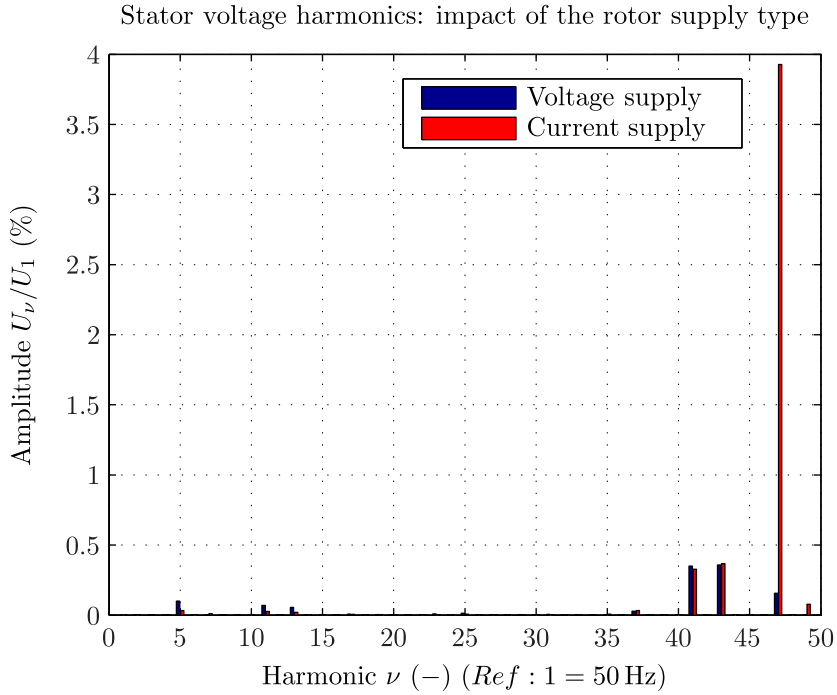

Figure 5.8: Comparison current and voltage supply (without fundamental)

pendency of the harmonic content of the stator voltage on the magnetic state of the machine, and secondly shows the presence of rotor circulating currents when the magnetic saturation increases. These rotor currents seem to play a non-negligible role by creating damping magnetic field components. This phenomena is studied in more details in the next part.

5.2.2 Analytic study

This part proposes an analytical method based on the airgap flux density model developed in Chapter 4, calculating the stator voltage harmonic content of DFIM. This makes it possible firstly to understand the origin of the harmonics highlighted by the previous FE results, secondly to test the impact of different elements, number of slots, winding configuration and slip on the results.

I. The method

As seen previously the airgap flux density can be expressed as a Fourier series given by Equation (5.3). In the studied case, the airgap flux density is only created by the rotor winding and written as:

$$B_\delta\left(\alpha_s, t\right) = \sum_{\nu=1}^{+\infty} B_\nu \cos\left(P_\nu \alpha_s + 2\pi F_\nu t + C_\nu\right) \tag{5.3}$$

Note that we consider the airgap flux density calculated at the stator bore diameter. The voltage V_j induced on the j^{th} stator phase is given by Equation (5.4), where Φ_j is the flux seen by the

j^{th} phase.

$$V_j(t) = -\frac{\mathrm{d}\Phi_j(t)}{\mathrm{d}t} \tag{5.4}$$

In order to calculate Φ_j we consider the stator winding configuration. Table 4.1 in Chapter 4 has shown an example of winding configuration. The flux Φ_{j,t_i} seen by one winding turn t_i (one top bar and one bottom bar in series) belonging to the j^{th} stator phase is given by:

$$\Phi_{j,\mathrm{t_i}}(\alpha_\mathrm{s}, t) = \frac{l_\mathrm{s} \cdot D_\mathrm{b,s}}{2} \sum_{\nu=1}^{+\infty} \int_{\alpha_{\mathrm{t_i}}}^{\mathrm{t_i}+s} \hat{B}_{\delta,\nu} \cos\left(P_\nu \alpha_\mathrm{s} + 2\pi F_\nu t + C_\nu\right) d\alpha \tag{5.5}$$

where $\mathrm{t_i}$ is the angular position of the t_i^{th} top bar of the j^{th} phase and s is the stator winding angular opening. Finally the total flux seen by the y^{th} phase is given by Equation (5.6), where $N_\mathrm{a,s}$ is the number of parallel circuits.

$$\Phi_j(t) = \frac{1}{N_\mathrm{a,s}} \sum_{t_i=1}^{N_\mathrm{z,s}/3} \Phi_{j,t_i}(\mathrm{t_i}, t) \tag{5.6}$$

Note that the presented calculation assumes that all parallel circuits of each phase are identical, as it is normally the case. In the exceptional case of unbalanced windings, the calculation of the voltage would have to be done separately on each parallel circuits. Finally the voltage induced on the j^{th} phase is obtained by applying Equation (5.4).

II. Validation with Finite Element

This part compares the analytical and the FE calculation. In a first stage, the magnetic saturation is not considered, Figure 5.9 shows the stator voltage harmonics when calculating the airgap permeance harmonics using the BE model developed in Chapter 4. For comparison purposes, Figure 5.10 shows the stator voltage harmonics when the simplified airgap permance according to Equation (4.17) is used.

One can clearly notice the better accuracy offered by the BE algorithm. Indeed the slot harmonics appear strongly over-estimated. In the following, only the results given by the BE model will be discussed. It appears that the results given by the analytical method match those obtained by FE. The main discrepancy arises regarding the slot harmonics $6q_\mathrm{s} \pm 1$ which are not as high in the analytical results. However given the low amplitude of such components, the results are satisfying.

In a second stage the impact of saturation is considered. Previous section has shown the strong dependency of the slot harmonics on the magnetic state and the presence of circulating currents in the rotor winding. Chapters 2 and 4 have shown that when the magnetization increases, extra airgap harmonics due to magnetic saturation appear leading to a modulation of the airgap permeance. These additional airgap flux density harmonics contribute to the amplification of the slot harmonics and in the studied case of the frequency component $6q_\mathrm{s} + 1$. In order to identify the responsible airgap harmonics, we use the expression of the airgap flux density developed in

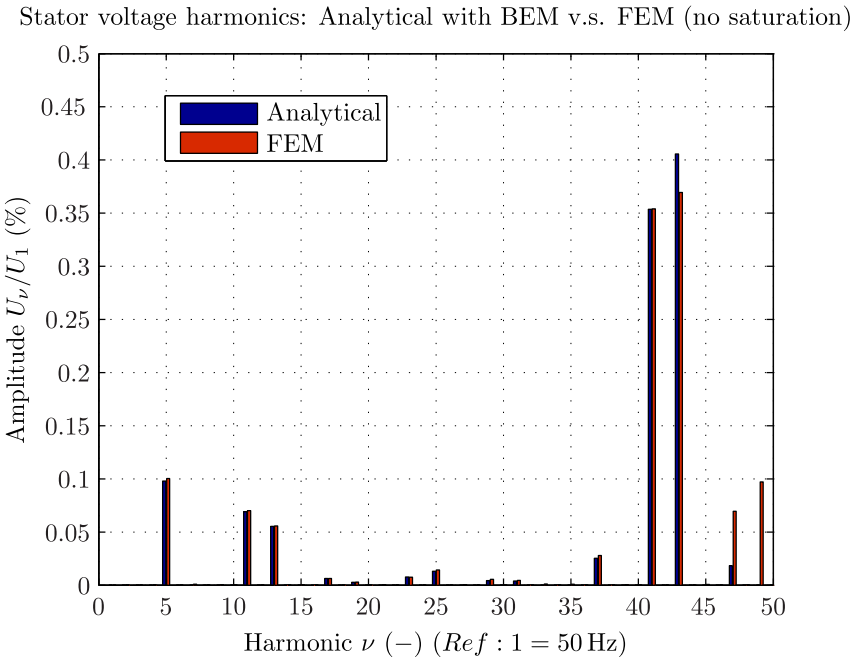

Figure 5.9: Comparison analytical with BEM and Finite Element method (FEM) (no saturation and without fundamental)

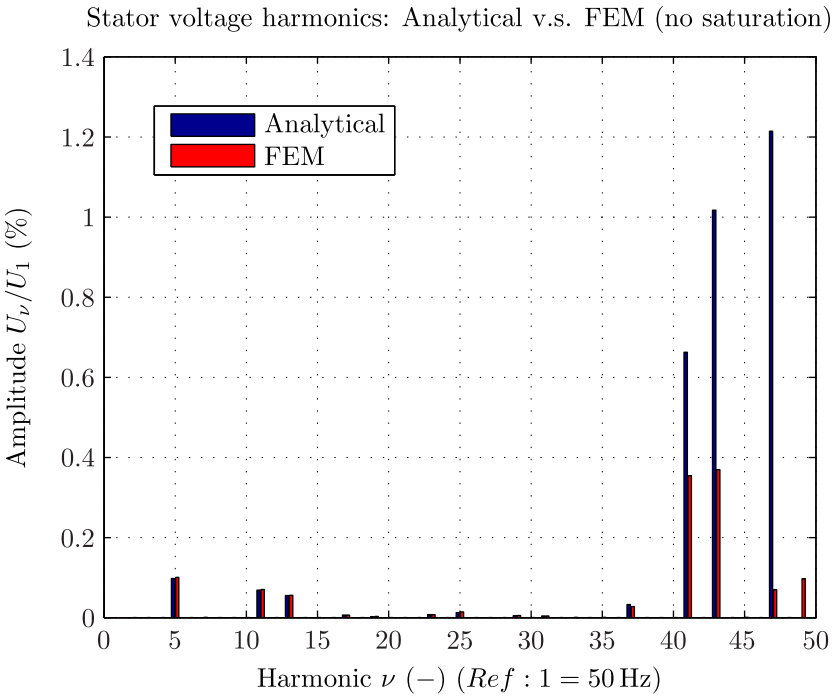

Figure 5.10: Comparison analytical, simple permeance formula and FEM (no saturation and without fundamental)

Chapter 4. More particularly at no-load the airgap flux density is given by:

$$B_{\delta}\left(\alpha_{\mathrm{s}},t\right)=B_{\delta,\mathrm{r},0}^{\mathcal{S}}\left(\alpha_{\mathrm{s}},t\right)\cdot\frac{\Lambda^{\mathcal{S}}\left(\alpha_{\mathrm{s}},t\right)}{\Lambda_{0}}\cdot K_{\mathrm{sat}}\left(\alpha_{\mathrm{s}},t\right) \tag{5.7}$$

Furthermore as seen in Chapter 4, B_r, Λ and K_{sat} can be expressed as a sum of harmonic waves written as:

$$A_{\nu}\cdot\cos\left(P_{\nu}\cdot\alpha+\cdot 2\pi F_{\nu}\cdot t+C_{\nu}\right) \tag{5.8}$$

where A_ν is the amplitude of the ν^{th} harmonic, P_ν is the number of pole pairs of the ν^{th} harmonic, F_ν is the frequency of the ν^{th} harmonic and C_ν is the frequency of the ν^{th} harmonic. Note that the product of two harmonics waves

$$\begin{aligned}&A_{\nu_1}\cdot\cos\left(P_{\nu_1}\cdot\alpha+2\pi\cdot F_{\nu_1}\cdot t+C_{\nu_1}\right)\\&A_{\nu_2}\cdot\cos\left(P_{\nu_2}\cdot\alpha+2\pi\cdot F_{\nu_2}\cdot t+C_{\nu_2}\right)\end{aligned} \tag{5.9}$$

gives two new harmonic waves:

$$\begin{aligned}&\frac{A_{\nu_1}\cdot A_{\nu_2}}{2}\cdot\cos\left(\left(P_{\nu_1}+P_{\nu_2}\right)\cdot\alpha+2\pi\cdot\left(F_{\nu_1}+F_{\nu_2}\right)\cdot t+C_{\nu_1}+C_{\nu_2}\right)\\&\frac{A_{\nu_1}\cdot A_{\nu_2}}{2}\cdot\cos\left(\left(P_{\nu_1}-P_{\nu_2}\right)\cdot\alpha+2\pi\cdot\left(F_{\nu_1}-F_{\nu_2}\right)\cdot t+C_{\nu_1}-C_{\nu_2}\right)\end{aligned} \tag{5.10}$$

In the following, in order to simplify the notations, each harmonic wave is written as:

$$A_{\nu}\cdot\left[P_{\nu},F_{\nu}\right] \tag{5.11}$$

the phase shift C_ν is not considered as it is irrelevant here. By convention F_ν positive, means that the wave rotates in the same direction as the fundamental airgap field. Considering for example the airgap permeance component due to the rotor and stator slots $\Lambda_{\mathrm{s},\mathrm{r},k_{\mathrm{s}},k_{\mathrm{r}}}\cdot[6p\cdot(k_{\mathrm{s}}q_{\mathrm{s}}-k_{\mathrm{r}}q_{\mathrm{s}}),-6k_{\mathrm{r}}q_{\mathrm{r}}f_{\mathrm{s}}]$ and the saturated airgap permeance component $K_{2n}\cdot[2n\cdot p,2\cdot nf_{\mathrm{s}}]$ where n is an integer. By multiplying these two components, emerge two airgap permeance components:

$$\begin{aligned}&\frac{\Lambda_{\mathrm{s},\mathrm{r},k_{\mathrm{s}},k_{\mathrm{r}}}\cdot K_{2n}}{2}\cdot\left[6\cdot p\cdot\left(k_{\mathrm{s}}q_{\mathrm{s}}-k_{\mathrm{r}}q_{\mathrm{s}}\right)+2n\cdot p,\left(-6k_{\mathrm{r}}q_{\mathrm{r}}+2n\right)f_{\mathrm{s}}\right]\\&\frac{\Lambda_{\mathrm{s},\mathrm{r},k_{\mathrm{s}},k_{\mathrm{r}}}\cdot K_{2n}}{2}\cdot\left[6\cdot p\cdot\left(k_{\mathrm{s}}q_{\mathrm{s}}-k_{\mathrm{r}}q_{\mathrm{s}}\right)-2n\cdot p,\left(-6k_{\mathrm{r}}q_{\mathrm{r}}-2n\right)f_{\mathrm{s}}\right]\end{aligned} \tag{5.12}$$

When combining this new airgap permeance component with the fundamental component of B_δ, i.e $\hat{B}_{\delta,\mathrm{f}}\cdot[p,1]$ the following airgap flux density component emerges:

$$\begin{aligned}&\frac{\hat{B}_{\delta,\mathrm{f}}\cdot\Lambda_{\mathrm{s},\mathrm{r},k_{\mathrm{s}},k_{\mathrm{r}}}\cdot K_{2n}}{4}\cdot\left[p+6\cdot p\cdot\left(\left(k_{\mathrm{s}}q_{\mathrm{s}}-k_{\mathrm{r}}q_{\mathrm{s}}\right)+2n\cdot p,\left(1-6k_{\mathrm{r}}q_{\mathrm{r}}+2n\right)f_{\mathrm{s}}\right]\right.\\&\frac{\hat{B}_{\delta,\mathrm{f}}\cdot\Lambda_{\mathrm{s},\mathrm{r},k_{\mathrm{s}},k_{\mathrm{r}}}\cdot K_{2n}}{4}\cdot\left[p+6\cdot p\cdot\left(\left(k_{\mathrm{s}}q_{\mathrm{s}}-k_{\mathrm{r}}q_{\mathrm{s}}\right)-2n\cdot p,\left(1-6k_{\mathrm{r}}q_{\mathrm{r}}-2n\right)f_{\mathrm{s}}\right]\right.\\&\frac{\hat{B}_{\delta,\mathrm{f}}\cdot\Lambda_{\mathrm{s},\mathrm{r},k_{\mathrm{s}},k_{\mathrm{r}}}\cdot K_{2n}}{4}\cdot\left[p-6\cdot p\cdot\left(\left(k_{\mathrm{s}}q_{\mathrm{s}}-k_{\mathrm{r}}q_{\mathrm{s}}\right)-2n\cdot p,\left(1+6k_{\mathrm{r}}q_{\mathrm{r}}-2n\right)f_{\mathrm{s}}\right]\right.\\&\frac{\hat{B}_{\delta,\mathrm{f}}\cdot\Lambda_{\mathrm{s},\mathrm{r},k_{\mathrm{s}},k_{\mathrm{r}}}\cdot K_{2n}}{4}\cdot\left[p-6\cdot p\cdot\left(\left(k_{\mathrm{s}}q_{\mathrm{s}}-k_{\mathrm{r}}q_{\mathrm{s}}\right)+2n\cdot p,\left(1+6k_{\mathrm{r}}q_{\mathrm{r}}+2n\right)f_{\mathrm{s}}\right]\right.\end{aligned} \tag{5.13}$$

We consider $k_{\mathrm{s}} = 1$, $k_{\mathrm{r}} = 1$. Furthermore in the studied case $q_{\mathrm{s}} - q_{\mathrm{r}} = 1$. If $n = 2$ a particular airgap flux density component arrises:

$$\frac{\hat{B}_{\delta,\mathrm{f}} \cdot \Lambda_{\mathrm{s,r},1,1} \cdot K_2}{4} \cdot [-p, (5 + 6q_{\mathrm{r}})f_{\mathrm{s}}] \tag{5.14}$$

which can be rewritten as:

$$\frac{\hat{B}_{\delta,\mathrm{f}} \cdot \Lambda_{\mathrm{s,r},1,1} \cdot K_2}{4} \cdot \cos(p \cdot \alpha_{\mathrm{s}} + (-6 \cdot q_{\mathrm{s}} + 1) \cdot 2\pi \cdot f_{\mathrm{s}} \cdot t) \tag{5.15}$$

Noting that the spatial rank of this component is exactly equal to the number of pole pairs, the corresponding induced phase stator voltage due to such component is obtained by:

$$V_{\mathrm{s}} = \frac{D_{\mathrm{b,s}} \cdot l_{\mathrm{s}}}{2} \cdot N_{\mathrm{s,s}} \xi_{\mathrm{f,s}} \cdot (6q_{\mathrm{s}} - 1) \cdot (2\pi \cdot f_{\mathrm{s}}) \cdot \frac{\hat{B}_{\delta,\mathrm{f}} \cdot \Lambda_{\mathrm{s,r},1,1} \cdot K_2}{4} \tag{5.16}$$

Given the fact that the spatial rank of this component is equal to the number of pole pairs of the winding the corresponding stator voltage harmonic will be high due to the winding coefficient amplification $\xi_{\mathrm{f,s}}$. In this case, because of saturation, there is resonance between the saturation harmonics and the stator winding. Consequently a high amplitude voltage harmonic having a frequency equal to $(6 \cdot q_{\mathrm{s}} - 1) \cdot f_{\mathrm{s}}$ Hz will be induced on the stator winding as it was shown in the previous section. However when expressing this flux density wave in the rotor frame we obtain the component:

$$\frac{\hat{B}_{\delta,\mathrm{f}} \cdot \Lambda_{\mathrm{s,r},1,1} \cdot K_2}{4} \cdot \cos(p \cdot \alpha_{\mathrm{r}} + (-6 \cdot q_{\mathrm{s}}) \cdot 2\pi \cdot f_{\mathrm{s}} \cdot t) \tag{5.17}$$

The corresponding induced rotor voltage due to such component is obtained by:

$$V_{\mathrm{r}} = \frac{D_{\mathrm{b,r}} \cdot l_{\mathrm{r}}}{2} \cdot N_{\mathrm{s,r}} \xi_{\mathrm{f,r}} \cdot 6q_{\mathrm{s}} \cdot (2\pi \cdot f_{\mathrm{s}}) \cdot \frac{\hat{B}_{\delta,\mathrm{f}} \cdot \Lambda_{\mathrm{s,r},1,1} \cdot K_2}{4} \tag{5.18}$$

As for the stator voltage, the induced voltage on the rotor winding will be high due to the winding coefficient amplification $\xi_{\mathrm{f,r}}$. Consequently a high amplitude voltage harmonic having a frequency equal to $6 \cdot q_{\mathrm{r}} \cdot f_{\mathrm{s}}$ Hz will be induced on the rotor winding short-circuited by the rotor winding impedance. These circulating rotor currents will create additional magnetic field components damping the parasitic airgap flux density component. This confirms the previous observations done when feeding the rotor winding with a current source or with a voltage source. One should pay attention to the fact that the amplitude of the circulating rotor current will depend on the rotor short-circuit impedance but also on the rotor converter configuration. Note that the amplification of the harmonic appears here mainly because of the studied winding configuration $q_{\mathrm{s}} = q_{\mathrm{r}} - 1$. In case the number of slots per pole and phase between the stator and rotor is greater than one, this resonance effect should not be so high.

Figure 5.11 shows the result of the comparison between our model and the FE computation when considering the saturation. One can see that the winding harmonics, for example $\nu = 5, 11, 13$, are overestimated by the analytical calculation. Furthermore, while the rotor slots harmonics $6q_r \pm 1$ amplitudes agree well with the FE results, the discrepancy is larger for the

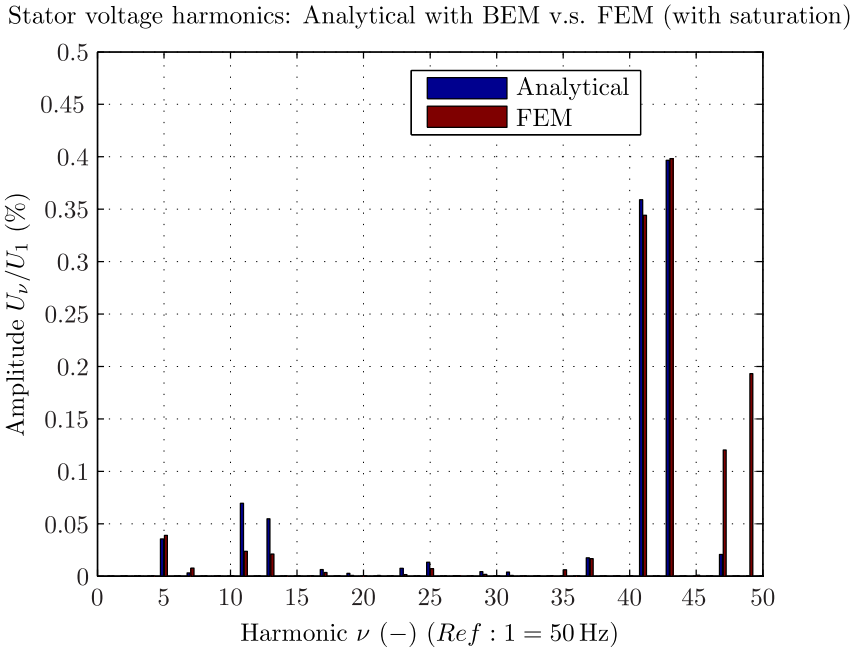

Figure 5.11: Comparison analytical with BEM and FEM (with saturation and without fundamental)

harmonics $6q_s \pm 1$. Although differences exist between both spectra, the THF and THD still match. Indeed for the analytical calculation we have THF = 0.98% and THD = 0.5% vs THF = 0.9% and THD = 0.5% for the FE calculation. One should note that although the circulating rotor currents are not considered in the analytical calculation, the slot harmonics $6q_s \pm 1$ remain almost unchanged which does not really agree with the FE results shown in the previous section (FE with current sources). It can be explained by the fact that our model does not make it possible to accurately consider the impact of the saturation on the teeth harmonics. We see here again the benefit of further developing the coupling of the BE with the magnetic permeance network.

Finally although the impact of the saturation is not as strong in our model compared to the FE simulation, our model makes it possible to determine the main stator voltage harmonics. In the following we study the impact of the slip on the harmonic content.

5.2.3 Effect of the slip

The last computations were done at the synchronous speed i.e. when the slip is zero. Here we analyzed the effect of the slip on the harmonic content. Chapter 4 demonstrated that when changing the slip, the frequency of the rotor winding field harmonics get shifted. It is the same for the airgap permeance harmonics due to rotor slots.

Figure 5.12 shows the evolution of the slots harmonic frequencies when changing the slip taking the fundamental stator frequency as reference. One can observe that out of the synchronous

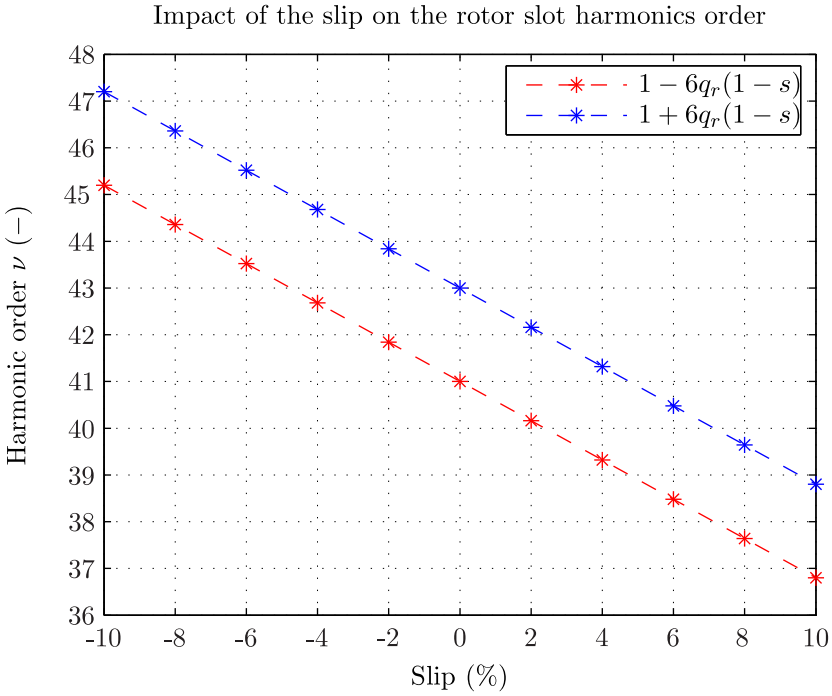

Figure 5.12: Impact of slip on rotor slot harmonics

speed, the slot harmonic frequency may not be any more integer multiple of the stator frequency which is confirmed by [Tag08]. This is also the case for the other rotor harmonics. Such harmonics are called inter-harmonics. Consequently when analyzing the stator voltage harmonic content, when the slip is different from zero, one has to make the Fourier analysis on more than one electrical period in order to extract as accurately as possible all the harmonics.

Figure 5.13 shows the impact of the slip on the THD. One can see that the THD is higher in hyper-synchronous mode than in hypo-synchronous mode. Indeed in hyper-synchronous mode, the frequencies of the airgap flux density harmonics (the ones sensitive to the slip) increase. Consequently the corresponding induced voltages amplitude also increase.

5.2.4 Effect of the rotor voltage source harmonics

Until now, the rotor supply was modeled as perfect sinusoidal voltage sources. In the reality the rotor is fed with a VSI converter. Figure 5.14 shows the electrical circuit used in the FE model in order to consider the converter harmonics. Only the inverter part is simulated and the voltage of the dc-bus is assumed constant. In order to perform efficiently the simulation and to avoid long initialization time, the control of the machine under no-load condition is implemented according to [Pan10]. This implementation is based on the same principles developed in Chapter 3. However instead of applying directly the rotor voltages $V_{\mathrm{r,a}}$ $V_{\mathrm{r,b}}$ $V_{\mathrm{r,c}}$ these ones are compared to a triangular signal with a certain frequency (here 300 Hz) as it is done usually for PWM converter control.

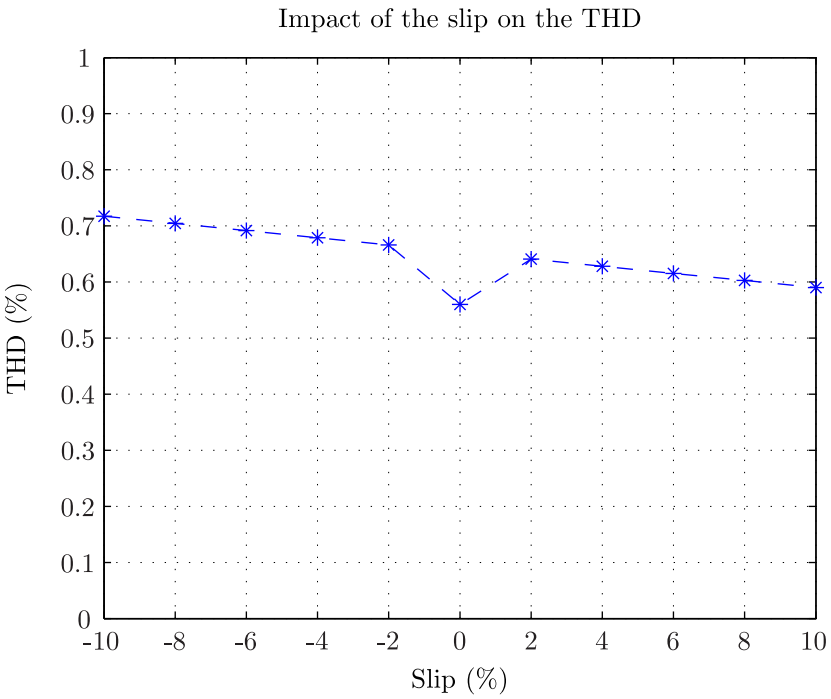

Figure 5.13: Impact of slip on THD (without converter harmonics)

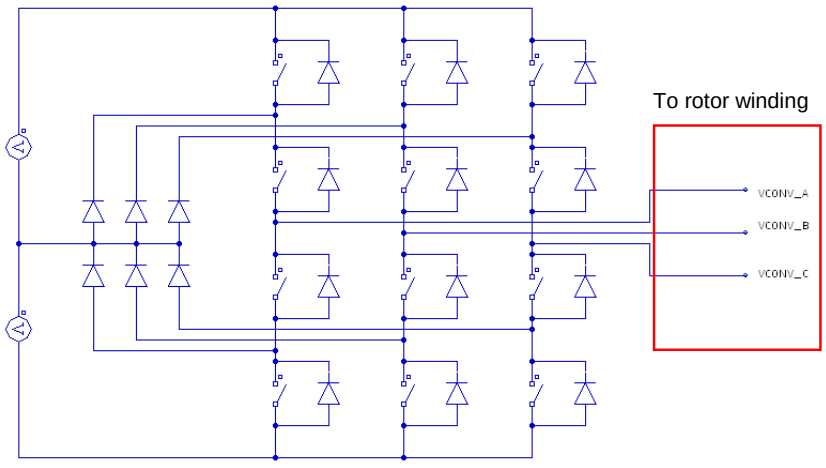

Figure 5.14: FEM: Coupling electrical circuit with simplified inverter

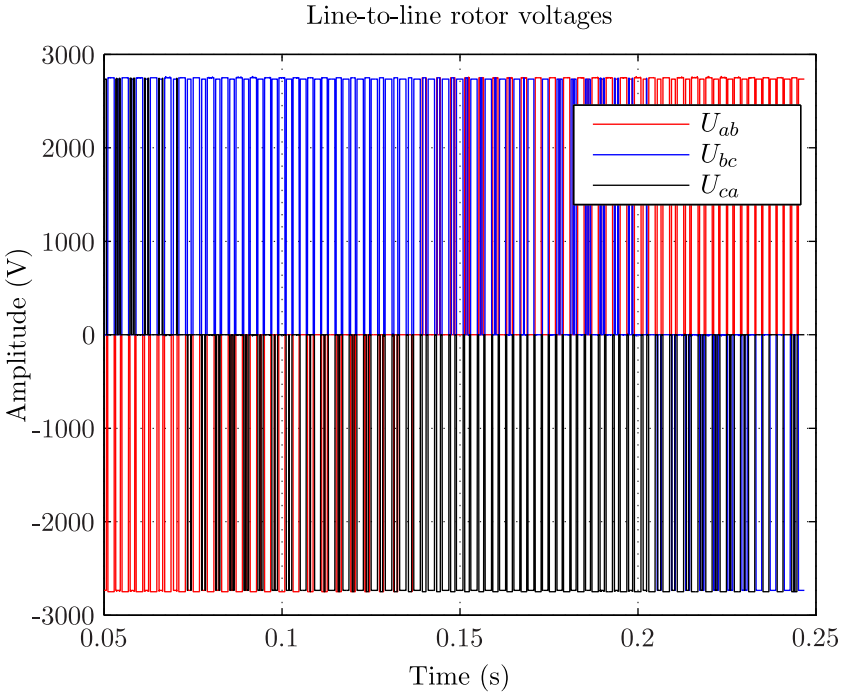

Figure 5.15: FEM: Rotor voltages with simplified inverter

Figure 5.14 and Figure 5.15 show the evolution of the line-to-line rotor voltages and rotor phase currents. It appears that the current remains sinusoidal which is due to the large machine inductance which filters the parasitic harmonics. The small ripples are due to the voltage pulses.

Figure 5.17 shows the evolution of the stator line-to-line voltages. Figure 5.18 shows the corresponding harmonics content. As we can see, introducing the VSI converter leads to new stator voltage harmonics, although the rotor currents remain clean. In this case the THD is about 3.8% while it was equal to 0.66% in the case of a sinusoidal rotor voltage supply. Although the methodology is correct, one should pay attention that the converter used for the calculation is here very simplified and may not correspond fully to the reality. However we have shown that our modeling methods can efficiently perform such complex simulation. This subject should be deeply studied in the future.

III. Reduction of slots harmonics

Last parts have shown, putting aside the rotor converter harmonics, that the slot harmonics were the highest component on the stator voltage spectrum. The possibilities to reduce such components could be:

- Increase the airgap length: this will have an impact on the slot permeance harmonics which should decrease when the airgap length increases. Furthermore as seen in Chapter 4 depending on their wave length, some harmonics will have more difficulties to cross the airgap. However increasing the airgap will lead to an increase of the magnetizing current

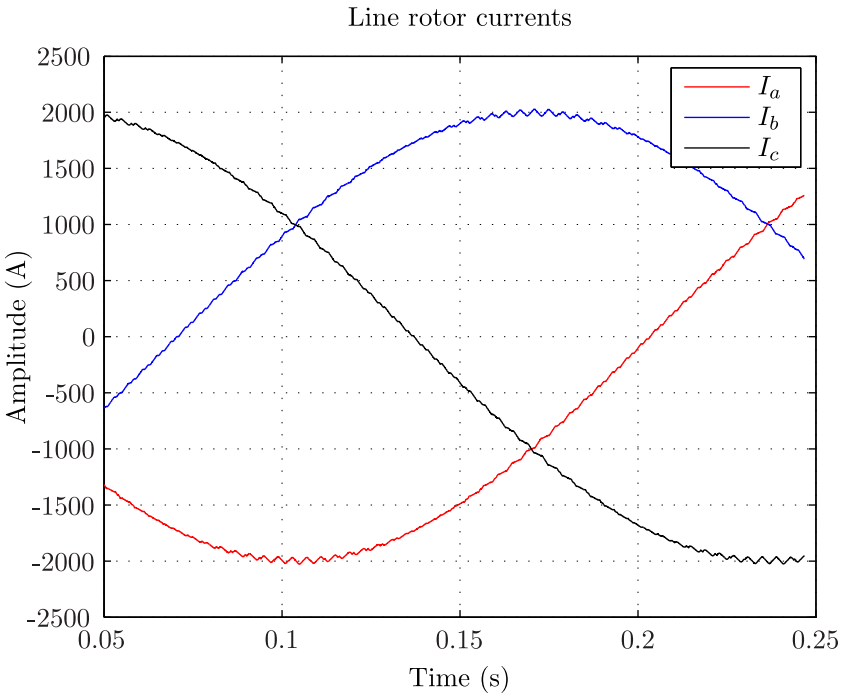

Figure 5.16: FEM: Rotor currents with converter

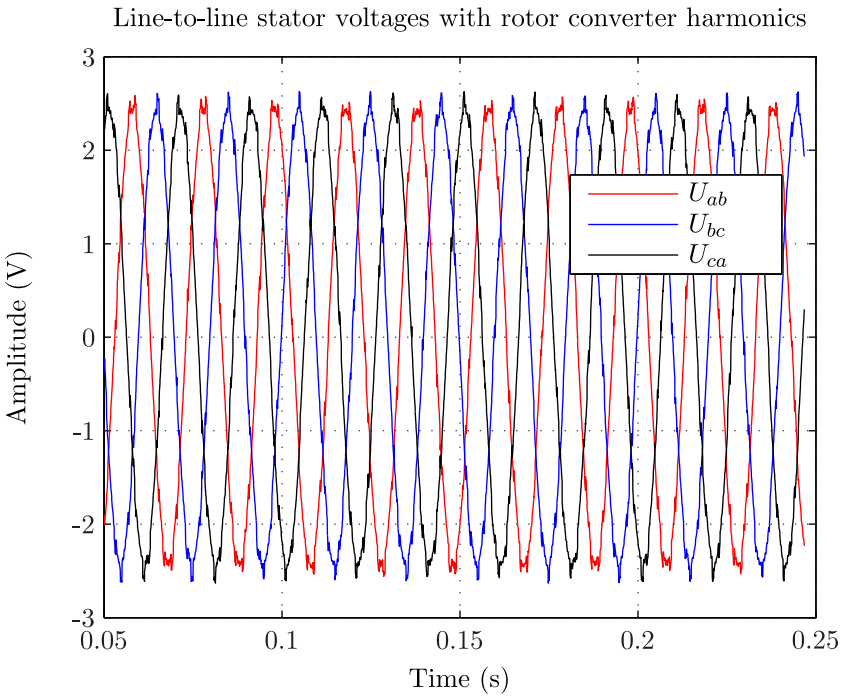

Figure 5.17: FEM: Stator voltages with converter

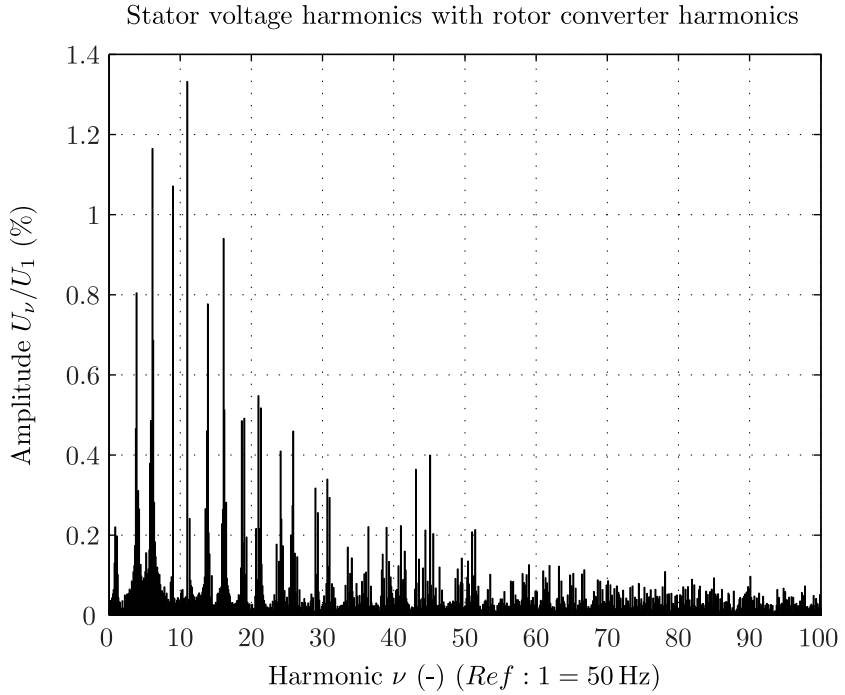

Figure 5.18: FEM: Stator voltages spectrum with converter (without fundamental)

and consequently of the copper losses (see Chapter 5). Figure 5.19 shows the evolution of the THD when changing the airgap length.

- Decrease the teeth saturation: this will have an impact on the airgap permeance harmonics will also the slot harmonics amplitude. Furthermore this will also lead to a diminution of the magnetizing current and consequently on the airgap flux density harmonics amplitudes. This can be done by changing the magnetic circuit geometry and for example by increasing the length of the machine.
- Decrease the slot opening: this will affect the slot permeance harmonics. In this case the slot height will have to be increased in order to keep constant the current densities.
- Use magnetic wedges: Figure 5.20 shows the impact of using magnetic wedges to close the stator or/and rotor slots. The results were obtained from FE simulations. It shows in particular the behavior of the slot harmonics. One can see that, depending on the configuration, it leads to a reduction of the slot harmonics. Note that given the low relative permeability $\mu_\mathrm{r} = 1.5 \cdots 3$ of such material, the slots are not completely closed so that the impact on the slot leakage inductance is not so big. Furthermore it leads to a decrease of the slot permeance harmonics and consequently of the Carter coefficient. Finally the magnetizing current also decreases when using magnetic-wedges. However for mechanical reasons it should be avoided to use magnetic wedges at the rotor. Indeed as the rotor bars are submitted to high centrifugal forces this leads to a deformation of the wedges. Therefore it is necessary to use high mechanical strength rotor wedges which is not possible with magnetic wedges. Given Figure 5.20, using only wedges at the stator

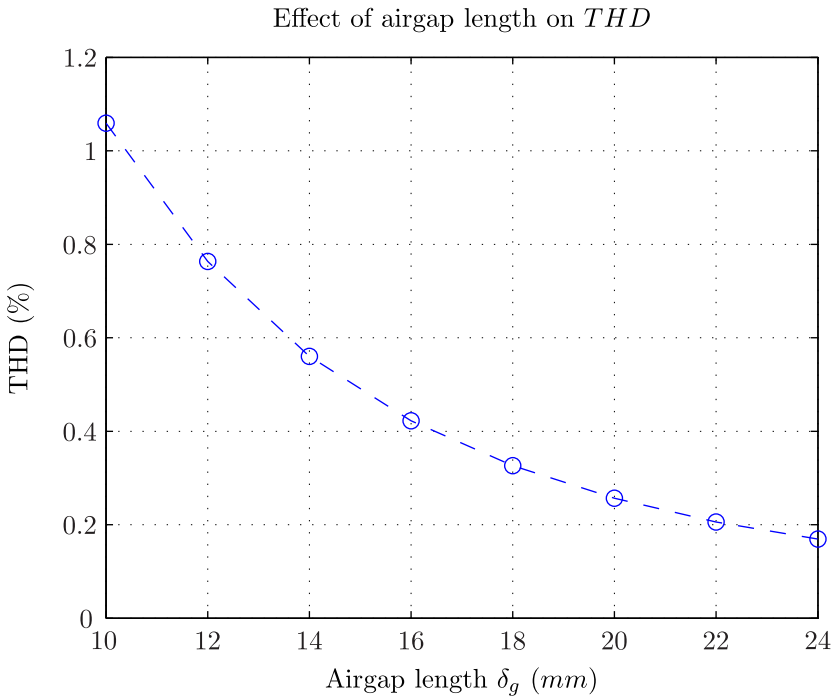

Figure 5.19: Effect of the airgap length on the THD

does not lead to a large reduction of the slot harmonics.

- Use a fractional slot winding: such a winding is often used in conventional synchronous machines. As shown in Chapter 6 this has a large impact on the stator voltage harmonic content. However as it will be shown in the next section such a winding is responsible for additional mmf harmonics which may lead to dangerous electromagnetic radial forces.

5.2.5 Summary

This part presented the computation of the stator voltage harmonics during the no-load operation. The harmonic content was first obtained from 2DFE computation and then explained by using an analytical method based on the airgap flux density model. It was shown that because of saturation some harmonics could be amplified but also that the rotor winding was acting as an efficient damper winding. The comparison between the analytical model and the FE have shown a good agreement although the impact of the saturation was not as high in the analytical model. Furthermore it was demonstrated that changing the slip shifts some harmonic frequencies and makes arise the so-called inter-harmonics. One should also pay attention to the fact that the rotor winding is supplied via a converter, and although the rotor currents are cleaned, the stator voltage shape can be disturbed. The simplified model of the converter should be replaced by a more accurate one in order to ensure of the reliability of the results. The already developed methodology i.e using the regulation of the machine was demonstrated to be very efficient.

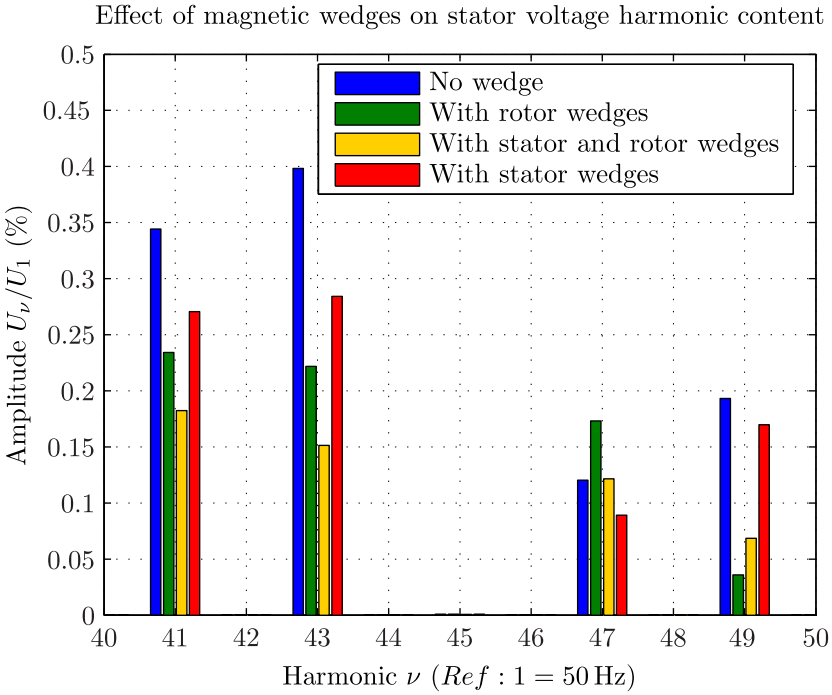

Figure 5.20: Effect of magnetic wedges on slot harmonics (zoom)

5.3 The electromagnetic radial forces

The electromagnetic radial forces issue is a relevant subject of study of hydro-motor/generator units as it can strongly reduce their range of operation and in extreme cases their life time. In one hand the electromagnetic radial forces are caused by several elements such as the configuration of the stator and rotor windings, the non-constant airgap due to the stator and rotor slots or a possible rotor eccentricity, the saturation of the magnetic circuit and the current harmonics emitted by the network or by the rotor power supply. On the other hand the stator core can be regarded as a solid ring with different natural oscillation frequencies also called eigen-frequencies which depend on several properties such as: iron mass, core stiffness, material etc. When a radial force harmonic component excites a mechanical eigen-frequency this may lead to vibration. The consequence on the machine can be noise, degradation of the bar insulation because of friction, or deterioration of the core supports [TLU12]. The problem of parasitic radial forces in rotating machines has been discussed in several studies. For example, Verma [VB94] and Le Besnerais [Bes08] propose analytical calculations of the radial forces using the stator and rotor mmf and airgap permeance method; they apply it to the study of standard induction motors. Recently Traxler-Samek [TLU12] presents a calculation of electromagnetic forces for large synchronous salient-pole hydro-motor/generator units considering tooth ripples phenomena and parasitic harmonics due to a fractional slot winding and validates the method from measurements.

This section investigates the problem of electromagnetic radial forces occurring in DFIM[1].

[1]This is a subject to an ongoing publication by Prof. H.W. Lorenzen, T. Lugand and A. Schwery

The study is even more relevant since such machines can operate at different speeds so that the risk of matching an eigen-frequency becomes higher and consequently the risk of resonance. Furthermore, such machines are designed with small airgap leading to higher amplitude of parasitic forces.

First part applies the airgap flux density model described in Chapter 4 and presents the general method of radial force calculation based on the evaluation of the Maxwell stress. The forces calculation using FEM is also described. For simplification reasons, neither the effect of static eccentricity nor the current harmonics from the converter are taken into account .

Second part compares both calculation results and identifies several parasitic forces components susceptible to excite an eigen-mode of the stator core and frame structure. A numerical study of the stator mechanical structure makes it possible to highlight the potential dangerous force components. The study is made for designs equipped with integer slot stator and rotor windings.

Third part applies the developed methodology to a real machine with a fractional-slot stator winding. Such winding makes it possible to reduce tooth ripple harmonics and to improve the stator voltage shape, furthermore it gives more flexibility to the electrical designer regarding the choice of the number slots. Despite those advantages, such winding introduces additional harmonics susceptible to create dangerous radial forces components. An optimization method is proposed in order to rearrange the winding configuration and to reduce the main MMF harmonics contributors to the force.

5.3.1 Identification of the dangerous radial forces

I. The analytical method

This part describes the general analytical method to calculate the radial electromagnetic forces acting in a DFIM. From the model developed in Chapter 4 one can calculate the radial airgap flux density $B_{\delta,r}$ and the corresponding radial magnetic pressure σ_r (expressed in $\mathrm{N/m^2}$) acting on the stator core obtained from the Maxwell stress tensor as shown by following equation

$$\sigma_r(\alpha_s, t) = \frac{1}{2\mu_0}\left(B^2_{\delta,r}(\alpha_s, t) - B^2_{\delta,t}(\alpha_s, t)\right) \approx \frac{1}{2\mu_0} B^2_{\delta,r}(\alpha_s, t) \tag{5.19}$$

Note that the evaluation of the tangential component of the flux density $B_{\delta,t}$ is not easily accessible with our model. The magnetic flux enters normally in the stator core because of the larger iron permeability compared to the air permeability so that the tangential component can be neglected. We will see in the next part, from the FE results, that this assumption is correct.

The quantity $B_{\delta,r}(\alpha_s, t)$ can be expressed as a sum of harmonics so one obtains:

$$\begin{aligned}\frac{1}{2\mu_0}B^2_{\delta,r}(\alpha_s,t) &= \frac{1}{2\mu_0}\left(\sum_{\nu=1}^{+\infty}\hat{B}_{\delta,\nu}\cos(P_\nu\alpha_s + 2\pi F_\nu t + C_\nu)\right)^2 \\ &= \sum_{\nu_1=1}^{+\infty}\sum_{\nu_2=1}^{+\infty}\frac{\hat{B}_{\delta,\nu_1}\hat{B}_{\delta,\nu_2}}{2\mu_0}\cos(P_{\nu_1}\alpha_s + 2\pi F_{\nu_1}t + C_{\nu_1})\cdot\cos(P_{\nu_2}\alpha_s + 2\pi F_{\nu_2}t + C_{\nu_2}) \\ &= \sum_{\nu_1=1}^{+\infty}\sum_{\nu_2=1}^{+\infty}\left(\sigma^-_{r\,\nu_1,\nu_2} + \sigma^+_{r\,\nu_1,\nu_2}\right)\end{aligned}$$

By applying trigonometric formula we have:

$$\sigma^-_{r\,\nu_1,\nu_2} = \frac{\hat{B}_{\delta,\nu_1}\hat{B}_{\delta,\nu_2}}{4\mu_0}\cos((P_{\nu_1} - P_{\nu_2})\alpha_s + 2\pi(F_{\nu_1} - F_{\nu_2})t + (C_{\nu_1} - C_{\nu_2}))$$
$$\sigma^+_{r\,\nu_1,\nu_2} = \frac{\hat{B}_{\delta,\nu_1}\hat{B}_{\delta,\nu_2}}{4\mu_0}\cos((P_{\nu_1} + P_{\nu_2})\alpha_s + 2\pi(F_{\nu_1} + F_{\nu_2})t + (C_{\nu_1} + C_{\nu_2}))$$

One can see that the interaction between two flux density harmonics creates two force components having different spatial orders $P_{\nu_1} \pm P_{\nu_2}$, different frequencies $F_{\nu_1} \pm F_{\nu_2}$ and different phase shifts $C_{\nu_1} \pm C_{\nu_2}$. As seen in Chapter 4 given the presence of several airgap harmonics, the evaluation of the previous equations gives rise to a lot of components (more than 500). However several single terms $\sigma_{\nu_1\nu_2}$ can have the same spatial order and the same frequency and can therefore be added as vectors. For example, consider a magnetic stress harmonic component $\sigma_{r,1}$ whose amplitude is $\hat{\sigma}_{r,1}$, spatial order is P', frequency is F' and phase shift is C_1 so that it can be expressed as:

$$\sigma_{r,1}(\alpha_s, t) = \hat{\sigma}_{r,1}\cos(P'\alpha_s + 2\pi F' t + C_1) \tag{5.20}$$

Let us consider another harmonic component $\sigma_{r,2}$ having the same spatial order and the same frequency but with the amplitude $\hat{\sigma}_{r,2}$ and the phase shift C_2:

$$\sigma_{r,2}(\alpha_s, t) = \hat{\sigma}_{r,2}\cos(P'\alpha_s + 2\pi F' t + C_2) \tag{5.21}$$

One can regroup these two components in one single term:

$$\sigma_{r,1,2}(\alpha_s, t) = \hat{\sigma}_{r,1,2}\cos(P'\alpha_s + 2\pi F' t + C_{12}) \tag{5.22}$$

where the resulting amplitude $\hat{\sigma}_{r,1,2}$ and phase shift C_{12} are given by Equations (5.23) and (5.24):

$$\hat{\sigma}_{r,12} = \sqrt{\hat{\sigma}^2_{r,1} + \hat{\sigma}^2_{r,2} + 2\hat{\sigma}_{r,1}\hat{\sigma}_{r,2}\cos(C_1 - C_2)} \tag{5.23}$$

$$C_{12} = \arctan\left(\frac{\hat{\sigma}_{r,1}\sin C_1 + \hat{\sigma}_{r,2}\sin C_2}{\hat{\sigma}_{r,1}\cos C_1 + \hat{\sigma}_{r,2}\cos C_2}\right) \tag{5.24}$$

Finally one can express the Maxwell stress as a sum of harmonics:

$$\sigma_r(\alpha_s, t) = \sum_{\nu=1}^{+\infty}\sigma_{r,\nu}(\alpha_s, t) = \sum_{\nu=1}^{+\infty}\hat{\sigma}_{r,\nu}\cos(P_\nu\alpha_s + 2\pi F_\nu t + C_\nu) \tag{5.25}$$

where P_ν is the number of pole pairs[2], F_ν is frequency and C_ν is the phase shift of the ν^{th} force component $\sigma_{r,\nu}$.

II. The numerical method

The FE computation of the radial electromagnetic forces has to be done by carrying out a time stepping simulation. By applying the procedure described in Chapter 4, one can simulate any steady-state operation point of the DFIM. The extraction of the forces is done by applying the following method:

- The radial and tangential flux densities are calculated along a path inside the airgap placed close to the stator bore diameter. This path has to cover at least the minimum repetitive section. In case of fractional-slot winding this may be several poles. The calculation is done for each time step of an electrical period. Figure 5.21 shows the obtained spacial and temporal variations of the radial airgap flux density corresponding to a certain load operation.
- The radial magnetic pressure is calculated by applying Equation (5.19). Figure 5.22 shows the corresponding spacial and temporal results.
- The harmonic content of the magnetic pressure is extracted by carrying out a bi-dimensional Fourier analysis [Bes08; Hub01] so that the magnetic pressure can be expressed as Equation (5.25). This makes it possible to define each force harmonic by its amplitude, its number of nodes and its frequency as shown in Figure 5.23.

Chapter 4 demonstrated that changing the speed and consequently the slip leads to a shift of certain magnetic flux density harmonics and consequently of some forces components. As already mentioned in Section 5.2 this can create inter-harmonics, i.e. harmonics whose frequency is not an integer of the fundamental frequency. Consequently one should carry out the FE simulation on an enough long period in order to extract accurately all frequency components. In the studied case, the simulation was carried out over 0.4 seconds which corresponds to the fundamental period of the rotor currents. Therefore one can see that FE simulation is not the most suitable method to extract parasitic forces as it might require a long computation time.

As already explained in the analytical part, evaluating the magnetic pressure gives rise to a huge number of force components. In order to extract the dangerous components, a mechanical study of the stator structure is necessary. This is the object of the next part.

III. Computation of the mechanical eigen-frequencies

The stator core of the studied machine can be seen as a solid ring with different resonance frequencies which depend on several properties such as: iron mass, core stiffness, material etc. In order to identify the eigen-modes of such structure one can perform a mode shape analysis. Rieck [Rie09], for example, uses a 3DFE model of the stator to perform this task as shown

[2]In the rest of this study we will talk mainly about number of nodes which is equal to twice the number of pole pairs

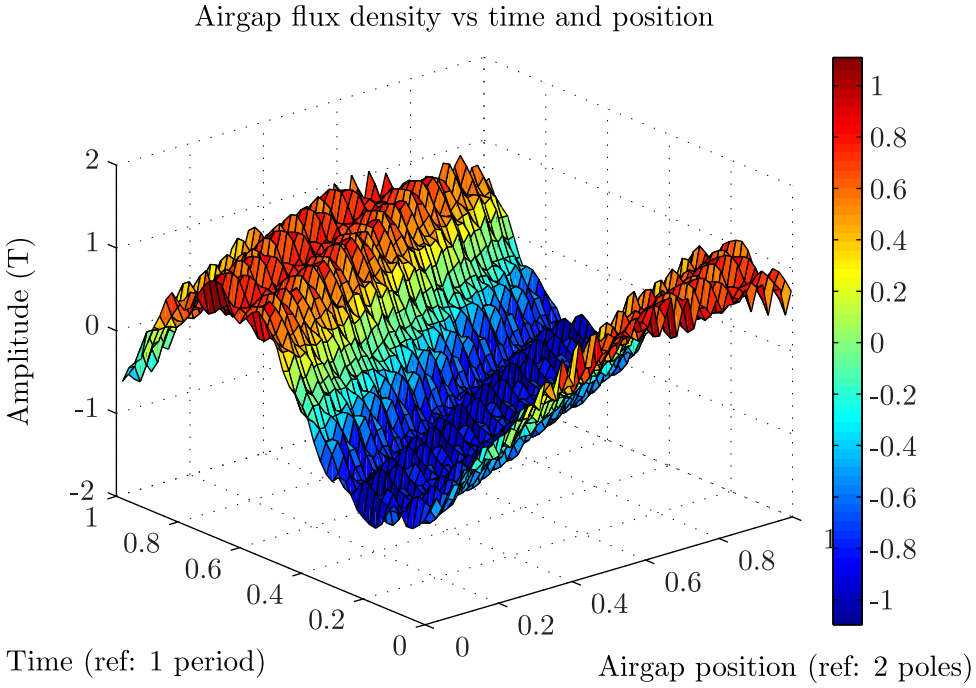

Figure 5.21: Radial airgap magnetic flux vs time and airgap position

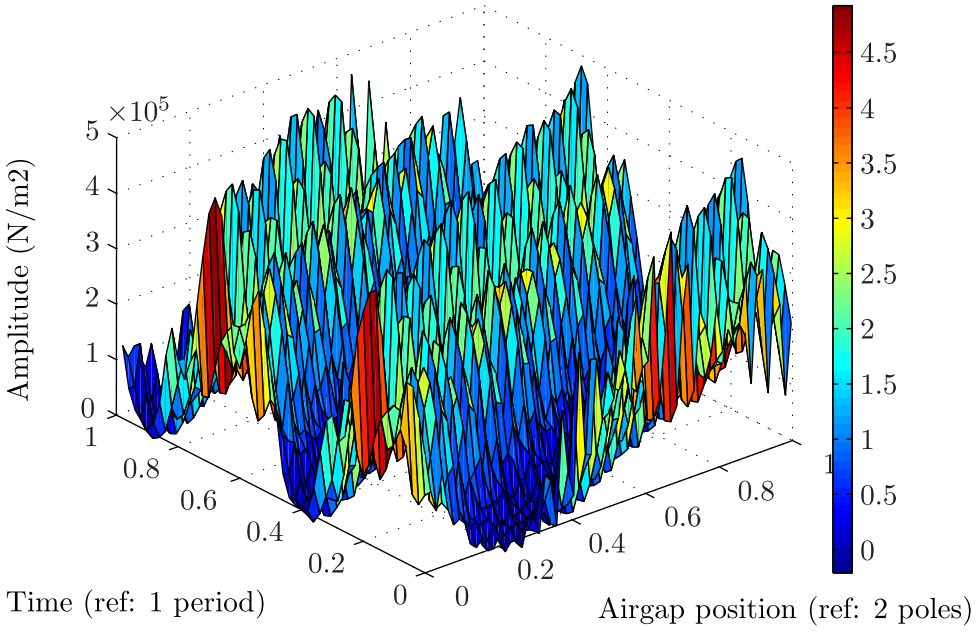

Figure 5.22: Radial magnetic pressure vs time and airgap position

in Figure 5.24. The stator frame (blue) and its support are completely modeled whereas the stator teeth and yoke are approximated with a solid ring (magenta) with equivalent mass and

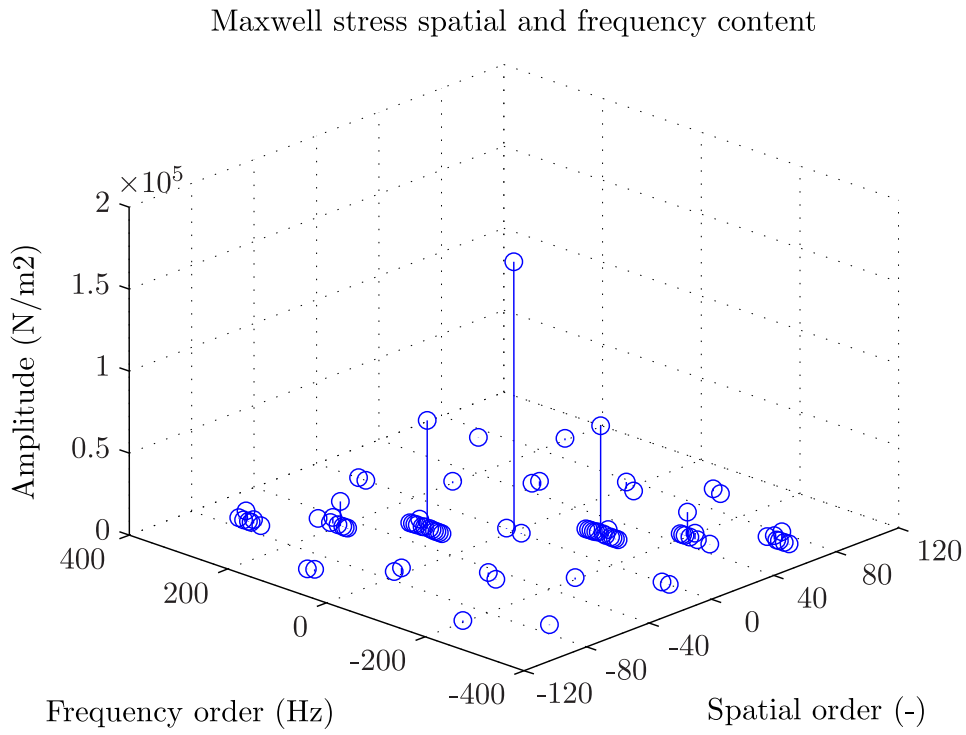

Figure 5.23: Space and time harmonics of the radial magnetic pressure

elasticity modulus. In order to simplify the model, the stator bars are not physically represented but as they affect the eigen-frequencies, they are introduced via an additional mass. Carvalhal [Car12a] develops an equivalent 2DFE model simulating the stator core and frame system as shown in Figure 5.25. Note that the so-called expanded view is only used to better visualize the geometry, finally the analysis remains 2D. This approach is faster to implement, easier to analyze and shows a good agreement with measurements. Therefore we use in this part the results of Carvalhal [Car12b].

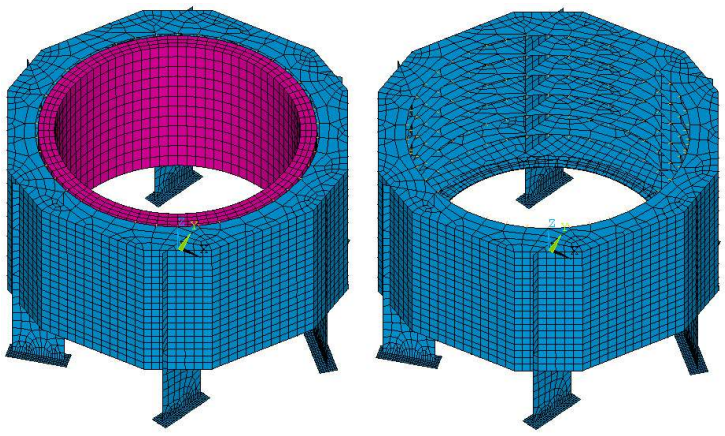

Figure 5.24: Model of the complete stator (left) and frame alone (right) [Rie09]

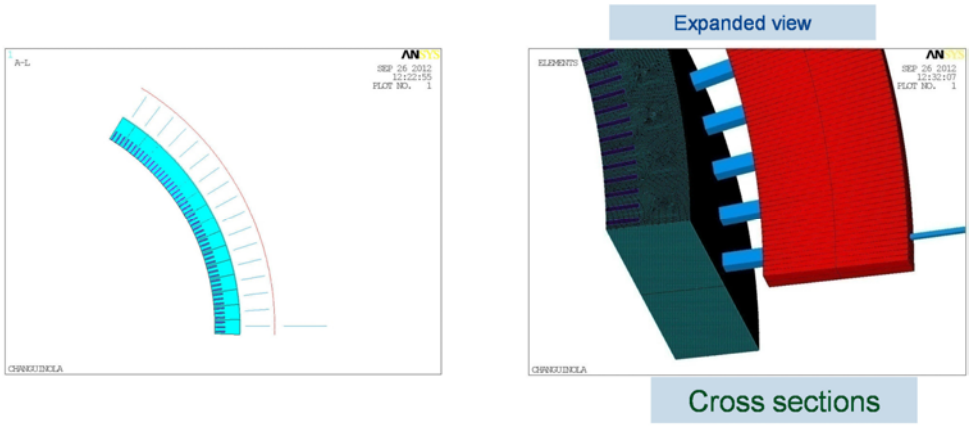

Figure 5.25: 2D FE model of the stator/frame system [Car12b]

The different mode shapes and eigen-frequencies are obtained by studying the harmonic response of the stator core and frame to a forced excitation applied on the inner surface of the stator. Figure 5.26 shows the result of such analysis and more particularly the deformation of the stator in a four-node shape and in a six-node shape.

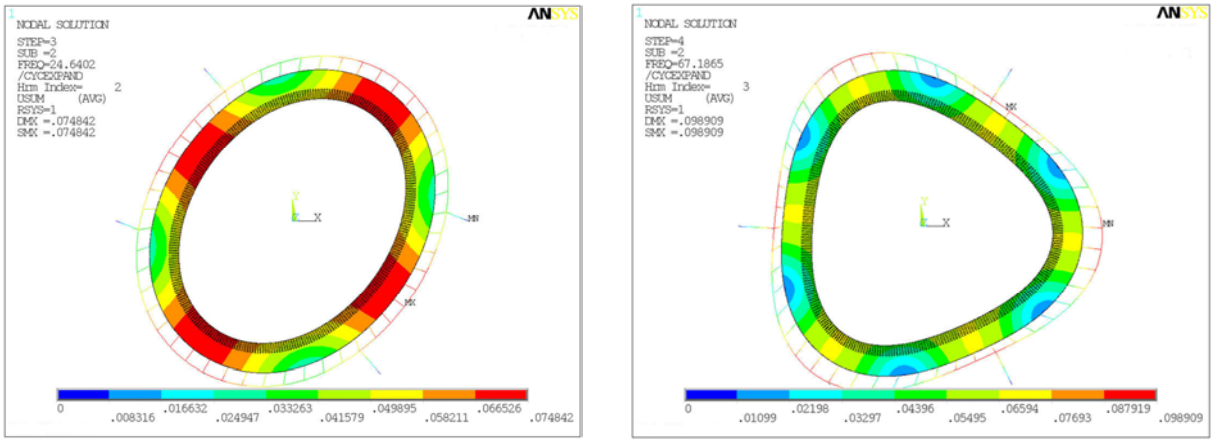

(a) Four-nodes, 24 Hz

(b) Six-node, 67 Hz

Figure 5.26: Examples stator structure eigen-modes [Car12b]

Such computation allows to determine accurately the main mechanical eigen-modes of the stator core-frame structure, each defined by a certain eigen-frequency and an unique number of nodes. Consequently an electromagnetic force component would be dangerous only if its number of nodes is equal to the number of nodes of the mechanical eigen-mode, if its frequency is close to corresponding natural frequency and if its amplitude is high enough. Therefore, in the next part we compare the results from the electromagnetic study and compare it with those of the mechanical study in order to extract the potential dangerous components.

OP	P_{mec} (MW)	U_{s} (V)	$\cos\varphi$ (−)	s (%)	mode (−)
1	256	18.0	0.9	−5	over-excited
2	256	18.0	0.9	0	over-excited
3	256	18.0	0.9	5	over-excited

Table 5.1: Machine M_1: load points characteristics

Rated apparent power S	170	MVA
Rated power factor $\cos\varphi$	0.9	
Rated stator voltage U_{s}	18	kV
Rated grid frequency f_{s}	50	Hz
Number of poles $2p$	12	
Stator bore diameter $D_{\text{b,s}}$	4700	mm
Stator core total length l_{s}	3200	mm
Airgap depth δ_{g}	14	mm
Number of stator winding slots $N_{\text{z,s}}$	288	
Number of rotor winding slots $N_{\text{z,r}}$	252	

Table 5.2: Machine M_1: design characteristics

IV. Comparison of both calculation and extraction of dangerous components

This part analyzes and compares the results obtained from the analytical and the FE magnetic studies. The analytical calculation is done for three load operation points, OP_1, OP_2 and OP_3 which are defined in Table 5.1. The FE simulation is only made for the operation point OP_1. Table 5.2 describes the machine characteristics used for the study; one can see that there are $q_{\text{s}} = 8$ stator slots per pole and phase and $q_{\text{r}} = 7$ rotor slots per pole and phase.

Table 5.3 lists the computed stator structure eigen-frequencies [Car12a]. The maximum calculated number of nodes is equal to 24 which is twice the number of poles of the studied machine; this is sufficient for the study as a vibration is unlikely to happen above this number. Table 5.4 lists the main electromagnetic forces calculated analytically for the three operation points. Note that a negative frequency means that the force wave rotates in opposite direction of the fundamental wave. Two high amplitude components arise: the (0-node, 0 Hz) and (24-node, 100 Hz). They are mainly due to the the fundamental airgap flux density. Indeed recalling the definition of the magnetic force given by Equation (5.19) and considering only the fundamental airgap flux density so that: $B_{\delta,\text{f}}(\alpha_{\text{s}}, t) = \hat{B}_{\delta,\text{f}} \cos(p\alpha_{\text{s}} - 2\pi f_{\text{s}} t)$ we obtain:

$$\sigma_{\text{r,f}}(\alpha_{\text{s}}, t) = \sigma^{-}_{\text{r},1,1} + \sigma^{+}_{\text{r},1,1} = \frac{\hat{B}^2_{\delta,\text{f}}}{4\mu_0} \left(1 + \cos(2p\alpha_{\text{s}} - 2\pi \cdot (2f_{\text{s}}) \cdot t)\right) \tag{5.26}$$

$\sigma_{\text{r,f}}$ is made of two terms, one (0-node, 0 Hz) term and one ($2 \cdot 2p$-node, $2 \cdot f_{\text{s}}$ Hz) term. The first one corresponds to a constant stress along the stator bore whereas the second term corresponds to a rotating stress. Figure 5.27 shows a spatial representation of these two stresses, and in particular of the components (24-node, 100 Hz) at three instants.

Nodes (−)	F_{eig} (Hz)
0	229
4	24.6
6	67.1
8	134.7
10	205.8
12	289.5
14	381.7
16	479.3
18	578.6
20	675.5
22	765.6
24	845

Table 5.3: Machine M_1: stator eigen-mode characteristics

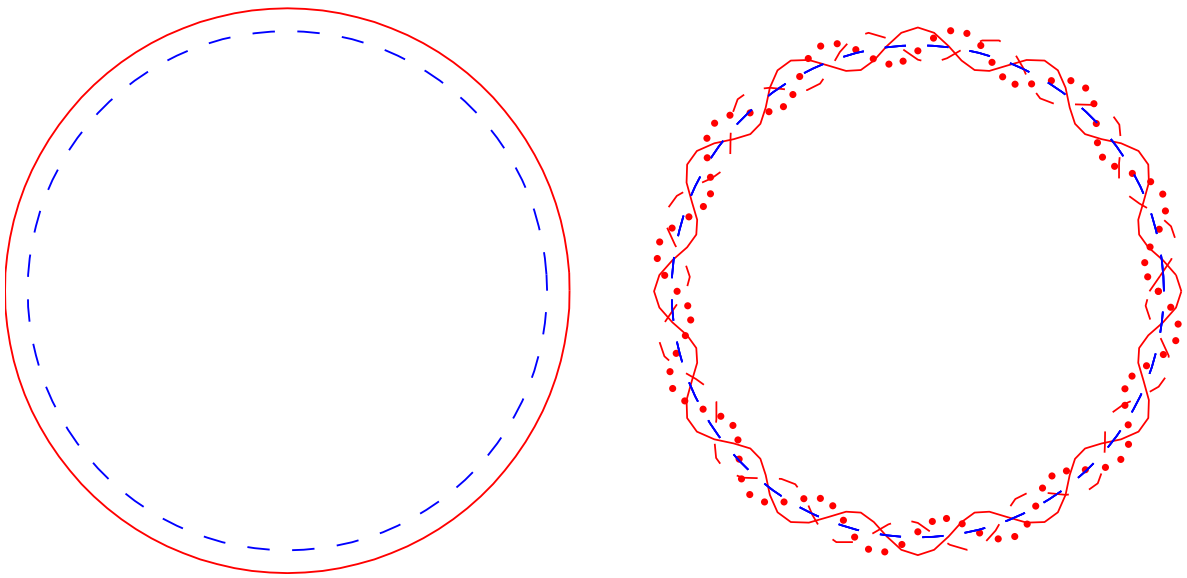

(a) 0-node (b) 24-nodes

Figure 5.27: Fundamental mode shape

(a) OP_1

Nodes (−)	F (Hz)	σ_r (N/m^2)
0	0	176 870
0	−15	671
0	−300	321
0	−315	810
0	−630	442
0	−1260	38
0	−1890	50
0	−1905	15
24	2005	73
24	1990	44
24	1360	26
24	745	10
24	730	259
24	430	24
24	415	108
24	400	30
24	115	3989
24	100	142 780
24	85	59
24	−200	2035
24	−215	402
24	−515	19
24	−530	220
24	−845	12
24	−1160	15
24	−2105	439

(b) OP_2

Nodes (−)	F (Hz)	σ_r (N/m^2)
0	0	177 540
0	−300	1007
0	−600	475
0	−1200	41
0	−1800	58
0	−2100	468
24	2200	147
24	1900	37
24	1300	26
24	700	270
24	400	156
24	100	144 090
24	−200	2554
24	−500	258
24	−800	16
24	−1100	18
24	−2000	461

(c) OP_3

Nodes (−)	F (Hz)	σ_r (N/m^2)
0	0	177 910
0	−15	716
0	−285	928
0	−300	349
0	−570	513
0	−1140	44
0	−1695	17
0	−1710	58
0	−1995	495
24	2095	151
24	1810	51
24	1795	80
24	1240	31
24	670	301
24	655	12
24	400	33
24	385	126
24	370	28
24	115	64
24	100	143 060
24	85	4270
24	−185	455
24	−200	2231
24	−470	257
24	−485	22
24	−755	13
24	−1040	18
24	−1895	480
24	−2180	516
24	−2195	570

Table 5.4: Machine M_1: Calculated radial forces with analytical model

Furthermore, one can observe that changing the slip leads to the apparition of new components but also shifts some frequencies. This phenomena was already highlighted in Chapter 4. In particular for the operation points OP_1 and OP_2, there are two large components, (0-node, 315 Hz) and (0-node, 285 Hz). These components come from the same origins as the component (0-node, 300 Hz) of OP_2 and their respective frequency is changed because of the slip. Indeed, we have seen previously that the interaction between two harmonics ν_1 and ν_2 gives rise to two forces having $2 \cdot (P_{\nu_1} \pm P_{\nu_2})$ nodes and $F_{\nu_1} \pm F_{\nu_2}$ as frequency. Assume that ν_1 is a harmonic due to the stator winding mmf and ν_2 is a harmonic due to the rotor winding mmf so that $F_{\nu_1} = f_s$ and $F_{\nu_2} = f_s \cdot (s + (1-s)\frac{P_{\nu_2}}{p})$. The conditions $2 \cdot (P_{\nu_1} \pm P_{\nu_2}) = 0$ and $F_{\nu_1} - F_{\nu_2} = 6f_s \cdot (1-s) = 300(1-s)$ are satisfied when considering the interaction between the 5^{th} or 7^{th} and 5^{th} or 7^{th} rotor winding harmonic.

Consequently we have $P_{\nu_1} = -5 \cdot p$ and $P_{\nu_2} = -5 \cdot p$ so that: $P_{\nu 1} - P_{\nu 2} = 0$ and $F_{\nu 1} - F_{\nu 2} = f_s(1 - s - (1-s) \cdot (-5)) = f_s \cdot (6 - 6s)$. In the same way, we have $P_{\nu_1} = +7 \cdot p$, $P_{\nu 2} = +7 \cdot p$ and $F_{\nu_1} - F_{\nu_2} = f_s(1 - s - (1-s) \cdot (+7)) = f_s \cdot (6s - 6)$.[3]

In OP_2, the slip s is equal to zero and consequently the frequency is equal to $6 \cdot f_s = 300$ Hz. In OP_1, and OP_3 the slip is either -5% or $+5\%$, so that the respective frequencies are 315 Hz and 285 Hz.

Note also the existence of the component (0-node, 300 Hz) for the operation points OP_1 and OP_3. When considering the last explanation, this component should be shifted in frequency according to the slip value, which is not the case. However, one can find an explanation when recalling the presence of additional airgap permeance harmonics due to the magnetic saturation as shown in Chapter 4. Indeed, it was demonstrated that magnetic saturation leads to modulation of the geometric airgap permeance with the wave K_{sat} defined as:

$$K_{\text{sat}}(\alpha_s, t) = K_0 + K_1 \cos(2 \cdot p\alpha_s - 2 \cdot 2\pi f_s t) + K_2 \cos(4 \cdot p\alpha_s - 4 \cdot 2\pi f_s t) \tag{5.27}$$

From Chapter 4, we know that a flux density harmonic is due to the interaction between a mmf harmonic and a particular permeance harmonic. When modulating the fundamental flux density harmonic with the second harmonic of K_{sat}, one obtains the new component: $K_2 \hat{B}_{\delta,f} \cos(5 \cdot p + 2\pi \cdot 5 \cdot f_s t$. The interaction between this flux density harmonic and the 5^{th} flux density stator harmonic (due to the interaction between average permeance and 5^{th} mmf harmonic) creates two forces and in particular the component (0-node, $6f_s$ Hz). Other combinations may be involved in this particular component, and one should note that it is independent of the slip value.

Table 5.5 lists the main electromagnetic forces extracted from the FE simulation for the operation point OP_1. For comparison purposes, it shows the results when using the complete Maxwell stress formula $\sigma_r(B_{\delta,r}, B_{\delta,t})$ and the approximated one $\sigma_r(B_{\delta,r})$. The difference is very small for the studied case and for the presented harmonic components. Comparison of the FE and the analytical results (only OP_1) shows a good agreement on the forces frequencies and number of nodes. However, some larger discrepancies arise when comparing the amplitudes. This is especially the case for the components, (0-node, 15 Hz), (0-node, 315 Hz), (0-node, 300 Hz), etc.

[3] As seen in Chapter 4, the 5^{th} harmonic rotates in opposite direction as the fundamental wave so the negative sign while the 7^{th} rotates in the same direction

Nodes (−)	F (Hz)	$\sigma_r(B_{\delta,r}, B_{\delta,t})$ (N/m^2)	$\sigma_r(B_{\delta,r})$ (N/m^2)
0	0	164 560	172 980
0	−15	922	949
0	−300	201	192
0	−315	395	364
0	−630	204	182
0	−1905	83	0
0	−2105	80	0
0	−2205	432	284
0	−2520	186	127
0	−3115	80	86
0	−3120	128	121
0	−3125	90	93
24	3230	108	108
24	3225	244	227
24	2205	97	0
24	2005	408	347
24	745	103	102
24	730	83	0
24	430	87	88
24	415	93	90
24	130	115	117
24	115	8173	8398
24	100	132 138	134 980
24	85	188	205
24	0	124	128
24	−200	2427	2437
24	−215	92	106
24	−500	133	134
24	−515	131	131
24	−530	83	81
24	−2105	304	160
24	−2405	510	457
24	−2420	203	125
24	−3015	135	136
24	−3020	95	88

Table 5.5: Machine M_1, OP_1: Calculated radial forces with FE

As seen previously these force components depend on the magnetic state. Although our model is able to manage the influence of magnetic saturation on airgap flux density harmonics, its implementation remains simplified and leads to inaccuracies especially because of the difficulty to assess correctly K_2. This is one more reason to further develop the BE model and magnetic network coupling introduced in Chapter 4.

Finally, the electromagnetic calculation results are compared to the mechanical eigen-mode calculation in order to extract the dangerous components. By considering a certain safety margin due to uncertainties in the mechanical model and considering only the high amplitude forces, one can first identify the forces (0-node, 300 Hz) and (0-node, $300 \cdot (s-1)$ Hz) as two critical components.

In order to study the risk of resonance one can compute the vibration response of the stator structure when applying a 0-node magnetic pressure along the stator inner diameter. Figure 5.28 shows the evolution of the vibration when sweeping the frequency of the exciting magnetic pressure between $0.95 \cdot f^0_{\text{eig}}$ Hz and $1.05 \cdot f^0_{\text{eig}}$ Hz where f^0_{eig} is the previously calculated 0-node mechanical eigen-frequency.[4] In addition we compare the vibration response to the acceptable vibration limit. Note that such limit is not officially specified in the standards; it is here only assumed according to other existing limits. Considering an uncertainty of 25% for the eigen-frequencies calculation, the frequency of the component 0-node, 285 Hz matches the resonant frequency of the motor/generator and an excitation of $400\,\text{N/m}^2$ (assumed from the FE results) leads to a vibration amplitude of 5.5 µm which is above the standard limits. Although we applied a safety margin on the calculated eigen-frequency, the excitation components (0-node, 300 Hz) and (0-node, $300(s-1)$ Hz) should be seriously considered as they will always exist[5]. The 0-node eigen-frequency can be evaluated by applying Equation (5.28) [Vog96].

$$f_0 = \frac{1}{\pi} \cdot \sqrt{\frac{E}{\rho \cdot \Delta_{\text{m,s}}} \cdot D^2_{\text{y,s}}} \tag{5.28}$$

where E is the modulus of elasticity (N/m^2) of the stator core, ρ is the stator iron specific mass (kg/m^3), $D_{\text{y,s}}$ is the mean stator yoke diameter (m) and $\Delta_{\text{m,s}}$ is given by:

$$\Delta_{\text{m,s}} = \frac{m_{\text{t,s}} + m_{\text{y,s}} + m_{\text{w,s}}}{m_{\text{y,s}}} \tag{5.29}$$

where $m_{\text{y,s}}$, $m_{\text{t,s}}$ and $m_{\text{y,s}}$ are respectively the mass of the stator yoke, stator teeth and stator winding. Consequently one can see that the 0-node eigen-mode will be influenced by the stator geometry and it is possible to set its parameters so that the eigen-frequency is far enough from the excitation frequencies 300 Hz or $300 \cdot (s-1)$ Hz.

An another critical excitation component is (24-node, 730 Hz) and (24-node, 745 Hz). The first component, (24-node, 730 Hz), arises by operation point OP_1 and its frequency is changed in 700 Hz by OP_2 and 670 Hz by operation point OP_3. This component is mainly due to the interaction between the 13^{th} rotor mmf harmonic and the 11^{th} stator mmf harmonic. Indeed

[4] The curve was obtained from a similar stator geometry from [Car12a]

[5] In case of a 60 Hz machine, one should replace 300 by 360

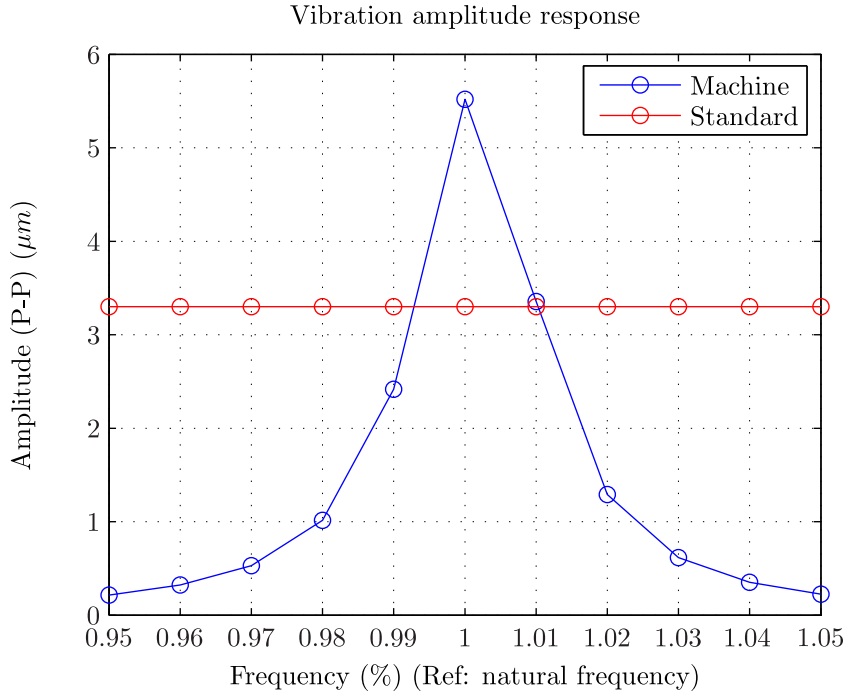

Figure 5.28: Vibration response

we have $P_{\nu 1} = 11p$ and $P_{\nu 2} = 13p$ so that $P_{\nu 2} - P_{\nu 1} = 2p = 12$. Furthermore $F_{\nu 1} = -f_s$ and $F_{\nu 2} = (s + (1-s)\frac{13p}{p})f_s$ so that $F_{\nu 2} - F_{\nu 1} = (s + (1-s)\frac{13p}{p} + 1)f_s$. When $s = 0$, $F_{\nu 2} - F_{\nu 1} = 700\,\text{Hz}$, when $s = -0.05$ $F_{\nu 2} - F_{\nu 1} = 730\,\text{Hz}$ and when $s = 0.05$, $F_{\nu 2} - F_{\nu 1} = 670\,\text{Hz}$. The second component, (24-node, 745 Hz), exists by operation point OP_1 and its frequency becomes 655 Hz by operation point OP_3. Note that the analytical calculation presents much lower amplitude than the FE simulation. One can show that this component is mainly due to the interaction between the 17^{th} rotor mmf harmonic, the 19^{th} stator mmf harmonic and the 2^{nd} saturated permeance harmonic. When $s = -0.05$ or $s = 0.05$ the frequency of the force is equal to 745 Hz or 655 Hz while it becomes 700 Hz when the slip is zero. Considering a safety margin 25% on the eigen-frequencies calculation, these two components could excite the stator eigen-mode (24-node 845 Hz) but given the low amplitude of the force amplitudes the risk is very low.

Finally we have seen in this part that there are several components susceptible to excite an eigen-mode of the stator. It was also demonstrated that changing the slip makes appear additional components and many of them arise because of the magnetic saturation. This shows the necessity to predict accurately the stator eigen-frequency in order to eliminate all the irrelevant components. Fortunately the amplitude of the dangerous components is low so that the risk of resonance is unlikely. Note that it is necessary to predict the risk of resonance as soon as possible during the design stage; indeed solutions to fix such problem when the machine is built are very limited and can be very costly [Ard+13]. One should add that this study could be extended from steady-state to startup operation for pumping mode. Indeed, during startup,

several resonances could be reached, although only temporarily as the speed is changing.

In the next part, we deal with fractional slot windings.

5.3.2 Application to a fractional slot winding machine

Fractional slot windings are often used when designing the stator winding of a salient-pole synchronous machine. In such a winding the number of slots per phase is not an integer multiple of the number of poles. Consequently the number of slots per pole and phase q is a fractional number $q = q_1/q_2$, where q_1 and q_2 are two integer numbers. The interests of using such winding are several:

- To give more choice to the electrical designer for the number of stator slots which is particularly relevant when designing slow-speed machine.
- To reduce the slots-ripple harmonics and consequently to improve the stator voltage shape.[6]

Consider a winding with $q = 5/4$ slots per pole and phase [TLU12]. Figure 5.29 shows the distribution of such winding and Figure 5.30 shows the corresponding mmf. In this case, the minimum repeatable period is equal to $p_0 = 2$ poles pairs. Furthermore, one can observe the non-regular variation of the mmf.

When equipping a generator with such winding, one takes the risk to generate unacceptable vibrations [TLU12; WK60]. These vibrations are mainly due to the existence of parasitic mmf harmonics linked to the non-regular distribution of the winding. By interacting with other harmonics, these components can create dangerous force components susceptible to excite an eigen-frequency of the stator core and frame. As the airgap length of the DFIM is normally smaller than in the salient-pole synchronous machine, the corresponding force amplitude can be very high. This part uses the previously developed method to compute the excitation forces in an existing fractional stator winding DFIM. The results are validated by comparison with experimental measurements.

I. The studied machine

The studied 12 MVA test generator was initially a synchronous generator from which the salient-pole rotor has been replaced by a wound rotor. Such transformation of a standard synchronous machine is very interesting for the refurbishment of PSP installations suitable for variable speed utilization as the stator core might not have to be replaced. The purpose of this project was to show the reliability and the benefit of using adjustable speed machines. The project was a success although some difficulties arose during the tests because of vibration problems. Table 5.6 gives the characteristics of the machine and Table 5.7 lists the main operation points of the machine.

[6] This can be seen in Chapter 6

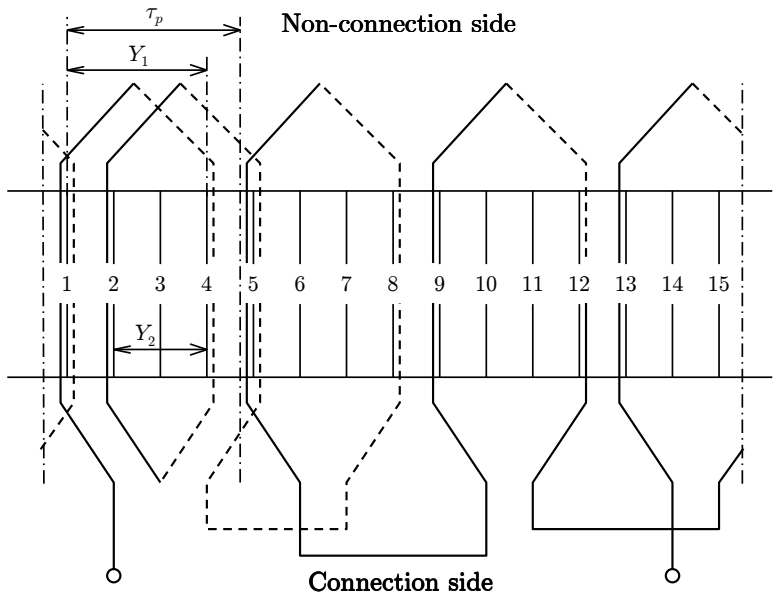

Figure 5.29: Example of a fractional slot winding diagram: only one phase q=5/4 $Y_1 = 3$ and $Y_2 = 2$

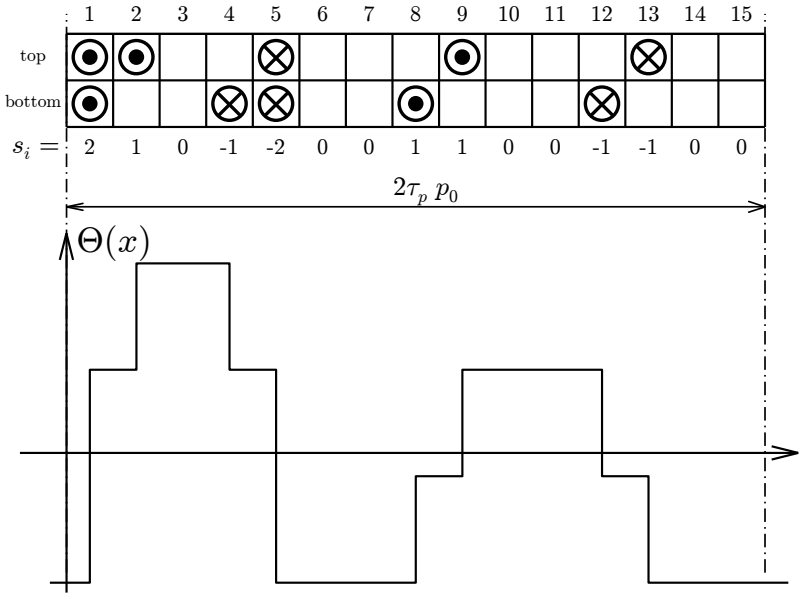

Figure 5.30: Example of a fractional-slot winding diagram and mmf

Rated apparent power S	12	MVA
Rated power factor $\cos\varphi$	0.90	
Rated stator voltage U_{s}	13.6	kV
Rated grid frequency f_{s}	50.0	Hz
Synchronous speed n_{s}	600.0	rpm
Number of poles $2p$	10	
Stator bore diameter $D_{\mathrm{b,s}}$	2000	mm
Stator core total length l_{s}	120	mm
Airgap depth δ_{g}	6	mm
Number of stator winding slots $N_{\mathrm{z,s}}$	102	
Number of rotor winding slots $N_{\mathrm{z,r}}$	120	

Table 5.6: Machine M_2: design characteristics

OP	P_{mec} (MW)	U_{s} (V)	$\cos\varphi$ (−)	s (%)	mode (−)
1	10	13.6	0.9	−15	over-excited
2	10	13.6	0.9	0	over-excited
3	10	13.6	0.9	15	over-excited

Table 5.7: Machine M_2: load points characteristics

II. The stator winding

The machine is built with a fractional slot winding on the stator. The corresponding number of slots per pole and phase is given by: $q_s = N_s/(6p) = 17/5$. Figure 5.31 shows the mmf of one phase of this winding and Figure 5.32 shows the corresponding harmonic content. The minimal repetitive section p_0 is here equal to five. One can notice the presence of non-negligible sub-harmonics i.e. harmonic whose spatial orders are smaller than the fundamental and also harmonics which are not integer multiple of the fundamental.

III. Identification of the parasitic forces

A vibration has been experienced during the operation of the machine. Accelerometers set on the frame of the machine made it possible to identify a strong 100 Hz vibration. In order to identify its origin one can calculate the radial electromagnetic forces by applying the method previously described.[7]

Table 5.8 gives the main results of this study for each operation point. Note that it only highlights a fraction of the total list, only the highest amplitudes are shown. When crossing these results with the ones obtained from the mechanical analysis of the stator structure given by Table 5.9, one can see a potential match between the force component (4-node, 100 Hz) and the mechanical eigen-mode (4-node 94 Hz). This component exists for all the operation

[7]Measurement results are provided in the next part

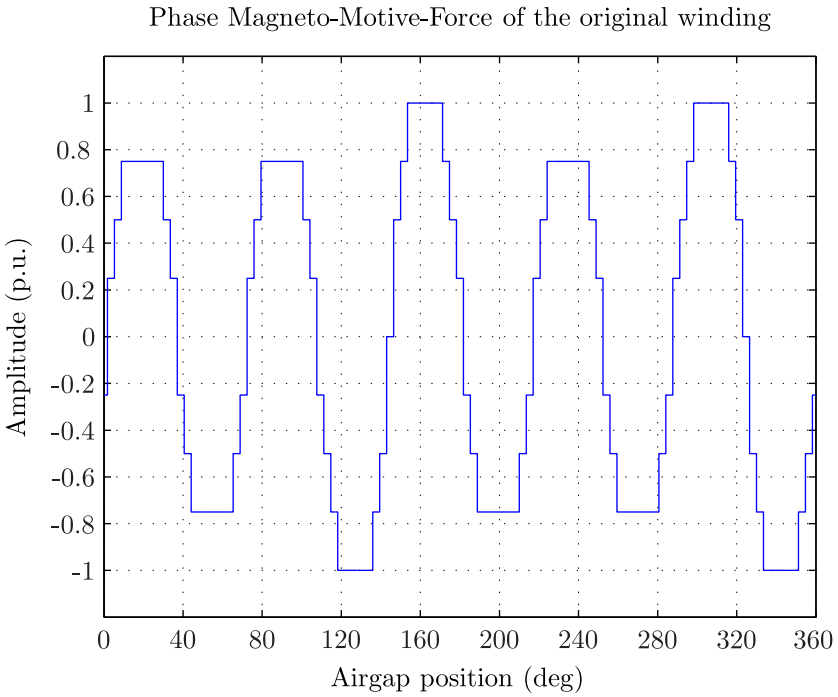

Figure 5.31: Stator mmf of the original winding

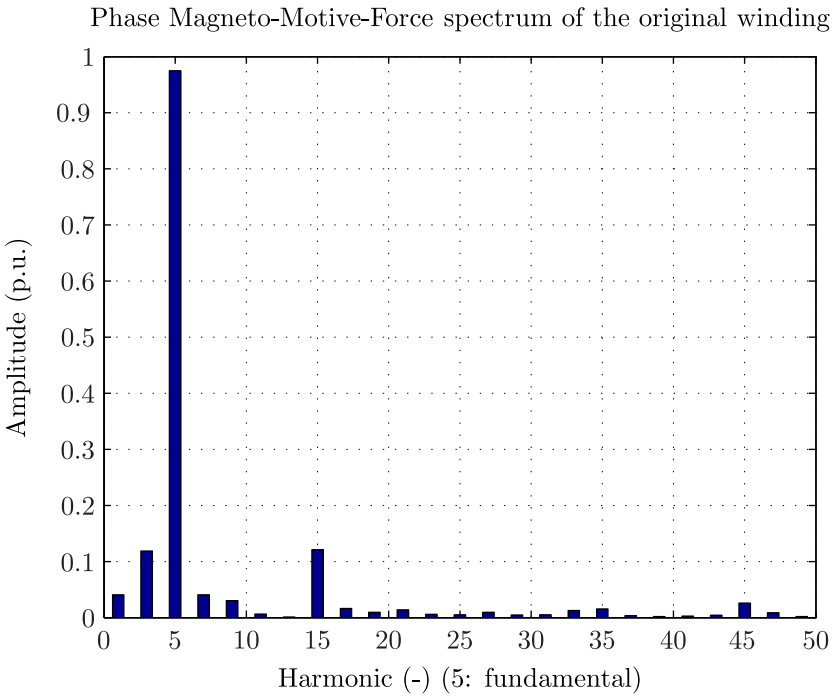

Figure 5.32: Stator mmf spectrum of the original winding

Nodes (−)	F (Hz)	σ_r (N/m^2)
0	0	232 000
0	−200	19 609
4	−100	25 239
8	100	24 697
20	−100	40 382
20	100	225 200

(a) OP_1

Nodes (−)	F (Hz)	σ_r (N/m^2)
0	0	233 230
0	−200	19 470
4	−100	27 832
8	100	27 249
20	−100	40 268
20	100	225 340

(b) OP_2

Nodes (−)	F (Hz)	σ_r (N/m^2)
0	0	244 260
0	−200	20 566
4	−100	32 871
8	100	32 155
20	100	42 790
20	100	234 590

(c) OP_3

Table 5.8: Machine M_2: Main electromagnetic forces

points with the same frequency but different amplitudes. In the next part we demonstrate why different amplitudes vary with the slip. Assuming that this component is mainly due to the stator winding, one may define the harmonics ν_1 and ν_2 so that: $2 \cdot (P_{\nu 1} \pm P_{\nu 2}) = 4$ and $F_{\nu 1} \pm F_{\nu 2} = 100$. These conditions are satisfied when $P_{\nu 1} = 5$ which is the fundamental wave and $P_{\nu 2} = -7$ which is a non-integer multiple of the fundamental. Note that these two harmonics rotate in opposite directions. Other interactions are possible such as between the harmonic $P_{\nu 1} = 11$ and the harmonic $P_{\nu 2} = -13$ or between the harmonic $P_{\nu 1} = 17$ and the harmonic $P_{\nu 2} = 19$, however only the first combination will create the highest force as it involves the fundamental. Finally the force $\sigma_{\mathrm{r},4}$ (4-node, 100 Hz) can be approximated as

$$\sigma_{\mathrm{r},4}(\alpha_\mathrm{s}, t) \approx \frac{\Lambda\Theta_{\mathrm{s},5} \cdot \Lambda\Theta_{\mathrm{s},-7}}{2\mu_0} \cdot \cos(2 \cdot \alpha_\mathrm{s} + 2f_\mathrm{s} \cdot t) \tag{5.30}$$

where $\Theta_{\mathrm{s},5}$ is the magnetic field due to the superposition of the fundamental field component created by the stator and the rotor, $\Theta_{\mathrm{s},-7}$ is the already discussed mmf harmonic created by

Nodes (−)	F_{eig} (Hz)
0	272
4	94.1
6	203.0
8	338.4
10	480.8
12	630.5
14	785.6
16	943.9
18	1103.8
20	1264.5
22	1425.5
24	1586.4

Table 5.9: Machine M_2: stator eigen-mode characteristics

the stator and $\Lambda = \mu_0/(\delta_{\mathrm{g}} \cdot k_{\mathrm{c}})$ is the airgap permeance assuming a constant airgap δ_{g} corrected by the Carter coefficient k_{c}. Note that the frequency of this component is independent of the slip contrary to the 300 Hz force described in the first part of this section.

The same force existed in the original machine but with a different amplitude. It was calculated according to [TLU12] for the same operation point and is around 1350 $\mathrm{N/m^2}$ which is almost twenty times less than the amplitude of the force occurring in the DFIM. Three main reasons explain this difference. Firstly the minimum airgap length of the synchronous machine is larger: 20 mm versus 6 mm in the new machine. Secondly the special pole shape of the original salient pole rotor leads to a decrease of the airgap permeance. Thirdly the rotor of the synchronous machine was equipped with a damper bar winding placed on the pole shoe of each pole. This damper winding aims to reduce torque and speed oscillations and more particularly damp the magnetic field harmonics generated by the stator winding.

The amplitude of the force $\sigma_{\mathrm{r},4}^{\mathrm{sync}}$ in the case of the synchronous machine can be written as

$$\sigma_{\mathrm{r},4}^{\mathrm{sync}} \approx \frac{\Lambda^{\mathrm{sync}} \hat{B}_{\delta,\mathrm{f}} \cdot \Theta_{\mathrm{s},-7} \cdot k_{\mathrm{D7}}}{2\mu_0} \tag{5.31}$$

where k_{D7} is the damping factor of the 7^{th} stator mmf harmonic due to the damper winding, $\Lambda^{\mathrm{sync}} = k_{\mathrm{p}} \cdot \mu_0/(\delta^{\mathrm{sync}} \cdot k_{\mathrm{c,s}})$ is the airgap permeance corrected by the pole shape factor k_{p} and the Carter factor $k_{\mathrm{c,s}}$ because of stator slots. $\hat{B}_{\delta,\mathrm{f}} = \Lambda^{\mathrm{sync}} \Theta_{\mathrm{s},5}$ is the fundamental airgap flux density.

The amplitude of the force $\sigma_{\mathrm{r},4}^{\mathrm{async}}$ in the case of the asynchronous machine is simply given by Equation (5.32). Note that both machines are at the same operation point so that the fundamental flux density $\hat{B}_{\delta,\mathrm{f}}$ and the harmonic mmf $\Theta_{\mathrm{s},-7}$ remain the same.

$$\sigma_{\mathrm{r},4}^{\mathrm{async}} \approx \frac{\Lambda \hat{B}_{\delta,\mathrm{f}} \cdot \Theta_{\mathrm{s},-7}}{2\mu_0} \tag{5.32}$$

a	a	a	a	-c	-c	-c	b	b	b	b	-a	-a	-a	c	c	c
-b	-b	-b	-b	a	a	a	-c	-c	-c	-c	b	b	b	-a	-a	-a
c	c	c	c	-b	-b	-b	a	a	a	a	-c	-c	-c	b	b	b
-a	-a	-a	-a	c	c	c	-b	-b	-b	-b	a	a	a	-c	-c	-c
b	b	b	b	-a	-a	-a	c	c	c	c	-b	-b	-b	a	a	a
-c	-c	-c	-c	b	b	b	-a	-a	-a	-a	c	c	c	-b	-b	-b

Table 5.10: Stator winding original configuration

Finally Equation (5.33) expresses the ratio $\sigma_{\mathrm{r},4}^{\mathrm{async}}/\sigma_{\mathrm{r},4}^{\mathrm{sync}}$ between the parasitic force amplitude in the new machine and in the old machine.

$$\frac{\sigma_{\mathrm{r},4}^{\mathrm{async}}}{\sigma_{\mathrm{r},4}^{\mathrm{sync}}} = \frac{\Lambda}{\Lambda^{\mathrm{sync}} \cdot k_{D7}} = \frac{k_{\mathrm{c,s}}\delta^{\mathrm{sync}}}{k_{\mathrm{c}}\delta} \cdot \frac{1}{k_{\mathrm{D7}} \cdot k_{\mathrm{p}}} \tag{5.33}$$

Considering $k_{\mathrm{D7}} = 0.1813$, $k_{\mathrm{c,s}} = 1.077$, $k_{\mathrm{p}} = 0.83$ and $k_{\mathrm{c}} = 1.2$, one finds $\sigma_{\mathrm{r},4}^{\mathrm{async}}/F_4^{\mathrm{sync}} \approx 20$ which agrees with our previous observation. Note that the original synchronous machine could operate normally with no major vibration. In the case of the new machine, the high exciting force led to unacceptable vibrations.

IV. Reduction of the vibration

As shown in the previous part, the stator winding configuration leads to a high exciting electromagnetic force and consequently to an unacceptable vibration. A first possibility to reduce the vibration is to shift the eigen-frequency of the stator structure by adding additional mass to the stator frame. The second possibility consists in finding an electrical solution. We will discuss here only the electrical solution, more details about possible mechanical solutions can be found in [Ard+13].

Last part has shown that the responsible force for the vibration was mainly due to the existence of parasitic harmonics in the mmf created by the stator winding. As shown in Chapter 4, the harmonic content of the mmf depends strongly on the winding configuration. When designing a winding, one has to connect correctly the bars located in the slots so as to obtain a three-phase balanced system. Several configurations exist but the one giving the highest winding coefficient for the fundamental is normally chosen.

Table 5.10 shows the current configuration of the winding. The 102-slot winding has been splitted into 6 bands covering 17 slots i.e. an angle of 60°. One can observe the change of sign after three bands i.e five poles and that the periodicity between each phase is made every two bands. Furthermore a periodic pattern $4-3-4-3-3$ can be identified, i.e. one group of four conductors from the same phase, then one group of three of another phase, then one group of four of another phase etc.

Assuming that the force is mainly due to the winding harmonic $\Theta_{\mathrm{s},-7}$, it is possible to rearrange the stator winding so that this particular harmonic is reduced but that the fundamental

-b	a	a	a	-c	-c	-c	b	b	b	**-a**	-a	-a	-a	c	c	c
c	-b	-b	-b	a	a	a	-c	-c	-c	**b**	b	b	b	-a	-a	-a
-a	c	c	c	-b	-b	-b	a	a	a	**-c**	-c	-c	-c	b	b	b
b	-a	-a	-a	c	c	c	-b	-b	-b	**a**	a	a	a	-c	-c	-c
-c	b	b	b	-a	-a	-a	c	c	c	**-b**	-b	-b	-b	a	a	a
a	-c	-c	-c	b	b	b	-a	-a	-a	**c**	c	c	c	-b	-b	-b

Table 5.11: Stator winding new configuration

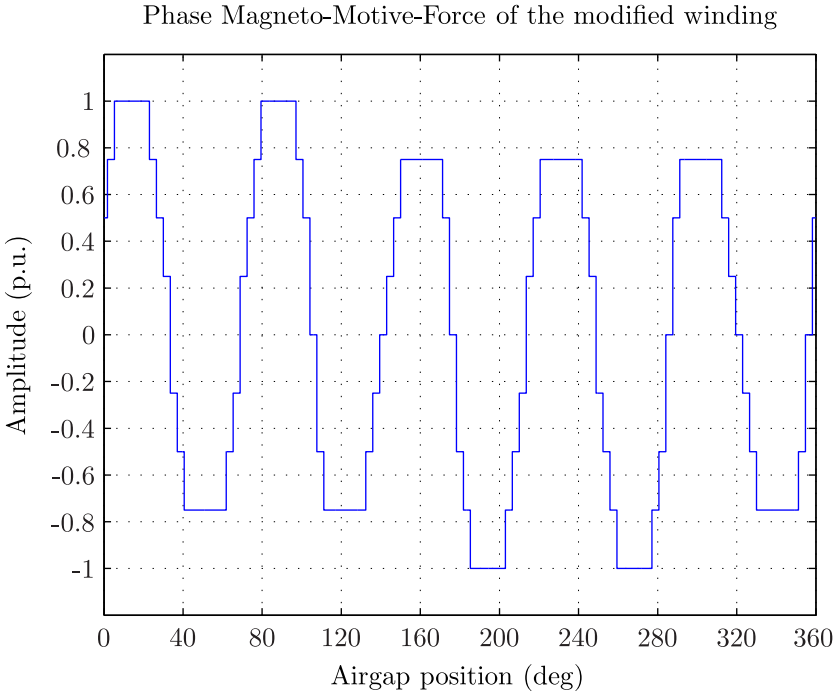

Figure 5.33: Stator mmf of the modified winding

amplitude remains at an acceptable level. This reconstruction is done iteratively by applying an optimization procedure described later in this section. Table 5.11 shows the new obtained winding. One can observe twelve changes of connections. Note that these changes are done on each phase so that the winding remains balanced. The new periodic pattern is $3-3-3-4-4$. Figure 5.33 shows the mmf of one phase of such winding and Figure 5.34 shows the corresponding harmonic content. When comparing with Figure 5.33, one can observe that the mmf harmonic $\Theta_{s,-7}$, has dropped while the fundamental harmonic remained almost unchanged.

Table 5.12 shows the result of the force computation when considering the modified winding. The comparison with previous results shows a sharp increase of the component (8-node, 100 Hz) which can be explained by the fact that mmf harmonic $\Theta_{s,1}$ gets higher. However one can also see that the component (4-node 100 Hz) has decreased by 80%. The machine winding has been modified accordingly and one could measure a decrease of the vibration as shown by this calculation. In the following we study the behavior of the remaining vibration for different

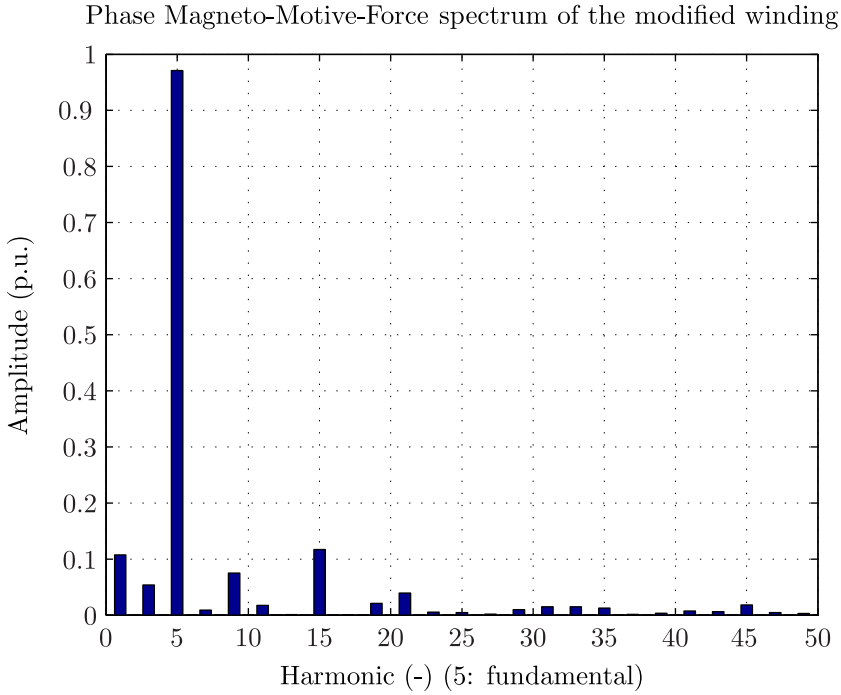

Figure 5.34: Stator mmf spectrum of the modified winding

operation conditions and compare with existing measurement data.

V. Effect of slip on the vibration

Figure 5.35 shows the level of vibration measured on the stator frame when operating the machine in over-excited generator mode in hyper-synchronous mode $s = -15\%$, in synchronous mode $s = 0\%$ and in hypo-synchronous mode $s = +15\%$, while the power factor and apparent power are constant. The calculated (4-node, 100 Hz) force correlates well the tendency of the measured vibration. As we can see the vibration gets lower when increasing the speed. Indeed when increasing the speed, the active power going through the stator decreases and with it the stator current. As seen previously, the force component is mainly due to the interaction between the fundamental airgap flux density and the 7^{th} mmf harmonic which is proportional to the stator current, consequently the force decreases.

VI. Effect of the power factor on the vibration

Figure 5.36 shows the evolution of the measured level of vibration under different power factors. In the studied case, the machine is running under synchronous speed in generator under-excited mode. This means that the machine delivers active power and absorbs reactive power.

Nodes (−)	F (Hz)	σ_r (N/m^2)
0	0	242 110
0	200	18 941
4	100	5108
8	−100	66 419
20	100	39 538
20	−100	231 810

(a) OP_1

Nodes (−)	F (Hz)	σ_r (N/m^2)
0	0	242 670
0	200	21 122
4	100	6122
8	−100	72 493
20	100	44 240
20	−100	231 610

(b) OP_2

Nodes (−)	F (Hz)	σ_r (N/m^2)
0	0	246 790
0	200	21 648
4	100	7772
8	−100	84 076
20	100	45 878
20	−100	232 800

(c) OP_3

Table 5.12: Machine M_2: Main electromagnetic forces for OP_1, OP_2 and OP_3 with new winding

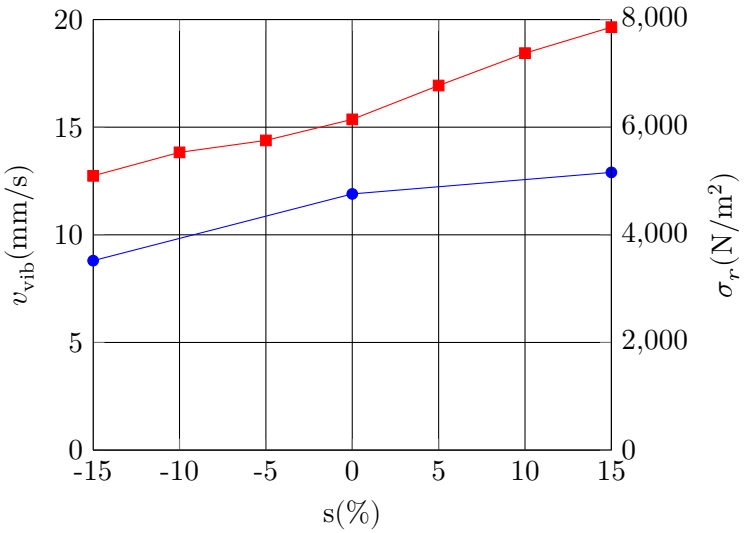

Figure 5.35: Evolution of vibration velocity v_{vib} (—●—) and force (4-node 100 Hz) amplitude F (—■—) vs slip s

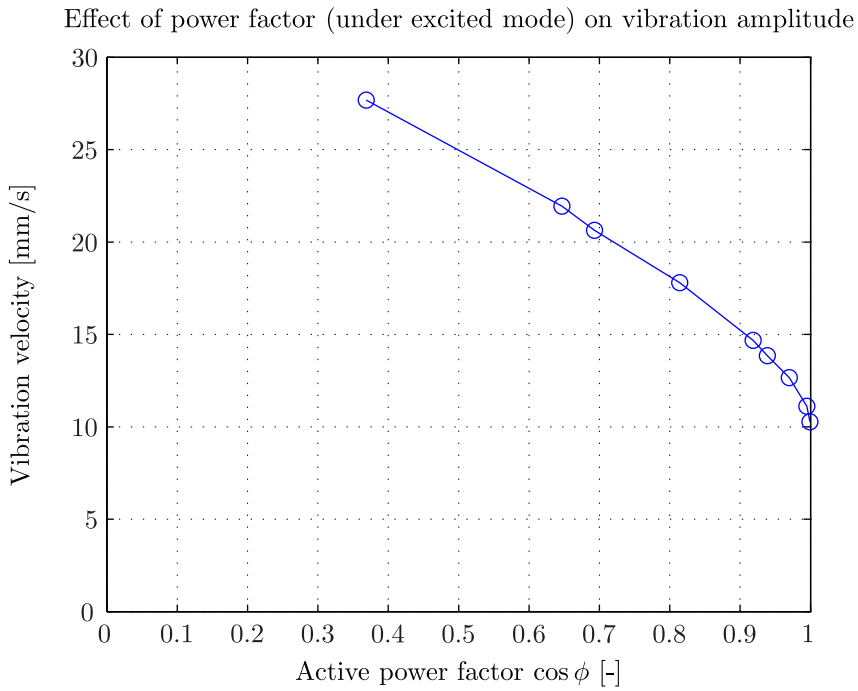

Figure 5.36: Effect of power factor on the vibration amplitude

OP	S (MVA)	U_s (V)	$\cos\varphi$ (−)	s (%)	mode (−)
1	8.6	13.6	1.0	0	under-excited
2	8.6	13.6	0.6	0	under-excited
3	8.6	13.6	0.3	0	under-excited

Table 5.13: Machine M_2: Operation points for the FE study

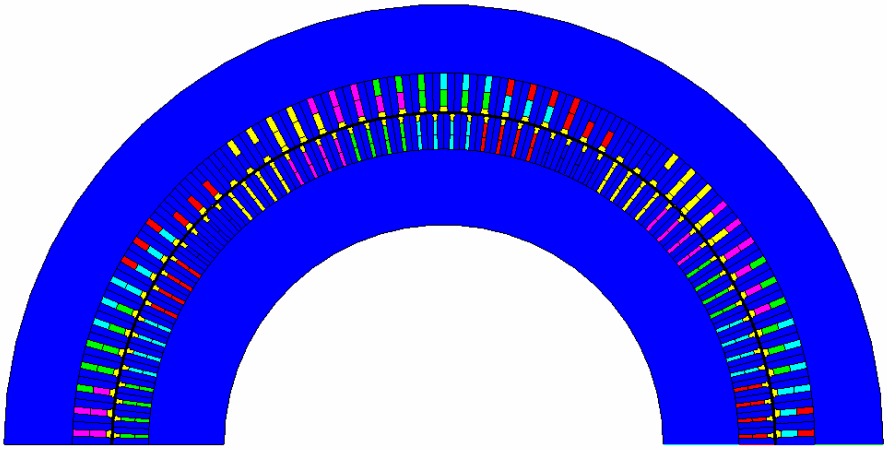

Figure 5.37: Machine M_2: 2DFE geometry

In the previous part we approximated the excitation force as:

$$\sigma_{r,4}(\alpha_s, t) \approx \frac{\hat{B}_{\delta,f} \Lambda \Theta_{s,-7}}{2\mu_0} \cos(2 \cdot \alpha_s + 2f_s \cdot t) \tag{5.34}$$

The fundamental component $\hat{B}_{\delta,f}$ is essentially proportional to the magnetizing voltage while the harmonic component $\Theta_{s,-7}$ depends on the stator current. The experimentation was done for a constant apparent power and constant stator voltage so that only the power factor is varying. In such case $\Theta_{s,-7}$ should remain constant and because the machine is running in under-excited mode the magnetizing voltage and eventually the component $\hat{B}_{\delta,f}$ should drop when the power factor goes down. Consequently when decreasing the power factor $\sigma_{r,4}$ should also decrease. However Figure 5.36 exhibits an opposite behaviour. In order to explain this phenomena, the three operation points defined in Table 5.13 are simulated by carrying out a FE simulation.

Figure 5.37 shows the 2DFE model used for the simulation. Because of the special stator winding configuration, one-half of the machine, i.e. five poles, needs to be modeled.

For each operation point we compute the space and time evolution of the radial airgap flux

density $B_{\delta,\mathrm{r}}(\alpha_\mathrm{s},t)$ and the corresponding harmonic content so that we can write:

$$B_{\delta,\mathrm{r}}(\alpha_\mathrm{s},t)=\sum_{\nu=1}^{+\infty}\hat{B}_{\delta,\nu}\cdot\cos(P_\nu\alpha_\mathrm{s}+2\pi F_\nu t+C_\nu) \tag{5.35}$$

From last part, we know that the interaction between two flux density harmonics ν_1 and ν_2 gives rise to radial forces with $2\cdot(P_{\nu_1}\pm P_{\nu_2})$-nodes and $F_{\nu_1}\pm F_{\nu_2}$ frequency. In the studied case we only focus on the component (4-node, 100 Hz) so that by using the FE simulation results, we track all the couples of harmonics $\{\nu_1,\nu_2\}$ leading to $2\cdot(P_{\nu_1}\pm P_{\nu_2})=4$ nodes and $F_{\nu_1}\pm F_{\nu_2}=100\,\mathrm{Hz}$. Note that each obtained couple of harmonics is defined by a certain $\sigma_{\mathrm{r},\nu_1,\nu_2}$ amplitude and a certain C_{ν_1,ν_2} phase shift so that the corresponding force can be represented as a vector.

Figure 5.38 displays the result of such treatment. One can see that several combinations are involved in the creation of the force. Nevertheless, only three of them appear really significant for the study:

1. The combination between the stator mmf harmonics $P_{\nu_1}=1$ and $P_{\nu_2}=1$
2. The combination between the fundamental $P_{\nu_1}=5$ and the stator mmf harmonics $P_{\nu_2}=7$
3. The combination between the fundamental $P_{\nu_1}=5$ and the harmonic $P_{\nu_2}=3$

While the first two combinations are directly linked to the stator fractional slot winding configuration, the third combination involving the third harmonic is due to the effect of the magnetic saturation as it was shown in Chapter 4.

Table 5.14 details for each operation point the values of the three main components involved in the force $\sigma_{\mathrm{r},4}$, (4-node, 100 Hz). The component $\sigma_{\mathrm{r},5,7}$ decreases while the power factor goes down as it was predicted previously while the component $\sigma_{\mathrm{r},1,1}$ increases by a factor of 30%. One can also observe a significant variation of the component $\sigma_{\mathrm{r},3,5}$. This can be explained by the fact that when decreasing the power factor in under-excited mode, the machine is getting less saturated so that the harmonics due to saturation go down and consequently the component $\sigma_{\mathrm{r},3,5}$. Finally the vector combination of each component results in an higher force. Note that such behavior is very difficult to predict analytically as the magnetic saturation seems to play a key role in the amplitude of the force; for such investigation only a FE simulation makes it possible to better consider this effect.

OP	$\sigma_{\mathrm{r},4}$ (N/m^2)	$\sigma_{\mathrm{r},5,7}$ (N/m^2)	$\sigma_{\mathrm{r},1,1}$ (N/m^2)	$\sigma_{\mathrm{r},3,5}$ (N/m^2)
1	4100	3888	1060	1600
2	5460	3584	1308	580
3	5585	3448	1364	436

Table 5.14: Characterization of the component 4-nodes, 100 Hz

Figure 5.39 compares the measured level of vibration to the calculated electromagnetic force (4-node, 100 Hz) amplitude. One can observe a good correlation between both curves.

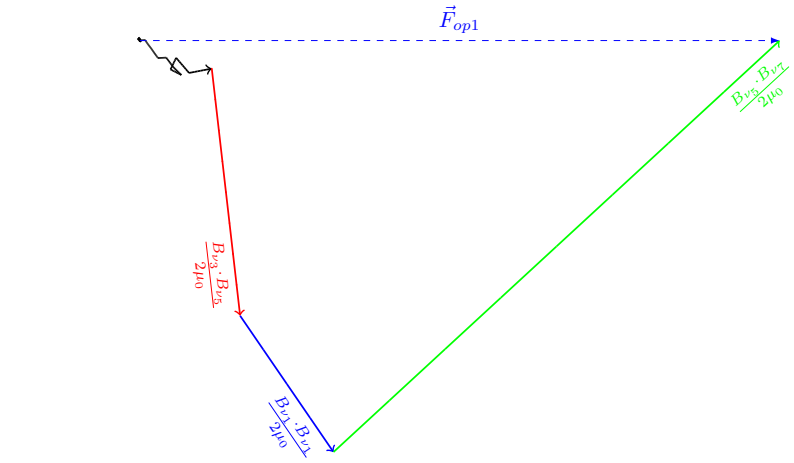

(a) OP_1

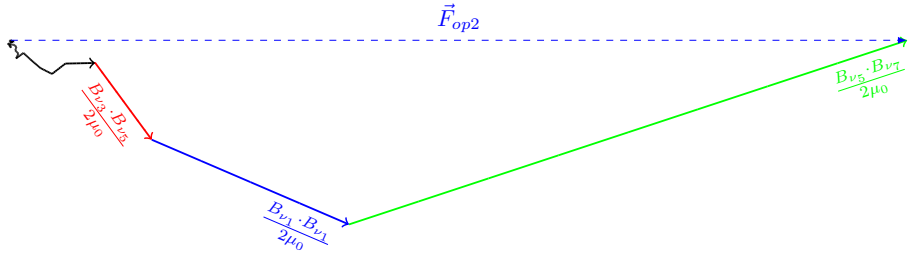

(b) OP_2

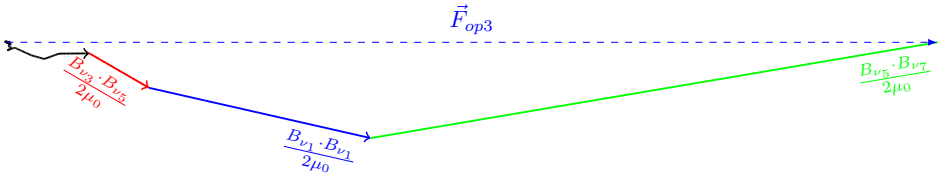

(c) OP_3

Figure 5.38: Force components 4-nodes, 100 Hz, three operation points

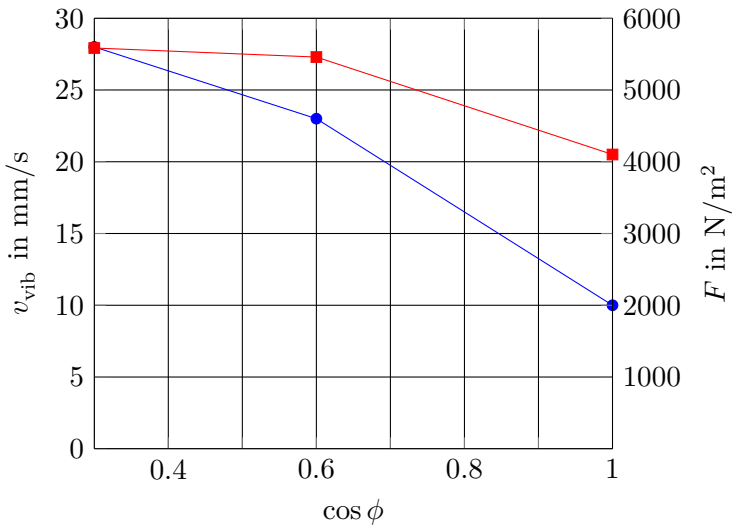

Figure 5.39: Evolution of vibration velocity v_{vib} (—●—) and force 4 nodes 100 Hz amplitude F (—■—) vs. power factor $\cos\phi$ (under-excited mode)

5.3.3 Winding optimization

As seen previously the mmf harmonics generated by the windings cause parasitic forces and in some cases are responsible for vibrations. The amplitude of such harmonics is directly connected to the configuration of the winding. We describe here a simple iteration method able to rearrange the winding so that a particular parasitic winding harmonic gets reduced keeping the fundamental harmonic at a high level. We focus only on balanced three-phase and two-layer windings.

Firstly, consider a winding having N_{z} slots and p pairs of poles. We consider that the coil span of the winding is known, constant and equal to Y_1. Define a coil as the serial connection between a top conductor and a bottom conductor as already described in Chapter 4 in Figure 4.1. The greatest common divider between N_{z} and p gives the number N_{F} of repeated sections of the winding [WK60]. Consequently the construction of the winding can be restricted to the study of one section, knowing that each section is made of p/N_{F} pairs of poles and $N_{\text{z,f}} = N_{\text{z,s}}/N_{\text{F}}$ slots. The remaining sections are obtained by periodicity. In addition, as only balanced three-phase windings are considered, the study can be limited to one phase only. The two other phases are obtained by periodicity of $N_{\text{z,f}}/3$ and $2 \cdot N_{\text{z,f}}/3$ slots.

Finally the work of the electrical designer is to select $N_{\text{z,f}}/3$ coils from a section and connect them so that when supplied with a current, the winding generates a mmf with the correct number of poles as close as possible to a sinusoid. Several possible configurations may arise and the one guaranteeing the maximum fundamental winding coefficient is normally chosen.

In the next we use the concept of the induced voltage diagram to calculate the winding coefficients of a particular winding.

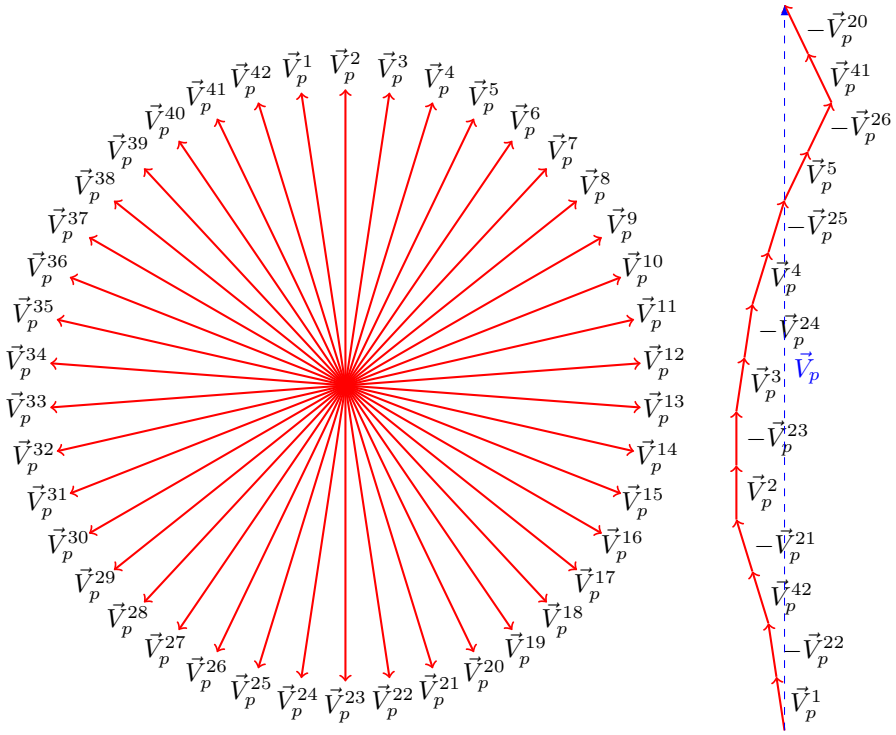

Figure 5.40: Induced fundamental voltage phasors

I. Description of the algorithm

Let us consider a winding having $q = 7$ slots per pole and phase and seven pairs of poles. The corresponding number of slots is $N_{\mathrm{z}} = 294$ and one can identify seven identical sections made of one pair of pole and $N_{\mathrm{z,f}} = 42$ coils. Figure 5.40 (left) shows the fundamental voltage diagram on which the voltage induced on each coil are represented as phasors. The angle between each phasor is expressed in electrical degrees.

A phasor is due to the superposition of the induced voltage phasor in a top bar and the induced voltage phasor in the bottom bar. So that for a particular harmonic ν, the induced voltage phasor V_ν^k is:

$$V_\nu^k = V_{\mathrm{top}} \cdot e^{\mathrm{i}\cdot\nu\cdot k\cdot\tau_s} - V_{\mathrm{bot}} \cdot e^{\mathrm{i}\cdot\nu\cdot(k+Y_1)\cdot\tau_s} \tag{5.36}$$

where k is the index number of the coil. In the next, we consider $|V_{\mathrm{top}}| = |V_{\mathrm{bot}}| = 1$. Furthermore the total induced harmonic voltage V_ν is due to the connection of $N_{\mathrm{z,f}}/3 = 14$ phasors and expressed as:

$$V_\nu = \sum_{k=1}^{N_{\mathrm{z,f}}} \alpha_k \cdot V_\nu^k \tag{5.37}$$

where α_k is either 0, 1 or -1, and we have:

$$\sum_{k=1}^{N_{\mathrm{z,f}}} |\alpha_k| = \frac{N_{\mathrm{z,f}}}{3} \tag{5.38}$$

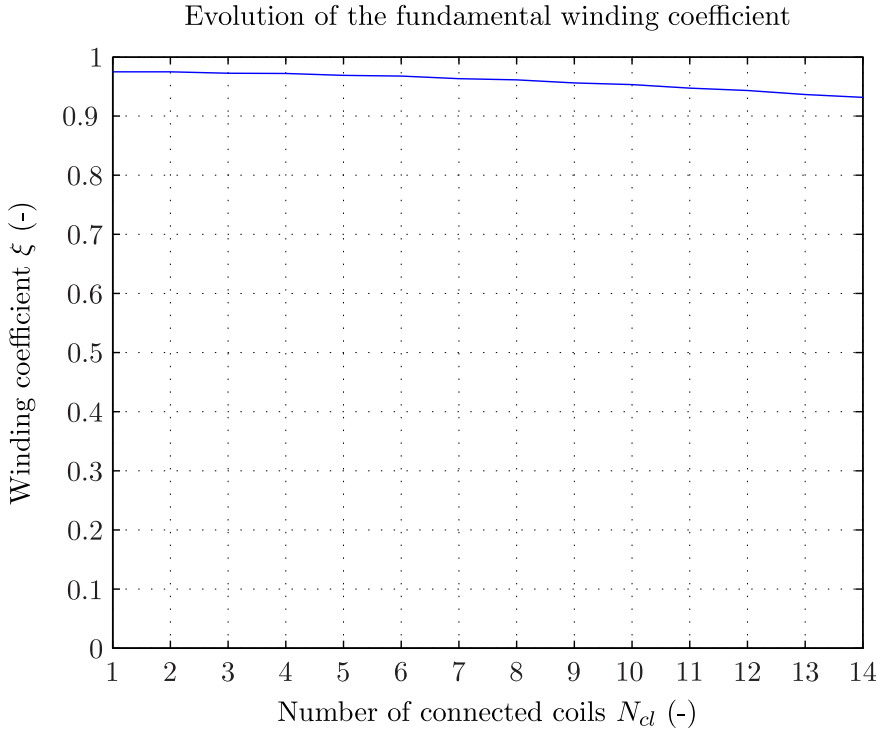

Figure 5.41: Simple winding: fundamental winding coefficient evolution

The winding coefficient of a particular harmonic can be expressed by Equation (5.39). The coefficient 2 comes from the fact that a coil is made of two bars.

$$\xi_\nu = \frac{V_\nu}{2 \cdot (N_{\mathrm{z,f}}/3)} \tag{5.39}$$

For standard windings, the objective is normally to select $N_{\mathrm{z,f}}/3 = 14$ phasors and connect them to obtain the maximum fundamental winding coefficient voltage ξ_{p}. This can be done manually when the number of coils is not high or automatically by using a special algorithm as we describe here.

Initially the algorithm selects arbitrarily a coil, for example the first one. Then it searches, from the list of non-used coils in the section, for the association with another coil, in one direction or the other, which gives the highest sum for the fundamental phasor. When the choice is made, the two other phases and other sections are constructed by periodicity. This ensures that the winding remains balanced, and it makes it possible to reduce the list of non-used coils in the section because of circularity of the winding. This process is repeated until $N_{\mathrm{z,f}}/3$ coils have been connected together. Figure 5.41 shows the variation of the fundamental winding coefficient along the winding construction. One can see that it always remains at a high value. Figure 5.40 (right) shows the phasors composition of the resulting fundamental induced voltage.

For more original windings such as the fractional winding, looking for the best fundamental winding coefficient is also the main objective. In this case, the construction of the winding is based on the same principles as described previously. However it may also be interesting

to reduce the winding coefficient of a particular harmonic responsible for parasitic forces for example. Consequently instead of looking for the maximum fundamental induced voltage, the algorithm searches for the minimum parasitic induced voltage. Yet, this choice has to be done so that the fundamental induced voltage remains at an acceptable level. We define the quantity ΔV_{p} expressed as:

$$\Delta V_{\mathrm{p}} = \left| \frac{V_{\mathrm{p}}^{\max} - V_{\mathrm{p}}^{k}}{V_{\mathrm{p}}^{\max}} \right| \tag{5.40}$$

where V_{p}^{k} is the fundamental induced voltage when selecting the coil k in one direction or the other and $V_{\mathrm{p}}^{\max}$ is the maximum induced voltage that can be obtained among the available coils of the section. Consequently, at each step, the algorithm chooses the next phasor so that the parasitic voltage harmonic decreases and that ΔV_{p} remains under a defined value $\Delta V_{\mathrm{p}}^{\max}$.

In the following, we apply this method to rearrange three fractional windings. Note that in each case the rearrangements were initially found manually. The developed algorithm confirms the modifications and appears to be more efficient as it allows to explore more possibilities than the manual method.

II. Winding 1: $p = 5$, $N_{\mathrm{z}} = 102$

As a first example, we consider the fractional winding of the last section. As we have five pairs of poles and 102 slots, the number of repetitive sections is equal to one. Previously, we identified the harmonic $P_{\nu} = 7$ as the main contributor to the parasitic force. Consequently the algorithm has to arrange $N_{\mathrm{z,f}}/3 = 34$ coils per phase so that the harmonic $P_{\nu} = 7$ decreases, but ensuring that the fundamental remains at a correct value.

Figure 5.42 shows the result of the algorithm. One can observe the evolution of the winding coefficient of the fundamental, the parasitic harmonic $P_{\nu} = 5$ and an additional harmonic $P_{\nu} = 1$ as a function of the parameter $\Delta V_{\mathrm{p}}^{\max}$. Note that the component $P_{\nu} = 1$ is only here for observation and is not part of the optimization.

One can see that among all iterations an optimum winding has been found (circle), i.e. the fundamental remains at a correct value while the parasitic harmonic is strongly reduced. Note that the same optimum can be reached several times. It appears that a strong reduction of the parasitic harmonic $P_{\nu} = 7$ cannot be done without a strong increase of the harmonic $P_{\nu} = 1$. Nevertheless, as we have seen previously, the harmonic $P_{\nu} = 7$ contributes more to the force than the harmonic $P_{\nu} = 1$.

One can notice that the reduction of the fundamental is not decreasing linearly as the parameter $\Delta V_{\mathrm{p}}^{\max}$ increases. The same comment can be done for the harmonic $P_{\nu} = 7$. This can be explained by the fact that at each step, the algorithm selects the local optimum phasor leading to the smallest winding harmonic but does not pay attention to the choices that will be made at the next steps. This phenomena can be denounced as the main drawback of the method as finally we are not sure to find the global optimum. However by setting correctly the variation range of $\Delta V_{\mathrm{p}}^{\max}$ one should cover all possible solutions.

Figures 5.43 and 5.44 show the variations of the fundamental winding coefficient as well as

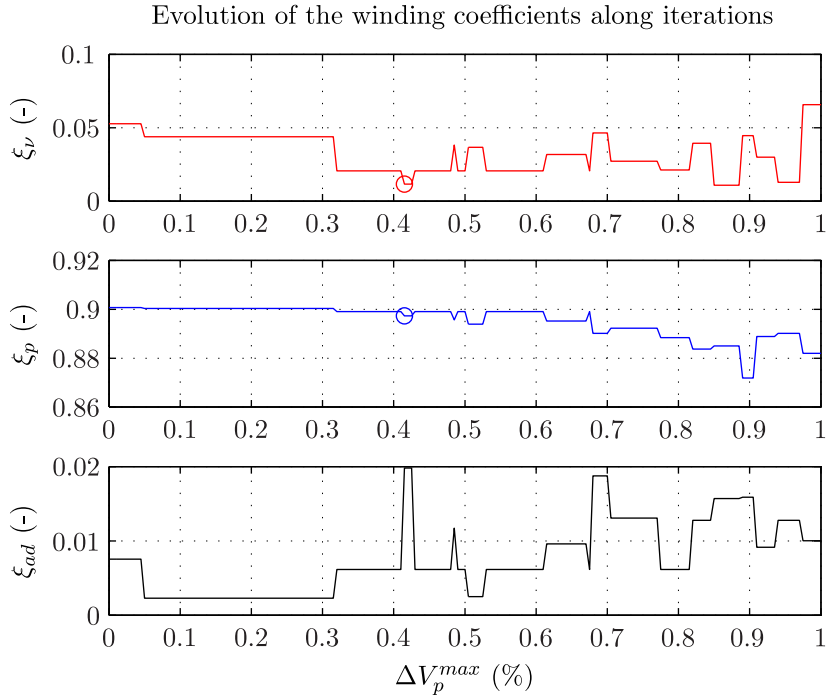

Figure 5.42: Iterative optimization results of the winding

the parasitic winding coefficient along the coil connection process. We display the results for the standard winding and the optimum arrangement leading to the decrease of the harmonic $P_\nu = 7$. One can first observe that the fundamental winding coefficient remains always at a very high value. Furthermore when looking to the parasitic winding harmonic, one can see that its variations are under control which is not the case when applying the standard winding construction.

III. Winding 2: $p = 48$, $N_z = 684$

As a second example, we consider a fractional winding having 48 pairs of poles and 684 slots. In this case there are $N_F = 12$ repetitive sections counting four pairs of poles and $N_{z,f} = 57$ sections. This winding equips the stator of a salient pole synchronous machine which presented a problem of vibration due to force component (24-node, 120 Hz)[TLU12]. The main contributor to this force is the winding harmonic $P_\nu = 60$.

Figure 5.45 shows the result of the algorithm. One can see that an optimum is found. It corresponds to a winding pattern equal to $[3, 3, 2, 2, 2, 3, 2, 2]$ while the original was $[3, 2, 3, 2, 2, 3, 2, 2]$ so that there is only one single permutation. As there are three phases and 12 sections, this new winding needs at least 36 changes of connection. This solution was implemented on the machine and one could measure a reduction of the vibration amplitude by 65% as described in [TLU12]. As already mentioned previously and demonstrated by Figures 5.46 and 5.47 one can see that the optimum solution ensures that the fundamental winding coefficient remains high while the

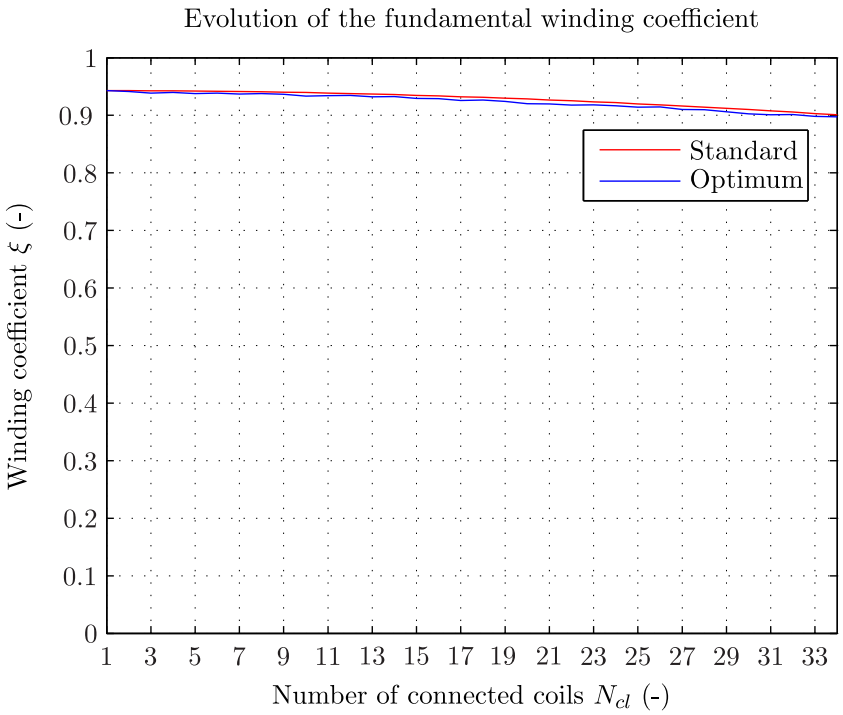

Figure 5.43: Iterative optimization results of the winding

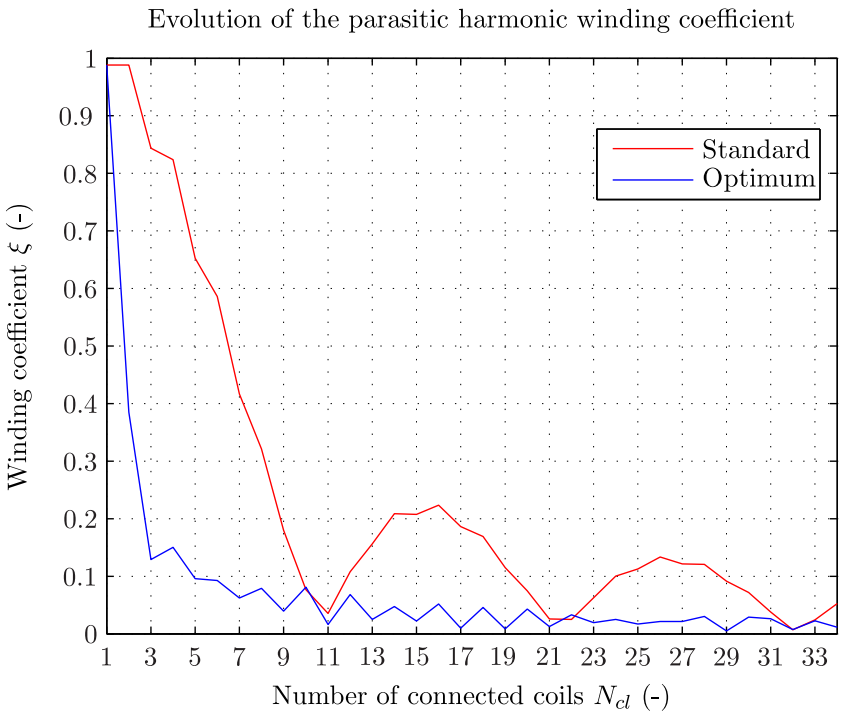

Figure 5.44: Iterative optimization results of the winding

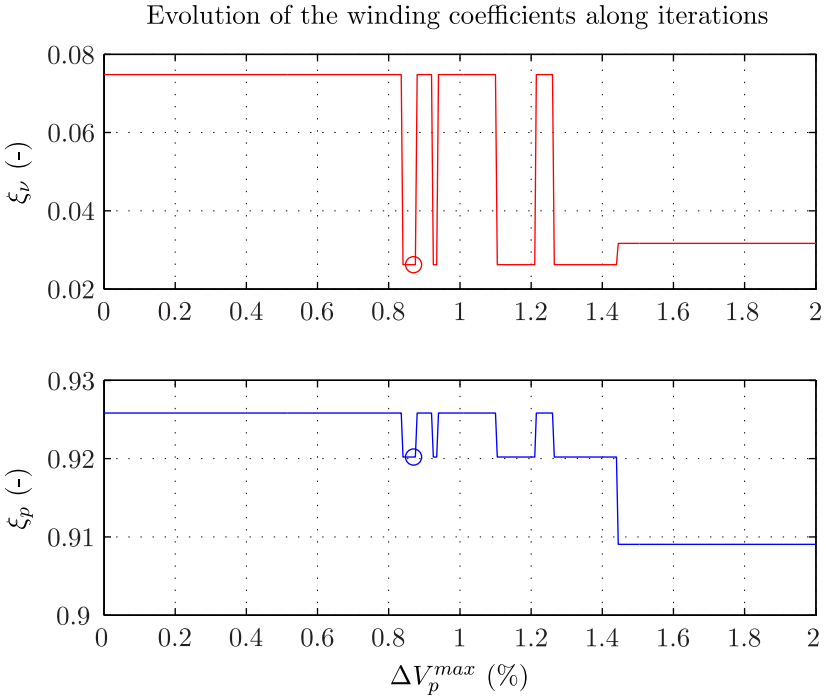

Figure 5.45: Iterative optimization results of the winding

parasitic harmonic is kept low.

IV. Winding 3: $p = 24$, $N_z = 396$

As a final example, we consider a fractional winding having 24 pairs of poles and 396 slots. In this case there are $N_{z,f} = 12$ minimum repetitive sections counting two pairs of poles and $N_F = 57$ sections. This winding equips the stator of a salient-pole synchronous machine which presented a problem of vibration due to the force component (24-node, 240 Hz). The main contributors of this force have been identified to be the winding harmonics $P_\nu = 84$ and $P_\nu = 132$.

Figure 5.48 shows the resulting evolution of the corresponding winding factors as well as the one of the fundamental along the iterations. A first optimum has been found (black circle) leading to the reduction of the winding harmonic $P_\nu = 84$ by 66% and to the complete suppression of the harmonic $P_\nu = 132$. However the corresponding force reduction was not enough, only 70%. Consequently the number of repetitive sections have been reduced to $N_F = 6$ according to [Fer13] in order to increase the number of possible connections. Therefore a second optimum appeared (green circle). This makes it possible to reduce the winding harmonic $P_\nu = 84$ by 92% while the harmonic $P_\nu = 132$ is kept at zero and finally to decrease the excitation force by 95%. One should pay attention to the fact that this solution leads to a higher decrease of the fundamental harmonic responsible for an increase of the field winding current and consequently of the rotor copper losses. Furthermore it could in other cases create additional exciting forces components responsible for vibrations.

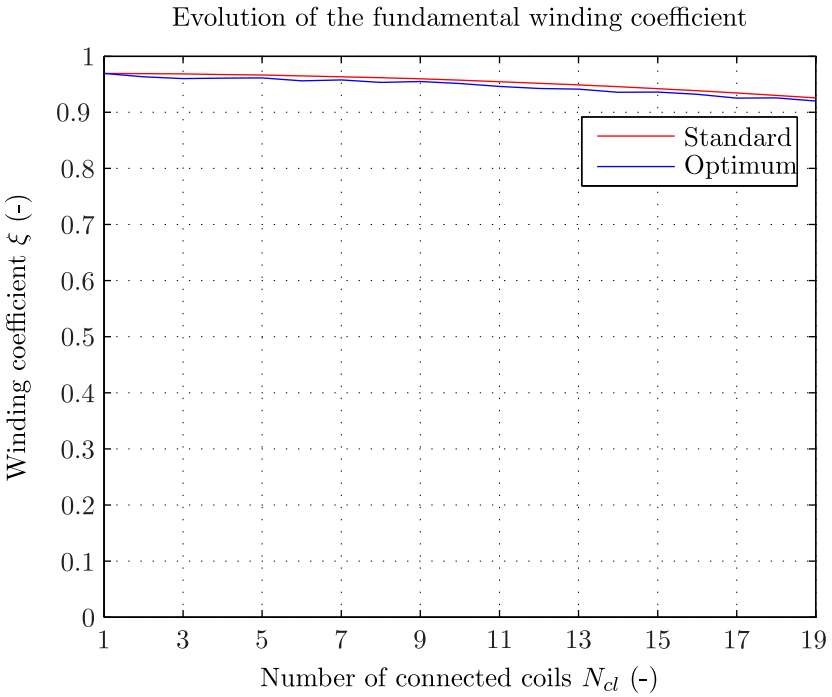

Figure 5.46: Iterative optimization results of the winding

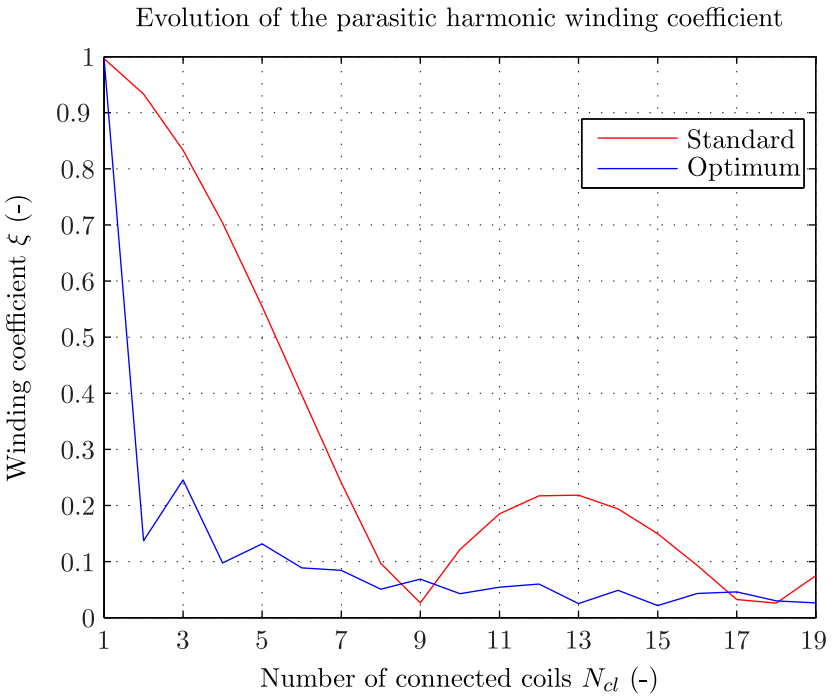

Figure 5.47: Iterative optimization results of the winding

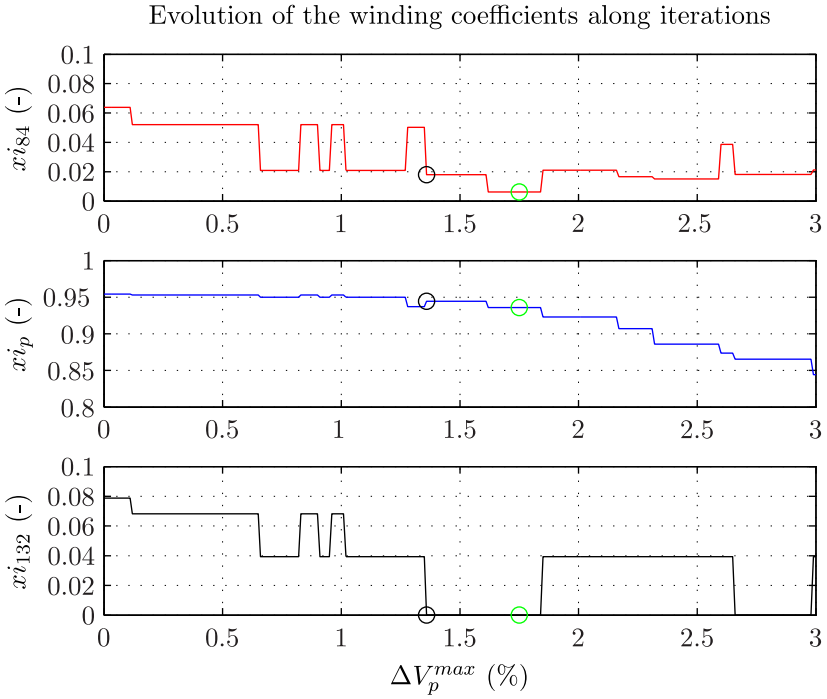

Figure 5.48: Iterative optimization results of the winding

Figures 5.49, 5.50 and 5.51 show the corresponding variation of the fundamental and the two parasitic harmonics winding coefficients. Again one can see that the developed method enables a better control of the winding harmonics.

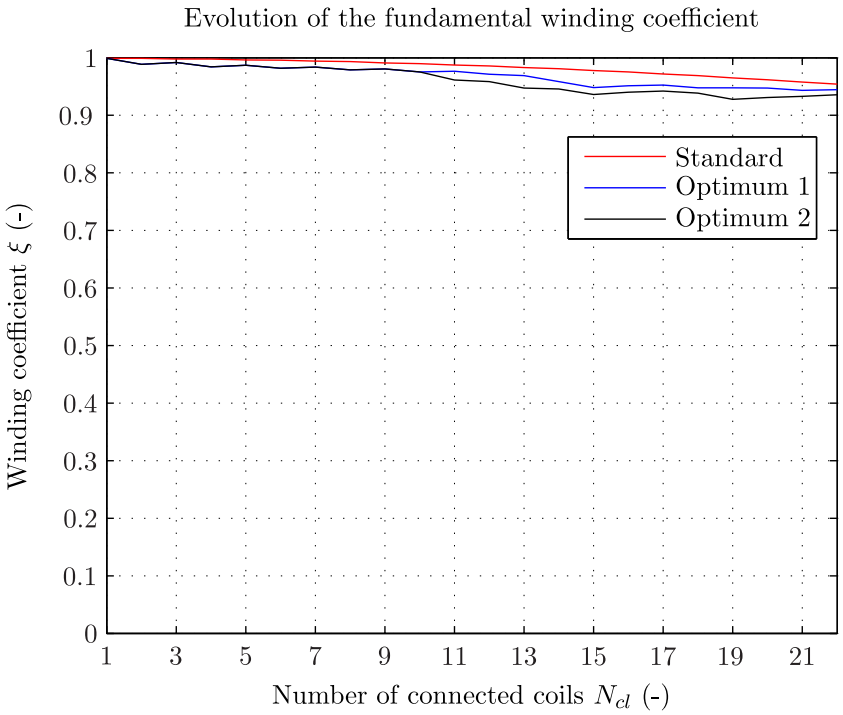

Figure 5.49: Iterative optimization results of the winding

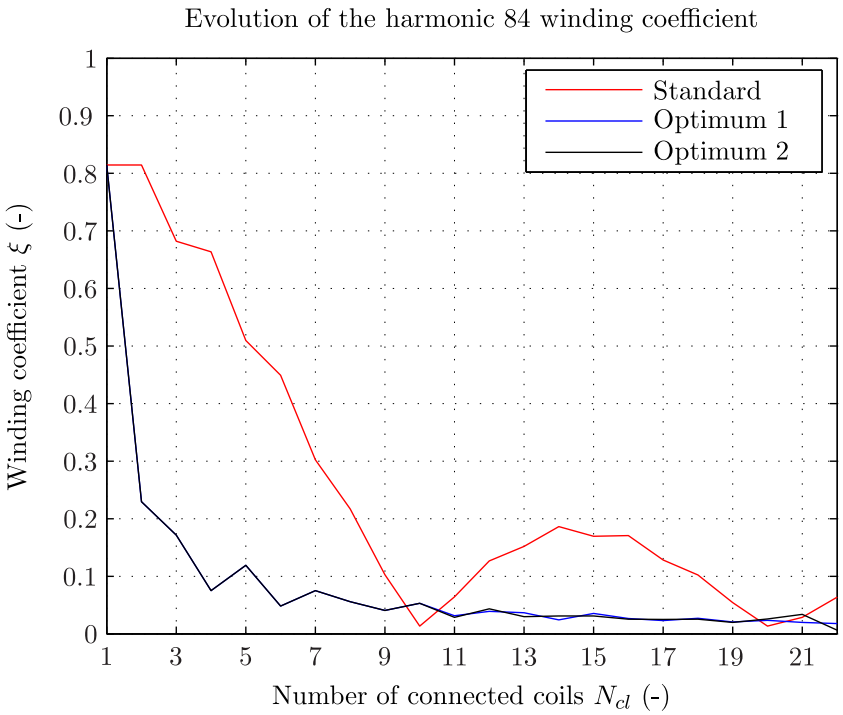

Figure 5.50: Iterative optimization results of the winding

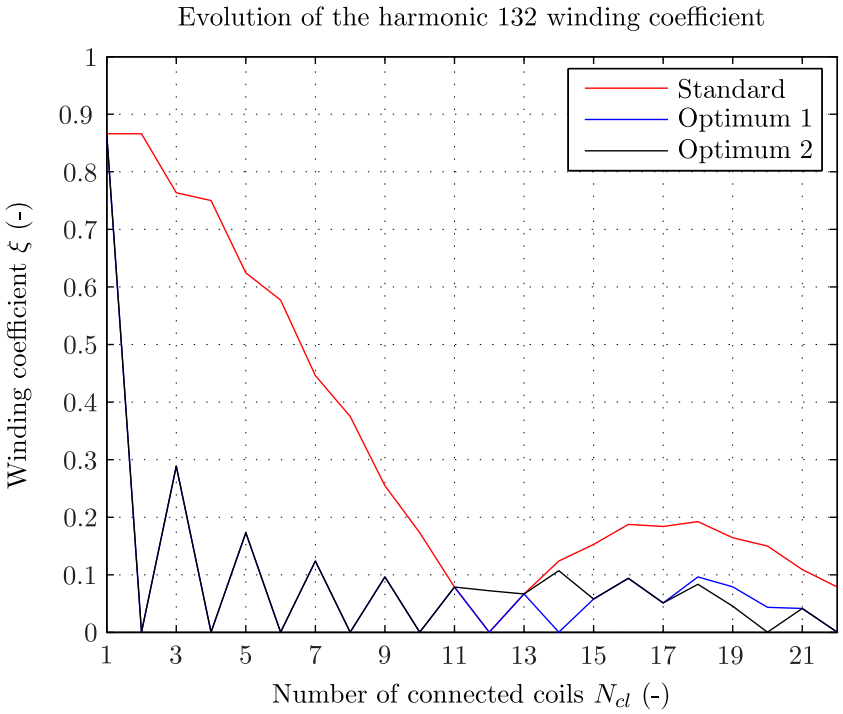

Figure 5.51: Iterative optimization results of the winding

5.3.4 Summary

This part studied the problem of the radial electromagnetic forces occurring in the DFIM. An analytical calculation made it possible to derive such force components and has shown a good agreement with a two-dimensional finite element computation. The results of the force calculation has been crossed with a mechanical analysis of the stator core and frame structure. The speed dependent component (0-node, $f_s \cdot (6s + 6)$Hz) has been identified as a potential dangerous component. The effect of a fractional stator winding has been investigated. It was shown through the study of a real example that such particular winding could be the source of dangerous vibrations which can be very high. This is due to the fact that the airgap of the DFIM is small, and that the harmonics responsible for the force are not damped contrarily to the conventional synchronous salient-pole machine. Furthermore, depending on the operation i.e. the speed or the amount of reactive power, the amplitude of the excitation force could change and consequently increase the level of vibration. However, after identifying the responsible mmf harmonics such winding can be optimized in order to reduce the amplitude of the exciting force. This part has shown the importance of considering radial electromagnetic forces as they might excite an eigen-mode of the stator core and frame mechanical structure. In the next section we extend the study to the parasitic airgap electromagnetic torques also called dynamic torques.

5.4 The parasitic dynamic torques

Previous part computed the electromagnetic radial forces and studied the potential risk of excitation of the stator core eigen-frequencies. Following section deals with the problem of parasitic pulsating electromagnetic torques also called dynamic airgap torques.

First part applies the FE time stepping method described in Chapter 3 in order to simulate several load-operation points of the machine and to extract for each case the corresponding electromagnetic torque variation. The obtained results demonstrate that several pulsating electromagnetic torques components arise in addition to the working constant torque. An additional calculation based on the harmonic airgap flux density model developed in Chapter 4 makes it possible to explain the obtained results.

Second part analyzes the impact of such parasitic torques on the shaft line coupling the machine rotor with the turbine. Indeed these dynamic torques may match with the shaft natural oscillation frequencies and lead to torsional vibrations of the shaft line. Depending on the severity of the vibration it can create noise and in extreme cases cracks in the shaft. An equivalent three-mass model of the shaft line makes it possible to calculate the torsional eigen-mode of the shaft line and to assess the potential risk of each parasitic electromagnetic torque.

Third part extends the steady-state operation study to the transient operation study and more particularly the startup of the machine as a motor. During this operation the stator of the machine is short-circuited and the rotor current is controlled in order to drive the machine from standstill to the synchronization speed. A regulated FE time stepping simulates this process. The variations of the electromagnetic torque are computed and analyzed in order to assess the risk of resonance.

5.4.1 Finite element computation of the electromagnetic torque

I. Finite element study

The electromagnetic torque is computed for three operation points as defined in Table 5.15 by applying the 2DFE time stepping method developed in Chapter 3. Note that the converter voltage harmonics are not considered although they can also have an impact on the results. As we can see the operation points are chosen in order to study the effect of the slip on the harmonic content and the effect of the excitation mode i.e. over-excited or under-excited which will have an impact on the saturation state of the magnetic circuit. In all cases the network frequency is constant and equal to 50 Hz.

Figures 5.52 and 5.53 show the variations of the electromagnetic torque for the operation points OP_1 and OP_2. One can observe in both cases the presence of strong ripples leading to a $\pm 1.5\%$ torque undulation. Furthermore a main difference between OP_1 and OP_3 is the existence of a low frequency component. These observations are confirmed by carrying out a Fourier analysis whose results are reported in Table 5.16. The harmonic content of the torque for OP_1 are similar to the operation points OP_2 and OP_3. However one can observe a shift

OP (−)	P_{mec} (MW)	U_{s} (kV)	$\cos\varphi$ (−)	s (%)	mode (−)
1	256	18	0.9	0	over-excited
2	256	18	0.9	−5	under-excited
3	256	18	0.9	−5	over-excited

Table 5.15: Load point characteristics for the electromagnetic torque computation

F_ν (Hz)	$\Gamma_\nu/\Gamma_{\mathrm{dc}}$ (%)
300	0.43
600	0.35
2100	0.00
2400	0.00

(a) OP_1

F_ν (Hz)	$\Gamma_\nu/\Gamma_{\mathrm{dc}}$ (%)
15	0.18
315	0.38
630	0.27
2205	0.85
2520	0.33

(b) OP_2

F_ν (Hz)	$\Gamma_\nu/\Gamma_{\mathrm{dc}}$ (%)
15	0.09
315	0.36
630	0.39
2205	0.80
2520	0.34

(c) OP_3

Table 5.16: Electromagnetic torque harmonics

in the frequency 300 Hz $\rightarrow$ 315 Hz, 600 Hz $\rightarrow$ 630 Hz, 2100 Hz $\rightarrow$ 2205 Hz... and the presence of the low frequency component 15 Hz in the case of operation points OP_2 and OP_3. Note that the amplitude of this component is doubled between the under-excited case OP_2 and the over-excited case OP_3. This can be explained by the difference of the magnetization leading to different airgap harmonics. In order to understand the obtained harmonic content and the impact of the speed on each harmonic, the airgap flux density model developed in the Chapter 4 is used.

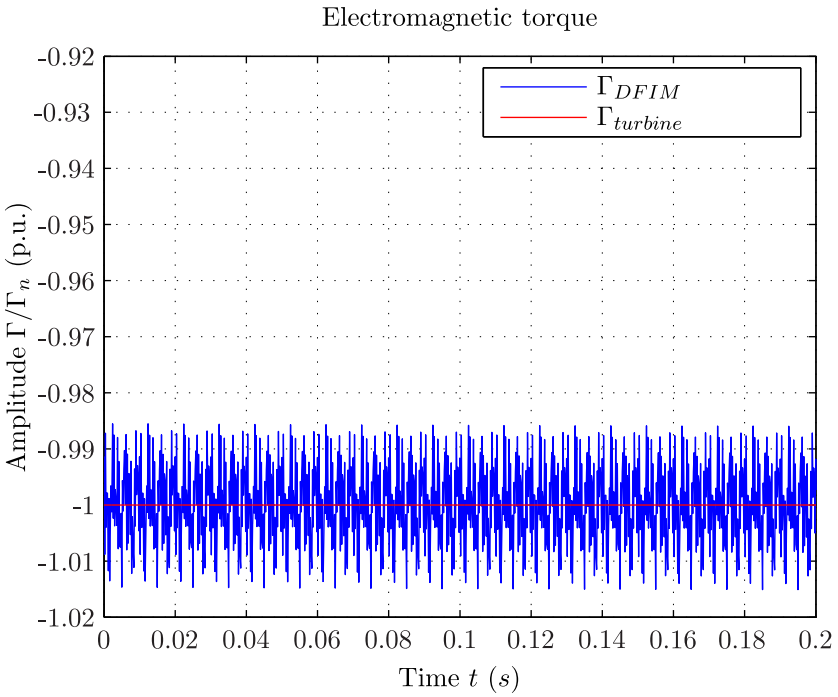

Figure 5.52: Electromagnetic torque for OP_3 $s = 0\%$

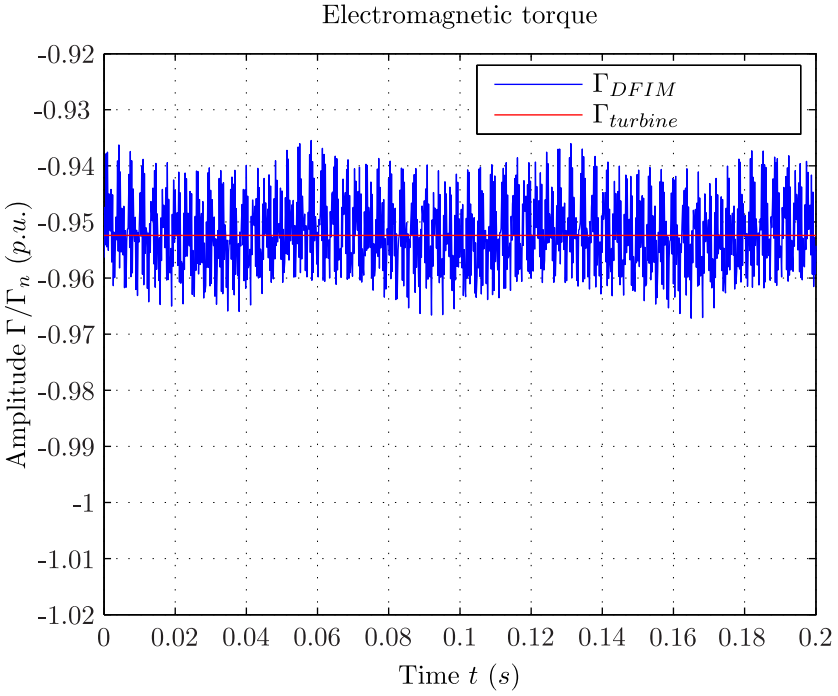

Figure 5.53: Electromagnetic torque for OP_1 $s = -5\%$

II. Analytical study

The electromagnetic torque due to the interaction of the stator and rotor magnetic field, considering a non-saturated magnetic state, can be expressed by Equation (5.41)

$$T(t) = \frac{\partial W(t)}{\partial \theta_0} \tag{5.41}$$

where θ_0 is the initial phase shift between the stator and rotor magnetic fields and W is the magnetic energy stored in the airgap given by Equation (5.42) [Bes08].

$$W(t) = \frac{\delta_g l}{2\mu_0} \int_0^{2\pi} \left(B_{\delta,s}(\alpha_s, t) + B_{\delta,r}(\alpha_s, t) \right)^2 d\alpha_s \tag{5.42}$$

We have seen in Chapter 4 that the stator and the rotor flux density can be expressed as:

$$\begin{aligned} B_{\delta,s}(\alpha_s, t) &= \Theta_s(\alpha_s, t)\, \Lambda_p(\alpha_s, t) \\ B_{\delta,r}(\alpha_s, t) &= \Theta_r(\alpha_s, t)\, \Lambda_p(\alpha_s, t) \end{aligned} \tag{5.43}$$

with:

$$\begin{aligned} \Theta_s(\alpha_s, t) &= \sum_{\nu_s=1}^{+\infty} \Theta_{s,\nu_s} \sin\left(P_{s,\nu_s}\alpha_s + 2\pi F_{s,\nu_s} t \right) \\ \Theta_r(\alpha_s, t) &= \sum_{\nu_r=1}^{+\infty} \Theta_{r,\nu_r} \sin\left(P_{r,\nu_r}\alpha_s + 2\pi F_{r,\nu_r} t + P_{r,\nu_r}\theta_0 \right) \\ \Lambda_p(\alpha_s, t) &= \sum_{\nu_p=1}^{+\infty} \hat{\Lambda}_{p,\nu_p} \cos\left(P_{p,\nu_p}\alpha_s + 2\pi F_{p,\nu_p} t + P_{p,\nu_p}\theta_0 \right) \end{aligned} \tag{5.44}$$

Consequently Equation (5.42) can be rewritten as:

$$W(t) = \frac{\delta l}{2\mu_0} \int_0^{2\pi} (\Theta_s + \Theta_r)^2\, \Lambda^2 d\alpha_s \tag{5.45}$$

Noticing that only the rotor mmf and the airgap permeance depends on the initial phase shift θ_0, Equation (5.41) becomes:

$$T(t) = \frac{\delta L}{\mu_0} \int_0^{2\pi} \frac{\partial \Theta_r}{\partial \theta_0} (\Theta_s + \Theta_r)\, \Lambda_p^2 + \frac{\partial \Lambda_p}{\partial \theta_0} (\Theta_s + \Theta_r)^2 \, d\alpha_s \tag{5.46}$$

We assume first a constant airgap. In this case the airgap permeance is constant and equal to Λ_{p_0} and Equation (5.46) can be simplified in Equation (5.47):

$$\begin{aligned} T(t) = \frac{\Lambda_0^2 \delta L}{\mu_0} \int_0^{2\pi} \frac{\partial \Theta_r}{\partial \theta_0} (\Theta_s + \Theta_r) d\alpha_s &= \frac{\Lambda_0^2 \delta L}{\mu_0} \left[\int_0^{2\pi} \frac{\partial \Theta_r}{\partial \theta_0} \Theta_s d\alpha_s + \int_0^{2\pi} \frac{\partial \Theta_r}{\partial \theta_0} \Theta_r d\alpha_s \right] \\ &= \frac{\Lambda_{p_0}^2 \delta L}{\mu_0} \left[I_1(t) + I_2(t) \right] \end{aligned}$$

The first integral I_1 is given by:

$$I_1(t) = \sum_{\nu_s=1}^{+\infty} \sum_{\nu_r=1}^{+\infty} \frac{\hat{\Theta}_{s,\nu_s} \hat{\Theta}_{r,\nu_r}}{2} \int_0^{2\pi} \Big[\sin\Big(\Big(P_{s,\nu_s} + P_{r,\nu_r} \Big) \alpha_s + 2\pi \Big(F_{s,\nu_s} + F_{r,\nu_r} \Big) t + P_{r,\nu_r} \theta_0 \Big) + \sin\Big(\Big(P_{s,\nu_s} - P_{r,\nu_r} \Big) \alpha_s + 2\pi \Big(F_{s,\nu_s} - F_{r,\nu_r} \Big) t - P_{r,\nu_r} \theta_0 \Big) \Big] \quad (5.47)$$

The second integral I_2 is given by:

$$I_2(t) = \sum_{\nu_r=1}^{+\infty} \sum_{\nu_r=1}^{+\infty} \frac{\hat{\Theta}_{s,\nu_s} \hat{\Theta}_{r,\nu_r}}{2} \int_0^{2\pi} \Big[\sin\Big(2P_{r,\nu_r} \alpha_s + 2\pi \cdot 2F_{r,\nu_r} \cdot t + 2P_{r,\nu_r} \theta_0 \Big) \Big]$$

The integral I_2 is always zero while the integral I_1 is non null if $P_{s,\nu_s} + P_{r,\nu_r} = 0$ or $P_{s,\nu_s} - P_{r,\nu_r} = 0$. Only the second condition is possible and in this case the harmonics ν_s and ν_r create a pulsating torque with a frequency f_Γ equal to $F_{s,\nu_s} - F_{r,\nu_r}$. Using the results of Chapter 4 the torque frequency f_Γ is equal to:

$$f_\Gamma = F_{s,\nu_s} - F_{r,\nu_r} = \left(1 - (s + (1-s) \frac{P_{r,\nu_r}}{p} \right) f_s \quad (5.48)$$

As an example, let us consider the fundamental harmonics of the stator and the rotor so that $P_{s,\nu_s} = p$ and $P_{r,\nu_r} = p$. The condition of existence of the torque is met and the resulting torque frequency is equal to $f_\Gamma = (1 - (s + (1-s)))\, f_s = 0$ which agrees with the theory. Note that the amplitude of the torque will also depend on the angle θ_0 i.e. on the phase shift between both magnetic fields. More generally two magnetic field waves can create a constant torque only if they have the same spatial order and if they rotate synchronously. In the studied case, as seen previously, in addition to the constant torque many pulsating components arise. We explain in the following the presence of each component.

I. The components 300 Hz and 600 Hz

The component 300 Hz is mainly due to the interaction between the 5^{th} or 7^{th} stator harmonic and the 5^{th} or 7^{th} rotor harmonic. The corresponding frequency $f_{\Gamma,5}$ or $f_{\Gamma,7}$ is obtained by Equation (5.49). When the slip is equal to zero, and considering $f_s = 50$ Hz one can find the 300 Hz component. When the slip is different from zero, one can observe the shift in frequency.

$$\begin{aligned} f_{\Gamma,5} &= \left(1 - \left(s + (1-s) \frac{-5p}{p} \right) \right) f_s = (6 - 6s)\, f_s \\ f_{\Gamma,7} &= \left(1 - \left(s + (1-s) \frac{7p}{p} \right) \right) f_s = (6s - 6)\, f_s \end{aligned} \quad (5.49)$$

The same process can be applied to find the 600 Hz component and its dependence on the slip but this time by considering the 11^{th} and 13^{th} stator and rotor winding harmonics.

$$\begin{aligned} f_{\Gamma,11} &= \left(1 - \left(s + (1-s) \frac{-11p}{p} \right) \right) f_s = 2\,(6 - 6s)\, f_s \\ f_{\Gamma,13} &= \left(1 - \left(s + (1-s) \frac{13p}{p} \right) \right) f_s = 2\,(6s - 6)\, f_s \end{aligned} \quad (5.50)$$

II. The components 2100 Hz **and** 2400 Hz

Until now we assumed a constant airgap permeance. However as seen in Chapter 4 the airgap permeance is modified because of the interaction between the stator and rotor slots. The previous method can be extended to consider the additional harmonics of the permeance.

Let us consider the interaction between a stator mmf harmonic $\Theta_{\mathrm{s},\nu_\mathrm{s}}$ with an airgap permeance harmonic $\Lambda_{\mathrm{p},\nu_{\mathrm{p}_1}}$ and the interaction between a rotor mmf harmonic $\Theta_{\mathrm{r},\nu_\mathrm{r}}$ with an airgap permeance harmonic $\Lambda_{\mathrm{p},\nu_{\mathrm{p}_2}}$. By using the notation of Section 5.2 we have:

$$\begin{aligned}
\Theta_{\mathrm{s},\nu_\mathrm{s}} &= \hat{\Theta}_{\mathrm{s},\nu_\mathrm{s}} \cdot [P_{\mathrm{s},\nu_\mathrm{s}}, F_{\mathrm{s},\nu_\mathrm{s}}] \\
\Lambda_{\mathrm{p},\nu_{\mathrm{p}_1}} &= \hat{\Lambda}_{\mathrm{p},\nu_{\mathrm{p}_1}} \cdot [P_{\mathrm{p},\nu_{\mathrm{p},1}}, F_{\mathrm{p},\nu_{\mathrm{p},1}}] \\
\Theta_{\mathrm{r},\nu_\mathrm{r}} &= \hat{\Theta}_{\mathrm{r},\nu_\mathrm{r}} \cdot [P_{\mathrm{r},\nu_\mathrm{r}}, F_{\mathrm{r},\nu_\mathrm{r}}] \\
\Lambda_{\mathrm{p},\nu_{\mathrm{p}_2}} &= \hat{\Lambda}_{\mathrm{p},\nu_{\mathrm{p}_2}} \cdot [P_{\mathrm{p},\nu_{\mathrm{p},2}}, F_{\mathrm{p},\nu_{\mathrm{p},2}}]
\end{aligned} \tag{5.51}$$

The corresponding airgap flux density waves are defined as:

$$\begin{aligned}
B_{\nu_\mathrm{s},\nu_{\mathrm{p}_1}} &= \hat{\Theta}_{\mathrm{s},\nu_\mathrm{s}} \hat{\Lambda}_{\mathrm{p},\nu_{\mathrm{p}_1}} \cdot [P_{\mathrm{s},\nu_\mathrm{s}} \pm P_{\mathrm{p},\nu_{\mathrm{p},1}}, F_{\mathrm{s},\nu_\mathrm{s}} \pm F_{\mathrm{p},\nu_{\mathrm{p},1}}] \\
B_{\nu_\mathrm{r},\nu_{\mathrm{p}_2}} &= \hat{\Theta}_{\mathrm{r},\nu_\mathrm{r}} \hat{\Lambda}_{\mathrm{p},\nu_{\mathrm{p}_2}} \cdot [P_{\mathrm{r},\nu_\mathrm{r}} \pm P_{\mathrm{p},\nu_{\mathrm{p},2}}, F_{\mathrm{r},\nu_\mathrm{r}} \pm F_{\mathrm{p},\nu_{\mathrm{p},2}}]
\end{aligned} \tag{5.52}$$

The interaction of these two waves will create a torque if $P_{\mathrm{s},\nu_\mathrm{s}} \pm P_{\mathrm{p},\nu_{\mathrm{p},1}} \pm P_{\mathrm{r},\nu_\mathrm{r}} \pm P_{\mathrm{p},\nu_{\mathrm{p},2}} = 0$. Considering the different winding harmonics and main airgap permeance harmonics, one can find that the 2100 Hz component is mainly due to a first group of waves defined as:

$$\begin{aligned}
\Theta_{\mathrm{s},\nu_\mathrm{s}} &= \hat{\Theta}_{\mathrm{s},\nu_\mathrm{s}} \cdot [-5p, 1] \\
\Lambda_{\mathrm{p},\nu_{\mathrm{p}_1}} &= \hat{\Lambda}_{\mathrm{p},\nu_{\mathrm{p}_1}} \cdot [0, 0] \\
\Theta_{\mathrm{r},\nu_\mathrm{r}} &= \hat{\Theta}_{\mathrm{r},\nu_\mathrm{r}} \cdot [p, +1] \\
\Lambda_{\mathrm{p},\nu_{\mathrm{p}_2}} &= \hat{\Lambda}_{\mathrm{p},\nu_{\mathrm{p}_2}} \cdot [-6(q_\mathrm{s} - q_\mathrm{r})p, 6q_\mathrm{r}(1-s)]
\end{aligned} \tag{5.53}$$

and a second group of waves defined as:

$$\begin{aligned}
\Theta_{\mathrm{s},\nu_\mathrm{s}} &= \hat{\Theta}_{\mathrm{s},\nu_\mathrm{s}} \cdot [7p, +1] \\
\Lambda_{\mathrm{p},\nu_{\mathrm{p}_1}} &= \hat{\Lambda}_{\mathrm{p},\nu_{\mathrm{p}_1}} \cdot [0, 0] \\
\Theta_{\mathrm{r},\nu_\mathrm{r}} &= \hat{\Theta}_{\mathrm{r},\nu_\mathrm{r}} \cdot [p, +1] \\
\Lambda_{\mathrm{p},\nu_{\mathrm{p}_2}} &= \hat{\Lambda}_{\mathrm{p},\nu_{\mathrm{p}_2}} \cdot [-6(q_\mathrm{s} - q_\mathrm{r})p, 6q_\mathrm{r}(1-s)]
\end{aligned} \tag{5.54}$$

Note that the fundamental wave Θ_1 is here involved in the creation of the torque which will lead to an high amplitude. In the studied case $q_\mathrm{s} - q_\mathrm{r} = 1$ so that in the first case we have:

$$P_{\mathrm{s},\nu_\mathrm{s}} \pm P_{\mathrm{p},\nu_{\mathrm{p},1}} - P_{\mathrm{r},\nu_\mathrm{r}} - P_{\mathrm{p},\nu_{\mathrm{p},2}} = -5p \pm 0 - p + 6p = 0 \tag{5.55}$$

and in the second case:

$$P_{\mathrm{s},\nu_\mathrm{s}} \pm P_{\mathrm{p},\nu_{\mathrm{p},1}} - P_{\mathrm{r},\nu_\mathrm{r}} + P_{\mathrm{p},\nu_{\mathrm{p},2}} = 7p \pm 0 - p - 6p = 0 \tag{5.56}$$

The corresponding frequencies are for both cases:

$$\begin{aligned} f_{\Gamma_1} &= (F_{\mathrm{s},\nu_\mathrm{s}} \pm F_{\mathrm{p},\nu_{\mathrm{p},1}} - F_{\mathrm{r},\nu_\mathrm{r}} - F_{\mathrm{p},\nu_{\mathrm{p},2}}) \cdot f_\mathrm{s} = (+1 \pm 0 - 1 - 6q_\mathrm{r}(1-s)) \cdot f_\mathrm{s} = -6q_\mathrm{r}(1-s)f_\mathrm{s} \\ f_{\Gamma_2} &= (F_{\mathrm{s},\nu_\mathrm{s}} \pm F_{\mathrm{p},\nu_{\mathrm{p},1}} - F_{\mathrm{r},\nu_\mathrm{r}} + F_{\mathrm{p},\nu_{\mathrm{p},2}}) \cdot f_\mathrm{s} = (+1 \pm 0 - 1 + 6q_\mathrm{r}(1-s)) \cdot f_\mathrm{s} = +6q_\mathrm{r}(1-s)f_\mathrm{s} \end{aligned} \tag{5.57}$$

In the studied case, $q_\mathrm{r} = 7$, and if the slip is zero we obtain $f_{\Gamma_1} = 2100\,\mathrm{Hz}$ and $f_{\Gamma_2} = -2100\,\mathrm{Hz}$. When the slip is different from zero, one can observe the shift in frequency. Regarding the component 2400 Hz, one can find a first group of waves defined as:

$$\begin{aligned} \Theta_{\mathrm{s},\nu_\mathrm{s}} &= \hat{\Theta}_{\mathrm{s},\nu_\mathrm{s}} \cdot [p, +1] \\ \Lambda_{\mathrm{p},\nu_{\mathrm{p}_1}} &= \hat{\Lambda}_{\mathrm{p},\nu_{\mathrm{p}_1}} \cdot [0, 0] \\ \Theta_{\mathrm{r},\nu_\mathrm{r}} &= \hat{\Theta}_{\mathrm{r},\nu_\mathrm{r}} \cdot [-5p, (s - 5(1-s))] \\ \Lambda_{\mathrm{p},\nu_{\mathrm{p}2}} &= \hat{\Lambda}_{\mathrm{p},\nu_{\mathrm{p}2}} \cdot [6(q_\mathrm{s} - q_\mathrm{r})p, -6q_\mathrm{r}(1-s)] \end{aligned} \tag{5.58}$$

and a second group of waves defined as:

$$\begin{aligned} \Theta_{\mathrm{s},\nu_\mathrm{s}} &= \hat{\Theta}_{\mathrm{s},\nu_\mathrm{s}} \cdot [p, +1] \\ \Lambda_{\mathrm{p},\nu_{\mathrm{p}_1}} &= \hat{\Lambda}_{\mathrm{p},\nu_{\mathrm{p}_1}} \cdot [0, 0] \\ \Theta_{\mathrm{r},\nu_\mathrm{r}} &= \hat{\Theta}_{\mathrm{r},\nu_\mathrm{r}} \cdot [7p, (s + 7(1-s))] \\ \Lambda_{\mathrm{p},\nu_{\mathrm{p}2}} &= \hat{\Lambda}_{\mathrm{p},\nu_{\mathrm{p}2}} \cdot [6(q_\mathrm{s} - q_\mathrm{r})p, -6q_\mathrm{r}(1-s)] \end{aligned} \tag{5.59}$$

Here $q_\mathrm{s} - q_\mathrm{r} = 1$ so that in the first case we have:

$$P_{\mathrm{s},\nu_\mathrm{s}} \pm P_{\mathrm{p},\nu_{\mathrm{p},1}} - P_{\mathrm{r},\nu_\mathrm{r}} - P_{\mathrm{p},\nu_{\mathrm{p},2}} = p \pm 0 + 5p - 6p = 0 \tag{5.60}$$

and in the second case:

$$P_{\mathrm{s},\nu_\mathrm{s}} \pm P_{\mathrm{p},\nu_{\mathrm{p},1}} - P_{\mathrm{r},\nu_\mathrm{r}} + P_{\mathrm{p},\nu_{\mathrm{p},2}} = p \pm 0 - 7p + 6p = 0 \tag{5.61}$$

The corresponding frequencies are:

$$\begin{aligned} f_{\Gamma_1} &= (F_{\mathrm{s},\nu_\mathrm{s}} \pm F_{\mathrm{p},\nu_{\mathrm{p},1}} - F_{\mathrm{r},\nu_\mathrm{r}} + F_{\mathrm{p},\nu_{\mathrm{p},2}}) \cdot f_\mathrm{s} = (+1 - (s - 5(1-s)) + 6q_\mathrm{r}(1-s)) \cdot f_\mathrm{s} \\ f_{\Gamma_2} &= (F_{\mathrm{s},\nu_\mathrm{s}} \pm F_{\mathrm{p},\nu_{\mathrm{p},1}} - F_{\mathrm{r},\nu_\mathrm{r}} - F_{\mathrm{p},\nu_{\mathrm{p},2}}) \cdot f_\mathrm{s} = (+1 - (s + 7(1-s)) - 6q_\mathrm{r}(1-s)) \cdot f_\mathrm{s} \end{aligned} \tag{5.62}$$

As $q_\mathrm{r} = 7$ and if the slip is zero, $f_{\Gamma_1} = 2400\,\mathrm{Hz}$ and $f_{\Gamma_2} = -2400\,\mathrm{Hz}$. When the slip is different form zero, one can observe the shift in frequency. Note that many other combinations can be found involving for example the slot harmonics of the rotor mmf or the stator mmf. Note also that the harmonic due to magnetic saturation will also create new harmonics as it is shown hereafter for the component 15 Hz.

III. The component 15 Hz

Until now the additional permeance harmonics due to the saturation were not considered. We neglect here the effect of the slots so that the airgap permeance is only modulated by the effect of the saturation so that by only considering the first two harmonics:

$$\Lambda(\alpha,t)=\Lambda_0+\sum_{n=1}^{2}\Lambda_n\cdot\cos\left(2np\alpha+2n\cdot 2\pi f_{\mathrm{s}}\cdot t\right) \tag{5.63}$$

Considering the first winding harmonics and these additional saturated airgap harmonics, we find that the 15 Hz component is mainly due the following group of waves:

$$\begin{aligned}
&\Theta_{\mathrm{s},\nu_{\mathrm{s}}}=\hat{\Theta}_{\mathrm{s},\nu_{\mathrm{s}}}\cdot[p,+1]\\
&\Lambda_{\mathrm{p},\nu_{\mathrm{p}1}}=\hat{\Lambda}_{\mathrm{p},\nu_{\mathrm{p}1}}\cdot[0,0]\\
&\Theta_{\mathrm{r},\nu_{\mathrm{r}}}=\hat{\Theta}_{\mathrm{r},\nu_{\mathrm{r}}}\cdot[-5p,(s-5(1-s))]\\
&\Lambda_{\mathrm{p},\nu_{\mathrm{p}2}}=\hat{\Lambda}_{\mathrm{p},\nu_{\mathrm{p}2}}\cdot[4p,4]
\end{aligned} \tag{5.64}$$

$$\begin{aligned}
&\Theta_{\nu s}=\hat{\Theta}_{\mathrm{s},\nu_{\mathrm{s}}}\cdot[p,+1]\\
&\Lambda_{\mathrm{p},\nu_{\mathrm{p}1}}=\hat{\Lambda}_{\mathrm{p},\nu_{\mathrm{p}1}}\cdot[2p,2]\\
&\Theta_{\mathrm{r},\nu_{\mathrm{r}}}=\hat{\Theta}_{\mathrm{r},\nu_{\mathrm{r}}}\cdot[-5p,(s-5(1-s))]\\
&\Lambda_{\mathrm{p},\nu_{\mathrm{p}2}}=\hat{\Lambda}_{\mathrm{p},\nu_{\mathrm{p}2}}\cdot[2p,2]
\end{aligned} \tag{5.65}$$

$$\begin{aligned}
&\Theta_{\nu s}=\hat{\Theta}_{\mathrm{s},\nu_{\mathrm{s}}}\cdot[p,+1]\\
&\Lambda_{\mathrm{p},\nu_{\mathrm{p}1}}=\hat{\Lambda}_{\mathrm{p},\nu_{\mathrm{p}1}}\cdot[2p,2]\\
&\Theta_{\mathrm{r},\nu_{\mathrm{r}}}=\hat{\Theta}_{\mathrm{r},\nu_{\mathrm{r}}}\cdot[7p,(s+7(1-s))]\\
&\Lambda_{\mathrm{p},\nu_{\mathrm{p}2}}=\hat{\Lambda}_{\mathrm{p},\nu_{\mathrm{p}2}}\cdot[4p,4]
\end{aligned} \tag{5.66}$$

The corresponding frequencies are:

$$\begin{aligned}
f_{\Gamma_1}&=(1\pm 0+(s-5(1-s))+4)\cdot f_{\mathrm{s}}=6sf_{\mathrm{s}}\\
f_{\Gamma_2}&=(1+2+(s-5(1-s))+2)\cdot f_{\mathrm{s}}=6sf_{\mathrm{s}}\\
f_{\Gamma_3}&=(1+2-(s+7(1-s))+4)\cdot f_{\mathrm{s}}=6sf_{\mathrm{s}}
\end{aligned} \tag{5.67}$$

When the slip is zero, the frequency equals zero and these torques superimpose with the working constant torque. When the slip is different from zero, a low frequency $6sf_{\mathrm{s}}$ torque appears as observed previously. Note that these torques only exist because of the saturation of the stator and rotor magnetic core.

This part studied the harmonic content of the electromagnetic torque during load operation. Changing the slip results in frequency shift of the harmonics, but also in the apparition of a low frequency harmonic. The corresponding harmonic amplitude is linked directly to the state of saturation as it was shown when comparing over-excited and under-excited mode. Parasitic

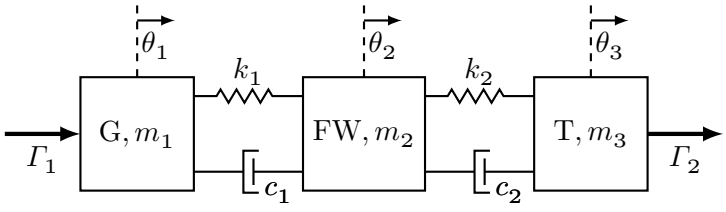

Figure 5.54: Shaft line as a three masses model

torques do not take part in power generation but might be responsible for vibrations of the shaft line coupling the alternator to the turbine. Consequently a modal analysis of the shaft line needs to be performed in order to assess this potential risk. This is the object of the next part.

5.4.2 Shaft line modal analysis

I. Three-mass spring model

The shaft line of an hydro-motor/generator unit consists in the following main components:

- The motor/generator rotor
- The fly wheel
- The turbine

Such system can be modeled as a three-mass oscillator as shown in Figure 5.54 where G, FW, T represent the generator rotor, the fly wheel and the turbine while θ_1, θ_2, θ_3 are the corresponding angular positions. The coupling between each mass is defined by springs and dampers characterized by a certain stiffness k and a damping coefficient c. Furthermore the excitation due to the airgap electromagnetic torque and the turbine torque are applied by external forces Γ_1 and Γ_2.

By applying the Newton's laws of motion, we describe such system by Equation (5.68) where θ is the vector of angular positions, $\boldsymbol{M}$ is the mass matrix, $\boldsymbol{C}$ is the damping matrix and $\boldsymbol{K}$ is the stiffness matrix. The different matrix coefficients of the mass matrix $\boldsymbol{M}$ and the stiffness matrix $\boldsymbol{K}$ are obtained by considering the whole structure of the shaft line and by carrying out FE computations [Paj12].

$$\boldsymbol{M} \cdot \ddot{\theta} - \boldsymbol{C} \cdot \dot{\theta} - \boldsymbol{K} \cdot \theta = \Gamma \tag{5.68}$$

$$\boldsymbol{M} = \begin{pmatrix} m_1 & 0 & 0 \\ 0 & m_2 & 0 \\ 0 & 0 & m_3 \end{pmatrix} \quad \boldsymbol{C} = \begin{pmatrix} -c_1 & c_1 & 0 \\ c_1 & c_1 - c_2 & c_2 \\ 0 & c_2 & -c_2 \end{pmatrix} \quad \boldsymbol{K} = \begin{pmatrix} -k_1 & k_1 & 0 \\ k_1 & -k_1 - k_2 & k_2 \\ 0 & k_2 & -k_2 \end{pmatrix} \tag{5.69}$$

Quantity	Value
m_1 (kg m^2)	$1.1 \cdot 10^6$
m_2 (kg m^2)	$6.5 \cdot 10^4$
m_3 (kg m^2)	$6.6 \cdot 10^4$
k_1 (N m/rad)	$1.14 \cdot 10^9$
k_2 (N m/rad)	$1.10 \cdot 10^9$

Table 5.17: Inertia and stiffness coefficients

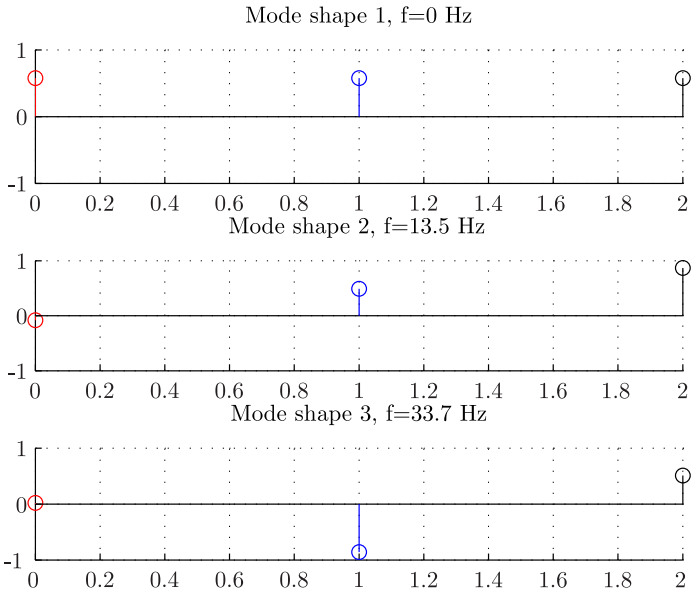

Figure 5.55: Shaft line mode shapes

$$\theta = \begin{pmatrix} \theta_1 \\ \theta_2 \\ \theta_3 \end{pmatrix} \qquad \Gamma = \begin{pmatrix} \Gamma_1 \\ 0 \\ \Gamma_2 \end{pmatrix} \tag{5.70}$$

II. Eigen-frequencies and harmonic response

The eigen-mode and corresponding frequencies are obtained by computing the eigen-values and eigen-vectors of the system matrix $\boldsymbol{A} = \boldsymbol{M}^{-1} \cdot \boldsymbol{K}$. For simplification reasons the damping matrix is not considered as it will not have a big impact on the eigen-frequencies. Table 5.17 gives the value of the mass and stiffness coefficients used for the calculation.

For each eigen-frequency we calculate three eigen-vectors. Figure 5.55 shows the three corresponding eigen-frequencies and mode shapes.

The first eigen-mode $f_{\text{eig},1} = 0\,\text{Hz}$ corresponds to the rotation of the shaft. One can see that the three eigen-vectors have the same amplitude and have the same phase shift. The second eigen-mode $f_{\text{eig},2} = 13.5\,\text{Hz}$ and third eigen-mode $f_{\text{eig},3} = 33.7\,\text{Hz}$ are the most relevant ones as

all vectors do not have any more the same phase. This corresponds to a torsion of the shaft.

We study now the harmonic response of the system to a forced excitation with a certain frequency $f = \omega/(2\pi)$. Equation (5.68) is solved by defining the complex solutions $\underline{\theta}_1 = \theta_1 \cdot \exp(\mathrm{i}\omega t)$, $\underline{\theta}_2 = \theta_2 \cdot \exp(\mathrm{i}\omega t)$ and $\underline{\theta}_3 = \theta_3 \cdot \exp(\mathrm{i}\omega t)$. The harmonic excitations are defined so that $\underline{\Gamma}_1 = \hat{\Gamma}_1 \cdot \exp(\mathrm{i}\omega t)$ and $\underline{\Gamma}_2 = 0$. Finally Equation (5.68) becomes:

$$(-\omega^2 \cdot \boldsymbol{M} - \mathrm{i} \cdot \omega \cdot \boldsymbol{C} - \boldsymbol{K}) \cdot \underline{\theta} = \Gamma \tag{5.71}$$

For each pulsation $\omega = 2\pi f$, Equation (5.71) is solved. The torsion torque acting between the generator and the fly wheel Γ_{t_1} and between the fly wheel and the turbine Γ_{t_2} are extracted according to Equation (5.72):

$$\begin{aligned} \Gamma_{t_1} &= k_1 \cdot (\theta_1 - \theta_2) \\ \Gamma_{t_1} &= k_2 \cdot (\theta_2 - \theta_3) \end{aligned} \tag{5.72}$$

Note that the coefficients of the damping matrix $\boldsymbol{C}$ are defined so that to have a damping equal to 1% of the critical damping as it is normally the case for such structure.

Figure 5.56 shows the obtained response of the relative angular position of the generator G of the flywheel FW and of the turbine T. Figure 5.57 shows the corresponding variation of the torsion torque Γ_{t_1} and Γ_{t_2} scaled relatively to the amplitude of the excitation torque.

One can observe that the angular response of the system is very low and this is mainly due to the consideration of the damping. However one can observe a certain amplification of the torsion torque at the resonance frequencies. The current mass model does not make it possible to consider the impact of the high frequency torques i.e. above 300 Hz, however these torques have normally no impact on such high inertia system. On the contrary the electromagnetic torque component with the low frequency $f = 6 \cdot sf_s$ appears critical. Indeed when the slip is equal to $\pm 4.5\%$, the torque frequency is $f_\Gamma = 13.5$ Hz which corresponds exactly to the second mode shape eigen-frequency. In the last section for a slip equals to 5%, we found this particular low frequency torque component equal to $\Gamma = (0.18/100) \cdot 4.65 \cdot 10^6 = 8\,4$ kNm. Assuming that the amplitude of this torque does not change between a slip of 5% and a slip of 4.5% and using the results of the harmonic response, one can predict the value of the torsion torque: $\Gamma_{t_1} = 3.2 \cdot T = 27$ kNm and $\Gamma_{t_2} = 42$ kNm. One should also pay attention to the fact that although these torques are relatively small compared to the working torque of the machine, that are not due to a temporary perturbation of the machine but may permanently exist as long as the machine is operating at this particular slip. Of course the answer of the shaft line will directly depend on the damping of the system and a more extensive mechanical study is therefore needed in order to better assess this parameter. In the extreme case, in order to guarantee a safe operation of the machine and the time length of the shaft line, the operation at this particular slip might have to be excluded or at least limited. The third mode shape is matched when the slip is equal to $\pm 11\%$m. However given Figure 5.57 the torsion torque response will be very small.

Until now only the steady-state operation of the machine has been studied, in the next part we investigate the content of the electromagnetic torque during the startup. Indeed during this

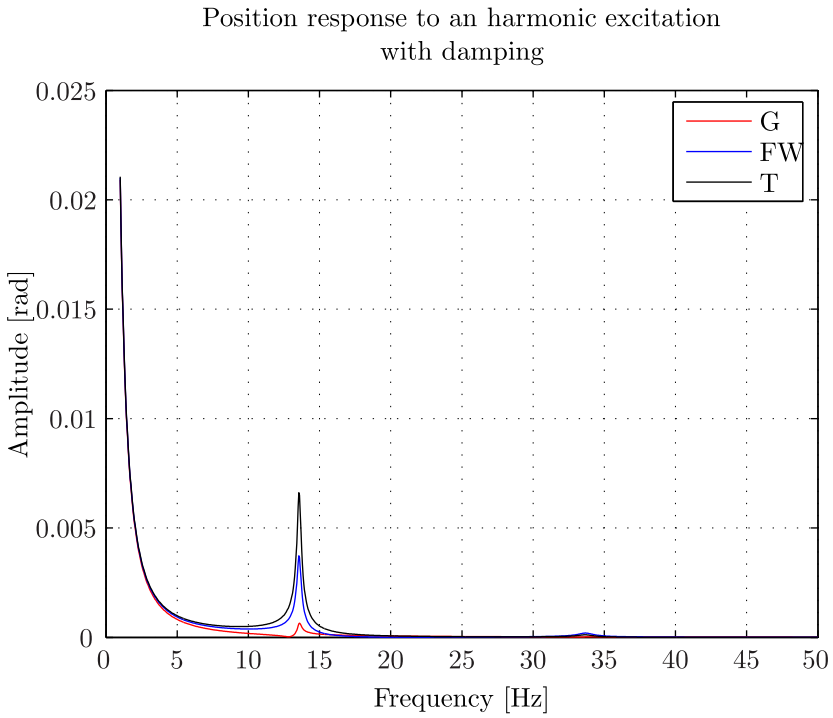

Figure 5.56: Shaft line: angular position response

phase, as the speed is varying, the harmonic content of the torque will dynamically change and goes along the resonance frequencies of the shaft line.

5.4.3 Study of the start up

In order to operate as a pump i.e as a motor, the DFIM has to be started without the help of the turbine. The machine is initially at stand-still and the stator terminal is disconnected from the network. The startup process is made of three main phases:

- The speed rise during which the stator terminal is short-circuited and the rotor winding currents are controlled to create the electromagnetic torque so that the machine reaches the synchronization speed.
- The synchronization during which the stator terminal is opened and the rotor winding currents are controlled so that the stator induced voltage matches exactly the network voltage.
- The connection to the network during which the stator terminal is connected to the network. After this phase, the machine is ready to operate as motor.

This part simulates only the first step of the motor startup. The startup regulation process described by [Pan10] is implemented as a Python program in the FE software *Flux2d* by using the same process described in Chapter 3. Such simulation makes it possible to determine accurately the starting time of the machine but also to extract the variation of the electromagnetic torque.

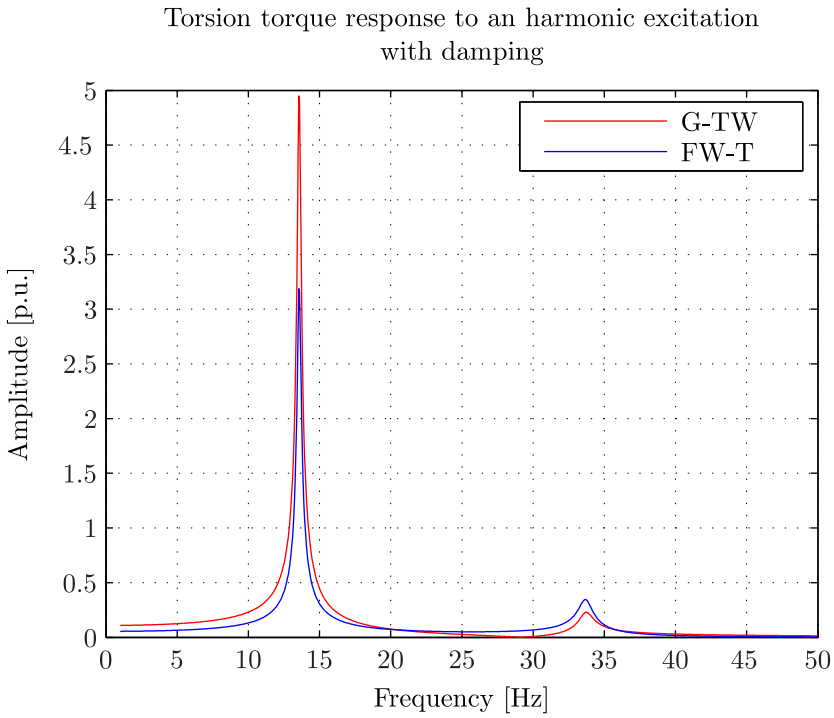

Figure 5.57: Shaft line: torsion torque response

Figures 5.58 and 5.59 show the evolution of the rotor and stator currents during the fist instants of the startup. One can observe the change in frequency in the rotor currents directly linked to the mechanical speed while the stator currents frequency is equal to the slip frequency. Figure 5.60 shows the evolution of the mechanical speed. Figure 5.61 shows the evolution of the electromagnetic torque and more particularly the presence of oscillations.

When analyzing the first instants of the startup one can observe some ripples on the electromagnetic torque as shown in Figure 5.62. Note that the frequency of these oscillations is changing while the motor is speeding up. These oscillations are mainly due to the interaction between the stator and rotor winding mmf harmonics. By performing a short-time Fourier analysis, one can extract the harmonic content of these oscillations and more particularly show that the frequency of these oscillations go through the eigen-frequencies of the shaft line. However these oscillations have very small amplitudes (about 0.01 p.u.) and appear only during a short time period. In the rest of the startup phase i.e. from 4 s emerge other oscillations but with much higher frequencies and low amplitude. Consequently they will not perturb the shaft line behavior. Note that the additional rotor current harmonics, due to the converter, which will lead to additional parasitic torques are not considered in this simulation. However by combining the simplified model of the converter shown in Section 5.2 and this regulation methodology, one could include its effect.

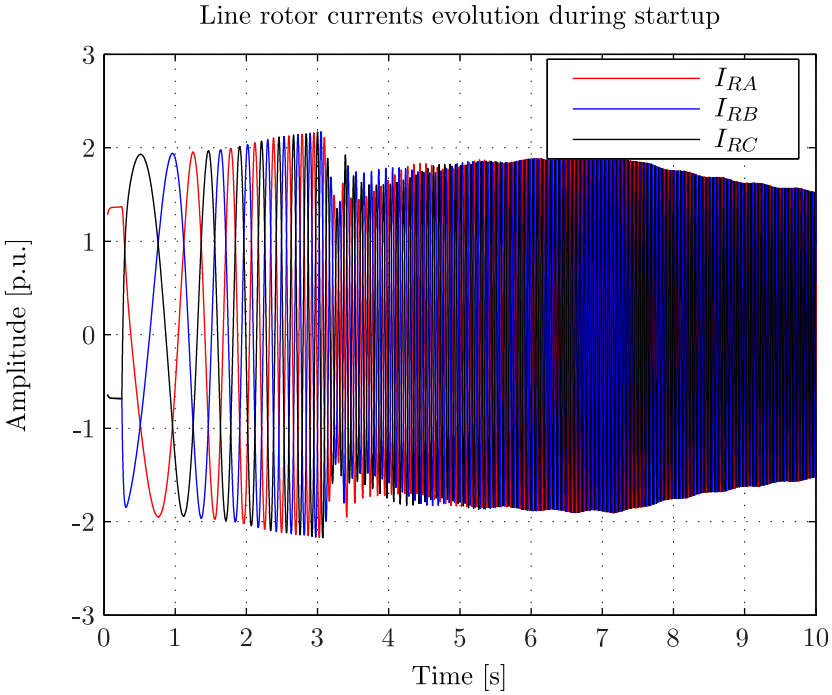

Figure 5.58: Startup: Rotor current

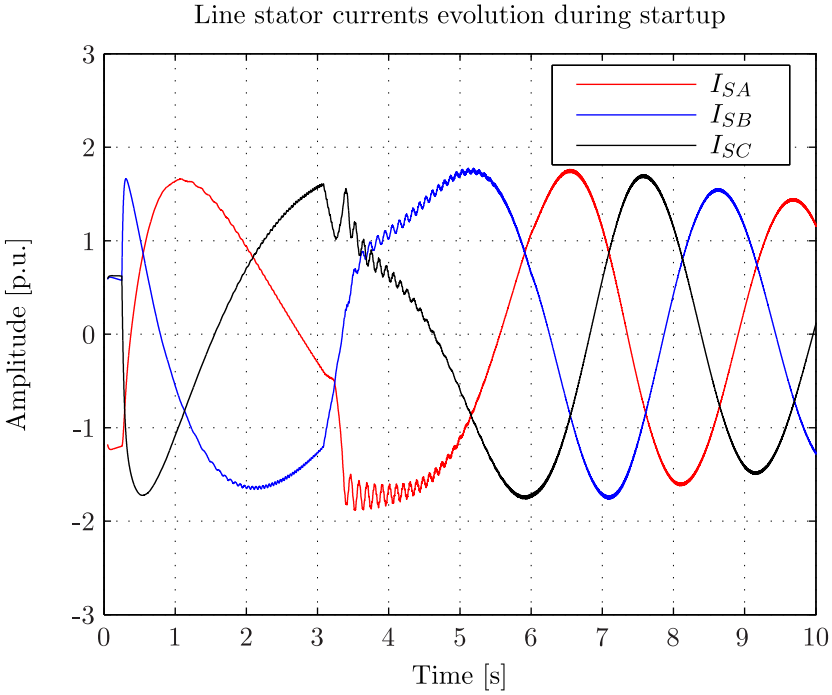

Figure 5.59: Startup: Stator current

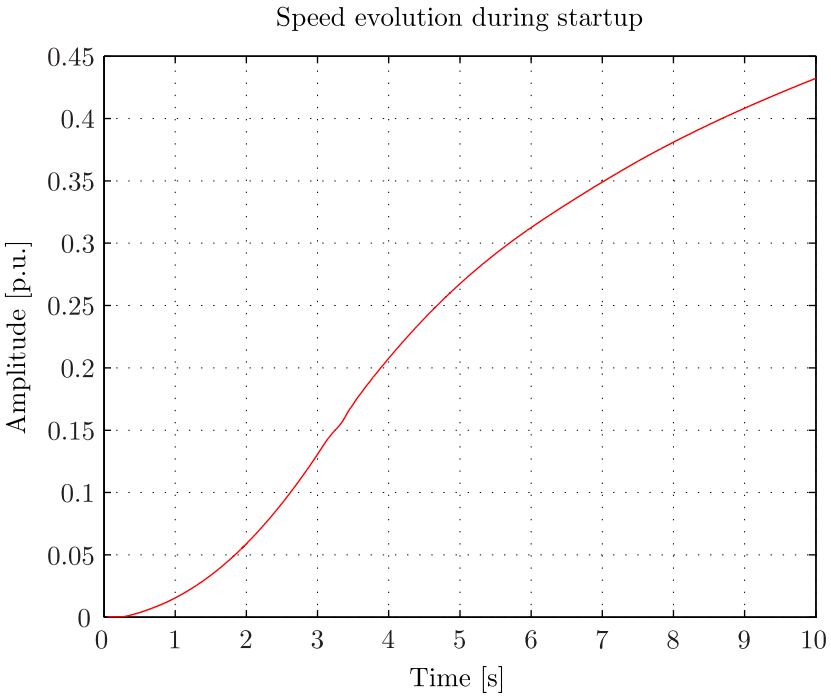

Figure 5.60: Startup: Mechanical speed

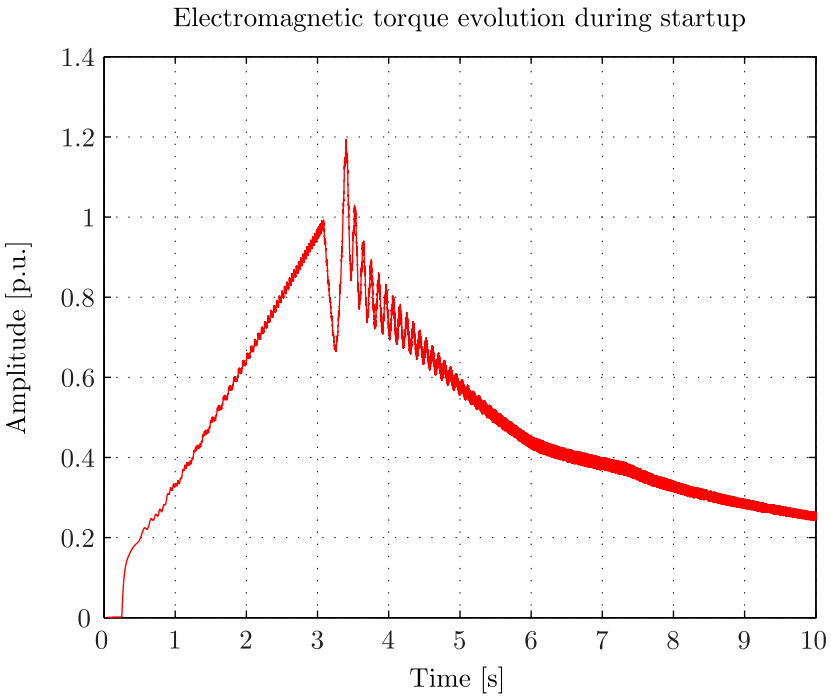

Figure 5.61: Startup: Electromagnetic torque

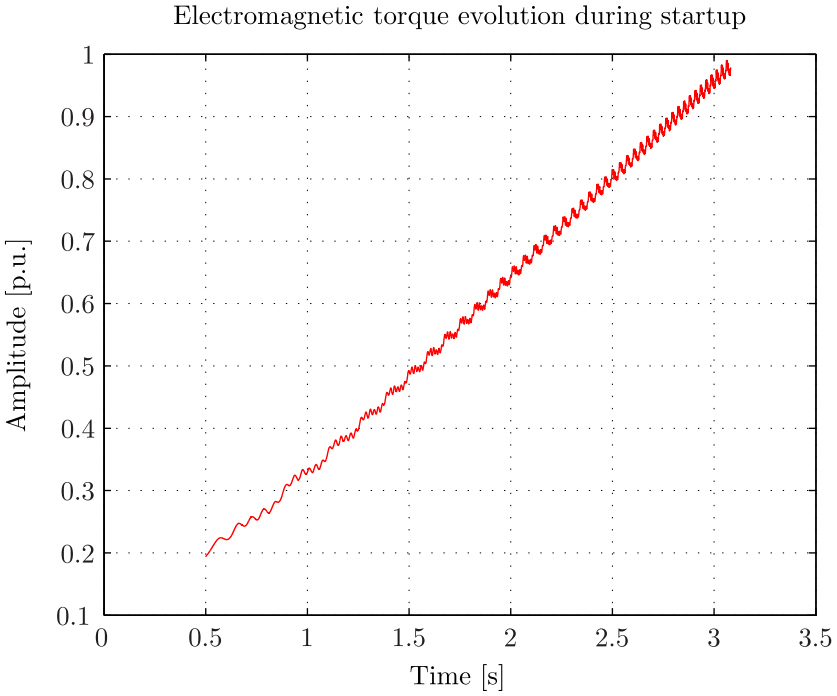

Figure 5.62: Startup: Electromagnetic torque (first instants)

5.4.4 Summary

This part studied the electromagnetic torque evolution during various load conditions. A Fourier decomposition has shown a rich harmonic content and in particular a low frequency component susceptible to excite a torsional eigen-mode of the shaft line. An analytical development has given the relation between this parasitic component frequency and the working mechanical speed, and demonstrated that it mainly appears due to the magnetic saturation and when the speed is different from the synchronous speed.

An equivalent three-mass model of the shaft line made it possible to study the consequences of this component on the shaft line behavior and by assuming a certain mechanical damping has shown that the risk of resonance was low. However such a torsional stress in these conditions can be damageable and lead to a life time reduction of the shaft line, that is why for safety reasons certain mechanical speeds might have to be excluded.

As the dynamic electromagnetic torque frequency content is directly linked to the working mechanical speed, it is natural to study the startup operation of the machine as a motor. A regulated FE based on the methodology developed in Chapter 3 has been carrying out. The electromagnetic torque obtained from the FE simulation has been analyzed and we could show that the risk of resonance was low. All computations were done without considering the harmonics emitted by the VSI converter. This could be checked by using the simplified converter model used previously for the stator voltage harmonic calculations.

5.5 The iron losses in stator and rotor core

Power losses quantification is a relevant element to consider during the design of an electrical machine since it impacts on the design, on the cooling and finally on the efficiency of the machine. The efficiency of actual hydro-alternators is today about 98% which is very high but it is clear that 2% of losses on a 300 MVA machine which gives 6 MVA is not negligible. Underestimating power losses may lead to the impossibility to exploit the machine under its nominal load. This results in an economic loss for the power plant owner and high cost penalties for the provider of the machine. Following section deals with the power losses, also called iron losses, computation in the stator and rotor core iron sheets of the DFIM.

5.5.1 State of the art

The iron losses computation has since long been studied by electrical engineers. Traxler-Samek [TA09] proposes an analytical approach to compute the iron losses in a hydro generator. The results are validated by using a statistic approach on more than thirty hydro-generators. Depending on the analyzed region, teeth or yoke, the uni-directional or elliptical behavior of the magnetic field is taken into account. Ranlöf [Ran+09] compares different frequency and time dependent models for iron losses computation, including or not the effect of rotational fields and compares the results to measurements carried out on twelve hydro-generators. Gautreau [Gau05] proposes a model taking into account the dynamic magnetic behavior of the materials. The method consists in fully characterizing a magnetic material at several levels of magnetic excitation B and at different rates $\mathrm{d}B/\mathrm{d}t$ to finally obtain the response surface $H(B, \mathrm{d}B/\mathrm{d}t)$. The model is then used to extract, from a 2DFE computation, the magnetic field strength H from the local variation of the flux density and to derive from it the corresponding power losses $P = \int H \cdot \mathrm{d}B$. This makes it possible to better consider the impact of flux density harmonics which can lead to the so-called minor loops and consequently extra losses. In a DFIM iron losses are expected to be higher as for a same-size conventional synchronous machine. This is mainly due to the fact that except at synchronous operation, the magnetic field is not fixed regarding the rotor which leads to non-negligible losses in the rotor iron sheets. It is even more relevant that for mechanical reasons the rotor core is made of high mechanical strength material which leads to a lower material magnetic quality. Furthermore as described in Chapter 4, the stator and rotor winding configurations lead to airgap harmonics rotating at various frequencies leading to additional power losses.

First part describes the model used for the computation of iron losses. It stands mainly on the Bertotti [Ber88] model splitting the losses between hysteresis, eddy-current and excess losses but also consider additional effects such as non-sinusoidal unidirectional or bidirectional magnetic flux excitations.

Second part computes analytically the flux densities in the stator and rotor teeth and yoke.

Third part applies the developed iron losses model to compute the corresponding losses in the stator and rotor core and compares the results to the ones obtained from a 2DFE computation.

5.5.2 Analytical model for iron losses computation

I. Decomposition of losses

The iron losses in a magnetic material considering an unidirectional flux excitation are generally splitted into three parts:

- Hysteresis losses: they depend on the Weiss domain structure of the material and are proportional to f.
- Classical: they are due to eddy-current losses in the material and proportional to f^2. They are called eddy-current losses in the following.
- Excess losses: they are proportional to $f^{1.5}$ and are due to eddy-current losses because of the movements in the Weiss domains structure.

Given this definition, the average density of iron losses $\mathrm{d}p_\mathrm{i}$ over one electrical period is generally obtained by the formula:

$$\mathrm{d}p_\mathrm{i} = k_\mathrm{h} f \hat{B}^\alpha + k_\mathrm{c} \frac{1}{T} \int_0^T \frac{\mathrm{d}B}{\mathrm{d}t}^2 \mathrm{d}t + k_\mathrm{e} \frac{1}{T} \int_0^T \left| \frac{\mathrm{d}B}{\mathrm{d}t} \right|^{1.5} \mathrm{d}t \tag{5.73}$$

where k_h, k_c, k_e are respectively hysteresis, eddy-current and excess coefficients whereas $\hat{B}$ is the maximum flux density over one period. Usually the Steinmetz coefficient α, also called hysteresis coefficient, depends on the level of saturation and varies between 1.5 and 2.5. In steady state and considering a sinusoidal flux density Equation (5.73) can be rewritten as:

$$\mathrm{d}p_\mathrm{i}(\hat{B}, f) = k_\mathrm{h} f \hat{B}^\alpha + k'_\mathrm{c} f^2 \hat{B}^2 + k'_\mathrm{e} f^{1.5} \hat{B}^{1.5} \tag{5.74}$$

Note that $k'_\mathrm{c} = (2\pi)^2 \cdot k_\mathrm{c}/2$ and $k'_\mathrm{e} \approx 8.67 \cdot k_\mathrm{e}$ The eddy-current losses coefficient is given by the following formula :

$$k'_\mathrm{c} = \frac{1}{\rho} \psi \frac{\kappa (2\pi)^2 \delta^2}{24} \tag{5.75}$$

with

$$\psi(\delta/d_E) = \frac{3}{\delta/d_E} \cdot \frac{\sinh(\delta/d_E) - \sin(\delta/d_E)}{\cosh(\delta/d_E) - \cos(\delta/d_E)} \tag{5.76}$$

where ρ is the iron sheet specific weight, κ is the iron sheet electrical conductivity, δ is the iron sheet thickness, $d_E = \sqrt{2/\omega\mu\kappa}$ is the depth of penetration, and $\omega = 2\pi f$ is the excitation frequency. Figure 5.63 shows a sinusoidal variation of the flux density and Figure 5.64 shows the corresponding hysteresis cycles $B(H)$ measured on an Epstein frame for typical stator and rotor materials used in a DFIM. One can notice the much larger area of the rotor material compared to the stator material which leads, at 50 Hz, to four times larger power losses.

Figure 5.65 shows the evolution of the losses, in the stator material (M250-50A), considering a sinusoidal excitation at 50 Hz and for different levels of magnetization. The measurement was done for the rolling and transverse directions.

In the following, for simplification reasons we consider the losses between losses in rolling and transverse directions. The coefficients k_h, k_e and α are computed from measurement power

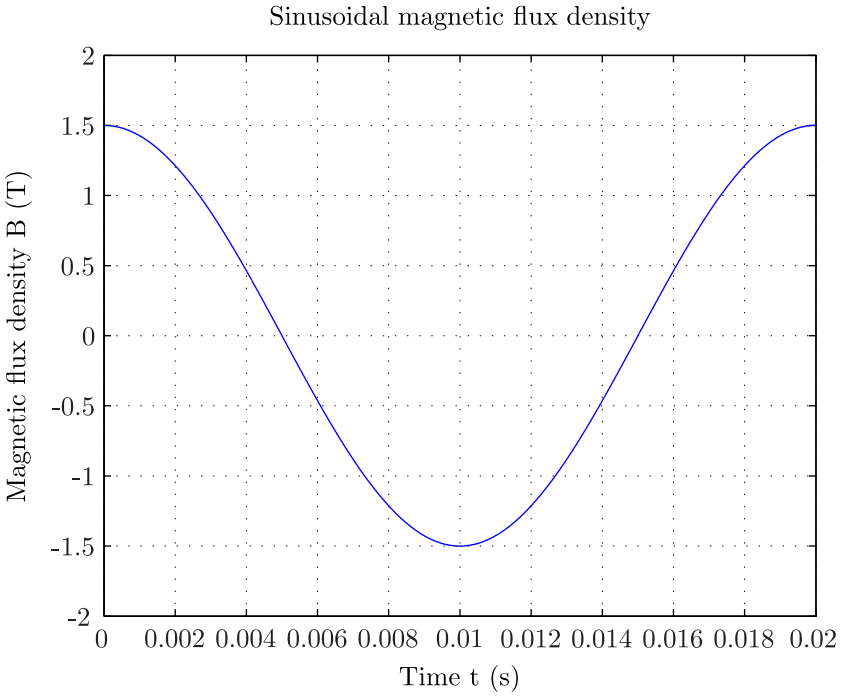

Figure 5.63: Sinusoidal flux density excitation

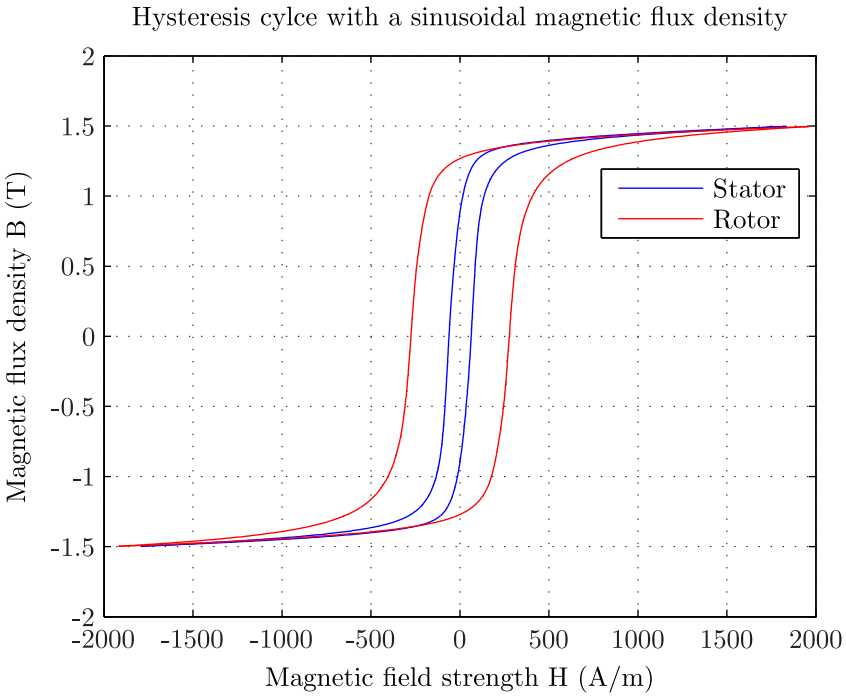

Figure 5.64: Hysteresis cycles at 50 Hz of typical stator and rotor materials with sinusoidal excitation

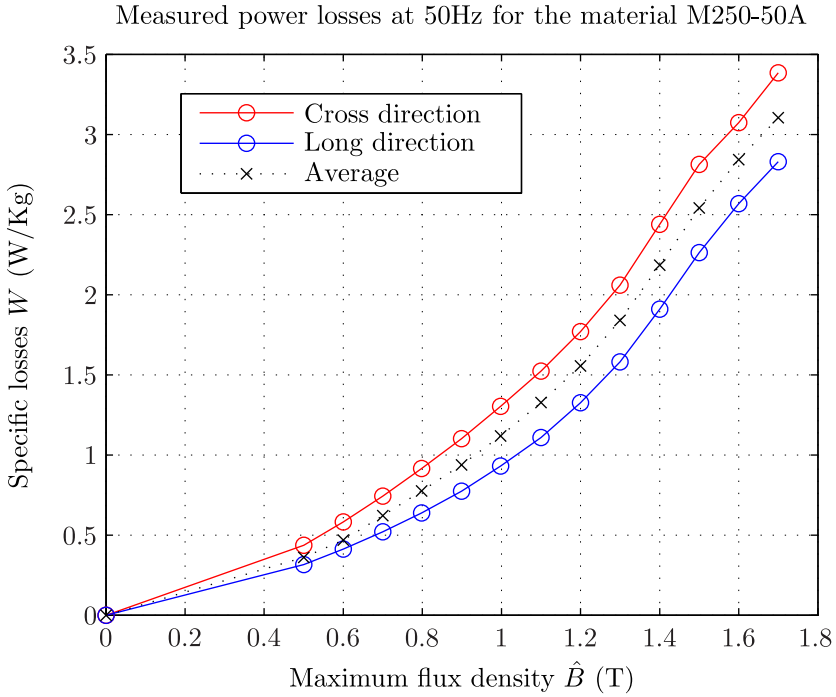

Figure 5.65: Measured losses at 50 Hz for the material $M250-50A$

losses data and from the analytical model given by Equation (5.74) by using an identification procedure based on the least mean squared method. Figure 5.66 compares the model results to the measurements and shows a good agreement. Figure 5.67 shows the evolution of the hysteresis coefficient α for the stator material.

II. Impact of a non-sinusoidal flux excitation

Until now only a pure sinusoidal flux excitation has been considered. However the flux density is scarcely sinusoidal and is distorted because of winding mmf harmonics, magnetic saturation harmonics, teeth harmonics or current harmonics as it was demonstrated in Chapter 4. Figure 5.68 shows the evolution of the flux density considering the superimposition of two components: a fundamental wave (1.44 T, 50 Hz) and an high-frequency harmonic (0.08 T, 1750 Hz). Such excitation might exist especially in the stator or the rotor teeth because of slots ripples harmonics. Figure 5.69 shows the measured hysteresis cycle $B(H)$ on an Epstein frame corresponding to this particular excitation. One can observe the presence of several small cycles also called minor loops in addition to the main fundamental hysteresis cycle. The corresponding measured losses are equal to 5.7 W/kg which is more than twice higher than the losses corresponding to the purely sinusoidal case. Minor loops can be considered as small hysteresis cycles occurring each time when the derivative of the flux excitation reverses. Figure 5.70 shows the identification of reversals. Until now only a pure sinusoidal flux excitation has been considered. However the flux density is scarcely sinusoidal and is distorted because of winding mmf harmonics, mag-

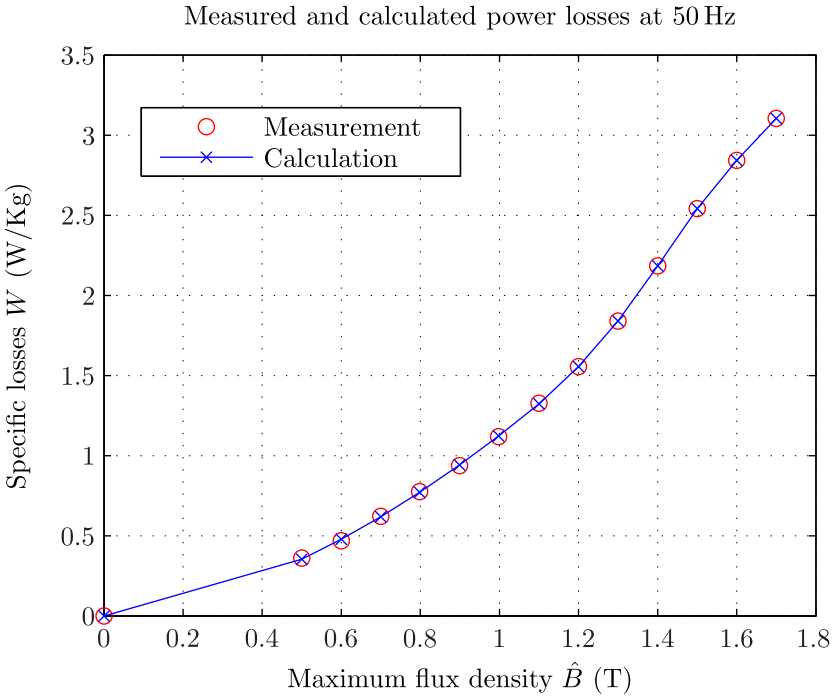

Figure 5.66: Measurement and model comparison for the material M250-50A at 50 Hz

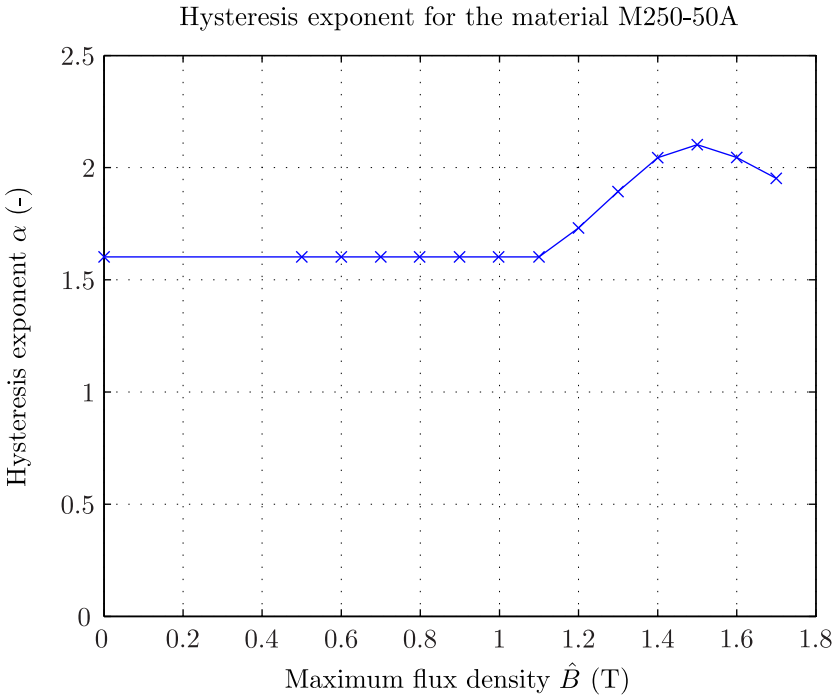

Figure 5.67: Evolution of exponential coefficient α for the material M250-50A

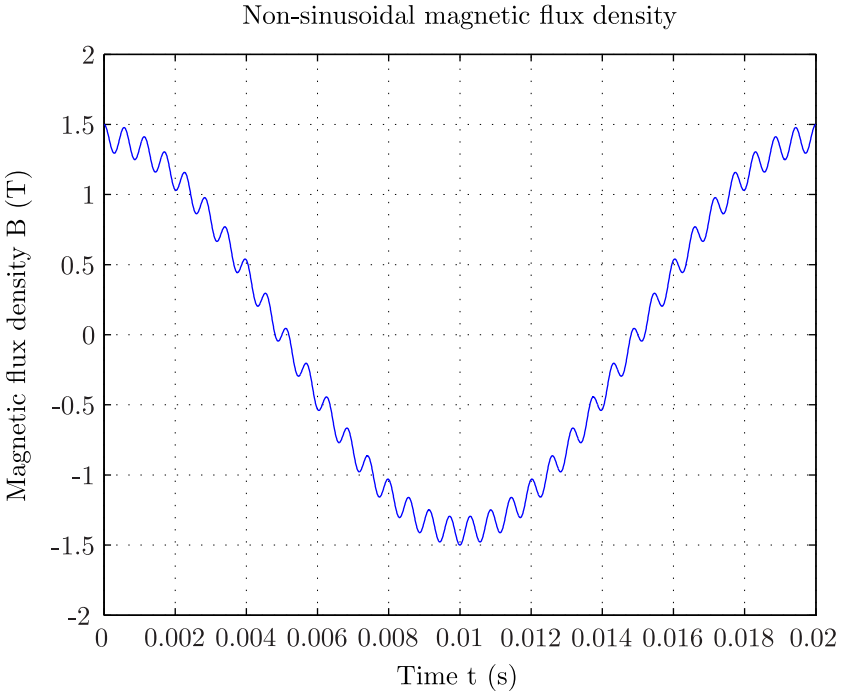

Figure 5.68: Non-sinusoidal flux excitation

netic saturation harmonics, teeth harmonics or current harmonics as it was demonstrated in Chapter 4. Figure 5.68 shows the evolution of the flux density considering the superimposition of two components: a fundamental wave (1.44 T, 50 Hz) and an high-frequency harmonic (0.08 T, 1750 Hz). Such excitation might exist especially in the stator or the rotor teeth because of slots ripples harmonics. Figure 5.69 shows the measured hysteresis cycle $B(H)$ on an Epstein frame corresponding to this particular excitation. One can observe the presence of several small cycles also called minor loops in addition to the main fundamental hysteresis cycle. The corresponding measured losses are equal to 5.7 W/kg which is more than twice higher than the losses corresponding to the purely sinusoidal case. Minor loops can be considered as small hysteresis cycles occurring each time when the derivative of the flux excitation reverses. Figure 5.70 shows the identification of reversals.

a) Effect on hysteresis losses So as to take into account the impact of existing minor loops on the losses, the hysteresis losses $\mathrm{d}P_h$ are modified as given by Equation (5.77):

$$\mathrm{d}p_{\mathrm{i,h}} = k_h f \cdot \left(\hat{B}^{\alpha} + \sum_{i=1}^{N_{\mathrm{l}}} \left(\frac{\Delta B_i}{2} \right)^{\alpha} \right) \tag{5.77}$$

where f is the frequency of the main cycle, $\hat{B}$ is the maximum of the flux density over one period, N_{l} is the number of minor loops and ΔB_i is the amplitude between two consecutive reversals. Note that the flux density wave forms present in our machine remain easy to analyze. Only the teeth harmonics (stator or rotor) and in some cases the third harmonic are high enough

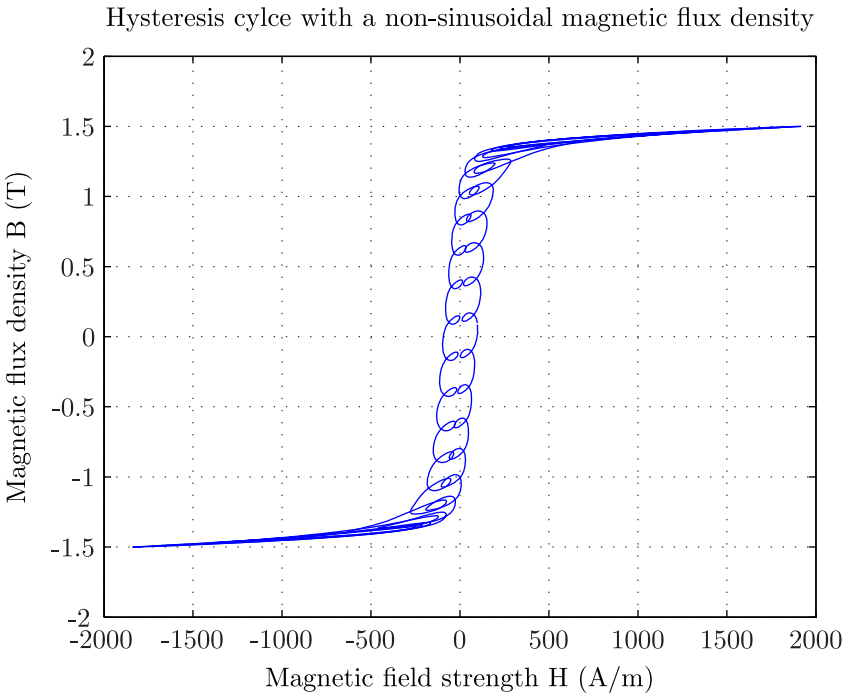

Figure 5.69: Effect of non-sinusoidal flux excitation

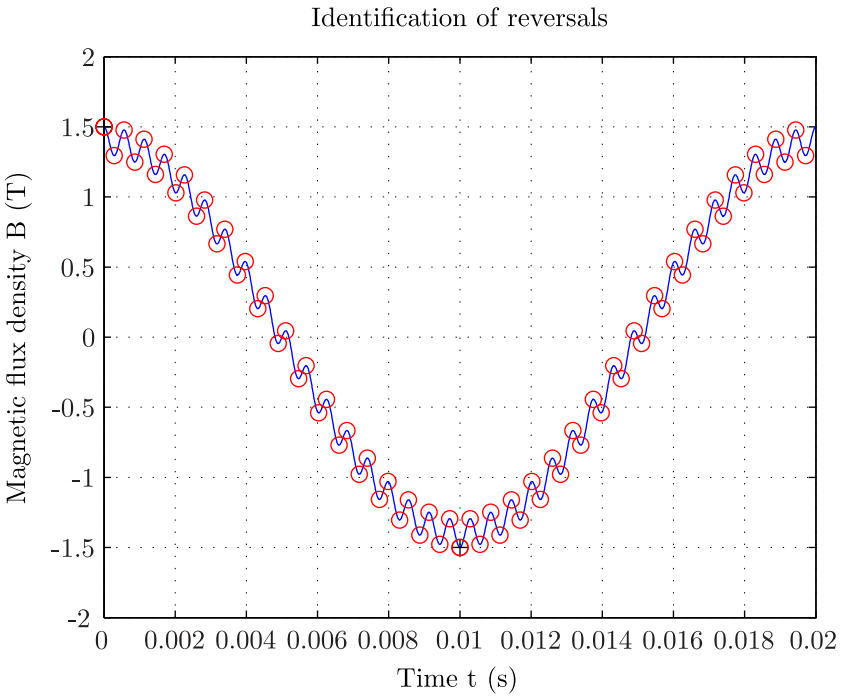

Figure 5.70: Identification of reversals

Signal	B_1 (T)	$B_3 5$ (T)
$S1$	0.95	0.055
$S2$	1.14	0.066
$S3$	1.43	0.081
$S4$	1.55	0.086

Table 5.18: Applied signals characteristics

Signal	Measure $\mathrm{d}p_\mathrm{i}$ (W/kg)	Computation $\mathrm{d}p_\mathrm{i}$ (W/kg)	Error (%)
$S1$	2.17	2.22	2.35
$S2$	3.14	3.16	0.72
$S3$	5.61	5.18	-7.53
$S4$	6.08	5.80	-4.59

Table 5.19: Comparison between measured losses and calculated losses

to create reversals. The treatment would become more difficult when several harmonics would cause minor loops. In such case, a signal processing becomes necessary in order to identify step by steps all the sources of minor loops.

b) Effect on eddy-current losses The consideration of additional harmonics on the eddy-current losses is done as following:

$$\mathrm{d}p_{\mathrm{i,c}} = \sum_{\nu=1}^{\infty} k_\mathrm{c}' \cdot {F_\nu}^2 \cdot {B_\nu}^2 \tag{5.78}$$

Note here that the k_e' depends on the frequency F_ν and the magnetic permeability μ. For simplifications reasons, we use $\hat{B}$ to determine μ.

c) Effect on excess losses Equation (5.73) is recalled so that the excess losses are expressed by:

$$\mathrm{d}p_{\mathrm{i,e}} = k_\mathrm{e} \frac{1}{T} \int_0^T \left| \frac{\mathrm{d}B}{\mathrm{d}t} \right|^{1.5} \mathrm{d}t \tag{5.79}$$

As a test of the model, several signals are simulated on an Epstein frame and for the material M250-50A. Each signal consists in the superposition of two harmonics, the fundamental harmonic (B_1, 50 Hz) and a high frequency harmonic (B_{35}, 1750 Hz) which is equivalent to a typical slot ripple frequency. Table 5.18 gives for each signal the amplitude of both harmonics. Table 5.19 compares for each signal the measured and the computed losses value. For the calculation, the variation of the coefficient α are shown in Figure 5.67 while $k_\mathrm{h} = 0.01345$ and $k_\mathrm{e} = 0.0005125$. One can see, given the simplicity of the model, a good match between the measurement and the calculation.

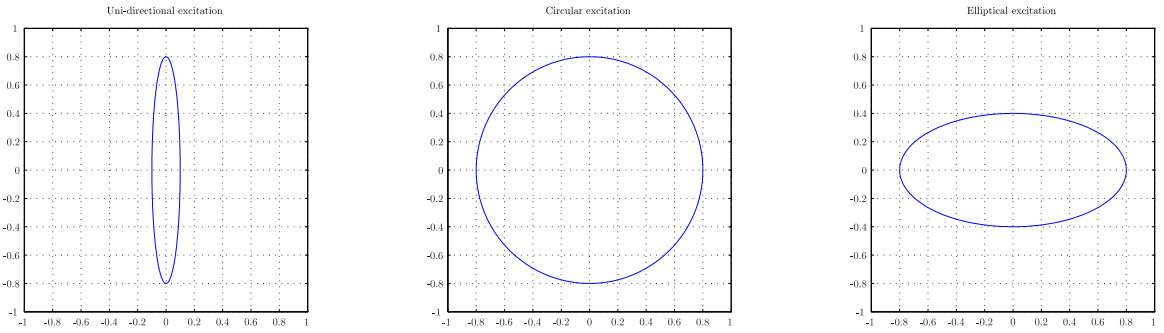

(a) Unidirectional excitation (b) Circular excitation (c) Elliptical excitation

Figure 5.71: Three possible excitations

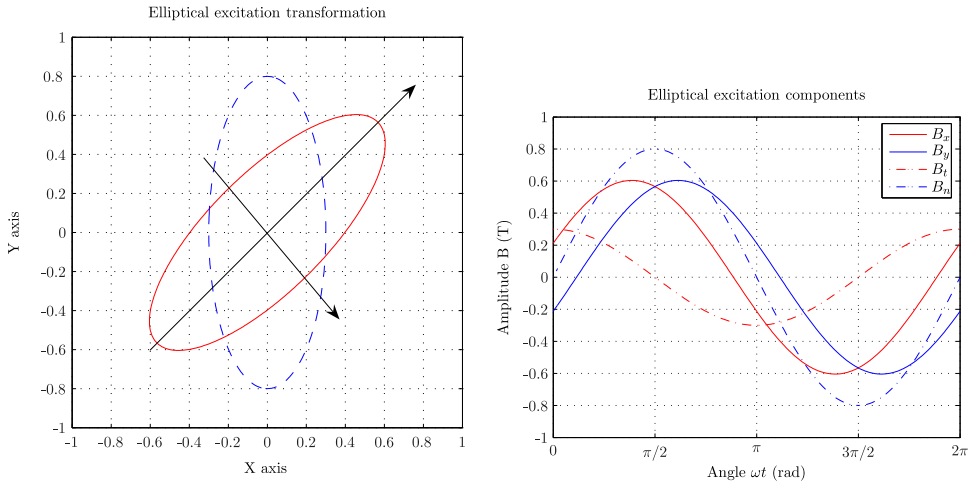

Figure 5.72: Elliptical excitation components

III. Effect of the direction of excitation

The characterization of the magnetic material was done until now by considering only an unidirectional magnetic excitation. However as it it will be shown in the next section, the flux behaves differently in the teeth and in the yoke. Figure 5.71 shows the three main types of excitation existing in the studied machine i.e unidirectional in the rotor and stator teeth and bidirectional (circular or elliptical) in the rotor and stator yoke.

The problem of dealing with bidirectional excitation has been discussed in the literature. One approach consists in analyzing the x and y variations of the flux density over one period and to search for the direction for which the flux density is maximum [Gau05]. A new axis system is created, one axis aligned with the maximum direction $\vec{n}$ and one axis perpendicular to the maximum direction $\vec{t}$. Figure 5.72 shows the results of such treatment and in particular the evolution of the new components B_{n} and B_{t}.

The density of losses for both directions $\mathrm{d}p_{\mathrm{i,n}}$ and $\mathrm{d}p_{\mathrm{i,t}}$ is calculated by applying Equation

(5.74) and then summed up in order to obtain the total density of losses $\mathrm{d}p_\mathrm{i}$ so that:

$$\mathrm{d}p_\mathrm{i} = \mathrm{d}p_{\mathrm{i,r}} + \mathrm{d}p_{\mathrm{i,t}} \tag{5.80}$$

This approach is used in the FE software *Flux2d*. An other strategy used by [TA09; Ran+09] completes this method by introducing the hysteresis loss correction factor R whose variations are shown in Figure 5.73. The hysteresis losses, because of the main cycle considering a bidirectional excitation $\mathrm{d}P_{\mathrm{i,h}}$ become:

$$\mathrm{d}p_{\mathrm{i,h}} = k_\mathrm{h} {B_\mathrm{n}}^\alpha f \left(1 + \frac{B_\mathrm{t}}{B_\mathrm{n}} \left(R(B_\mathrm{n}) - 1\right)\right) \tag{5.81}$$

Note that $\vec{n}$ is the direction in which the flux density is maximum. The effect of harmonics is included by calculated the minor hysteresis losses by applying Equation 5.77 for both direction of excitation but without considering the term $f \cdot \left(\hat{B}^\alpha\right)$. The eddy-current and excess losses remain unchanged and are computed for both directions so that:

$$\begin{aligned} \mathrm{d}p_{\mathrm{i,c}} &= \mathrm{d}p_{\mathrm{i,c}}(B_\mathrm{n}) + \mathrm{d}p_{\mathrm{i,c}}(B_\mathrm{t}) \\ \mathrm{d}p_{\mathrm{i,e}} &= \mathrm{d}p_{\mathrm{i,e}}(B_\mathrm{n}) + \mathrm{d}p_{\mathrm{i,e}}(B_\mathrm{t}) \end{aligned} \tag{5.82}$$

Depending on the ratio $B_\mathrm{n}/B_\mathrm{t}$ and on the value of the maximum magnetic flux density $\hat{B}$, this second approach may lead to a lower density of losses. The curve presented in Figure 5.73 is assumed to be independent of the iron sheet type and valid for the considered magnetic iron sheets in this study. We use here this second approach as it makes it possible to better consider the rotating behavior of the flux density in the yoke.

5.5.3 Analytical calculation of the flux density loci

The general method consists in calculating the flux density in the tooth and in the yoke [TA09] from the airgap flux density harmonics. Note that for the stator, we use the airgap flux density harmonics calculated at the inner stator diameter. For the rotor, we use the airgap flux density harmonics applied on the outer rotor diameter. This makes it possible to consider the fact that not all the harmonics cross the airgap as it was discussed already in Chapter 4.

I. In the teeth

The magnetic flux Φ_t going through a stator or rotor tooth can be expressed as:

$$\Phi_\mathrm{t} = \frac{D_\mathrm{b}}{2} \cdot l_\mathrm{i} \int_{-\frac{\alpha_\mathrm{z}}{2}}^{+\frac{\alpha_\mathrm{z}}{2}} B_\delta(\alpha, t)\mathrm{d}\alpha \tag{5.83}$$

where α_z is the slot pitch angle, D_b is the bore radius (inner diameter for the stator and outer diameter for the rotor), and the airgap flux density B_δ is expressed as:

$$B_\delta(\alpha, t) = \sum_{\nu=1}^{+\infty} \hat{B}_{\delta,\nu} \cos(P_\nu \alpha + 2\pi F_\nu t + C_\nu) \tag{5.84}$$

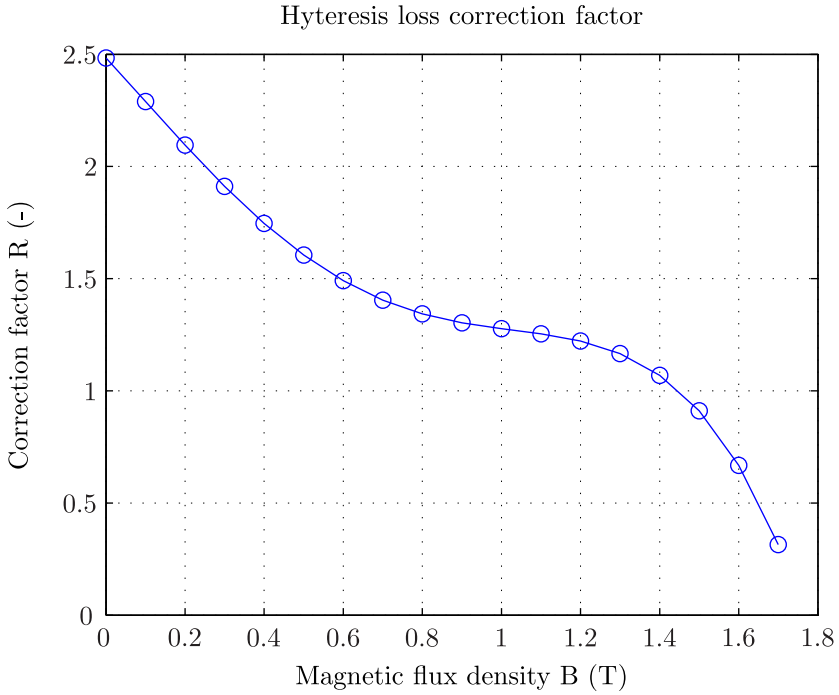

Figure 5.73: Hysteresis loss correction factor

One can show that the mean flux density in the tooth is given by [TA09]:

$$B_{\mathrm{t}}(\alpha,t) = \frac{\Phi_{\mathrm{t}}}{l_{\mathrm{f}} w_{\mathrm{t}}} = f_{\mathrm{S_t}} \sum_{\nu=1}^{+\infty} \hat{B}_{\delta,\nu} f_{\mathrm{t},\nu} \cos(2\pi F_{\nu} t + C_{\nu}) \tag{5.85}$$

where w_{t} is the stator or rotor tooth width, $f_{\mathrm{S_t}}$ is the tooth area reduction factor given by Equation (5.86) and f_{ν} is the harmonic reduction factor given by Equation (5.87). l_{f} is the effective stator or rotor iron length considering the presence of ventilation ducts. N_{z} is the number of stator or rotor slots.

$$f_{\mathrm{S_t}} = \frac{l_{\mathrm{i}}}{l_{\mathrm{f}}} \frac{\tau_s}{w_{\mathrm{t}}} \tag{5.86}$$

$$f_{\mathrm{t},\nu} = \frac{\sin(P_{\nu}\alpha_{\mathrm{z}}/2)}{P_{\nu}\alpha_{\mathrm{z}}/2} \tag{5.87}$$

As the width of tooth is not constant over the tooth height, as shown in Chapter 2, the tooth flux density has to be calculated at several positions. Figure 5.74 shows the evolution of the harmonic reduction factor due to slotting. One can see that high spatial order harmonics will get filtered along the teeth. Furthermore a part of the magnetic flux is passing into the slot because of magnetic saturation leading to a reduction of $\hat{B}$. One considers this effect by calculating the equivalent magnetic characteristics considering the slot as described in Chapter 2. Indeed one deduces from it and from $\hat{B}$ the corresponding magnetic field strength and by using the real magnetic material characteristics the reduced magnetic flux density.

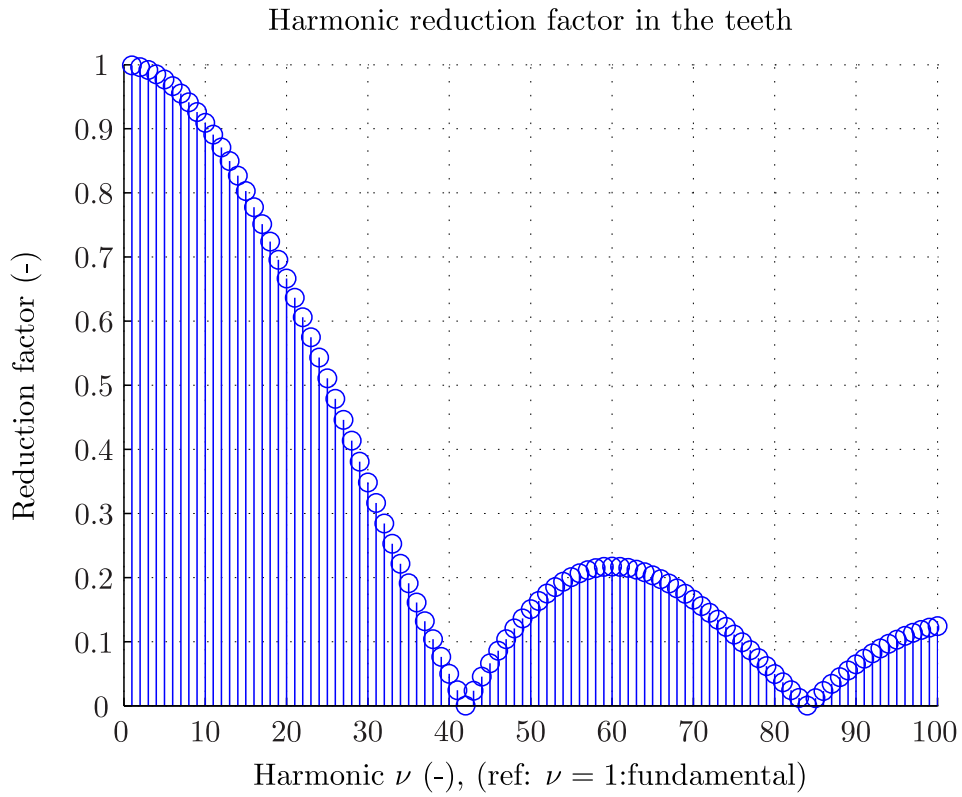

Figure 5.74: Harmonic reduction factor due to slotting (example: $p = 7$, $N_z = 294$)

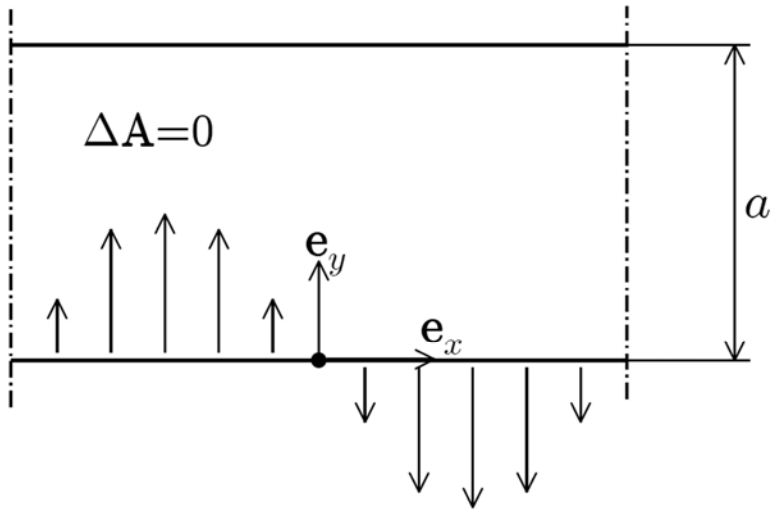

Figure 5.75: Simnplified yoke geometry [TA09]

II. In the yoke

A flux density harmonic acting in the yoke can be expressed as:

$$\hat{B}_{\mathrm{y},\nu} = \frac{l_{\mathrm{i}}}{l_{\mathrm{f}}} \cdot \frac{D_{\mathrm{b}}}{D_{\mathrm{b}} + 2h_{\mathrm{s}}} \cdot \hat{B}_{\delta,\nu} \tag{5.88}$$

where h_{s} is slot height (stator or rotor), and $\hat{B}_{\delta,\nu}$ is the exciting airgap harmonic. This formula is valid for both the stator and the rotor, but in the case of the rotor, $D_{\mathrm{b}} + 2h_{\mathrm{s}}$ has to be replaced by $D_{\mathrm{b}} - 2h_{\mathrm{s}}$. Equation (5.88) is only valid for the airgap harmonics whose wave length $\pi/k_\nu \geq \tau_s$ is greater than the slot pitch ($k_\nu = (P_\nu/P)(\pi/\tau_{\mathrm{p}})$). We assume other harmonics to close inside the the tooth and to be reduced by the harmonic reduction factor defined by Equation (5.87) [TA09].

In order to compute the distribution of the flux density inside the yoke, a simplified model is applied as explained by [TA09]. The principle consists in considering a simplified rectangular geometry for the yoke as described in Figure 5.75 and to solve inside it the Laplace equation $\Delta\vec{A} = 0$, where A is the magnetic vector potential. In the studied case, A has only one component in axial direction so that $\vec{A} = \left|\vec{A}\right| \cdot \vec{e_z}$. The applied boundary conditions are the following:

- The radial flux density is set on the inner border by the function $B_{\mathrm{Y},\nu}(x,t) = \hat{B}_{\mathrm{Y},\nu} \cos(k_\nu x + 2\pi F_\nu \cdot t + C_\nu)$
- The radial flux density on the outer border is zero, which means that all the flux is driven by the yoke

The following expressions give the spacial and time-dependent components x_1, y_1 of the flux density harmonic in the yoke:

$$B_{\mathrm{x}_1,\nu}(x,y,t) = -\hat{B}_{\mathrm{y},\nu} \cdot \frac{\cosh(k_\nu(a-y))}{\sinh(k_\nu a)} \cdot \sin(k_\nu x + 2\pi F_\nu \cdot t + C_\nu) \tag{5.89}$$

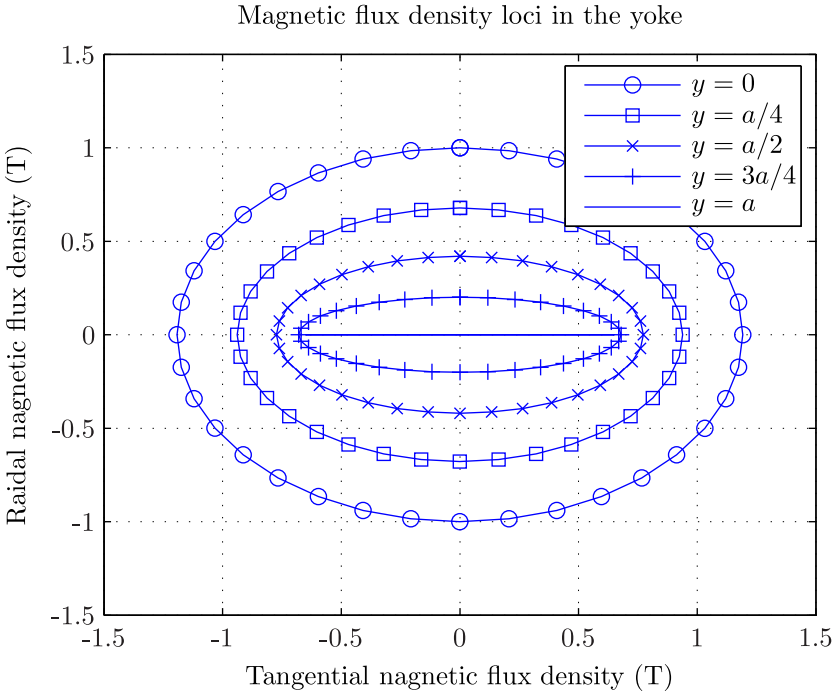

Figure 5.76: Magnetic flux density in the yoke ($\nu = p$, $\hat{B}_{\mathrm{Y},\nu} = 1\,\mathrm{T}$)

$$B_{\mathrm{y}_1,\nu}(x,y,t) = \hat{B}_{\mathrm{y},\nu} \cdot \frac{\sinh(k_\nu(a-y))}{\sinh(k_\nu a)} \cdot \cos(k_\nu x + 2\pi F_\nu \cdot t + C_\nu) \tag{5.90}$$

Figure 5.76 plots, as example, the corresponding variations of the flux density in the yoke at different radial positions. One can observe the rotational behavior of the magnetic flux along the yoke height.

5.5.4 Analytical calculation of iron losses and comparison with Finite-Element

In this part we calculate the iron losses for two operation points using the analytical method: one point at no-load and one point at rated load. Furthermore both points are at maximum speed. The results are compared with the ones obtained from a time stepping FE simulation.

I. Calculation of iron losses with finite element

The FE computations are done by using a time-stepping simulation. If the slip is zero, the simulation is done on one exact period according to the stator electrical frequency. Otherwise it has to be carried out on at least one exact period corresponding to the fundamental rotor current frequency. In the studied case, the slip is $s = -10\%$, so that the simulation period is 0.2 s.

For the extraction of the losses, we use the simple Bertotti model provided in the FE software. Note that the local flux densities in the core regions have to be corrected in order to reflect the shorter effective core length compared to the axial length of the machine. Chapter 2 has shown

that the rotor and stator magnetic characteristics where modified using the factors $l_{\mathrm{f,r}}/l_{\mathrm{i}}$ and $l_{\mathrm{f,s}}/l_{\mathrm{i}}$.

Consequently the stator $\mathrm{p_{i,s}}$ and rotor iron losses $\mathrm{p_{i,r}}$ according to the real stator and rotor flux density values are extracted from the FE results using Equations (5.91) and (5.92). $p_{\mathrm{h,s}}$, $p_{\mathrm{i,h,r}}$, $p_{\mathrm{i,c,s}}$, $p_{\mathrm{i,c,r}}$, $P_{\mathrm{i,e,s}}$ and $p_{\mathrm{i,e,r}}$ are the original computed hysteresis, classical and excess stator and rotor losses.

$$\mathrm{p_{i,s}} = \frac{l_{\mathrm{f,s}}}{l_{\mathrm{i}}}\left(p_{\mathrm{i,h,s}} \cdot (l_{\mathrm{i}}/l_{\mathrm{f,s}})^2 \cdot f_{\mathrm{s}} + p_{\mathrm{i,c,s}} \cdot (l_{\mathrm{i}}/l_{\mathrm{f,s}})^2 + p_{\mathrm{i,e,s}} \cdot (l_{\mathrm{i}}/l_{\mathrm{f,s}})^{1.5}\right) \tag{5.91}$$

$$\mathrm{p_{i,r}} = \frac{l_{\mathrm{f,r}}}{l_{\mathrm{i}}}\left(p_{\mathrm{i,h,r}} \cdot (l_{\mathrm{i}}/l_{\mathrm{f,r}})^2 \cdot f_{\mathrm{r}} + p_{\mathrm{i,c,r}} \cdot (l_{\mathrm{i}}/l_{\mathrm{f,r}})^2 + p_{\mathrm{i,e,r}} \cdot (l_{\mathrm{i}}/l_{\mathrm{f,r}})^{1.5}\right) \tag{5.92}$$

II. Comparison at no-load and load

The iron losses calculation model included in the FE does not consider neither the additional hysteresis losses because of minor loops nor the rotational effect. Consequently for validation purpose, we will first calculate analytically using the same model as the FE program (results $\mathrm{A_1}$) and then using the previously presented model (results $\mathrm{A_2}$).

Figure 5.78 shows the different results. One can first notice the non negligible amount of losses in the rotor regions. Secondly although both calculations, FE and $\mathrm{A_1}$, use the same iron losses calculation model, one can see some difference in the results. This can be explained by the fact that the magnetic flux densities calculated analytically may be too high or too low in the teeth and in the yoke regions. This problem could be solved by adding some correction based on the results of the magnetic model of Chapter 2. When comparing the results between the analytical methods $\mathrm{A_1}$ and $\mathrm{A_2}$ one can notice slight differences due to the new considered effects such as the minor loops and the rotational effects. Finally despite some differences between the FE results and the analytical model, the later is considered valid to quantify the iron losses in the machine.

III. Effect of magnetic wedges

Section 5.2 has shown the impact of magnetic wedges on the stator voltage harmonics content. Here we study the impact of such wedges on the iron losses. Figure 5.79 shows the results of the study made with FE. One can see they lead to a decrease of the losses mainly in the stator and in rotor teeth. As mentioned before using magnetic wedges at the rotor is unlikely because of mechanical constraints; however only using them at the stator still leads to a decrease of 25% of the losses in the rotor teeth which is not negligible. Note that the FE calculation does not consider the minor loops. However the magnetic wedges reduce the slot harmonics and those are large contributors of minor loops in the teeth. Consequently the results of this study should remain valid even with the complete model or iron-losses.

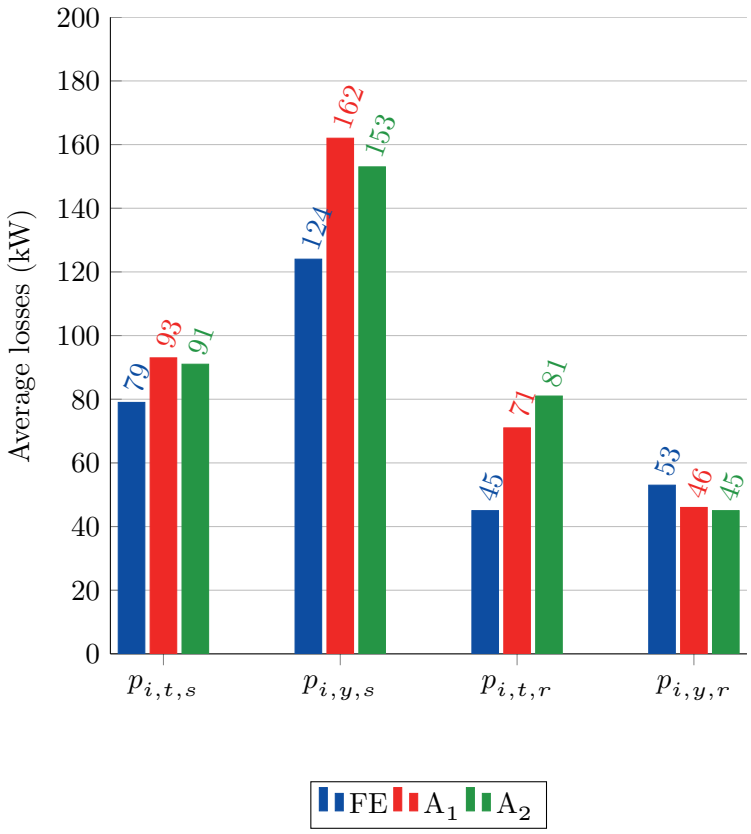

Figure 5.77: Comparison of iron losses at no-load operation, hyper-synchronous mode

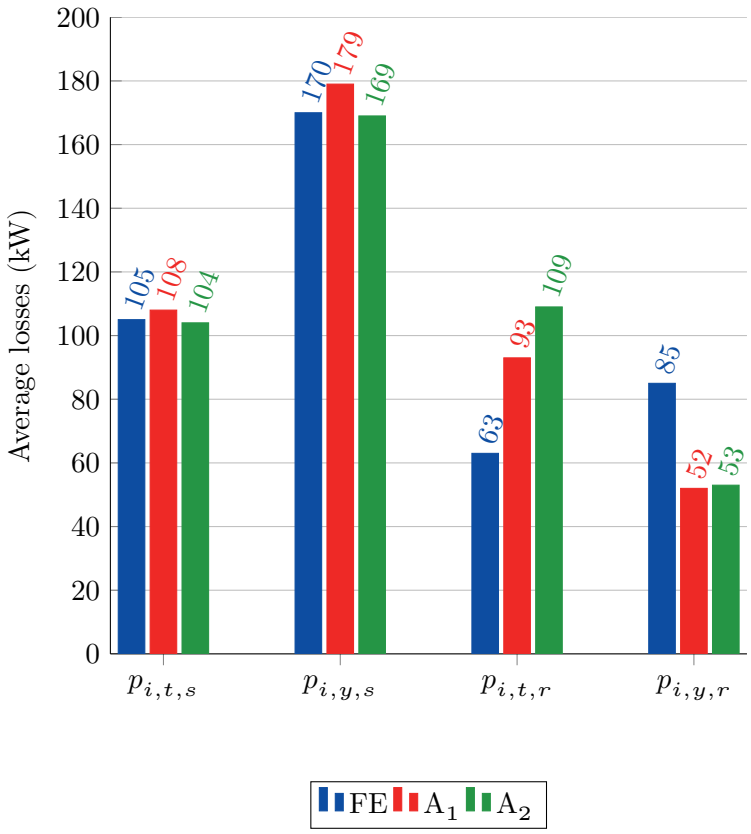

Figure 5.78: Comparison of iron losses at load operation, hyper-synchronous mode

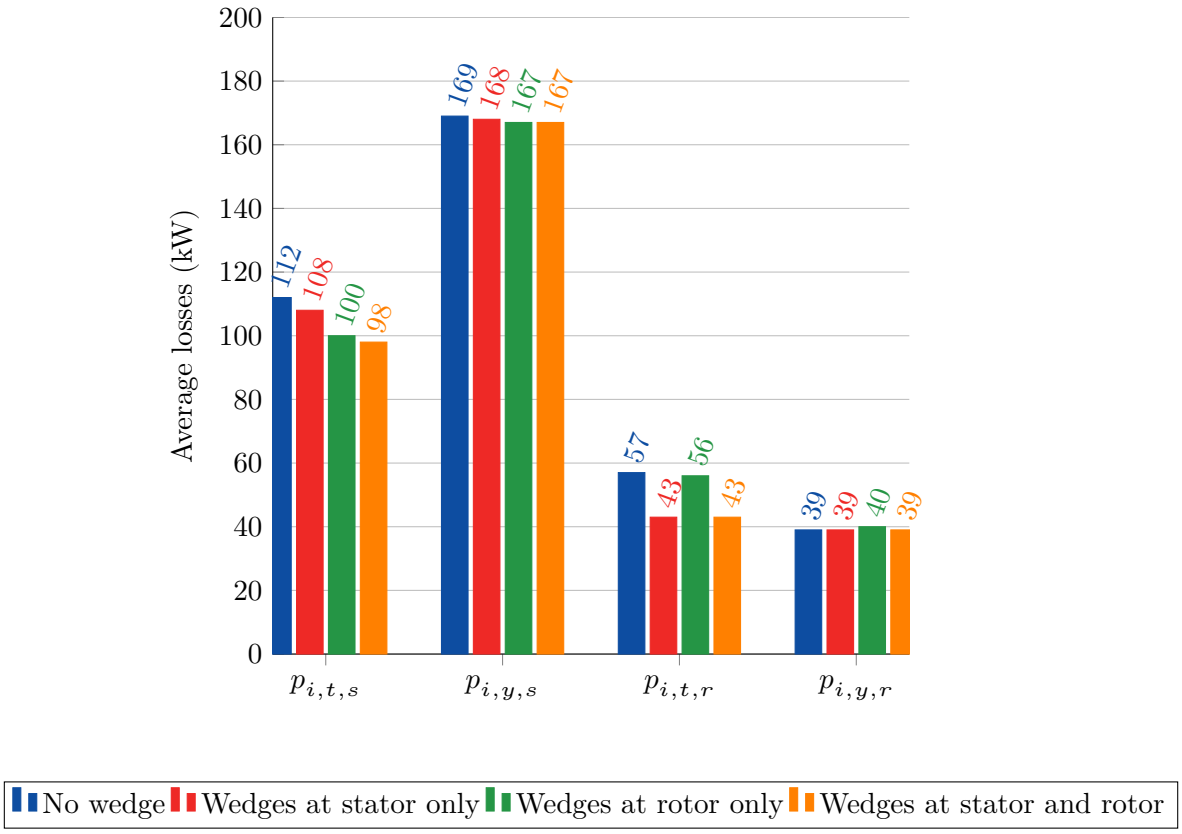

Figure 5.79: Impact of magnetic wedges in iron losses under no-load operation

5.5.5 Summary

This section detailed the iron losses calculation in the DFIM. The calculation was based on the results of the airgap harmonics model developed in Chapter 4 and the well known iron-losses Bertotti model. The latter was extended in order to consider additional phenomena such as the minor-hysteresis cycles and the rotational behavior of the flux density inside the stator and yoke regions. The developed model agrees with the results obtained from 2DFE simulations. Note that the presented calculation does not include additional effects such as the punching which can have a large impact on the losses as shown by Gautreau [Gau05]. However this is normally considered by adding correction factors on the total amount of losses based on experience. Furthermore the impact of the converter is expected small as this one generates rotor currents with low harmonics content. Finally we have shown that the iron losses occurring at the rotor were not at all negligible especially due to the magnetic characteristics of the material. Using magnetic wedges at the stator arose as an efficient means to reduce the losses in the teeth.

5.6 Conclusion

This chapter applied the previously presented analytic and numeric methods in order to study four topics relevant for the electrical engineer. The consideration of these elements is capital as they can lead to perturbation of the normal operations. In particular we dealt with the pollution of the network because of stator harmonics, as well as vibration or noise issue because of parasitic forces and finally of the magnetic power losses. For each case we described in detail the formulations and the calculation techniques. The developed airgap harmonic model appeared as an efficient tool to understand the origin of particular quantities such as the stator harmonics or the parasitic forces. The knowledge acquired when dealing with transient FE simulations contributed to efficiently extract components such as dynamic torques. Furthermore Part 5.3, when dealing with parasitic forces, has shown that a fractional slot winding could be reconfigured in order to decrease a particular harmonic and reduce the amplitude of vibration. The other dimensioning parameters of the machine can also be modified in order to improve the performance of the machine. This is the subject of the next chapter.

6 Application to the dimensioning of the double-fed induction machine

6.1 Introduction

This chapter applies the different knowledge acquired along the previous chapters to the dimensioning of a DFIM for hydraulic applications. It defines the key points of the design and demonstrates how an optimization tool can be used efficiently to perform the dimensioning of such machine.

First part explains the basic process and criteria leading to the choice of the main dimensions. It develops as well the choice of the rated parameters such as the power and the synchronous speed.

Second part introduces the dimensioning methodology based on the use of an optimization tool. It defines more particularly the optimization technique, the optimization problem and the constraints due to thermal, mechanical, electrical or manufacturing limitations.

Third part solves the previously defined optimization problem. The objective is to upgrade an existing standard salient-pole synchronous motor/generator to an equivalently rated DFIM motor/generator. Two cases are analyzed: the first case only replaces the salient-pole rotor core by a three-phase wound rotor, the second case re-designs both the rotor and the stator cores. While the first case enables an easy and a fast comparison of both technology designs on the same stator basis, the second case gives more flexibility to the dimensioning and proposes a safer design.

6.2 Rated characteristics and dimensioning of a double-fed induction machine

This part explains the different steps when selecting the rated characteristics and main dimensions of a DFIM.

6.2.1 Choice of the rated characteristics

I. The rated apparent power

The rated apparent power S of the motor/generator is linked to the available mechanical power P_{turbine} on the shaft provided by the turbine. P_{turbine} depends directly on the location of the

power plant i.e. on the available water volume flow Q (m^3/s) and on the water head H (m). Finally P_{turbine} is expressed as:

$$P_{\text{turbine}} = \eta_{\text{t}} \cdot g \cdot H \cdot Q \tag{6.1}$$

where $g \approx 9.81\,\text{m/s}^2$ is the gravitation constant and η_t is the hydraulic efficiency lying between 85% and 90%, calculated according to the different hydraulic losses in the pentstocks and in the turbine. Finally S is defined as:

$$S = \eta_{\text{g}} \cdot \frac{P_{\text{turbine}}}{cos\varphi} \tag{6.2}$$

where $\cos\varphi$ is the rated power factor of the motor/generator, about 0.9, and η_{g} is the motor/generator efficiency which can be considered between 98% and 99%.

II. The synchronous speed

The choice of the synchronous speed for a standard installation i.e. with fixed speed machines depends on the turbine manufacturer who considering the installation location proposes the optimum rotational speed. In the case of a variable speed unit, the turbine manufacturer defines an optimum speed range $[n_{\min}, n_{\max}]$. The choice of the synchronous speed n_{s} within this interval is made in order to minimize the rotor active power along the whole speed range [Cou98]. When neglecting the losses one can express the rotor active power P_{r} as:

$$|P_{\text{r}}(n)| \approx P_{\text{turbine}}(n)\,|1 - n_{\text{s}}/n| \tag{6.3}$$

where n is a speed belonging to $[n_{\min}, n_{\max}]$. Given the power/speed characteristics of the pump/turbine in turbine mode and taking as reference one speed n of the defined speed range $[n_{\min}, n_{\max}]$, one can calculate the corresponding rotor active power by applying Equation (6.3). Repeating this for every speed of the speed range one obtains the Figure 6.1. Note that the variation of the mechanical power provided by the pump/turbine in turbine mode is built considering the speeds giving the best efficiency points; this characteristic is here assumed linearly speed dependent. One can see that the rotor active power is either minimum or maximum at minimum and maximum speed. Finally the reference speed giving the minimum rotor active power is chosen as the reference speed. As the motor/generator unit is also operating as a motor, one has to apply the same procedure considering the power/speed characteristics of the pump/turbine in pumping mode. In the case that two different synchronous speeds for the turbine and pump mode are found, the speed giving the lowest maximum slip is kept.

6.2.2 Choice of the main dimensions

The choice of the main dimensions is strongly linked to the rated characteristics of the machine, but also to the cooling type. The cooling type has an effect on the maximum thermal constraints of the machine and consequently on its dimensions. In case of very large power and high speed motor/generator units, one can use a water cooling system at the stator and in extreme and rare cases at the rotor, too. In the following we only consider the air cooling type, which is sufficient

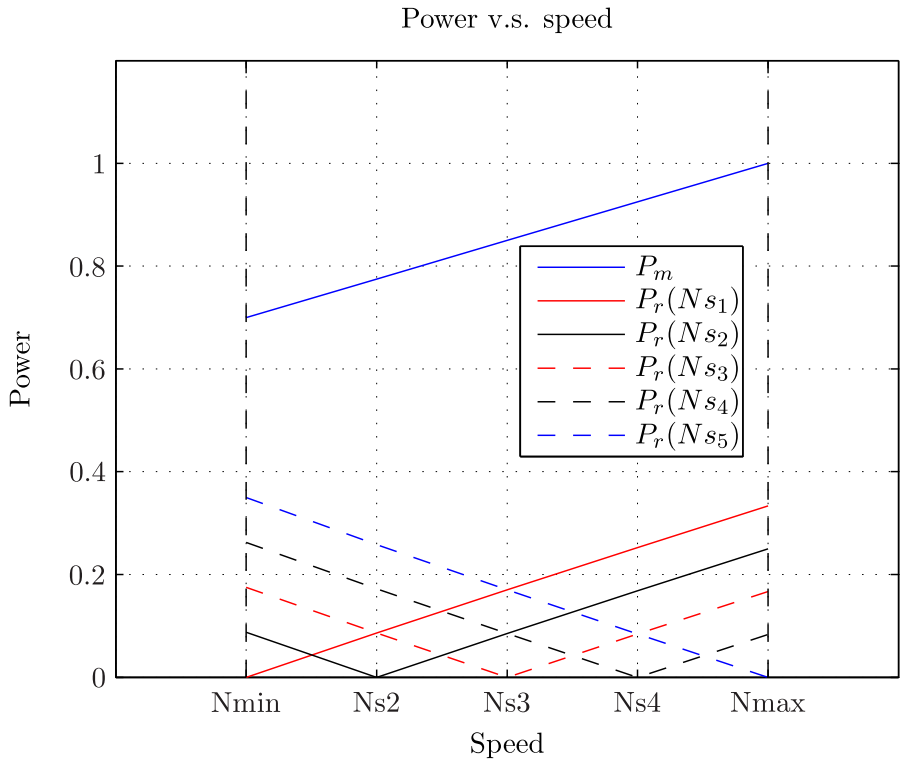

Figure 6.1: Variation of mechanical and rotor active power v.s speed

for the power and speed defined range studied in this thesis. The rotor center and rotor rim act as a radial fan; the generated air flow is driven trough radial ducts in order to cool respectively the rotor and the stator.

I. The number of poles

The number of poles N_{p} is chosen according to the synchronous speed and the network frequency:

$$N_{\mathrm{p}} = \frac{f_{\mathrm{s}}}{f_{\mathrm{m}}} \tag{6.4}$$

where f_{s} is the network electrical frequency and f_{m} is the mechanical rotational frequency. One can then derive the number of pole-pairs $p = N_{\mathrm{p}}/2$.

II. The bore diameter and length

The bore diameter $D_{\mathrm{b,s}}$, i.e the internal stator core diameter, and the stator core length l_{s} are found by using the concepts of the electrical and mechanical utilization. Firstly the electrical utilization is defined by the electrical coefficient C, also called Esson factor given by Equation (6.5). This coefficient represents the apparent power per volume and speed and is expressed in

VAs/m^3. Note that the speed n is in Hz.

$$C = \frac{S}{D_{\mathrm{b,s}}^2 \cdot l_{\mathrm{s}} \cdot n} \tag{6.5}$$

One can show that C is directly proportional to the product of the linear stator current density A and the airgap flux density B so that: $C \propto A \cdot B$. Consequently C makes it possible to have an indication of the magnetic and electrical loading of the machine. The limiting values for A and B are respectively determined by the cooling method, and the magnetic saturation in the core regions. Normally motor/generator manufacturers use curves, based on experience, giving the relation between the utilization factor and the rated power per pole. From these curves, one can determine the product $D_{\mathrm{b,s}}^2 \cdot l_{\mathrm{s}}$.

Secondly the mechanical utilization is defined by the inertia factor k_{Θ} given by Equation (6.6) and expressed in kg/m^3.

$$k_{\Theta} = \frac{\Theta_{\mathrm{j}}}{D_{\mathrm{b,s}}^4 \cdot l_{\mathrm{s}}} \tag{6.6}$$

Θ_{j} is the rotor moment of inertia (kg m). Note that the constant k_{Θ} considers that the rotor is made from different materials with different specific weights. The rotor inertia plays a capital role in case of full load rejection, i.e. when the machine terminals are suddenly disconnected from the network. In this case, the electromagnetic torque of the machine becomes zero. Because of the necessary time to close the turbine valves, the machine is accelerating. A high enough inertia is therefore needed in order to limit mechanical constraints in the hydraulic pipes. Furthermore an high inertia may also be required for stability reasons. As for the coefficient C, motor/generator manufacturers use empiric curves giving the relation between the inertia factor and the number of poles. Consequently assuming a certain inertia, one can assess the product $D_{\mathrm{b,s}}^4 \cdot l_{\mathrm{s}}$. Finally from these two factors one can estimate the values of $D_{\mathrm{b,s}}$ and l_{s}.

III. The number and dimensions of stator slots and rotor slots

The number of stator and rotor slots is selected in order to obtain three-phase balanced windings. A theoretical number of stator slots can be found considering the rated line-to-line stator voltage U_{s} and an optimum fundamental airgap magnetic flux density $\hat{B}_{\delta,\mathrm{f}}$. $\hat{B}_{\delta,\mathrm{f}}$ is normally chosen in the range $0.9 \cdots 1$ in order to guarantee acceptable flux density values in the rotor and stator iron regions. From Equation (6.7), one can determine the theoretical number of turns in series per stator phase $N_{\mathrm{s,s}}$.

$$N_{\mathrm{s,s}} = \sqrt{\frac{2}{3}} \cdot \frac{U_{\mathrm{s}}}{\xi_{\mathrm{f,s}} \cdot 2\pi \cdot f_{\mathrm{s}} \cdot \hat{B}_{\delta,\mathrm{f}} \cdot \tau_{\mathrm{p,s}} \cdot l_{\mathrm{s}}} \tag{6.7}$$

At this step of the pre-design, the stator pole pitch $\tau_{\mathrm{p,s}}$ can be derived from the known values of $D_{\mathrm{b,s}}$ and N_{p}. The winding factor $\xi_{\mathrm{f,s}}$ can be assumed to a typical value i.e. 0.92. Using Equation (6.8) one can express the number of stator slots $N_{\mathrm{z,s}}$ as a function $N_{\mathrm{s,s}}$, the number of stator parallel circuits $N_{\mathrm{a,s}}$ and the number of conductors per stator slots $N_{\mathrm{c,s}}$.

$$N_{\mathrm{z,s}} = \frac{6 \cdot N_{\mathrm{s,s}} \cdot N_{\mathrm{a,s}}}{N_{\mathrm{c,s}}} \tag{6.8}$$

The stator and rotor windings are made of single turn bar and double-layer winding so that $N_{\mathrm{c,s}} = 2$. Limitations on the choice of $N_{\mathrm{z,s}}$ can be set given thermal limits [Wal81]. Indeed, considering a constant number of series turns, reducing the number of slots and consequently the number of parallel paths leads to an increase of the bar current. Assuming a constant current density, the power losses to evacuate get larger. The heat dissipating surface gets also increased but not in the same proportion as the increase of the power losses, so that the temperature might also increase. Another limitation due to a minimal insulation distance between two bars of different phases can also be set. According to the voltage value, on can define the minimum slot pitch $\tau_{s,\mathrm{s}}^{\min}$ and consequently the maximum number of slots as shown by Equation (6.9).

$$N_{\mathrm{z,s}}^{\max} = \frac{\pi \cdot D_{\mathrm{b,s}}}{\tau_{s,\mathrm{s}}^{\min}} \tag{6.9}$$

The chosen number of slots must also fulfill symmetry conditions. As seen previously the number of slots can be expressed as a function of the number of poles and slots per pole and phase q_{s}. For a three-phase winding system, we have:

$$N_{\mathrm{z,s}} = 3 \cdot q_{\mathrm{s}} \cdot 2p \tag{6.10}$$

As seen in Chapter 5 q_s can be written as the ratio $q_{\mathrm{s}} = q_{\mathrm{s},1}/q_{\mathrm{s},2}$ where $q_{\mathrm{s},1}$ and $q_{\mathrm{s},2}$ are two integer numbers. In case of an integral slot winding $q_{\mathrm{s},2}$ is equal to 1. In case of a fractional winding, $q_{\mathrm{s},2}$ is different from 1 and must be chosen so that it is not divisible by 3 and that it can divide the integer $2p/N_{\mathrm{a,s}}$.

After determining the number of stator slots, one has to define the number of rotor slots. By experience, in order to guarantee an efficient startup, the transformation ratio $\mathrm{u_t}$ has to be larger than a certain value $\mathrm{u_t^{min}}$. Recalling the definition of $\mathrm{u_t}$ we have:

$$\mathrm{u_t} = \frac{N_{\mathrm{s,s}} \cdot \xi_{\mathrm{f,s}}}{N_{\mathrm{s,r}} \cdot \xi_{\mathrm{f,r}}} \tag{6.11}$$

Assuming $\xi_{\mathrm{f,s}} \approx \xi_{\mathrm{f,r}}$, one can find the theoretical number of rotor turns in series $N_{\mathrm{s,r}}$:

$$N_{\mathrm{s,r}} \leq \frac{N_{\mathrm{s,s}}}{\mathrm{u_t^{min}}} \tag{6.12}$$

Knowing the number of rotor turns in series, the choice of the number of rotor slots is made according to the same principles applied for the stator winding. However, a first list of the forbidden relations between the number of rotor slots and stator slots can be given:

1. $N_{\mathrm{z,r}} = N_{\mathrm{z,s}}$: this creates a resonance between rotor slot harmonics and stator slots harmonics.
2. $N_{\mathrm{z,r}} = N_{\mathrm{z,s}} \pm 2$: this can create parasitic forces. This comes from experience with small induction machines [Kro31].

Note that these last two rules may not cover all the forbidden combinations. The main criteria for judging of the correct choice of $N_{\mathrm{z,r}}$ and $N_{\mathrm{z,s}}$ will mainly be the risk of parasitic radial forces as seen in Chapter 5.

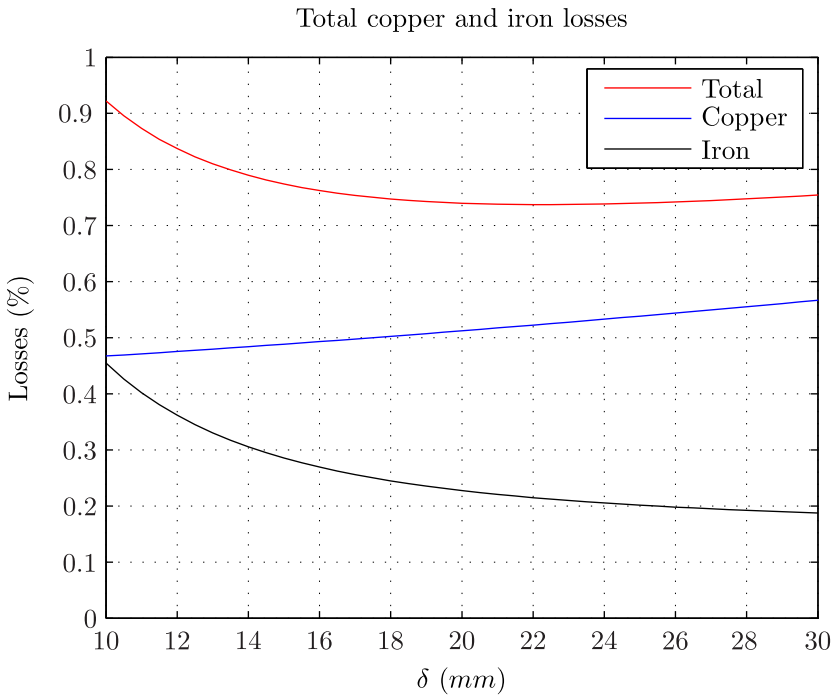

Figure 6.2: Total, copper and iron losses vs airgap depth

IV. The airgap length

The choice of the airgap length for a standard synchronous machine is made considering two main constraints. First, the mechanical constraint imposes a minimal airgap length because of the expansion of the rotor due to centrifugal forces and thermal heating. Second, electrically, a limit on the direct-axis reactance, which can be seen as a stability limit, sets a minimal value for the airgap length. The choice of the airgap length is finally done according to these constraints and a compromise between two physical behaviors: the first one being that a reduction of the airgap increases the power losses on the pole shoe surface because of stator teeth pulsations; the second one being that the increase of the airgap demands an higher magnetizing current and consequently leads to higher joule losses in the rotor winding.

Regarding the DFIM, the stability constraint on the airgap length is not relevant because of the active control of the rotor currents. However the mechanical limit is still valid and in the same way as for the standard machine, the choice will be governed according to factors such as: power iron losses, joules losses and current densities.

We analyze here the effect of changing the airgap while keeping constant other dimensions (i.e. bore diameter, number of slots, etc...) of a DFIM. Figure 6.2 shows the behavior of total, copper, and iron losses when the airgap gets larger. While increasing the airgap, the iron losses decrease and the joule losses increase. At one point a minimum amount of losses is reached leading to an optimum efficiency. However one should also take care of the evolution of the current density in the winding as shown in Figure 6.3.

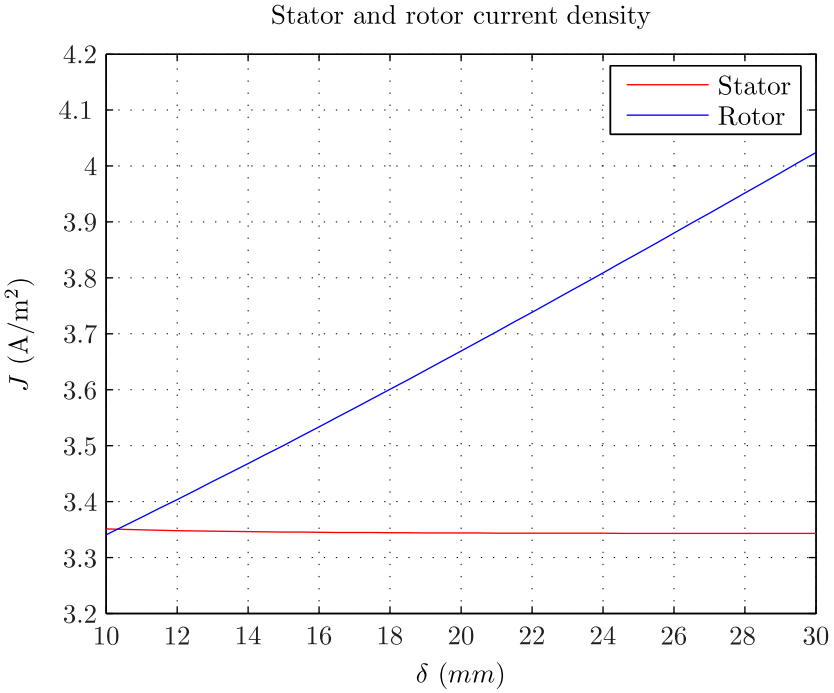

Figure 6.3: Stator and rotor current density vs airgap depth

V. The rotor and stator yoke height

The rotor and stator heights are chosen according to electromagnetic criteria, considering the maximum flux density and the amount of iron losses but also economic criteria. Indeed increasing the yoke height might result in better efficiency but leads also to a higher iron volume and consequently an higher cost. Normally the stator yoke height is obtained by first calculating the magnetic flux flowing in the yoke from one pole to another pole $\hat{\Phi}_{\mathrm{y,s}} = \hat{\Phi}/2$. From Chapter 2 we have:

$$\hat{\Phi} = l_{\mathrm{s}}\tau_{\mathrm{p,s}}\alpha_{\mathrm{i}} \cdot \hat{B}_{\delta} = l_{\mathrm{s}}\tau_{\mathrm{p,s}}(\alpha_{\mathrm{i}}/\mathrm{C}_1) \cdot \hat{B}_{\delta\,,\mathrm{f}} \tag{6.13}$$

$\hat{\Phi}_{\mathrm{y,s}}$ can also be expressed as function of the maximum stator flux density Bys, the stator yoke height $h_{\mathrm{y,s}}$ and the stator effective length $l_{\mathrm{f,s}}$:

$$\hat{\Phi}_{\mathrm{y,s}} = \hat{B}_{\mathrm{y,s}} \cdot l_{\mathrm{f,s}} \cdot h_{\mathrm{y,s}} \tag{6.14}$$

so that $h_{\mathrm{y,s}}$ can be written as:

$$h_{\mathrm{y,s}} = \frac{0.5 \cdot l_{\mathrm{s}}\tau_{\mathrm{p,s}}(\alpha_{\mathrm{i}}/\mathrm{C}_1) \cdot \hat{B}_{\delta\,,\mathrm{f}}}{\hat{B}_{\mathrm{y,s}} \cdot l_{\mathrm{f,s}}} \tag{6.15}$$

Note that $l_{\mathrm{f,s}}$ is the effective stator iron length assuming a certain number of ventilation stator ducts $N_{\mathrm{d,s}}$ and a ventilation stator duct width $w_{\mathrm{d,s}}$. Normally a typically acceptable value for the $\hat{B}_{\mathrm{y,s}}$ lies in the range $[1.1 \cdots 1.4]$ T, while $\mathrm{C}_1 \approx 1.1$ and $\alpha_{\mathrm{i}} \approx 0.72$ in rated operation i.e. for $\mathrm{K}_{\mathrm{s}} \in [0.2, 0.4]$. The rotor yoke height $h_{\mathrm{y,r}}$ is chosen according to the same principles.

6.3 Dimensioning by solving an optimization problem

The previous part introduced the process enabling a pre-dimensioning of the machine. Several iterations in the choice of the dimensions and in the winding configurations are necessary to converge to an acceptable design: respect of maximum current densities, maximum flux densities, maximum temperature rises, maximization of the efficiency or optimization of the volume. So as to perform efficiently this iteration process, one can formulate the design problem into an optimization problem. An optimization problem is defined by three elements: the objective function, the constraints and the optimization algorithm.

6.3.1 Definition of the objective function

When designing a hydro motor/generator it is natural to try to maximize the efficiency while trying to minimize the iron volume and to respect constraints because of thermal, mechanical or manufacturing limitations. We choose to define the objective function $f_{\text{obj}}(X) = -\eta_{\text{g}}$. The objective is to determine the family of N input parameters $X = x_1, x_2, \cdots, x_{N-1}, x_N$ so that the motor/generator efficiency η_{g} is maximized and consequently $f_{\text{obj}}(X)$ is minimized. In our case x_i can for example represent the width of a stator copper strand, the number of rotor parallel circuits, the stator bore diameter etc. However one must also take into account the different problem constraints as listed in the next section.

6.3.2 Definition of the constraints

This section defines all the constraints set on output parameters:

I. Thermal and magnetic constraints

The temperature calculation model is not described in this thesis, it stands on the similar concepts as the one described in [TZS10]. The internal company tool provides us the maximum temperature rise in several regions of the machine and in particular between top and bottom bar. Such temperature rise can be measured in operation by the so-called RTD sensors.

Finally the electric magnetic and thermal constraints are:

1. The flux densities in the stator and rotor teeth and stator and rotor yoke $\hat{B}_{\text{t,s}}, \hat{B}_{\text{t,r}}$ and $\hat{B}_{\text{y,s}}, \hat{B}_{\text{y,r}}$: they have to be lower than maximum admissible values in order to limit the magnetization current. We will take as extreme values 1.9 T for the teeth and 1.4 T for the yoke.
2. The maximum stator and rotor winding temperature rise ΔT_{s} and ΔT_{r}: this maximum admissible value depends on the insulation system of the winding and on the assumed cold air temperature. For a class $\mathcal{B}$ insulation system, it is 85 K and 110 K for a class $\mathcal{F}$.
3. The stator and rotor current densities J_{s} and J_{r}: they have to be lower than admissible values. We choose as extreme value 3.5 A/mm^2 for the stator and 4 A/mm^2 for the rotor.

II. Manufacturing and dimensions constraints

1. The external stator diameter $D_{\mathrm{out,s}}$: it must be smaller than the maximum allowed dimension which depends on the dimensions of the pit where the motor/generator is placed.
2. The diagonal length of a non-insulated stator bar $d_{\mathrm{b,ni,s}} = \sqrt{w_{\mathrm{b,ni,s}}^2 + h_{\mathrm{b,ni,s}}^2}$ and of a rotor bar $d_{\mathrm{b,ni,r}} = \sqrt{h_{\mathrm{b,ni,r}}^2 + h_{\mathrm{b,ni,r}}^2}$: it must be lower than the maximum allowed dimension. $h_{\mathrm{b,ni}}$ and $h_{\mathrm{b,ni}}$ are respectively the width and the height of a non-insulated bar.

III. Balanced winding constraints

1. The number of stator and rotor parallel path $N_{\mathrm{a,s}}, N_{\mathrm{a,r}}$ must divide the number of poles $2p$.
2. The number of stator and rotor slots per pole and phase $q_{\mathrm{s},2}, q_{\mathrm{r},2}$ must not be divisible by 3.
3. The denominator of the number of stator slots per pole and phase $q_{\mathrm{s},2}$ must divide $2p/N_{\mathrm{a,s}}$.
4. The denominator of the number of rotor slots per pole and phase $q_{\mathrm{r},2}$ must divide $2p/N_{\mathrm{a,r}}$.

IV. Converter constraints

1. The rotor voltage U_{r} must be lower than the maximum value allowed by the rotor converter.
2. The rotor current I_{r} must be lower than the maximum value allowed by the rotor converter.

V. Insulation, mechanical constraints

1. The stator slot-pitch $\tau_{s,\mathrm{s}}$: it has to be larger than a minimum insulation distance. This distance depends on the stator voltage amplitude and insulation system. This constraint is irrelevant regarding the rotor as the voltage amplitude is there much lower.
2. The maximum peripheral speed n_{periph}: it has to be lower than the maximum admissible value.

Note that this list does not include all the constraints. In practice there are also constraints relative to the lifting weight, the transport. The cost can also be a criteria, it is not considered here.

6.3.3 Definition of the optimization algorithm

Two main methods can be used to solve an optimization problem: the determinist methods and the stochastic methods. The fist category stands on the evaluation of the gradient of the objective function in order to orient the research of the solution. The Newton-Raphson method is an example of determinist method. Such method presents the advantage to converge

quickly, but not necessarily to the global optimum. Furthermore the obtained results are very sensitive to the initial solution. The second category is based on chance and probabilities. For example the evolutionist algorithms and more particularly the genetic algorithms is based on these principles. Contrarily to the first category, it can better converge to the the optimum solution and independently of the initial solution. However the number of necessary evaluations of the objective function is much larger.

Regarding our optimization problem, using a determinist method would require the knowledge of the objective function gradient. Wurtz [Wur96] in his thesis proposed an optimization tool, where the user defines with simple equations the electromagnetic behavior of the device to optimize. The determination of the gradient is done by the tool itself using standards derivation methods. The described principles are applied in the tool *Cades* [Del+07]. However, as shown in the previous chapters, the calculation of the efficiency will require the solving of several problems such as the calculation of the circuit parameters, the no-load characteristics calculation considering magnetic saturation or the calculation of the load operation point characteristics including the iron losses. These algorithms require often programing procedures including loops and test conditions. To solve this issue, Petre [Pet09] implemented in *Cades* a technique of automatic code derivation accepting such advanced programing procedure. Consequently the tool *Cades* and the determinist method appear as interesting solutions. Nevertheless, our problem contains several input parameters such as the number of slots, the number of strands or the number of parallel paths which have to be integer numbers. Unfortunately, the determinist method can not deal with such parameters so that it cannot be used for our study. On the contrary, the stochastic methods allow discrete parameters. These methods are even more interesting as evaluating our objective function is not at all time consuming, about 1.5 second. Consequently the previously denounced large number of necessary evaluations drawback is here irrelevant.

Finally we choose the stochastic method and more particularly the genetic algorithms. The implementation of the optimization problem, i.e. the inputs parameters with acceptable variation range, the objective function and the constraints, is made inside the dedicated optimization tool *FGOT* (G2Elab). The evaluation of the objective function according to the input parameters is done inside the Alstom calculation tool. The communication between both tools is managed by using a server based on an exchanged files protocol.

6.4 Application to the conversion of a synchronous machine to a double-fed induction machine

This part deals with the upgrade of an existing constant speed installation into a variable speed installation. The existing salient-pole synchronous machine parameters are given in Table 6.1. The characteristics of the created DFIM, i.e. the rated power, the stator voltage and the synchronous speed will remain the same. Firstly we only replace the salient pole rotor by a suitable three-phase winding wound rotor while the stator remains identical. Secondly we redesign totally the machine, i.e. the rotor and the stator, according to rated specifications. For

Rated apparent power S	230	MVA
Rated power factor $\cos\varphi$	0.90	
Rated stator voltage U_{s}	15.75	kV
Rated grid frequency f_{s}	50.0	Hz
Rated synchronous speed n_{s}	333.0	rpm
Number of poles $2p$	18	
Stator bore diameter $D_{\mathrm{b,s}}$	5400	mm
Stator core total length l_{s}	2750	mm
Airgap depth δ_{g}	28	mm
Number of stator winding slots $N_{\mathrm{z,s}}$	243	
Number of stator winding parallel paths $N_{\mathrm{a,s}}$	3	

Table 6.1: Example Machine Data 200-MVA Generator

Quantity	Type	Values
Number of rotor slots $N_{\mathrm{z,r}}$ (-)	Discrete	162,189,216,270,297
Number of rotor parallel circuit $N_{\mathrm{a,r}}$ (-)	Discrete	1,2,3,6
Number of strands in height per rotor bar $N_{\mathrm{st,r}}$ (-)	Discrete	$10, 11, \cdots, 49, 50$
Width of a rotor bar strand $w_{\mathrm{st,r}}$ (mm)	Continuous	$5 \rightarrow 10$
Height of a rotor bar strand $h_{\mathrm{st,r}}$ (mm)	Continuous	$2 \rightarrow 5$
Height of the rotor yoke $h_{\mathrm{y,r}}$ (mm)	Continuous	$200 \rightarrow 400$
Length of the minimal airgap δ_{g} (mm)	Continuous	$10 \rightarrow 30$

Table 6.2: Optimization 1: variable input parameters and variation intervals

each case, we solve an optimization problem using the software *FGOT* and the Alstom design tool.

6.4.1 Only the rotor is replaced

Table 6.2 defines the varying input parameters and the corresponding variation intervals. The possible values of the number of rotor parallel circuits and the number of rotor slots are determined considering the previously detailed symmetry conditions of a three-phase balance winding. For example, the rule $2p/N_{\mathrm{a,r}} \in \mathbb{N}$ is matched if only $N_{\mathrm{a,r}} \in [1, 2, 3, 6, 18]$. Note that it is unlikely to have 18 rotor paths as this would lead to a too complicated winding configuration; this solution is excluded. The current stator winding is a fractional slot winding with $qsOne = 9$ and $qsTwo = 2$. Considering the possible number of parallel paths, and reminding the rule $q_{\mathrm{s},2}/3 \notin \mathbb{N}$, we obtain $q_{\mathrm{s},2} \in [1, 2]$. Consequently we have $q_r = 1, 1.5, 2, 2.5, 3, 3.5, 4, 4.5, 5, 5.5, 6.5 \ldots$. Keeping only reasonable values we finally find $N_{\mathrm{z,r}} = 3 \cdot 2p \cdot [3, 3.5, 4, 4.5, 5, 5.5] = [162, 189, 216, 270, 297]$. The width and height of a rotor strand variation ranges are chosen based on experience as well as the rotor yoke height and the minimal airgap length.

Table 6.3 describes the operation point chosen for the evaluation of the design. This point

OP	P_{mec} (MW)	U_{s} (V)	$\cos\varphi$ (−)	s (%)	mode (−)
1	212	15.75	0.9	−5	over-excited

Table 6.3: Operation point for dimensioning

Quantity	Value
Number of rotor slots $N_{\mathrm{z,r}}$ (-)	216
Number of rotor parallel circuit $N_{\mathrm{a,r}}$ (-)	2
Number of strands in height per rotor bar $N_{\mathrm{st,r}}$ (-)	33
Width of a rotor bar strand $w_{\mathrm{st,r}}$ (mm)	7.9
Height of a rotor bar strand $h_{\mathrm{st,r}}$ (mm)	2.9
Height of the rotor yoke $h_{\mathrm{y,r}}$ (mm)	300
Length of the minimal airgap δ_{g} (mm)	13

Table 6.4: Optimization 1 results: main input parameters

is considered as the worst rated point. Indeed the stator winding has to carry in addition the rotor active power as it was shown in Chapter 3. Note that we did not consider a possible shift in stator voltage and frequency as mentioned in Chapter 3.

I. Optimization results

Table 6.4 lists the main parameter values obtained after solving of the optimization problem. One can see in particular that the chosen number of rotor slots is very close to the number of stator slots, indeed we have $q_{\mathrm{s}} = q_{\mathrm{r}} + 0.5$. One can also notice the large reduction of the airgap depth compared to the original synchronous machine.

Table 6.5 lists the main output values corresponding to the rated operation point. One can see in particular the large value of the electrical utilization factor. The large temperature rise of the stator and rotor windings and stator and rotor flux density are additional indicators of this high electrical and magnetic loading.

II. Comparison at no-load

Figures 6.4 and 6.5 show the flux density variation at no-load calculated at the middle of the airgap for both machines and Figure 6.6 compares the corresponding spatial harmonics content. One can observe in particular the presence of the rotor slots harmonics in the case of the DFIM ranks $= 23, 25$. The stator slot harmonics ranks $= 26, 28$ are more amplified in the case of the DFIM which is essentially due to the smaller airgap.

Figures 6.7 and 6.8 show the variation of the stator line-to-line voltages. Figure 6.9 compares the corresponding harmonic content. One can see that the harmonic amplitudes are very low in the case of the DFIM which is essentially due to the stator fractional slot winding which filters most harmonic and especially the slot harmonics.

Quantity	Value
Max airgap flux density $\hat{B}_{\delta}$ (T)	1.1
Max rotor teeth flux density $\hat{B}_{\mathrm{t,r}}$ (T)	1.9
Max rotor yoke flux density $\hat{B}_{\mathrm{y,r}}$ (T)	1.36
Max stator teeth flux density $\hat{B}_{\mathrm{t,s}}$ (T)	1.87
Max stator yoke flux density $\hat{B}_{\mathrm{y,s}}$ (T)	1.31
Max stator winding temperature rise ΔT_{s} (K)	87
Max rotor winding temperature rise ΔT_{r} (K)	51
Stator current density J_{s} (A/mm^2)	3.1
Rotor current density J_{r} (A/mm^2)	3.3
Rotor line-to line voltage U_{r} (V)	1382
Rotor current I_{r} (A)	9451.9
Electrical utilization C (MVAmin/m^3)	9.8
Efficiency η_{g} (%)	98.40

Table 6.5: Optimization 1 results: main output values

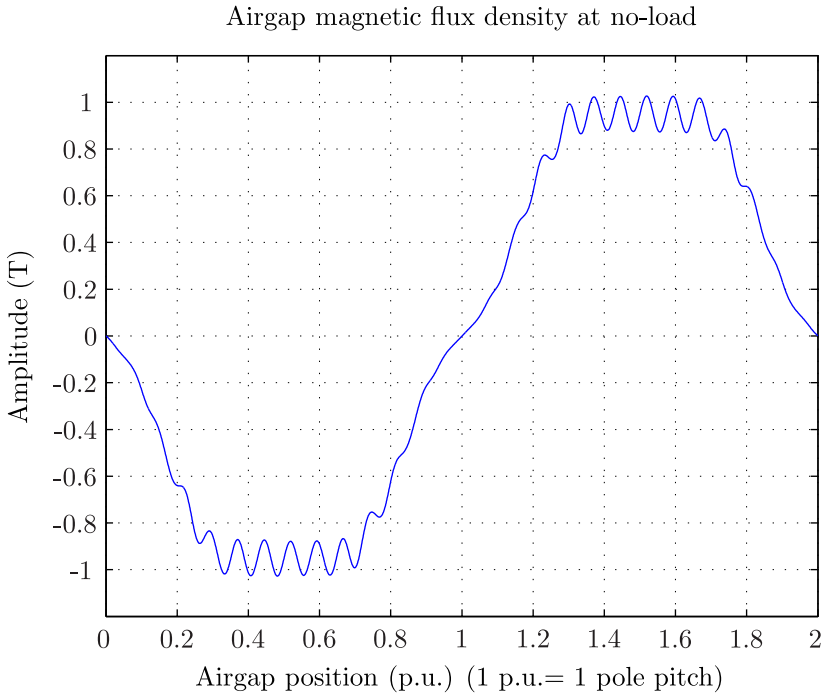

Figure 6.4: Airgap flux density of the salient pole synchronous machine at no-load

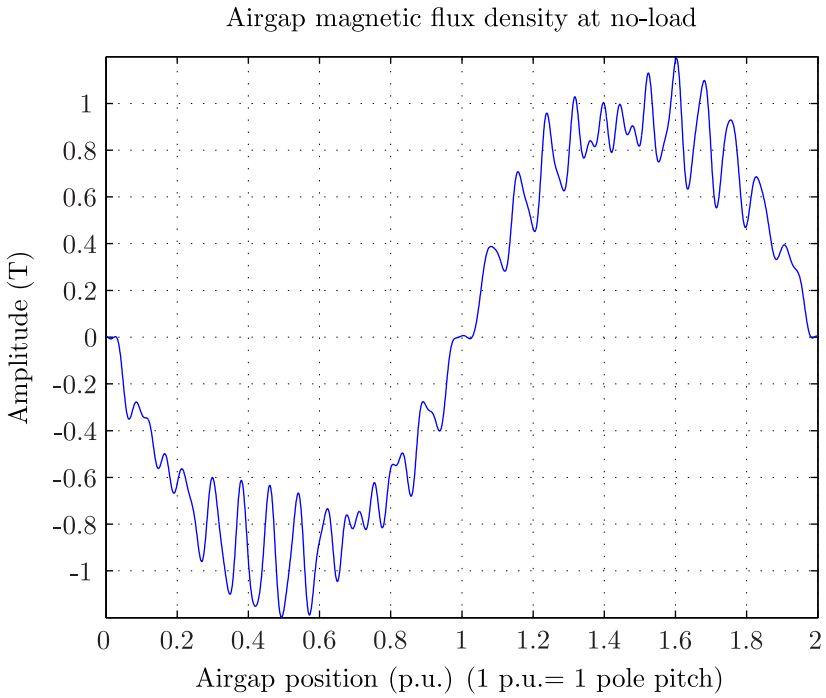

Figure 6.5: Airgap flux density of the double-fed induction machine at no-load

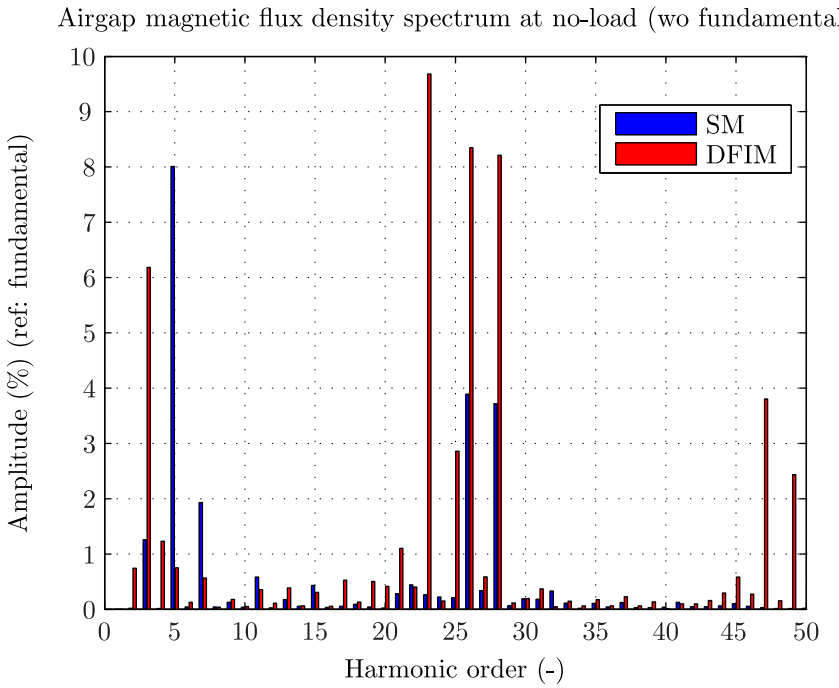

Figure 6.6: Airgap flux density spectrum comparison at no-load

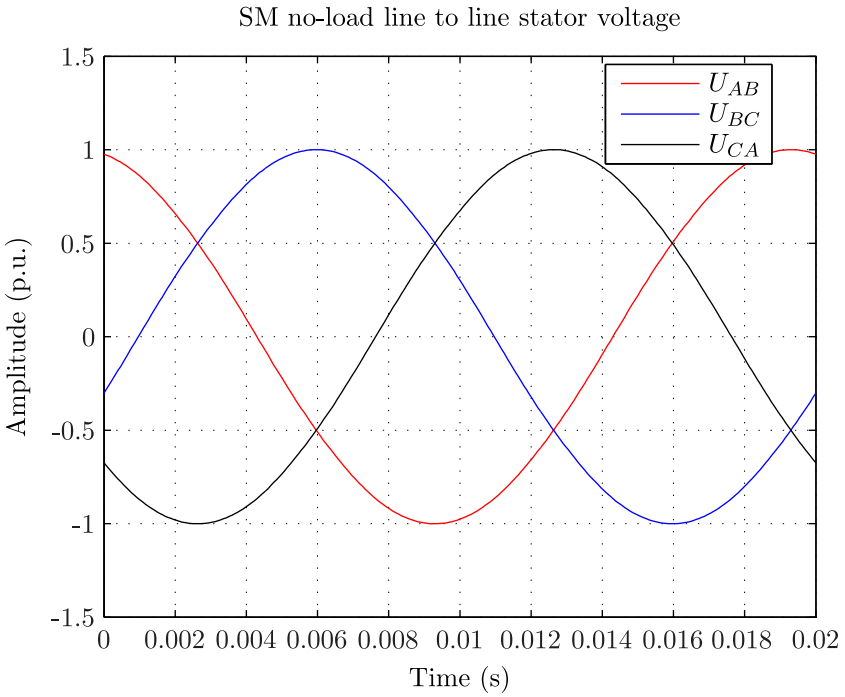

Figure 6.7: Stator line-to-line voltages of the salient-pole synchronous machine at no-load

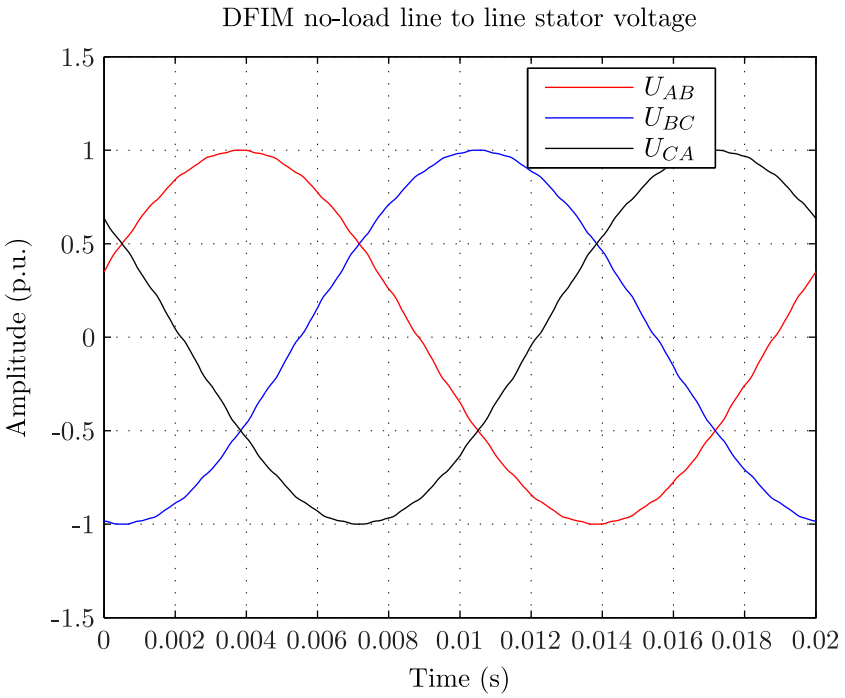

Figure 6.8: Stator line-to-line voltages of the double-fed induction machine at no-load

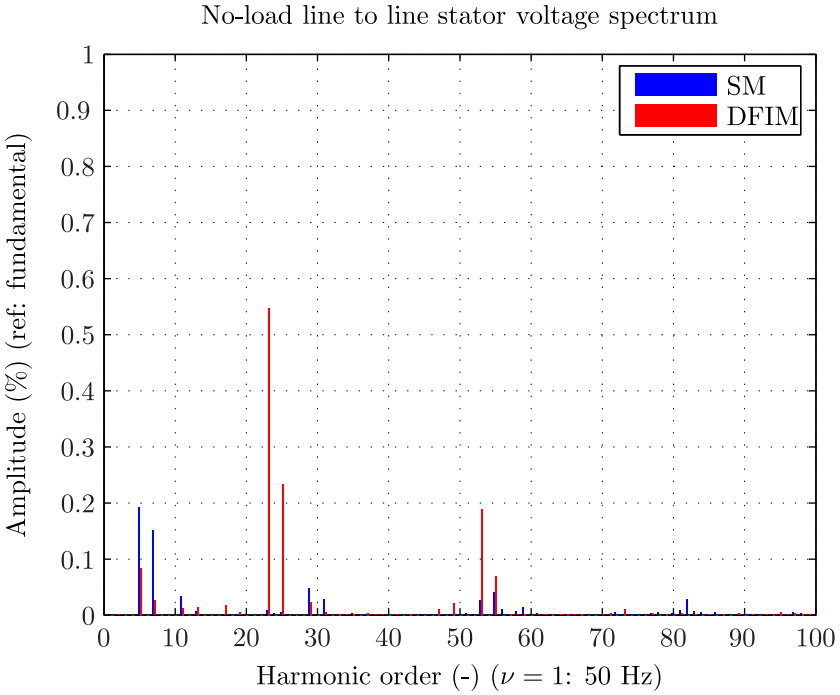

Figure 6.9: Stator line-to-line voltage spectrum comparison at no-load

Location	SM	DFIM
Stator teeth (W)	130000	138000
Stator yoke (W)	174000	180000
TOTAL (teeth+yoke) (W)	304000	318000

Table 6.6: Iron losses comparison at rated no-load operation (synchronous speed)

Table 6.6 compares the amount of iron losses in the stator teeth and yoke regions at no-load. One can see that the iron losses are slightly higher for the DFIM .

III. Comparison at load operation

Table 6.7 compares the amount of iron losses in the stator teeth and yoke regions at no-load. One can see that the iron losses are slightly higher for the DFIM.

6.4.2 The rotor and stator are both re-designed

We consider here the same rated characteristics as given in Table 6.1. However the parameters relative to the stator are not any more fixed which enables more flexibility for the design. The new parameter ranges are defined in Table 6.8.

Location	SM	DFIM
Stator teeth (W)	186000	202000
Stator yoke (W)	177000	209300
TOTAL (teeth+yoke) (W)	363000	411300

Table 6.7: Iron losses comparison at rated load operation (synchronous speed)

Quantity	Type	Values
Length of the minimal airgap δ_{g} (mm)	Continuous	$10 \rightarrow 30$
Stator bore diameter $D_{\mathrm{b,s}}$ (mm)	Continuous	$5 \rightarrow 6$
Stator core length l_{s} (mm)	Continuous	$2.5 \rightarrow 3.2$
Number of stator slots $N_{\mathrm{z,s}}$ (-)	Discrete	162,189,216,243,270,297
Number of stator parallel circuit $N_{\mathrm{a,s}}$ (-)	Discrete	1,2,3,6
Number of strands in height per stator bar $N_{\mathrm{st,s}}$ (-)	Discrete	$10, 11, \cdots, 49, 50$
Width of a stator bar strand $w_{\mathrm{st,s}}$ (mm)	Continuous	$5 \rightarrow 10$
Height of a stator bar strand $h_{\mathrm{st,s}}$ (mm)	Continuous	$2 \rightarrow 5$
Height of the stator yoke $h_{\mathrm{y,s}}$ (mm)	Continuous	$200 \rightarrow 400$
Number of rotor slots $N_{\mathrm{z,r}}$ (-)	Discrete	162,189,216,243,270,297
Number of rotor parallel circuit $N_{\mathrm{a,r}}$ (-)	Discrete	1,2,3,6
Number of strands in height per rotor bar $N_{\mathrm{st,r}}$ (-)	Discrete	$10, 11, \cdots, 49, 50$
Width of a rotor bar strand $w_{\mathrm{st,r}}$ (mm)	Continuous	$5 \rightarrow 10$
Height of a rotor bar strand $h_{\mathrm{st,r}}$ (mm)	Continuous	$2 \rightarrow 5$
Height of the rotor yoke $h_{\mathrm{y,r}}$ (mm)	Continuous	$200 \rightarrow 400$

Table 6.8: Optimization 2: variable input parameters and variation intervals

Quantity	Value
Length of the minimal airgap δ_{g} (mm)	16.75
Stator bore diameter $D_{\mathrm{b,s}}$ (mm)	5.42
Stator core length l_{s} (mm)	3.2
Number of stator slots $N_{\mathrm{z,s}}$ (-)	243
Number of stator parallel circuit $N_{\mathrm{a,s}}$ (-)	3
Number of strands in height per stator bar $N_{\mathrm{st,s}}$ (-)	30
Width of a stator bar strand $w_{\mathrm{st,s}}$ (mm)	9.5
Height of a stator bar strand $h_{\mathrm{st,s}}$ (mm)	1.9
Height of the stator yoke $h_{\mathrm{y,s}}$ (mm)	315
Number of rotor slots $N_{\mathrm{z,r}}$ (-)	216
Number of rotor parallel circuit $N_{\mathrm{a,r}}$ (-)	2
Number of strands in height per rotor bar $N_{\mathrm{st,r}}$ (-)	31
Width of a rotor bar strand $w_{\mathrm{st,r}}$ (mm)	10.0
Height of a rotor bar strand $h_{\mathrm{st,r}}$ (mm)	2.9
Height of the rotor yoke $h_{\mathrm{y,r}}$ (mm)	246

Table 6.9: Optimization 2 results: main input parameters

I. Optimization results

Table 6.9 lists the main parameter values after solving the optimization problem. One can observe that the chosen number of stator and rotor slots did not change between both optimizations. The stator bore diameter remains almost the same because of the constraint on the external diameter. The main change comes from the core length, the rotor and stator strands dimensions which lead to wider slots.

Table 6.10 lists the main output values computed for the rated operation point. The new core length leads to a large decrease of the maximum airgap flux density and consequently of the maximum stator and rotor tooth magnetic flux densities. One can also observe that stator and rotor winding temperature rise have significantly decreased. One can make the same comments on the stator and rotor current density. Finally all these elements lead to a lower magnetic and electrical loading of the machine.

II. Comparison at load operation

Table 6.11 compares the amount of iron losses for both designs under rated load operation at the rated minimum speed. One can observe a non-negligible decrease of the total losses especially because of lower magnetic loading in the stator and rotor core of the new design.

Quantity	Value
Max airgap flux density $\hat{B}_{\delta}$ (T)	0.94
Max rotor teeth flux density $\hat{B}_{\mathrm{t,r}}$ (T)	1.87
Max rotor yoke flux density $\hat{B}_{\mathrm{y,r}}$ (T)	1.39
Max stator teeth flux density $\hat{B}_{\mathrm{t,s}}$ (T)	1.84
Max stator yoke flux density $\hat{B}_{\mathrm{y,s}}$ (T)	1.12
Max stator winding temperature rise ΔT_{s} (K)	73
Max rotor winding temperature rise ΔT_{r} (K)	44
Stator current density J_{s} (A/mm^2)	2.57
Rotor current density J_{r} (A/mm^2)	2.75
Rotor line-to line voltage U_{r} (V)	1390
Rotor current I_{r} (A)	9372
Electrical utilization C (MVAmin/m^3)	8.31
Efficiency η_{g} (%)	98.4

Table 6.10: Optimization 2 results: main output values for the first design

Location	DFIM1	DFIM2
Stator teeth (W)	203000	180000
Stator yoke (W)	209000	181000
Rotor teeth (W)	143000	120000
Rotor yoke (W)	23000	20000
TOTAL (W)	578000	493000

Table 6.11: Iron losses comparison at rated load operation (hypo-synchronous speed)

Nodes (−)	σ_r (N/m^2)	F_{elec} (Hz)	F_{eig} (Hz)
0	64	300	275
0	122.2	285	275
36	65	1325	1226
36	62	1340	1226
36	335	1240	1226

Table 6.12: Parasitic forces at rated load operation and minimum speed

III. Calculation of parasitic radial electromagnetic forces

Note that in the studied case, given the stator and rotor possible windings, the risk of vibration due to the mmf subharmonics as shown as example in Chapter 5 which is the most dangerous, is not possible. Therefore we did not include the risk of vibration as a criteria. Other problems could also arise, because of other winding harmonics or because of slot ripples harmonics for example. In the future we could set a constraint on the risk of vibration. Indeed this risk of vibration can be estimated first by comparing the existing parasitic forces to the eigen-modes of the stator and then by sorting the obtained dangerous forces according to the amplitude and the distance from the exciting frequency to the eigen-frequency. Of course this assumes to have a very accurate analytical model describing the stator eigen-frequencies. If it is possible to detect accurately the risk of resonance because of a 100 Hz or 120 Hz magnetic excitation, it becomes more difficult when dealing with higher frequency problems, such as 700 Hz to 1000 Hz.

Finally from the new design, we apply the methodology presented in Chapter 5 to extract the dangerous radial electromagnetic forces. Table 6.12 lists the potential dangerous forces. Note that for each component, we detail the amplitude, the exciting frequency F_{elec} and the eigen-mode frequency F_{mec} corresponding to the number of nodes. Most existing forces are two small in amplitude to represent a danger. The most dangerous force appears to be the component (36-node, 1240 Hz). This component is mainly due to interaction between the stator slot harmonics and the rotor slot harmonics and its frequency depends on the slip. However given the amplitude of the force it should not be a problem.

6.5 Conclusion

This part described a methodology used to determine the main dimensions and rated characteristics of a DFIM. In order to take into account all the existing constraints due to thermal, mechanical, manufacturing, converter rating limitations, it is proposed to formulate the designing of the machine as an optimization problem. The stochastic method and more particularly the genetic algorithm method is used to solve the defined constraint problem. Indeed it allows to manage discrete parameters such as the number of slots, number of parallel paths or number of strands per bar. The special case of the upgrading of a standard constant speed installation to an equivalently rated variable speed installation was treated into two steps.

In the first step, the stator of the existing salient-pole synchronous motor/generator was kept whereas the rotor was replaced with a three-phase winding rotor. This made it possible to compare on the same basis both technologies and to demonstrate that the DFIM introduces more harmonics responsible for higher iron losses and higher torque harmonics.

In the second step, both the stator and the rotor were re-designed. This made it possible to obtain a safer design on the thermal side and to allow an higher flexibility in the choice of the parameters value. It should be noted, that in reality, the complete re-design will be more likely, as it will allow an increase of the rating of the machine and in particular of the output power.

Using an optimization tool as a help for dimensioning makes it possible to determine in a fast way the main parameters of the machine. However one should add that, the optimization tool does not replace the work of the engineer. Indeed the setting of the constraints, the choice of the input variation intervals can not be done without a clear knowledge about rotating machines design and the operating behavior of the studied machine. Furthermore to be more complete, the optimization should include in future the cost of the machine as well as materials sourcing and additional manufacturing constraints.

7 Final conclusion and perspectives

7.1 Final conclusion

The objectives of the thesis were firstly to better understand the operation of the doubly-fed induction machine and secondly to propose efficient methods to study and predict its electromagnetic performances.

Firstly the presented work contributes to a better knowledge and to an improvement of the techniques of analytical and numerical modeling. Chapters 2, 3 and 4 have presented and validated an analytical model. This model considers several phenomena such as the saturation of the stator and rotor magnetic circuit, the stator and rotor winding harmonics and the airgap permeance harmonics, which affect the performances of the machine. In particular, an original approach based on the boundary element method modeling the double-slotted airgap of the machine was presented; this made it possible to accurately define the main generated airgap flux density harmonics. This approach was combined with the definition of the magneto-motive forces generated by the stator and rotor winding and with the exploitation of a simplified magnetic network considering the magnetic voltage drop inside the stator and rotor core. The resulting airgap flux density harmonics could be calculated for various steady-state load conditions thanks in one hand to the definition of an equivalent scheme as well as its parameters and in the other hand to the resolution of its characteristics equations. The validation of the model was done step by step by carrying out finite element computations. In order to reduce the initialization time of those computations, an unconventional method implementing a regulation of the double-fed induction machine inside the finite element simulation was described. This method enabled not only to simulate more efficiently the behavior of the machine under various operation conditions such as no-load and load conditions but also later to deal with elements such as dynamic torques or emitted parasitic harmonics on the network.

Secondly the developed models make it possible to identify and to quantify the potential risks of an electromagnetic design. Chapter 5 studied diverse subjects such as the stator voltage harmonics, the parasitic radial forces, the dynamic torques or the iron losses. It was demonstrated how such elements impact the performance of the machine and the importance to consider them during electromagnetic design phase.

Eventually based on the studies above, Chapter 6 proposed one methodology to obtain an efficient design of the double-fed induction machine using an optimization algorithm. This methodology was successfully applied on the upgrading of an existing conventional synchronous alternator. This enabled to compare both conventional design and upgrade, as well as to highlight the relevance of using an optimization algorithm.

7.2 Perspectives

The thesis covered a wide range of subjects. The experience acquired during the present work makes it possible to identify possible future investigations and improvements.

Firstly the airgap permeance harmonics were efficiently extracted by using a boundary element model of the double-slotted airgap while the additional harmonics due to magnetic saturation were simply included by adding a correction to the linear airgap permeance. However a direct coupling between this boundary element model and a detailed magnetic permeance network was fully described and compared with FE results. Satisfying results were obtained which demonstrates a potential way of improvement for the future. Proceeding this way would make it possible to better describe the effect of magnetic saturation of airgap flux density harmonics in load operation and consequently to compute more accurately parasitic forces and iron losses.

Secondly the coupling between the FE simulation and its regulation should be further studied. It was already shown that it is possible to simulate several operation modes such as no-load or load condition but also transient operations such as the start-up of the machine. A simplified model of the converter could be included during the no-load operation in order to quantify the harmonic content of the stator voltage. This could be extended to load operation or start operation in order to study the impact of the converter harmonics on electromagnetic parasitic torques or radial forces.

Finally Chapter 6 has shown the benefit of using an optimization algorithm when designing the machine. As mentioned before, the setting of the constraints, the choice of the input variation intervals can not be done without a clear knowledge about rotating machine design and the operating behavior of the studied machine. However such methods arise as a non-negligible help when looking for the main parameters of the design and could be further exploited to consider other elements such as ventilation and cooling performances. Furthermore, the credibility of the optimization results will become even higher after acquiring more experimental data contributing to the validation of the model.

Nomenclature

List of Indices

ac	alternative-current
c	rotor converter
d	d-axis
dc	direct-current
δ	airgap
f	fundamental
g	gap
i	tooth region
j	phase
μ	magnetizing
n	network
ν	harmonic rank
q	q-axis
r	rotor,radial component
s	stator, synchronous
st	slot
st	strand
t	tooth, tangential component
x	x-coordinate
y	yoke, y-coordinate

List of Symbols

A	magnetic vector potential
α	airgap angular position

A_ν	harmonic amplitude
B	magnetic flux density
B_δ	airgap flux density
B_t	tooth flux density
B_y	yoke flux density
C	electrical utilization
χ_ov	overhang inclination angle
C_ν	harmonic phase shift
$\cos_\varphi$	power factor
$D_\mathrm{b,r}$	rotor outer diameter
$D_\mathrm{b,s}$	stator inner diameter
δ_g	airgap length
ΔT	temperature rise
η	efficiency
f	frequency
F_eig	stator eigen mode frequency
F_elec	excitation force frequency
F_ν	harmonic frequency
g	gravitation constant
Γ	torque
H	magnetic field strength, water head
$h_\mathrm{b,ni}$	height of the non insulated bar
h_s	slot height
h_st	strand height
h_y	yoke height
I	current
J	current density
k_c	Carter coefficient

$\mathrm{k_m}$	mean eddy-current loss coefficient of the whole stator or rotor winding
$\mathrm{k_r}$	mean eddy-current loss coefficient of the all strands belonging to the stator or rotor core
L	inductance
λ	leakage inductance coefficient
Λ_p	airgap permeance
Λ_c	airgap permeance of a constant airgap
Λ_0	airgap permeance with constant airgap corrected with Carter coefficient
l_b	bar length
l_c	core length
l_f	effective iron length
L_h	main inductance
l_i	ideal length
l_ov	overhang length
L_σ	leakage inductance
μ	magnetic permeability
μ_0	vacuum magnetic permeability
n	rotational speed
N_a	number of parallel paths
N_d	number of cooling air ducts
N_s	number of series turns
n_s	rotational synchronous speed
N_st	number of strands in the bar height
N_z	number of slots
P	active power
p	number of pole-pairs
$\mathrm{p_c}$	copper losses
Φ	magnetic flux, field function
φ	phase shift angle

$\mathrm{p_i}$	iron losses
P_{mec}	mechanical power
P_ν	harmonic pole-pairs number
Ψ	field function
Q	reactive power
Q	water volume flow
q	number of slots per pole and phase
q_2	denominator of q
q_1	numerator of q
R	resistance
R_{b}	bar resistance
s	slip, winding coil opening
σ_{r}	radial electromagnetic stress
τ_{p}	pole pitch
τ_{s}	slot pitch
Θ	magneto-motive force
θ_0	initial phase shift between stator and rotor magnetic fields
$\hat{U}_{\mathrm{m}}$	magnetic potential drop
$w_{\mathrm{b,ni}}$	width of the non insulated bar
w_{d}	duct width
w_{s}	slot width
w_{st}	strand width
w_{t}	tooth width
X	reactance
X_{h}	main reactance
ξ_ν	winding coefficient
ξ_{st}	reduced strand height
Y_1	winding coil pitch
Z	impedance

Bibliography

[Alg51] P. L. Alger. *The NATURE of POLYPHASE INDUCTION MACHINES*. 1951 (cit. on pp. 47, 54).

[ALP08] W. M. Arshad, H. Lendenmann, and H. Persson. 'End-Winding inductances of MVA machines through FEM computations and IEC-Specified Measurements'. In: *IEEE transactions of industry applications* 44 (Nov. 2008) (cit. on pp. 16, 51).

[Ard+13] G. H. Ardley, M. W. Spiridon, T. Lugand, and A. Schwery. 'Parasitic Forces, Noise & Vibration in Hydroelectric Generators'. In: HydroVision. 2013 (cit. on pp. 154, 161).

[BD92] C. A. Brebbia and J. Dominguez. *Boundary elements - an introductory course*. Ed. by WITPress. Southampton (UK), 1992 (cit. on pp. 91, 113).

[Bel82] A. Belot. 'Calcul des fuites et inductances de fuites de l'induit'. In: *Techniques de l'ingénieur* sd440 (1982) (cit. on pp. 47 sq.).

[Ber88] Giorgio Bertotti. 'General properties of power losses in soft ferromagnetic materials'. In: *Magnetics, IEEE Transactions on* 24.1 (1988), pp. 621–630 (cit. on p. 196).

[Bes08] J. Le Besnerais. 'Reduction of magnetic noise in PWM-supplied induction machines-low-noise design rules and multi-objective optimisation'. PhD thesis. Laboratoire d'Electricité et d'Electronique de Puissance de Lille, Ecole centrale de Lille, Nov. 2008 (cit. on pp. 141, 144, 183).

[Bra92] A. Taieb Brahimi. 'Contribution à la modélisation de la machine asynchrone à cage par logiciels d'éléments finis 2d et 3d'. PHD. INPG, Juin 1992 (cit. on p. 51).

[Bru97] J.F. Brudny. 'Modélisation de la denture des machines asynchrones. Phénomène de résonance'. In: *Journal Physique* (1997), pp. 1009–1023 (cit. on pp. 82, 90, 99).

[Can67] I.M. Canay. 'Procédés de démarrage des machines asynchrones'. In: *Revue Brown Boveri* (Sept. 1967) (cit. on p. 8).

[Can83] I.M. Canay. 'Determination of model parameters of synchronous machines'. In: *Electric Power Applications, IEE Proceedings B* 130.2 (1983), pp. 86–94 (cit. on p. 16).

[Car+06] R. Carlson, H. Voltolini, F. Runcos, and P. Kuo-Peng. 'A performance comparison between brush and brushless doubly fed asynchronous generators for wind power systems'. In: *ICREPQ* 2 (2006) (cit. on p. 11).

[Car12a] R. Carvalhal. *Radial Stator Natural Frequencies and Mode Shapes Calculation*. Tech. rep. ALSTOM Internal report, Dec. 2012 (cit. on pp. 146, 148, 153).

[Car12b] R. Carvalhal. 'Radial stator vibration investigation'. Nov. 2012 (cit. on pp. 146 sq.).

[Ced13] Cedrat. *Flux user manual*. 2013 (cit. on pp. 70, 111).

[Cha80] J.C. Chatelain. *Machines Electriques, Traite d'electricite, Volume X*. 1980 (cit. on pp. 6, 8, 54, 74).

[CJ00] S.S. Choi and X. M. Jia. 'Under excitation limiter and its role in preventing excessive synchronous generator stator end-core heating'. In: *Power Systems, IEEE Transactions on* 15.1 (2000), pp. 95–101 (cit. on p. 67).

[Cou98] J. Coulon. 'Alternateurs synchrones à vitesse variable pour centrales hydrauliques'. In: *SEE club 12* (Mar. 1998) (cit. on p. 216).

[Del+07] B. Delinchant, D. Duret, L. Estrabaut, L. Gerbaud, H. Nguyen Huu, B. Du Peloux, H.L. Rakotoarison, and F. Wurtz F. Verdiere. 'An optimizer using the software component paradigm for the optimization of engineering systems'. In: *COMPEL, The International Journal for Computation and Mathematics in Electrical and Electronic Engineering*. Vol. 26. 2007, pp. 368–379 (cit. on pp. 108, 224).

[DO10] T. P. DO. 'Simulation dynamique des actionneurs et capteurs électromagnétiques par réseaux de réluctances : modèles, méthodes et outils'. PHD. INPG, G2ELAB, 2010 (cit. on p. 108).

[Fer13] Y. Ferland. *Winding connection study*. Calculation sheet. Internal report Alstom, 2013 (cit. on p. 175).

[Fog99] A. Foggia. 'Méthodes de calcul des inductances de fuites'. In: *Techniques de l'ingénieur* D6 (1999) (cit. on pp. 46–48).

[Gau05] T. Gautreau. 'Estimation des pertes fer dans les machines électriques. Modèle d'hysteresis loss surface et application aux machines synchrones à aimants'. PHD. Laboratoire d'electrotechnique de Grenoble, INPG, Décembre 2005 (cit. on pp. 196, 204, 214).

[Gre94] D. A. Green. 'Generating more efficiently with adjustable-speed machineS'. In: *Hydro Review* (1994) (cit. on p. 15).

[Gue94] C. Guerrin. 'Determining of eddy current losses in the transformers curves – Modeling of narrow regions and taking into consideration of magnetic materials in harmonic regime'. PHD. INPG, 1994 (cit. on p. 70).

[GWE12] GWEC. *Global Wind Report Annual Market Update*. Tech. rep. GWEC: Global Wind Energy Council, 2012 (cit. on p. 1).

[Hod04] A. Hodder.
'Double-Fed asynchronous motor-generator equipped with a 3-level VSI cascade'.
PHD. EPFL, Lausanne, 2004 (cit. on pp. 16, 75).

[Hub01] A. Hubert. 'Contribution à l'étude des bruits acoustiques générés lors de l'association machines électriques-convertisseurs de puissance. Applcation à la machine asynchrone'. PHD. UTC, Jan. 2001 (cit. on p. 144).

[Kan05] S. Kanerva. 'Simulation of electrical machines, circuits and control systems using Finite Element Method and circuit cimulator.'
PhD thesis. Helsinki University of Technology, Department of Electrical and Communications Engineering, Laboratory of Electromechanics, 2005
(cit. on p. 74).

[Kro31] G. Kron. 'Induction Motor Slot Combinations Rules to Predetermine Crawling, Vibration, Noise and Hooks in the Speed-Torque Curve'. In: *American Institute of Electrical Engineers, Transactions of the* 50.2 (1931), pp. 757–767
(cit. on pp. 90, 219).

[Kuc] Z. M. Kuchinskaia. 'New design of hydrogenerator poles'.
In: *International conference on renewable energies and power quality* ()
(cit. on p. 67).

[KXS06] S. Keller, M. Tu Xuan, and J-J. Simond. 'Computation of the no-load voltage waveform of laminated salient-pole synchronous generators'.
In: *Industry Applications, IEEE Transactions on* 42.3 (2006), pp. 681–687
(cit. on p. 16).

[LH93] H.W. Lorenzen and H.G Herzog.
The describing system of equations of a doubly-fed, symmetrical integral slot winding three-phase induction machine being triple-phase in stator and rotor.
Tech. rep. 539.
Chair for Electrical Machines, Institute of Technology Munich, Jan. 1993
(cit. on pp. 17, 59).

[Lia96] Y. Liao. 'Design of a brushless doubly-fed induction motor for adjustable speed drive applications'. In: *Industry Applications Conference, 1996. Thirty-First IAS Annual Meeting, IAS '96., Conference Record of the 1996 IEEE.* Vol. 2. 1996, 850–855 vol.2 (cit. on p. 11).

[Liu09] Y. Liu. *Fast Multipole Boundary Element Method: Theory and Applications in Engineering.* 2009 (cit. on pp. 91, 121).

[Lor09] H. W. Lorenzen. *DASM – magnetisch verursachtes Geräusch : mechanische Radialspannungen im Luftspalt.* Tech. rep.
Institut für Energietechnik, Technische Universität München, 2009 (cit. on p. 17).

[Lor11] H. W. Lorenzen. *Verfahren zur analytischen Berechnung der Eigen-frequenzen des Statoreisenkörpers von DASM mechanische Eigenfrequenzen des Statorblechkörpers.* Tech. rep.
Institut für Energietechnik, Technische Universität München, 2011 (cit. on p. 17).

[Lor96a] H. W. Lorenzen. *Bemessung des magnetischen Kreises leerlaufender, 3-strängiger doppelt gepeister Drehstromasynchronmotoren.* Tech. rep. 605.
Institut für Energietechnik, Technische Universität München, 1996 (cit. on p. 16).

[Lor96b] H. W. Lorenzen. *Die Berechnung der Verluste in Drehstromasynchronmotor mit Kurzschlussankerwicklung.* Tech. rep. 609.
Institut für Energietechnik, Technische Universität München, 1996 (cit. on p. 17).

[Lor97] H.W. Lorenzen. *Die Bestimmung der Betriebspunkte einer DASM unter Berücksichtigung der Eisenverluste, Zusatzverluste und der Stromverdrängung.* Tech. rep. 650.
Institut für Energietechnik, Technische Universität München, Dec. 1997 (cit. on pp. 16, 59).

[Lor98] H. W. Lorenzen. *Grundlagen zur Bestimmung des Arbeitspunktes oder des BetrieBetriebspunkte einer DASM mit DUR im Rotorkreis.* Tech. rep. 613.
Institut für Energietechnik, Technische Universität München, 1998 (cit. on pp. 16, 37).

[LW61] M. Liwschitz-Garik and C.C. Whipple. *Alternating current machines.* 1961 (cit. on p. 44).

[McM+06] R.A. McMahon, P.C. Roberts, X. Wang, and P.J. Tavner. 'Performance of BDFM as generator and motor'.
In: *Electric Power Applications, IEE Proceedings* - 153.2 (2006), pp. 289–299 (cit. on p. 11).

[Mil10] T.J.E. Miller. 'Theory of the doubly-fed induction machine in the steady state'.
In: *Electrical Machines (ICEM), 2010 XIX International Conference on.* 2010, pp. 1–6 (cit. on pp. 16, 37).

[Mul06] M. Muller-Feugga. 'Study of a 200 MVA DFIM with Flux2d'.
MA thesis. INPG Grenoble, 2006 (cit. on p. 17).

[NK88] N. Nose and N. Kondo. 'The Ohkawachi pumped-storage scheme in Japan'.
In: *Water Power and Dam Construction* (1988) (cit. on p. 15).

[Paj12] P. Pajaczkowski. *Shaft line calculation Hydro Power Plant.* Tech. rep.
Internal report Alstom, 2012 (cit. on p. 188).

[Pan10] Y. Pannatier. 'Optimisation des stratégies de réglage d'une installation de pompage-turbinage à vitesse variable'. PHD. EPFL, Lausanne, 2010 (cit. on pp. 16, 135, 191).

[Pel06] B. du Peloux de Saint Romain.
'Modélisation des actionneurs électromagnétiques par réseaux de reluctances. Création d'un outil métier dédié au prédimensionnement par optimisation'.
PHD. Laboratoire d'electrotechnique de Grenoble, INPG, Oct. 2006
(cit. on pp. 108, 111).

[Per02] J. Perho. 'Reluctance network for analysing induction machines'.
PHD. Laboratory of Electromechanics, Helsinky university of technology, 2002
(cit. on pp. 108 sq., 111, 113).

[Pet05] A. Petersson.
'Analysis, and Control of Doubly-Fed Induction Generators for Wind Turbines'.
PhD thesis. Chalmers university of technology, Göteborg, Sweden, 2005
(cit. on p. 16).

[Pet08] D. Petrichenko. 'Contribution la la modélisation et à la conception optimale des turbo-alternateurs de faible puissance'.
PhD thesis. L2EP Ecole Centrale de Lille, Décembre 2008
(cit. on pp. 71, 108, 111, 113).

[Pet09] E. Petre. 'Dérivation Automatique pour le calcul des sensibilités appliqué au dimensionnement en génie électrique'. PhD thesis. INPG, 2009 (cit. on p. 224).

[PJH08] J. Pyrhonen, T. Jokinen, and V. Hrabovcov.
Design of rotating electrical machines. 2008 (cit. on pp. 27, 31, 48).

[Poz+02] J. Poza, A. Foggia, E. Oyarbide, and D. Roye.
'Brushless Doubly fed Machine Model'. In: ICEM. 2002 (cit. on p. 11).

[Ram03] C. Ramirez.
'Plate-forme numérique d'éssais pour machines électriques de puissance'.
PhD thesis. EPFL, 2003 (cit. on pp. 16, 31).

[Ran+09] M. Ranlöf, A. Wolfbrandt, J. Lidenholm, and U. Lundin. 'Core Loss Prediction in Large Hydropower Generators: Influence of Rotational Fields'.
In: *Magnetics, IEEE Transactions on* 45.8 (2009), pp. 3200–3206
(cit. on pp. 16, 196, 205).

[Ric97] S. Richard. 'Etude électromagnétique des parties frontales des alternateurs en régimes permanents et transitoires'. PhD thesis. INPG, 1997
(cit. on pp. 16, 48, 51).

[Rie09] S. Rieck. *Vibration Analysis of the Stator Structure*. Tech. rep.
Internal report Alstom, 2009 (cit. on pp. 144, 146).

[Rob04] P.C. Roberts. 'A study of brushless doubly-fed (Induction) Machines'.
PhD thesis. Emmanuel College, University of Cambridge, Sept. 2004
(cit. on p. 16).

[Sch] A. Schwery. 'Commutable poles machines (Alstom document)'. In: (cit. on p. 10).

[Sch+05] A. Schwery, E. Fass, J-M. Henry, W. Bach, and A. Mirzaian. 'Pump Storage Power Plants, ALSTOM's long experience and Technological Innovation'. In: Hydro. 2005 (cit. on pp. 3, 5 sq., 12 sq.).

[Sch06] A. Schwery. 'Varspeed Pump Storage Power Plants: Technology and Operation'. In: IEEE presentation. Feb. 2006 (cit. on pp. 2, 7, 11).

[SF97] S.Williamson and A.C. Ferreira. 'Generalised theory of the brushless doubly-fed machine. 2. Model verification and performance'. In: *Electric Power Applications, IEE Proceedings* - 144.2 (1997), pp. 123–129 (cit. on p. 11).

[SFW97] S.Williamson, A.C. Ferreira, and A. K. Wallace. 'Generalised theory of the brushless doubly-fed machine. I. Analysis'. In: *Electric Power Applications, IEE Proceedings* - 144.2 (1997), pp. 111–122 (cit. on p. 11).

[Sil94] V. C. Silva. 'Etude tridimensionnel par éléments finis des effets d'extrémités dans des parties frontales des machines synchrones'. PHD. LEG INPG, 1994 (cit. on pp. 16, 48, 51).

[SS97] D. Schafer and Prof. J-J. Simond. 'Advantages for the Electric Grid using a Doubly Fed Asynchronous Machine-Numerical simulations'. In: Hydropower. 1997 (cit. on pp. 3, 16).

[STS06] E. Schmidt, G. Traxler-Samek, and A. Schwery. '3d nonlinear transient finite element analysis of edd ccurrent in the stator clamping system of large hydrogenerators'. In: *COMPEL: The International Journal for Computation and Mathematics in Electrical and Electronic Engineering* 25.2 (2006) (cit. on p. 68).

[SV96] J. Schwanda and H. Voegele. 'Rotor of an electric machine'. EP0736953. 1996 (cit. on p. 13).

[Swi09] SwissGrid. *Transmission Code 2010*. Tech. rep. SwissGrid, Nov. 2009 (cit. on p. 62).

[TA09] G. Traxler-Samek and G. Ardley. 'Iron losses in salient-pole synchronous machines considering unidirectional and elliptic magnetization'. In: *Advanced Electromechanical Motion Systems Electric Drives Joint Symposium, 2009. ELECTROMOTION 2009. 8th International Symposium on*. 2009, pp. 1–6 (cit. on pp. 16, 196, 205 sq., 208).

[Tag08] D. Taghezout. *Rotor Slot Harmonics in a DFIM*. Tech. rep. Applied Magnetics, 2008 (cit. on p. 135).

[Tag11] D. Taghezout. *3D FEM Computation of End Windings Forces. Application to the Induction Machine 'Linthal Limmern'*. Tech. rep. Applied Magnetics, 2011 (cit. on pp. 51–53).

[TD08] D. Taghezout and G. Dutoit.
ALSTOM POWER Doubly Fed Induction Machine (DFIM). Tech. rep.
Applied Magnetics, 2008 (cit. on p. 50).

[TLS10] G. Traxler-Samek, T. Lugand, and A. Schwery. 'Additional Losses in the Damper Winding of Large Hydrogenerators at Open-Circuit and Load Conditions'.
In: *Industrial Electronics, IEEE Transactions on* 57.1 (2010), pp. 154–160
(cit. on pp. 16, 105).

[TLU12] G. Traxler-Samek, T. Lugand, and M. Uemori. 'Vibrational forces in Salient Pole synchronous machines considering tooth ripple effects'.
In: *IEE Transactions on industrial electronics* 59.5 (2012), pp. 2258–2266
(cit. on pp. 16, 89, 141, 155, 160, 173).

[Tra03] G. Traxler-Samek.
'Zusatzverlust im Stirnraum von Hydogeneratoren mit Roebelstabwicklung'.
PhD thesis. Technischen Universität Wien, Fakultät für Elektrotechnik und Informationstechnik, 2003 (cit. on pp. 16, 42).

[TSS03] G. Traxler-Samek, A. Schwery, and E. Schmidt.
'Analytic calculation of the voltage shape of salient pole synchronous generators including damper winding and saturation effects'.
In: *COMPEL: The International Journal for Computation and Mathematics in Electrical and Electronic Engineering* 22 (2003), pp. 1126–1141
(cit. on pp. 16, 105).

[TZS10] G. Traxler-Samek, R. Zickerman, and A. Schwery. 'Cooling Airflow, Losses, and Temperatures in Large Air-Cooled Synchronous Machines'.
In: *IEEE transactions on industrial electronics* 57 (2010), pp. 172–180
(cit. on pp. 16, 222).

[VB94] S.P. Verma and A. Balan. 'Determination of radial-forces in relation to noise and vibration problems of squirrel-cage induction motors'.
In: *IEEE transactions on energy conversion* 9.2 (1994), pp. 404–412
(cit. on p. 141).

[Vog96] K. Vogt. *Berechnung elektrischer Maschinen.* 1996 (cit. on p. 153).

[Wal81] J. H. Walker. *Large synchronous machines Design, Manufacture, and Operations.* Oxord University Press, New York, 1981 (cit. on p. 219).

[Wit98] W. Witt. *Doppelt gepesite Asynchronmaschine, Berechnung zur Berücksichtigung der Sättigung.* Tech. rep. 670.
Institut für Energietechnik, Technische Universität München, 1998 (cit. on p. 17).

[WK60] J. Walker and N. Kerruish. 'Open-circuit noise in synchronous machines'. In: *Proceedings of the IEE - Part A: Power Engineering* 107.36 (1960), pp. 505–512
(cit. on pp. 16, 155, 169).

[Wur96] F. Wurtz. 'Une nouvelle approche pour la conception sous contraintes de machines électriques'. PhD thesis. INPG, May 1996 (cit. on pp. 27, 224).

[Xua76] M. Tu Xuan. 'Machines synchrones à poles saillants commutables'. PHD. EPFL, 1976 (cit. on p. 8).

[Yao06] L. Yao. 'Magnetic field modelling of machine and multiple machine systems using dynamic reluctance mesh modelling'. PHD. University of Nottingham, May 2006 (cit. on p. 113).

Contribution to the Modeling and Optimization of the Double-Fed Induction Machine for Pumped-Storage Hydro Power Plant Applications

Abstract Pumped-storage hydro power plants have been mainly working with fixed-speed synchronous motor-generators. However, using variable-speed machines and more particularly, Double-Fed Induction Machines (DFIM) brings many benefits: control of the power in pump mode, operation at the best efficiency point in turbine mode, higher stability in case of a perturbation. This work improves the knowledge of the electromagnetic behavior of the DFIM and proposes an optimization process of its design. The first part develops an analytical model standing mainly on the boundary element method and validates it using finite element simulations. This model makes it possible to consider several phenomena such as the magnetic circuit saturation, the harmonics generated by the stator and rotor windings and also the harmonics due to the doubly-slotted airgap. The second part applies the developed model to four subjects of interest for the machine designer: study of the no-load stator-voltage shape, calculation of the iron losses, electromagnetic torque harmonics and radial electromagnetic forces. Finally, the third part studies the dimensioning of the DFIM by using a genetic optimization algorithm. The process is applied to the transformation of an existing salient-pole synchronous machine into a DFIM. Two cases are treated: first, only the rotor is replaced while the stator remains unchanged and second, the machine is completely redesigned.

Contribution à la Modélisation et à l'Optimisation de la Machine Asynchrone Double Alimentation pour des Applications Hydrauliques de Pompage Turbinage

Résumé Les centrales hydrauliques de pompage turbinage fonctionnent principalement en utilisant des alternateurs de type synchrone évoluant à vitesse fixe. Cependant, utiliser des alternateurs à vitesse variable et, en particulier, des Machines Asynchrones à Double Alimentation (MADA) apporte des avantages non négligeables : contrôle de la puissance en mode pompe, opération au point de meilleur rendement en mode turbine et plus grande stabilité en cas de perturbation. Cette thèse a pour objectifs la progression des connaissances des phénomènes électromagnétiques régissant le fonctionnement de la MADA et d'établir une démarche en vue de son optimisation. Tout d'abord, un modèle analytique reposant en partie sur la méthode des intégrales de frontière est proposé et validé par simulations éléments finis. Ce modèle analytique prend en compte plusieurs éléments tels que la saturation du circuit magnétique, les harmoniques générés par les bobinages du stator et du rotor mais également les harmoniques dus à la forme non constante de l'entrefer. Ensuite, le modèle est appliqué à l'étude de quatre sujets d'importance pour l'ingénieur électricien : calcul des harmoniques de tension statorique à vide, calcul des pertes fer, calcul des harmoniques de couple et calcul des forces radiales électromagnétiques. Enfin une procédure de dimensionnement de la MADA reposant sur l'optimisation par algorithme génétique est décrite. Cette procédure est appliquée à la transformation d'une machine synchrone existante à pôles saillants en une MADA. Deux cas sont traités : dans un premier temps seul le rotor est remplacé tandis que le stator reste le même, dans un deuxième temps la machine est entièrement redimensionnée.